

# Thermodynamics and kinetics of phase transformations in supercooled liquid silicon



A thesis submitted towards partial fulfilment of  
PhD Degree Programme

by

YAGYIK GOSWAMI

under the guidance of

PROF. SRIKANTH SASTRY

THEORETICAL SCIENCES UNIT

JAWAHARLAL NEHRU CENTRE FOR ADVANCED SCIENTIFIC  
RESEARCH, BENGALURU

“History is a constant race between invention and catastrophe. Education helps  
but it’s never enough. You also must [submit your] run[s]”

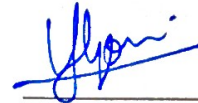
from ‘*God Emperor of Dune*’  
by Frank Herbert

This thesis is dedicated to you, the reader!  
Whether it be deep bonds, compulsion or dire need that have led you to turn these many pages, know that the plan has always been to make your life (and mine!) just a little bit better.

## DECLARATION

I hereby declare that the matter embodied in the thesis entitled "**Thermodynamics and kinetics of phase transformations in supercooled liquid silicon**" is the result of investigations carried out by me at the Theoretical Sciences Unit, Jawaharlal Nehru Centre for Advanced Scientific Research, Bangalore, India under the supervision of Prof. Srikanth Sastry and that it has not been submitted elsewhere for the award of any degree or diploma.

In keeping with the general practice in reporting scientific observations, due acknowledgement has been made whenever the work described is based on the findings of other investigators.



---

Yagyik Goswami



## CERTIFICATE

I hereby certify that the matter embodied in this thesis entitled “**Thermodynamics and kinetics of phase transformations in supercooled liquid silicon**” has been carried out by Mr. Yagyik Goswami at the Theoretical Sciences Unit, Jawaharlal Nehru Centre for Advanced Scientific Research, Bangalore, India under my supervision and that it has not been submitted elsewhere for the award of any degree or diploma.



---

Prof. Srikanth Sastry  
(Research Supervisor)



## Acknowledgements

I would like to begin by thanking Prof. Srikanth Sastry, my advisor. He has guided me throughout this effort and given me the means and the opportunity to do well. I am thankful for all that I have learned during my time here and I am certain it will stay with me for many years to come. His guidance has often reminded me to aspire to contribute, and also helped me appreciate how hard it can be to really make a contribution.

I would also like to thank my Graduate Student Advisory Committee members, Prof. Mustansir Barma, Prof. Subir Das and Prof. Meher Prakash, who along with my advisor gave valuable input at important times. I would like to extend my thanks to my group members, both past and present. Pallabi has been an incredible comrade and colleague through this journey, and our friendship is one that I cherish. Thanks also to my other dear friends in the group, Monoj, Anshul, Vinutha, Dheeraj, Varghese, Pushkar, Krishna, Swarnendu, Debargha, Shivakumar, Sebastiano, Prem Kumar, Rajneesh, Arun and Himangsu who have been wonderful colleagues. I would like to thank Vishwas Vasisht, for his help and advice as a senior colleague. In this context I will mention Sebastiano Bernini again for helping me get started during the early stages.

The faculty at the Theoretical Sciences Unit have been great teachers and well-wishers, Prof. Subir Das, Prof. Kavita Jain, Prof. Shobhana Narasimhan, Prof. Meher Prakash, Prof. Swapan Pati, Prof. Vidhyadhiraja and Prof. Umesh Waghmare – have taught me or given feedback at various times. Working in this group has given me the opportunity to learn from and receive feedback from some incredible people. Prof. Daan Frenkel, Prof. Mustansir Barma, Prof. Pablo Debenedetti, Prof. Nisanth Nair, Prof. C. A. Angell, Prof. Sapna Sarupria, Prof. Aleks Reinhardt, Prof. Pratyush Tiwary, Prof. Francis Starr, Prof. Laura Filion, Prof. Francesco Sciortino all took the time to listen and give their feedback at various points. The Centre as a whole has been of massive support in this work. In particular, Suresh, Anoop, Basavaraj and others with CCMS and with PARAM-Yukti have lent their hand on many occasions. I would also like to thank Rajeev, Chandan and the others at Complab for their help on many occasions. Those at the Dining hall, the Students Residence and security staff have become friendly and familiar faces over the years.

The JNCASR football crowd! It has been a big part of my time here, long may it continue. I have also made some dear friends as a student here. I cannot but

mention Deepak, Biswadeep, Dheeraj, Anjali, Niloy, Piyush, Mayank for keeping it interesting and for returning my bag at my wedding. A big thank you goes to my alma-mater, IISER-Pune, where I was an undergraduate. My experiences there are what led me to choose this path. I need to particularly mention Prof. Sutirth Dey and Prof. M. S. Santhanam, who have been lasting influences. Going further back, my school, The Frank Anthony Public School, played a foundational role. Especially Ms. Nirmala, who taught me to code and built my interest in algorithms which has never left me since. My extended family and my parents-in-law, who have always wished me well, offered their advice and their love. It is no small thing to know that they will be happy for me. I would finally like to mention my parents, who have given me a blessed and privileged life, and all manner of support through the years.

I am grateful, for the generosity of those around me, for the opportunities I have been given, and for whatever can perhaps only be attributed to luck.

And for Meghna. For everything she does, every day, and for painting my life with a solid shade of “better”.

# Synopsis

This is a summary of the work done under the title “**Thermodynamics and kinetics of phase transformations in supercooled liquid silicon**” by Yagyik Goswami.

We study the thermodynamics of supercooled liquid silicon with the goal of determining whether a first order liquid-liquid phase transition exists between two liquid phases. In this work, silicon is modelled using the classical Stillinger-Weber potential. This model is known to reproduce the behaviour of the real liquid well. Researchers have also previously shown evidence for a liquid-liquid phase transition based on reconstructions of the equation of state for this model. However, other subsequent work has challenged these findings. The conclusion from these studies is that slow, spontaneous crystallisation has been misinterpreted as a second metastable liquid state. Free energy calculations are argued to be necessary for an accurate study of thermodynamics because reversible sampling needs to be ensured to confirm equilibrium properties. This argument mirrors that made for the study of some models of water. Liquid silicon is known to display anomalies reminiscent of those seen in water, such as an anomalous density maximum, and a maximum in isothermal compressibility. These similarities, including similarities in microscopic structuring in the liquid, motivate comparisons between the two liquids. In the case of those specific models of water, this debate has been resolved, but an analogous investigation has not been made for silicon.

The aim of this thesis is to determine through free energy calculations whether a first order liquid-liquid phase transition occurs in silicon. Large parts of the discussion are also devoted to methods to numerically calculate the Landau free energy as a function of relevant order parameters at the state points of interest. Attention is also paid to the allied concepts of choice of order parameter and of performing free energy calculations. The first central question is whether crystallisation is in fact spontaneous in the conditions of interest. We answer this by performing a calculation of the free energy barriers to crystallisation using two independent methods and a careful choice of order parameters to distinguish the liquid state from the crystalline state. One of these methods uses constrained simulations whereas the other can be used to reconstruct the free energy kinetically from unconstrained, crystallising simulations. We find that a small but finite barrier to crystallisation exists at the relevant conditions. Therefore, the liquid state is well-defined and not

spontaneously crystallising. Results from both methods are found to agree quantitatively, removing uncertainty arising from the choice of sampling protocol. In order to understand why free energy calculations performed previously suggest barrierless crystallisation, the role of choice of order parameter is investigated in some more detail. The main conclusion is that the use of global measures of crystallinity, such as those used previously, obscure the barrier when used in some advanced sampling protocols that employ constraints. The use of a local measure, such as the size of crystalline clusters, is thus the appropriate choice. Having determined that a well-defined liquid state exists across the reported liquid-liquid phase transition line, and identified an appropriate set of order parameters to use in a constrained sampling protocol, we next investigate whether there is in fact a phase transition between two metastable liquid states. We find that there is and are able to identify conditions where these two liquids can co-exist, both being metastable with respect to crystallisation. The barrier between them is small but significant. The results are also robust when tested for thermodynamic consistency, such as with a system size analysis. The final part of this thesis is the description of a novel method to reconstruct the free energy from unconstrained simulations of the crystallising liquid. The prescription for the method is derived from the principles of reaction rates and demonstrated to work on a number of test cases where quantitative comparisons can be made.

The work is organised as follows:

**(1): Introduction** - This chapter begins by a brief motivation of the contents of this thesis. We then briefly discuss the basic framework in which the thermodynamics and kinetics of phase transitions is understood. Extended derivations are placed in an Appendix to avoid breaking the flow of the discussion. The history of the problem is described, highlighting similar classical simulation studies investigating the possibility of a liquid-liquid phase transition. Computational studies of crystallisation, specifically studies where the free energy to crystallisation is calculated, are also discussed. Related work for other model liquids and various theoretical frameworks that have been developed to make predictions and connections across different systems are also introduced.

**(2): Model and methods** - The second chapter in this work discusses the model potential, computational methods, various important quantities and the order parameters used to distinguish the crystalline phase, crystalline particles and

the metastable liquid(s).

**(3): Crystal nucleation in the deeply supercooled liquid** - In the third chapter, we investigate the possibility that the liquid loses metastability altogether with respect to the globally stable crystalline phase as suggested in recent free energy studies. Given that earlier work has shown that the metastable liquid persists in the liquid state for long periods of time at the same state point, a free energy study of crystallisation assumes some significance. This question is answered through the use of two independent methods, described in the literature, to calculate the free energy barrier to crystallisation that are most appropriate for the case of low free energy barriers where conventional methods may not work. We find through this study that there is a finite but small free energy barrier to crystallisation at all the state points considered, and therefore, that the liquid does not lose metastability with respect to the crystalline state.

**(4): Study of order parameters** - The third chapter delves deeper into the choice of sampling protocols and of the order parameter to identify the crystalline phase used in earlier work. We find that the order parameter used in earlier work, a global measure of orientational ordering (global  $Q_l$ ), does not reflect the true measure of crystalline ordering when used in simulations that use a bias potential to enhance sampling, such as conventional umbrella sampling. Two novel methods of measuring structural ordering are discussed in this chapter. This chapter also discusses other order parameters described in the literature, with results from their application to silicon.

**(5): Two order parameter reconstruction applied to Stillinger-Weber silicon** - The next part of this thesis concerns the investigation into whether a liquid-liquid phase transition occurs in metastable liquid silicon. Using the methods described in the previous chapters, extended to a two-order parameter free energy reconstruction, one observes a discontinuous change in the properties of the liquid. The co-existence conditions for the two liquids are identified and found to be in agreement with the estimates of previously published work. Finally, an analysis of the system-size dependence of the free energy surfaces is performed, as well as a characterisation of the structural changes in the liquid.

**(6): Method to reconstruct free energy surfaces as a function of two order parameters** - The final chapter describes a novel method to reconstruct Landau free energy surfaces. The method relates steady state sampling probabilities in order parameter space, such as those obtained from unconstrained simulations, to the underlying equilibrium sampling. This relationship is non-trivial because achieving reversible equilibrium sampling requires a condition of zero net flux to be met. A number of enhanced sampling methods are used to ensure that this condition is satisfied. In the novel method described here, we describe how the steady state sampling in the presence of constant flux is related to the underlying equilibrium sampling. This relation enables free energy calculations as a function of multiple order parameters from unconstrained simulations.

We end with a summary of outstanding issues. Firstly, the use of certain approximations in the free energy calculation method for two order parameters described in (6) is an issue that limits the applicability of this method. Moreover, this method has not been tested on a system such as metastable liquid silicon yet. This test is one of the first outstanding items to address. Understanding the role of interconversion timescales between the different microscopic structures on the phase behaviour of the metastable liquid is important. Lastly, one outstanding issue is to understand the mechanism of crystallisation, the geometry of growing clusters and the role of the metastable liquid in crystallisation.



# Contents

<b>1</b>	<b>Introduction</b>	<b>1</b>
1.1	Thermodynamics of the liquid state . . . . .	8
1.2	The kinetics of phase transformations – transition paths, free energies and rates . . . . .	11
1.2.1	Transition state theory . . . . .	13
1.2.2	Kramers’ escape rate to model transitions . . . . .	14
1.2.3	Computing rates from simulations . . . . .	16
1.2.4	Order parameters . . . . .	16
1.3	The crystallisation transition . . . . .	18
1.3.1	Classical nucleation theory . . . . .	19
	Critical size and barrier height . . . . .	20
	Equilibrium cluster distribution . . . . .	21
1.3.2	General derivation of the rate expression . . . . .	21
1.3.3	Crystal growth rate . . . . .	22
1.3.4	Non-classical nucleation . . . . .	23
1.3.5	Studies of crystallisation . . . . .	24
1.4	Studies of the LLPT . . . . .	28
1.4.1	Silicon . . . . .	29
1.4.2	Water . . . . .	34
1.4.3	Silica . . . . .	36
1.4.4	Phosphorus . . . . .	38

1.4.5	Carbon . . . . .	38
1.4.6	Sulphur . . . . .	38
1.4.7	Triphenylphosphine . . . . .	39
1.4.8	Solutions and biological water . . . . .	39
1.5	Phenomenology of the LLPT . . . . .	40
1.5.1	Thermodynamic scenarios . . . . .	42
	The stability limit conjecture . . . . .	42
	The two critical point scenario . . . . .	43
	The singularity free scenario . . . . .	44
	Spontaneous crystallisation . . . . .	45
1.5.2	Microscopic lattice models . . . . .	48
1.5.3	Two-state thermodynamic models . . . . .	50
1.5.4	Characterising the liquid-liquid critical point . . . . .	54
1.5.5	Connecting simulations to phenomenological models . . . . .	56
1.6	Scope of the thesis . . . . .	57
<b>2</b>	<b>Model and methods</b>	<b>58</b>
2.1	The Stillinger-Weber potential . . . . .	58
2.2	Molecular dynamics . . . . .	59
2.3	Monte Carlo . . . . .	61
2.4	Structural parameters - Radial distribution function and static structure factor . . . . .	62
2.5	Dynamical quantities . . . . .	63
2.5.1	Time auto-correlation functions . . . . .	63
2.5.2	Self-intermediate scattering function . . . . .	64
2.6	Order parameters . . . . .	65
2.6.1	Bond orientational order . . . . .	66
2.6.2	Defining crystalline particles . . . . .	67

2.7	Kinetic reconstruction of the free energy from the mean first passage time . . . . .	69
2.8	Umbrella sampling . . . . .	73
2.8.1	Parallel tempering . . . . .	77
2.9	Histogram reweighting . . . . .	80
2.10	Thermodynamic integration . . . . .	81
2.11	Measuring compressibility . . . . .	82
<b>3</b>	<b>Crystallisation in deeply supercooled Stillinger-Weber silicon</b>	<b>83</b>
3.1	Introduction . . . . .	83
3.2	Defining crystalline particles . . . . .	86
3.3	Simulation methods . . . . .	87
3.3.1	Molecular dynamics simulations: Initial conditions . . . . .	89
3.3.2	Variation of the properties of the metastable liquid with temperature . . . . .	89
3.3.3	Umbrella sampling Monte Carlo simulations: Initial conditions	91
3.3.4	Consistency of free energy reconstructions at small cluster sizes . . . . .	93
3.4	Results . . . . .	95
3.4.1	Comparing results at small cluster sizes . . . . .	95
3.4.2	Kinetic reconstruction of free energy from MFPT . . . . .	97
3.4.3	Free Energy profiles across the Widom line . . . . .	99
3.4.4	Dependence of barrier height and critical size on temperature	102
3.4.5	Microscopic structuring of the liquid around crystalline particles	105
3.4.6	Effect of changing the ensemble of starting configurations at $T = 1055\text{K}$ . . . . .	107
3.4.7	Measuring the chemical potential from thermodynamic integration . . . . .	107
3.5	Discussion . . . . .	110
<b>4</b>	<b>Order parameters</b>	<b>112</b>

4.1	Global vs local measures of crystalline ordering . . . . .	113
4.1.1	$Q_6$ bias does not constrain the degree of crystallinity . . . . .	115
4.1.2	Configurations sampled under $Q_6$ bias have higher degree of polycrystallinity . . . . .	119
4.1.3	Kinetic reconstruction of free energy as a function of $Q_6$ ) . . . . .	125
4.1.4	Umbrella sampling results with $Q_6$ . . . . .	135
	Summary . . . . .	137
4.2	Other order parameters to distinguish phases . . . . .	138
4.2.1	Ring statistics . . . . .	138
4.2.2	Local average bond orientational order $q_l$ . . . . .	141
4.2.3	Coordination number and fraction of 4-coordinated particles . . . . .	146
4.3	Overview of the literature on order parameters . . . . .	148
4.4	Discussion . . . . .	149
<b>5</b>	<b>Metastable liquid-liquid phase transition in silicon</b> . . . . .	<b>151</b>
5.1	Methods . . . . .	154
5.1.1	Order parameters . . . . .	154
5.1.2	Umbrella sampling . . . . .	155
	Parallel tempering . . . . .	159
5.1.3	Convergence and sampling tests for umbrella sampling runs . . . . .	160
5.2	Results . . . . .	161
5.2.1	Results for $P = 0.75$ GPa . . . . .	162
	Convergence tests for full two-order parameter umbrella sampling simulations . . . . .	162
	Histogram reweighting at $P = 0.75$ GPa to test for equilibrium sampling . . . . .	165
5.2.2	Convergence of simulations far from co-existence conditions . . . . .	171
5.2.3	Equivalence of reconstruction methods far from co-existence . . . . .	173
5.2.4	Results along other isobars . . . . .	174
5.2.5	Absence of bi-modality beyond the critical point . . . . .	178

5.2.6	Free energy reconstructions at larger system sizes . . . . .	178
5.2.7	Coexistence curves for the liquid-liquid phase transition . . .	187
5.3	Discussion . . . . .	188
<b>6</b>	<b>Kinetic reconstruction of free energies as a function of multiple order parameters</b>	<b>190</b>
6.1	2D kinetic reconstruction method . . . . .	191
6.2	Description of test system . . . . .	193
6.2.1	MFPT and steady state probability . . . . .	194
6.2.2	1D free energy barrier . . . . .	195
6.2.3	Sampling along orthogonal order parameters . . . . .	195
6.2.4	Summary - Sampling errors for high T/low barrier cases . .	196
6.3	Relating steady state sampling to equilibrium sampling . . . . .	197
6.3.1	Partition functions over trajectories and defining the rate . .	197
6.3.2	Effect of modifying the sampling probability on the rate . .	200
6.3.3	Adding an alternate absorbing condition – steady state flux	202
6.3.4	Inferring equilibrium sampling to steady state sampling at constant flux . . . . .	208
6.3.5	Using this prescription . . . . .	209
6.4	Tests . . . . .	211
6.4.1	Improving estimates of $\Phi_{so \rightarrow xy}$ and $\Phi_{xy \rightarrow so}$ . . . . .	212
	Comparison of results with improved estimates . . . . .	214
6.4.2	Introducing a reflecting boundary . . . . .	214
6.4.3	Tests on an alternate potential - 3 metastable basins . . . .	218
6.4.4	Tests on an alternate potential - two saddles . . . . .	219
6.5	Discussion . . . . .	220
<b>7</b>	<b>Conclusions</b>	<b>222</b>
<b>A</b>	<b>Appendix</b>	<b>226</b>

A.1	Thermodynamics of the liquid state . . . . .	226
A.1.1	The thermodynamic state of a substance . . . . .	227
	Limits of stability . . . . .	229
	Phase transitions from the metastable to the stable state . .	230
	The Landau free energy . . . . .	232
A.2	Phase transformations as diffusive barrier crossing . . . . .	233
A.2.1	The Smoluchowski equation . . . . .	233
A.2.2	The mean first passage time . . . . .	235
A.3	Crystallisation . . . . .	238
A.3.1	The driving force for crystallisation . . . . .	238
A.3.2	Classical nucleation theory . . . . .	239
A.3.3	Excess free energy and surface term . . . . .	240
A.3.4	The surface term . . . . .	242
A.3.5	Equilibrium cluster distribution . . . . .	243
A.3.6	General derivation of the rate expression . . . . .	243
	Stationary nucleation rate . . . . .	245
A.4	Deriving the WHAM equations . . . . .	247
	<b>Bibliography</b>	<b>252</b>

# List of Figures

1.1	Schematic phase diagram and free energy reconstruction showing barrier-less crystallisation. . . . .	4
1.2	Schematic for transition state. . . . .	12
1.3	Schematic of nuclei of the new phase in the parent phase and of the interface separating them. . . . .	20
1.4	Schematics for Forward Flux sampling and for Metadynamics. . . . .	28
1.5	First principles molecular dynamics results from the literature. . . . .	31
1.6	Results from Sastry and Angell [1]. . . . .	33
1.7	Equation of state and phase diagram for SW silicon from Vasisht <i>et al</i> [2]. . . . .	33
1.8	Free energy calculations for water from the literature. . . . .	35
1.9	Free energy calculations for silica from the literature. . . . .	37
1.10	Schematic of thermodynamic scenarios. . . . .	45
1.11	Schematic annotated phase diagram for silicon. . . . .	47
1.12	Schematics for lattice models of water from Sastry <i>et al.</i> [3]. . . . .	49
1.13	Schematic for the free energy of mixtures. . . . .	53
1.14	Schematic showing solutions of the fraction of $B$ type particles in a mixture model. . . . .	54
2.1	Distribution of order parameters ( $q_3$ and $Re(q_3(i).q_3(j))$ ) for HDL, LDL and non-crystallised configurations. . . . .	69
2.2	Distribution of order parameters ( $q_6$ and $Re(q_6(i).q_6(j))$ ) for HDL, LDL and non-crystallised configurations. . . . .	69

2.3	The dimensionless potential/free energy function, corresponding mean first passage times and steady state sampling probabilities as a function of some general coordinate $x$ . . . . .	72
2.4	Reconstruction of the free energy from umbrella sampling for $n$ from HWUS MC, and for density, $\rho$ , with harmonic bias USMC. . . . .	77
2.5	Representative image tracking time series of the order parameter for simulations with different bias potentials in umbrella sampling scheme. 79	
3.1	Distribution of order parameters ( $q_3$ and $Re(q_3(i).q_3(j))$ ) for HDL, LDL and non-crystallised configurations. . . . .	86
3.2	Mean first passage time of density, $\rho$ , from independent MD runs at five temperatures. . . . .	90
3.3	Density profile for first 0.5 $ns$ from independent MD runs at five temperatures. . . . .	90
3.4	Average density and inherent structure energy vs temperature from two sets of starting conditions. . . . .	91
3.5	Comparison of free energy reconstructions at $T = 1070K$ , $P = 0$ GPa using both $n$ and $n_{max}$ at two system sizes. . . . .	97
3.6	$-\ln(P_{st}(n_{max}))$ and $\tau_{MFPT}(n_{max})$ plotted against $n_{max}$ for different temperatures. . . . .	98
3.7	1D nucleation barrier obtained using MFPT and HW bias methods at different temperatures. . . . .	100
3.8	The phase diagram of SW silicon showing the loci of interest and iso-lines along which the free energy barrier to crystallisation is calculated.101	
3.9	Free energy difference $\beta\Delta G$ against the nucleus size obtained from NPT umbrella sampling MC simulation at $P = -1.88GPa$ . . . . .	102
3.10	Critical cluster size $n^*$ and height of the free energy barrier, $\beta\Delta G^*$ as a function of temperature at different pressures. . . . .	103
3.11	A parametric plot of the barrier height, $\beta\Delta G^*$ and the corresponding critical cluster size, $n^*$ obtained from different isobars. . . . .	104
3.12	Radial distribution of LDL-like and HDL-like particles around crystalline clusters at $T = 1055K$ , $P = 0$ GPa. . . . .	106



3.13	Radial distribution of LDL-like and HDL-like particles around crystalline clusters at $T = 1080K$ , $P = 0 \text{ GPa}$ . . . . .	106
3.14	Comparison of free energy reconstructions from two sets of umbrella sampling runs with hard wall bias. . . . .	108
3.15	Isotherms (EOS) for the liquid and for the crystal. . . . .	109
3.16	Difference in chemical potential vs temperature and barrier height along the $P = 0 \text{ GPa}$ isobar vs the corresponding value of $1/ - \Delta\mu^2$ . . . . .	109
4.1	Non-crystallising trajectories at $T = 1055K$ , $1070K$ at two system sizes, $N = 512, 4000$ at $P = 0 \text{ GPa}$ . . . . .	114
4.2	Distribution of $Q_6$ values for the liquid from unbiased MD runs with the distribution from biased USMC runs. . . . .	115
4.3	Negative log of the steady state $P_{st}(Q_6, n_{\max})$ from the set of crystallising trajectories for 5 temperatures at $P = 0 \text{ GPa}$ . . . . .	116
4.4	$Q_6$ bias applied at $Q_6^0 = 0.05$ , $k_{Q_6} = 10^4\epsilon$ for $N = 512$ particles at different temperatures. . . . .	117
4.5	Slice of $P(n_{\max}; Q_6 = 0.05)$ compared for the unconstrained case vs the case of a constraint on $Q_6$ and heat map showing the probability of sampling different $Q_6, n_{\max}$ values when a harmonic bias is applied. . . . .	117
4.6	$Q_6$ vs $n_{\text{tot}}$ for freely crystallising MD runs at different temperatures and system sizes. . . . .	118
4.7	Typical $n_{\text{tot}}$ values sampled under the application of $Q_6$ constraint. . . . .	118
4.8	Average global $Q_6$ from a number of realisations where a fraction of well-spaced diamond cubic unit cells are rotated about the $y - \text{axis}$ through an arbitrarily chosen angle. . . . .	119
4.9	Schematic showing superposed neighbourhoods to calculate $d_v^{RMS}$ . . . . .	121
4.10	Algorithm to identify grain boundaries applied to a toy 2D case. . . . .	122
4.11	Snapshot of an NPT MC simulation of SW Si starting from diamond cubic and simulated at $T=1260K$ . . . . .	122
4.12	Schematic of “upward” and “downward” tetrahedron sites and rotation by 90 degrees. . . . .	122

4.13 Schematic of “upward” and “downward” tetrahedron sites and rotation by 60 degrees. . . . .	123
4.14 Comparison of the number of crystalline clusters of a given size, $n$ , and of crystallites of size $n$ for $N = 512$ at two temperatures. . . . .	124
4.15 Comparison of the number of crystalline clusters of a given size, $n$ , and of crystallites of size $n$ for $N = 4000$ at two temperatures. . . . .	124
4.16 MFPT, $\tau_{MFPT}(Q_6)$ and the steady state probability $P_{st}(Q_6)$ . . . . .	126
4.17 Average $n_{\max}$ for a given $Q_6$ and the average $Q_6$ for a given $n_{\max}$ . . . . .	128
4.18 Mapping $n_{\max}$ and $Q_6$ from values at first passage. . . . .	129
4.19 Numerical calculation of the derivative $dn_{\max}(Q_6)/dQ_6$ or $dQ_6/dn_{\max}$ from each of the two parametric equations. . . . .	131
4.20 Numerical calculation of the derivative $dn_{\max}(Q_6)/dQ_6$ or $dQ_6/dn_{\max}$ from each of the two parametric equations. . . . .	132
4.21 Negative log of the steady state $P_{st}(Q_6, n_{\max})$ from a set of 10 crystallising trajectories. . . . .	134
4.22 Raw histograms of $Q_6$ under application of bias potential, the negative log of the unbiased distributions and the stitched free energy at $T = 1070K, P = 0\text{GPa}$ . . . . .	135
4.23 Free energy curves as a function of $Q_6$ performed at 3 temperatures at $P = 0$ GPa with $N = 512$ . . . . .	136
4.24 Comparison between the kinetic reconstruction using $Q_6$ , umbrella sampling results for $Q_6$ , and the mapping of kinetic reconstruction results from $Q_6$ to $n_{\max}$ . . . . .	136
4.25 Distribution of number and average length of the rings each particle participates in for the crystal and the liquid at different temperatures at $P = 0$ GPa. . . . .	142
4.26 Distribution of $q_3$ and $q_6$ for the crystal and the liquid at different temperatures at $P = 0$ GPa. . . . .	146
4.27 Distribution of $q_3$ for the crystal and the liquid at different temperatures at $P = 0$ GPa. . . . .	147

5.1	Decay of time auto-correlation function for density, $Q_6$ , and for density window index for each of the density bias windows, $\rho_0$ , subject to the constraint of $n_{\max} \leq 3$ at $T = 985\text{K}$ , $P = 0.75$ GPa. . . . .	163
5.2	Decay of time auto-correlation function for density, $Q_6$ , and for density window index for each of the density bias windows, $\rho_0$ , subject to the constraint of $n_{\max} \leq 3$ at $T = 992\text{K}$ , $P = 0.75$ GPa. . . . .	164
5.3	$\beta\Delta G(\rho)$ at $T = 992\text{K}$ , $P = 0.75$ GPa from histogram reweighting .	165
5.4	$\beta\Delta G(\rho)$ from histogram reweighting across $P = 0.75$ GPa . . . . .	166
5.5	Free energy barrier to crystal nucleation, free energy as a function of density, and free energy from the joint distribution of density and cluster size. . . . .	167
5.6	$\beta\Delta G(n, \rho)$ for $N = 512$ across $P = 0.75$ GPa . . . . .	168
5.7	$\beta\Delta G(n, \rho)$ for $N = 512$ across $P = 0.75$ GPa zoomed to small $n$ . . .	169
5.8	$-\ln(P(\rho, PE))$ at $T = 992\text{K}$ , $P = 0.75$ GPa from histogram reweighting at other temperatures across $P = 0.75$ GPa . . . . .	170
5.9	Negative log of the distribution of density and potential energy per particle at different temperatures. . . . .	171
5.10	Autocorrelation of density, $C_\rho(t)$ , and $Q_6$ , $C_{Q_6}(t)$ at $T = 96\text{K}$ , $P = 0.75$ GPa with $N = 512$ . . . . .	172
5.11	Autocorrelation of density, $C_\rho(t)$ , and $Q_6$ , $C_{Q_6}(t)$ at $T = 975\text{K}$ , $P = 0.75$ GPa with $N = 512$ . . . . .	172
5.12	Autocorrelation of density, $C_\rho(t)$ , and $Q_6$ , $C_{Q_6}(t)$ at $T = 1005\text{K}$ , $P = 0.75$ GPa with $N = 512$ . . . . .	172
5.13	Autocorrelation of density, $C_\rho(t)$ , and $Q_6$ , $C_{Q_6}(t)$ at $T = 1015\text{K}$ , $P = 0.75$ GPa with $N = 512$ . . . . .	172
5.14	Comparison of $\beta\Delta G(\rho)$ at different temperatures along the $P = 0.75$ GPa isobar. . . . .	173
5.15	Average length and number of excursions, and the number of visits to the lowest or highest temperature. . . . .	174
5.16	Decay of time auto-correlation function for density, $Q_6$ , and for density window index for each of the density bias windows, $\rho_0$ , subject to the constraint of $n_{\max} \leq 3$ at $T = 1060\text{K}$ , $P = 0$ GPa. . . . .	175

5.17	Decay of time auto-correlation function for density, $Q_6$ , and for density window index for each of the density bias windows, $\rho_0$ , subject to the constraint of $n_{\max} \leq 3$ at $T = 915\text{K}$ , $P = 1.5$ GPa. . . . .	176
5.18	Free energy barrier to crystallisation and free energy as a function of density along the $P = 0$ GPa isobar. . . . .	177
5.19	Free energy barrier to crystallisation and free energy as a function of density along the $P = 1.5$ GPa isobar. . . . .	177
5.20	Equilibrium sampled density distributions from USMC simulations and mean fraction of 4-coordinated particles from the equilibrium sampling probability. . . . .	179
5.21	Decay of time auto-correlation function for density, $Q_6$ , and for density window index for each of the density bias windows, $\rho_0$ , subject to the constraint of $n_{\max} \leq 3$ at $T = 992\text{K}$ , $P = 0.75$ GPa. . . . .	180
5.22	Decay of time auto-correlation function for density, $Q_6$ , and for density window index for each of the density bias windows, $\rho_0$ , subject to the constraint of $n_{\max} \leq 3$ at $T = 992\text{K}$ , $P = 0.75$ GPa. . . . .	181
5.23	Decay of time auto-correlation function for density, $Q_6$ , and for density window index for each of the density bias windows, $\rho_0$ , subject to the constraint of $n_{\max} \leq 4$ at $T = 992\text{K}$ , $P = 0.75$ GPa. . . . .	182
5.24	$\beta\Delta G(\rho)$ from USMC simulations at $T = 985\text{K}$ and $P = 0.75$ GPa at $N = 512, 1000, 1500, 2000$ particles. . . . .	183
5.25	$\beta\Delta G(\rho)$ from USMC simulations at $T = 992\text{K}$ and $P = 0.75$ GPa at $N = 512, 1000, 1500, 2000$ particles. . . . .	184
5.26	$\beta\Delta G(n, \rho)$ for $N = 800$ across $P = 0.75$ GPa. . . . .	185
5.27	$\beta\Delta G(n, \rho)$ for $N = 800$ across $P = 0.75$ GPa zoomed to small $n$ . . .	186
5.28	Coexistence curves for the LLPT. . . . .	187
5.29	Reweighted free energies to determine coexistence curves. . . . .	188
6.1	Model potential energy landscape . . . . .	194
6.2	Mean first passage time, $\tau_{MFPT}(x)$ and the steady state probability $P_{st}(x)$ . . . . .	194
6.3	1D free energy $\Delta G(x)$ obtained from Eq. 6.9. . . . .	195

6.4	Slices at $x = 0.01$ taken along the $y$ direction. . . . .	196
6.5	Schematic of trajectories going from state $A$ to state $B$ . . . . .	199
6.6	Schematic depicting a case with an additional absorbing state introduced at $C$ . . . . .	202
6.7	Results for the two order parameter kinetic reconstruction at $T = 0.08$ for different barrier heights. . . . .	212
6.8	Reconstruction of the 2OP free energy. . . . .	212
6.9	Potential surface and its reconstruction for improved estimates using an interface. . . . .	214
6.10	The case of imposing a reflecting boundary. Reconstructing the potential and error after $4 \times 10^6$ and $10 \times 10^6$ MC steps. . . . .	215
6.11	The case of imposing a reflecting boundary. Reconstructing the potential and error after $3 \times 10^6$ and $20 \times 10^6$ MC steps. . . . .	216
6.12	The case of imposing a reflecting boundary. Reconstructing the potential and error after $5 \times 10^6$ and $20 \times 10^6$ MC steps. . . . .	217
6.13	Reconstructions of the one order parameter free energy along $x$ and for a slice along $y$ for landscape with three metastable states. . . . .	218
6.14	Reconstruction of the 2OP free energy for landscape with three metastable states. . . . .	219
6.15	A potential with 2 saddles separating metastable states. . . . .	219
6.16	Reconstruction of the two order parameter free energy for a potential with two saddles. . . . .	220
A.1	Schematic for thermodynamics of the liquid state. . . . .	231

# Chapter 1

## Introduction

Silicon as a substance is most familiar as a solid and for its utility in electronics and, as a result, in computing. It is perhaps appropriate, therefore, to conduct a computational, *in silico*, study of the properties of silicon. There is an extensive body of literature of such studies, and a number of them focus on the liquid state, where it also has interesting properties which have generated intense scientific interest. Liquid silicon is known to freeze at 1687K at ambient pressure [4]. Some of its most interesting behaviour, however, is seen when the liquid is supercooled (cooled below the melting temperature) or in simulations where it is stretched (negative pressures) [4,5]. The state in which a substance will exist under a given set of conditions is addressed through a study of thermodynamics. Spaepen and Turnbull [6] and Bagley and Chen [7] conducted a thermodynamic study through calorimetric data and brought attention to an apparent transition from the liquid to an amorphous solid around 300K below the melting point. Around the same time, Aptekar [8] used a two-state model to propose a phase diagram with two distinct non-crystalline states, suggesting that the transition was between two liquid states.

At the time of these studies, the semiconductor and electronics industries were burgeoning, and the computing revolution was accelerating. Interest in both silicon and germanium at the time was motivated by this. However, it is important to note that the current state-of-the-art in the use of silicon in electronics and microcircuitry relies on the use of monocrystalline semiconducting silicon wafers, which are a monolithic, defect-free slice of pure crystalline silicon on which microscopic integrated circuits are supported [9, 10]. The primary challenge is to produce a large, continuously defect-free piece of crystalline silicon at near-ambient

---

conditions, which are deeply supercooled for liquid silicon. Aside from purification, glassiness of the liquid and polycrystallinity hinder their production. These wafers are usually produced through the Czochralski method, itself first proposed in the early 20<sup>th</sup> century but since then improved and perfected [11,12]. Amorphous silicon is used in lower-end and larger electronics devices. The liquid-liquid phase transition (LLPT) was proposed as an underlying cause for the presence of different amorphous forms with different electronic properties at a time when the production of the monocrystalline wafer was not as prevalent as it is today. The question of the LLPT thus has fewer implications for how silicon is used than it does for how phase transitions and thermodynamics are understood, and this latter interest has endured due to the conceptual challenges involved.

Interest in the peculiar thermodynamics of supercooled liquid silicon was heightened due to concurrent investigations into the behaviour of liquid water, which was well-known at the time to behave anomalously upon cooling [13]. Subsequent attempts to understand anomalies in water through numerical investigations suggested, among others, the possibility of a LLPT [14]. Similarities between the behaviour of liquid water and liquid silicon will perhaps not come as a surprise to some. Both crystallise to open, four-coordinated diamond structures, due to hydrogen bonding in water, and due to tetravalency in silicon, and show significant degrees of tetrahedral ordering in the liquid state. Moreover, the anomalous maximum in the density of liquid water is also observed in liquid silicon under conditions of metastability. Both expand when cooled below a certain temperature, unlike so-called simple liquids. Other substances such as germanium, carbon, phosphorous, triphenyl phosphite are known to show similar behaviour [15,16]. In the schematic phase diagram in the left panel of Fig. 1.1, we see that at temperatures lower than liquid-crystal co-existence, to the left of the brown line, i.e., at lower temperatures, one observes the curve of density maxima, marked as a red line with solid red symbols. The volume of the liquid increases when cooled to temperatures to the left of the red line – behaviour that is also well-known for water. One also observes that the compressibility of the liquid, which is a measure of how much the volume of the fluid fluctuates at constant temperature and pressure, peaks at certain values. The peak value gets progressively higher as we trace the line of compressibility maxima from low to high pressures, and diverges at the critical point – marking an instability in the liquid. These concepts are discussed in Section 1.1, with the relevant studies on silicon summarised in Section 1.4.1

This range of interesting behaviour is observed significantly below the freezing

---

temperature, where the liquid is metastable and the eventual fate of the substance is the crystalline state. The propensity to crystallise in fact poses a significant challenge in investigating and verifying proposed thermodynamic scenarios [4]. The methods described in the literature to study crystallisation computationally are included in section 1.3.5. The estimated location of the transition line and the critical point in the temperature-pressure phase diagram mean that observing the liquid for reasonable timescales before crystallisation occurs proves to be difficult, this region of the phase diagram being termed “no man’s land” as a consequence [17]. A combination of sluggish dynamics and fast crystallisation stand as obstacles to experimental investigations under these conditions. If we consider the schematic phase diagram for model silicon in the left panel of Fig. 1.1, we see the liquid-crystal co-existence line in brown. Studies performed at these conditions are challenging because the crystalline state is the most stable state and the liquid can be observed only for finite timescales. As we move further away from the brown line, crystallisation becomes more rapid, and the dynamics also become slower. At the conditions where the LLPT is said to occur, both simulations and experiments are extremely difficult to perform, and this is a central challenge to addressing the question of whether the LLPT does in fact occur.

Recent progress in experimental studies is due in large part to sophisticated techniques to prevent crystallisation by avoiding interaction with the walls and probing the liquid at high temporal resolution [5]. Notable experimental works, probing the phase behaviour of deeply supercooled silicon include the work of Kim *et al.*, where electrostatic levitation was used to prevent crystallisation induced by the container walls and temperatures as low as  $T = 1350\text{K}$  were probed [19]. Subsequently, Beye *et al* used ultra-fast pump probe spectroscopy to discern changes in the electronic structure to identify a two-step change in the melt from semiconductor to semi-metal to a high temperature metallic liquid [20]. However, a large number of studies on the metastable liquid have been computational, given that expected LLPT is expected to occur at  $\sim 1060\text{K}$ , significantly lower than the temperatures accessed in recent experiments ( $T \approx 1350\text{K}$ ) [1]. However, in the case of computational simulations as well, slow dynamics and the certainty of crystallisation pose a challenge to effectively observing and measuring the properties of the metastable liquid using conventional methods.

A combination of small system sizes (measured crystallisation rates scale with the volume), advanced sampling techniques and other computational tricks provide promising avenues to address the challenges posed by crystallisation and arrive at



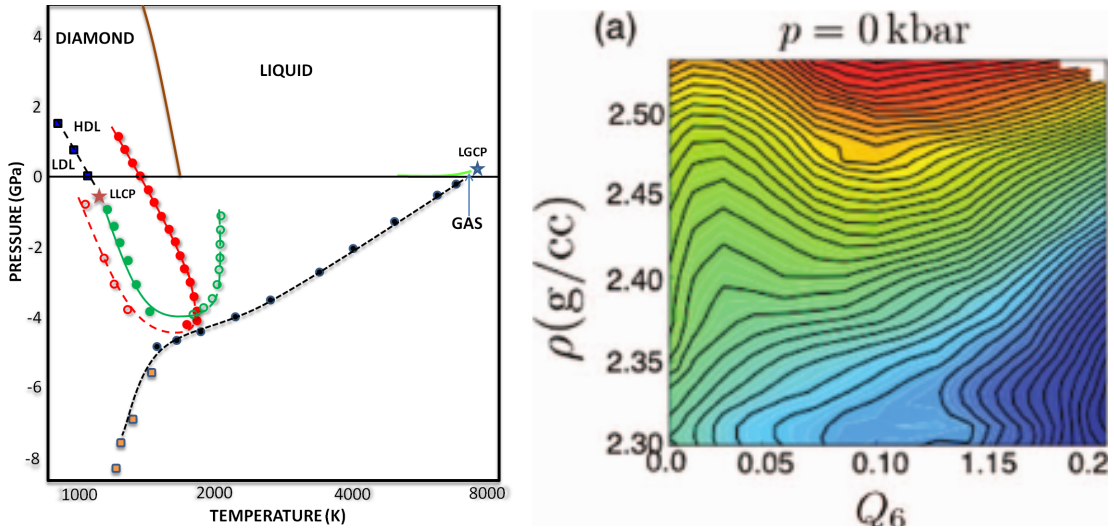


Figure 1.1: (*Left*) Schematic of the phase diagram for Stillinger-Weber (SW) silicon showing loci of thermodynamic anomalies and location of the LLPT and LLCP from equation of state studies. The brown curve is the melting line, the red curve is the line of density extrema with solid circles for maxima and hollow circles for minima. The green curve is for compressibility extrema with the solid circles for maxima and the hollow circles for minima. The line marked “LLPT” with dark blues squares is the LLPT line. The red star is the liquid-liquid critical point “LLCP”. The liquid is the most stable state at higher temperatures, i.e., to the right of the brown line. The crystal is more stable to the left. Note the negative slope of the line, which is because the crystal has lower volume than the liquid (see Section 1.5 for more on this). The high density liquid (HDL) is the more stable metastable state to the right and the LDL is the predominant metastable state to the left. A cone of co-existence conditions where both are metastable exists on either side of the LLPT line, converging at the critical point “LLCP”. [From Vasisht and Sastry [4] with permission.] (*Right*) The free energy surface as a function of density,  $\rho$  and a crystallinity order parameter,  $Q_6$ , from umbrella sampling simulations at  $T = 1050\text{K}$ ,  $P = 0$  GPa for  $N = 512$  particles. Contours are spaced  $2k_B T$  apart. There appears to be no barrier to crystallisation (along  $Q_6$ ) at these conditions. This is in contradiction to the phase diagram on the left, according to which one should observe a well-defined metastable low density liquid and a finite barrier to crystallisation. [From Limmer and Chandler [18] with permission.]

---

robust conclusions regarding the existence of the LLPT – insofar as the model potential used to describe silicon is appropriate. *Ab-initio* methods have proved successful, given that changes in amorphous silicon are accompanied by changes in electronic structure; silicon is a semiconductor in the solid-state, a semi-metal in the low density liquid state and a metallic liquid in the high temperature, high density liquid state [21–24]. Classical simulations typically use the empirical Stillinger-Weber (SW) potential [25] for which a schematic phase diagram is shown in Fig 1.1. The subject of this thesis is the behaviour of SW silicon, and the existing body of work for SW silicon will be discussed in detail. The SW potential is known to reproduce the experimentally observed behaviour of silicon remarkably well [4]. While the SW potential underestimates the density, the deviations are noted to be within the errors reported across different experimental studies. Ref. [4] discusses this aspect in greater detail. A more in-depth review of the literature on silicon is presented in Section 1.4.1.

Within the family of such liquids, i.e., displaying anomalies and demonstrating a tendency to form open, network-like structures, silicon’s more illustrious cousin is most certainly water. This is not without reason, since the metastability of water and the gamut of behaviour seen in near-ambient conditions has far-reaching implications in biology, in weather systems, industrial applications and many other contexts. In the case of water too, computational investigations with a number of different model potentials have yielded considerable insight into the behaviour of the supercooled liquid. The large majority of theoretical frameworks developed to describe and make predictions regarding the behaviour of anomalous liquids have been conceived with water in mind – motivated by the need to explain the observed anomalies, rather than by the need to verify the presence of a LLPT. A number of scenarios have been proposed to explain the presence of these anomalies, and their interaction with the LLPT. These are summarised below, with details in Section 1.5.1. Early investigations attempting to understand the implications of the anomalous density maximum suggested a change in slope of the liquid-vapour limit of stability. Speedy argued that this was necessitated by thermodynamic consistency [13], keeping in mind the observation of an imminent line of compressibility maxima – itself potentially a sign of a limit of stability or of a phase transition. These arguments were formulated with the important assumption that the line of density maxima in the temperature-pressure phase diagram had a negative slope throughout. This scenario to explain anomalies came to be known as Speedy’s stability limit conjecture. Subsequent to this, simulation studies using the ST2 model

of water by Poole *et al* found that this assumption did not hold; the line of density maxima changed slope [14]. How about the line of compressibility maxima? Poole *et al* found that rather than intersect with any other important thermodynamic locus, the line of maxima ended in a critical point, thus presenting the possibility of a LLPT in a non-mixture context. This scenario is referred to as the two-critical-point or liquid-liquid critical point (LLCP) scenario. Sastry *et al* [3,26] later presented a scenario where the line of compressibility maxima as well as the line of maximum heat capacity could be shown to be consistent with the presence of a line of density maxima which changed slope, without the need for any singularities or phase transitions. Using a microscopic model based on the lattice-gas, they went on to make predictions for relevant quantities across the temperature-pressure phase diagram. This scenario is called the “singularity free” scenario. Angell further proposed another scenario where the LLCP was situated at conditions where the liquid was unstable with respect to the vapour, i.e., at deeply negative pressures [27]. Limmer and Chandler, on the basis of computational free energy calculations, argued that the apparent LLPT was in fact a result of the loss of metastability of the liquid with respect to crystallisation, i.e., spontaneous crystallisation where the free energy barrier between liquid and crystal reduces to zero [18,28]. This scenario was proposed for a number of variants of the ST2 model of water, as well as for SW silicon. This brought into question a lot of the work that came before it that showed evidence of a LLPT in these model liquids. Limmer and Chandler’s arguments were found to be erroneous for the case of water, as shown by extensive subsequent studies. In particular, Palmer *et al* [29] performed free energy calculations for the ST2 model of water with a number of different methods and showed that two distinct liquid phases exist. For the case of silicon, such an analysis has not been done. The details of these various arguments will be discussed more thoroughly in Section 1.5.1.

The existing body of evidence for a LLPT in SW silicon comes primarily from equation of state studies (see Section 1.4.1 for details). Sastry and Angell [1] performed molecular dynamics simulations and observed a discontinuous change in enthalpy below the melting temperature in the equation of state, suggesting a first order phase transition between two states. These were identified to be liquid-like based on structural and dynamical properties. Vasisht *et al* [2] identified a co-existence region and a transition line that ended at a critical point at negative pressures. Vasisht *et al* further characterised a number of other features of silicon across the temperature-pressure phase diagram (see Fig. 1.1 for schematic). These works estimated the transition temperature to be  $\sim 1060\text{K}$  at  $P = 0$  GPa.

---

Limmer and Chandler [18], evaluating the free energy surfaces for SW silicon, did not find any evidence of a metastable LDL, also arguing that the liquid was no longer stable with respect to crystallisation. Ricci *et al* [30] performed a similar study and came to the same conclusion. They did however mention possible issues with their choice of the order parameter, *viz.* its ability to effectively distinguish between the liquid and the crystal. Such details are at the heart of a computational investigation of an LLPT in silicon. These will be discussed thoroughly over the course of this thesis. A review of the literature on calculating free energy barriers and rates of crystallisation is presented in Section 1.3.5.

At this point, we are well-placed to motivate the contents of this thesis. Our interest is in determining whether a first order liquid-liquid phase transition occurs for metastable SW silicon at deep supercooling. Past work has presented a number of disparate scenarios, and as well highlighted the challenges posed by slow dynamics and fast crystallisation. A calculation of free energies, performed carefully, enables us to understand the thermodynamics of the system. Here too, challenges exist in ensuring that the conditions under which we can perform free energy calculations, namely equilibrium/reversible sampling, are maintained. Further, the choice of order parameters used to describe the different possible phases is an important one. A characterisation of crystallisation is pivotal to our understanding, and is therefore the first question that we seek to address.

We find that crystallisation is not spontaneous at any of the conditions of interest. The liquid retains metastability with respect to the globally stable crystalline state with significant free energy barriers to crystal nucleation. An analysis of the choice of order parameter by Limmer and Chandler [18] and by Ricci *et al* [30] reveals the source of discrepancy to be the use of a global measure of crystallinity as a bias parameter in enhanced sampling simulations. This choice is found to be the reason for observing apparently spontaneous, barrier-less crystallisation.

But what then of the metastable liquid? We first consider a number of order parameters that are used to distinguish the various phases of interest. The merits and demerits of each are also discussed in detail. With a suitable choice of sampling scheme and of order parameters, we find that SW silicon does indeed display a LLPT under the conditions where it has been shown earlier. We estimate conditions of coexistence between the two liquids and explore the behaviour of the transition across the phase diagram. Further, we perform consistency checks on the effects of changes in system size and sampling protocol and obtain consistent results throughout.

We next consider a novel method to perform free energy calculations from either constrained or unconstrained simulations, with an in-depth discussion of considerations arising from the need to obtain equilibrium sampling probabilities. Through this effort, we identify an interesting result relating sampling probabilities in order parameter space, obtained at steady state under constant flux to some absorbing condition (e.g., from molecular dynamics trajectories), to the underlying equilibrium probabilities – which are related to free energies, otherwise accessible only if zero flux and reversible sampling is maintained. A number of advanced sampling techniques rely on sophisticated algorithms to efficiently maintain the zero flux equilibrium condition.

The rest of this chapter has two main components:

- Preliminaries – background on metastable liquids, on the thermodynamics and kinetics of phase transitions and on crystal nucleation
- Review of the existing literature on the LLPT. This section motivates the problem in greater detail. It includes a brief description of other contexts and systems where LLPTs have been studied, of historical development of methods and of various other theoretical and computational approaches.

The scope of this thesis and a brief description of the contents of the other chapters is in Sec. 1.6.

## 1.1 Thermodynamics of the liquid state

Colloquial definitions of the different states of matter focus on the interaction of the substance with the container and the effect of the container on the shape and volume. Solids have a fixed shape regardless of the container, liquids assume the shape of the container without necessarily filling the volume, while gases expand to occupy the available volume of the container, and cannot be contained if the container is not closed. These definitions have been around for a long time and over time, their limitations, both apparent and presumed have spawned entire fields of study. Key questions that are not addressed by these definitions are, what of the most viscous liquids, which do not assume the shape of the container in any reasonable time scale? What of sand, which can flow like water but also be packed into a solid? And what of the near opposite, fluids with seemingly zero viscosity?

Considerable progress has been made through the quantitative study of thermodynamics. The identification of the appropriate state variables and their response to externally applied stimulus allows one to describe the state of a substance in detail. Importantly, it also enables one to identify the phase boundaries between different states of matter. Appendix A.1 contains a detailed walkthrough of these concepts. A quick summary is included below. We start with an equation of state, for example for the internal energy of a homogeneous system of identical particles:

$$U(S, V, N) = TS - PV + \mu N \quad (1.1)$$

The internal energy is a function of six variables. Importantly, however, 3 of these are control variables whose values specify the state. The internal energy is therefore an explicit function of these 3. For a system to be stable,

$$\delta U|_{S,V,N} = 0, \quad (1.2)$$

and,

$$\delta^2 U|_{S,V,N} > 0. \quad (1.3)$$

Consider  $dU$  written in the following way,

$$dU = \sum_{j=1}^{n+2} \xi_j dX_j, \quad (1.4)$$

where the  $\xi_j$  are the partial derivatives of  $U$  with respect to the independent variables  $X_j$  (entropy, volume, number of particles) and  $n$  is the number of components in the case of a mixture. Legendre transforms allow the definition of other thermodynamic potentials, also called free energies, based on the ensemble of interest. First derivatives of the free energies are discontinuous across first order phase transitions. Second derivatives of the free energies are response functions, such as the compressibility or the heat capacity.

$$\left( \frac{\delta T}{\delta s} \right)_P = \frac{T}{c_p} > 0, \quad (1.5)$$

and,

$$- \left( \frac{\delta P}{\delta v} \right)_T = \frac{1}{v\kappa_T} > 0. \quad (1.6)$$

These are discontinuous across a *continuous phase transition*. The LLPT is a first order phase transition with a discontinuity in the density across the transition.

At conditions where the two phases co-exist, the chemical potentials and the free energies are equal. Across the transition, the chemical potential of one phase is lower than the other, indicating relative stability or relative metastability. Far from co-existence conditions, one or the other phase ceases to be (meta)stable, the boundary of co-existence is called the *spinodal*. Unstable states are those for which the compressibility,  $\kappa_T$ , is negative, i.e., those which expand on applying pressures. The locus of limit of stability of a phase is given by

$$\left(\frac{\partial P}{\partial V}\right)_{T,N} = 0 \quad (1.7)$$

Details are included in Appendix A.1. At conditions where both states are metastable, with a first order phase transition separating the two states, one can define a *Landau* free energy as a function of an order parameter,  $\phi$ , that distinguishes the two states.

$$P(\phi) = \frac{\int d\mathbf{r} e^{-\beta H'(\phi(\mathbf{r}))} \delta(\phi(\mathbf{r}) - \phi)}{\int d\mathbf{r} e^{-\beta H'(\phi(\mathbf{r}))}}, \quad (1.8)$$

where  $H'$  specifies the ensemble in which the order parameter is sampled. The Landau free energy, which is phenomenological expression for the free energy as a Taylor expansion in the order parameter, can also be related to the sampling probability  $P(\phi)$  in the following way:

$$G_L(\phi) = -k_B T \ln[P(\phi)] + \text{const.} \quad (1.9)$$

The Landau free energy is usually written as a mean field expression and for a global order parameter,  $\phi$ . However, in many cases, the transformation from one phase to another is driven by the occurrence of local fluctuations of the new phase in the metastable parent phase.

One can also write the free energy from the size distribution of these fluctuations using the equation above. A system-spanning fluctuation represents a complete transformation to the new phase. When there is a free energy penalty to the growth of these fluctuations, such as due to surface tension between old and new phase, then the free energy as a function of fluctuation size has a barrier profile due to competition of the free energy penalty with the free energy gain from forming some amount of the more stable new phase. This barrier will separate two basins corresponding to the metastable states. Well-defined metastable states will thus be characterised by such basins, with the more stable state corresponding to the deeper basin. The value of  $\phi$  takes non-intersecting sets of values for the two phases. This

requirement places a restriction on the choice of order parameter. The kinetics of phase transitions described in the forthcoming section describes how the timescales over which phase transitions occur can be related to the rate with which the free energy barrier is crossed.

## 1.2 The kinetics of phase transformations – transition paths, free energies and rates

We next turn our attention to the timescales over which phase transformations occur. Often the transformation itself involves the crossing of a high barrier, the transition thus being a rare event. The two main quantities of interest are often the rate and the height of the barrier. Both quantities are challenging to compute when the occurrences are few and far between in unconstrained molecular dynamics or Monte Carlo simulations. A number of methods have been developed to enhance sampling and obtain converged estimates of the rate, most of which are formulated on a picture where, in the phase space of collective variables, there exist disjoint regions for the metastable and the stable state and one or many paths between them. Fig. 1.2 depicts the barrier crossing scenario with trajectories from  $A$  to  $B$  marking complete transitions.

When thinking in terms of a barrier-crossing, the problem of determining the rate of crossing can be split into two components:

- What is the probability of being at the top of the barrier?
- What is the probability of going to the state  $B$ , thus completing the transition, from the top of the barrier?

Of these two quantities, the first is generally treated as a static quantity, invoking the assumption of a steady state being achieved in the “reactant” side,  $A$ , before rare crossings occur. The probability of being at the top is then typically weighted by a Boltzmann factor, similar to the Arrhenius rate expression.

$$P(\phi^*) \propto e^{-\beta\Delta G^*} \quad (1.10)$$

In the treatment of the second quantity, we will briefly discuss two treatments. The first is related to Transition State Theory, and the second is attributed to Kramers.



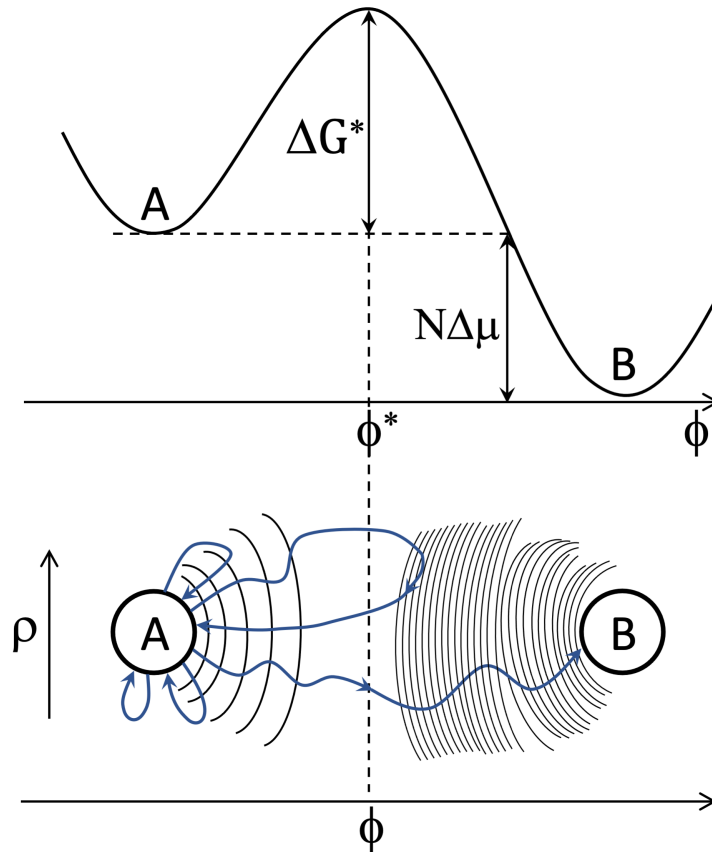


Figure 1.2: (*Top*) Depiction of the barrier separating metastable state  $A$  from the globally stable state  $B$  as a function of the order parameter  $\phi$ . The barrier height  $\beta\Delta G^*$  determines the rate while the difference in chemical potentials,  $\Delta\mu$ , is a measure of the degree of supercooling. The transition state is marked  $\phi^*$  and is the state with highest free energy cost to a first approximation. (*Bottom*) A phase space depiction of the two states  $A$  and  $B$  as a function of two order parameters  $\phi$  and  $\rho$ . The lines represent contours on the free energy surface – the number of contours between  $A$  and  $\phi^*$  is less than those from  $B$  to  $\phi^*$  since  $B$  is a deeper minimum. Note that the majority of trajectories exiting  $A$  do not reach the transition state, and that of the fraction that do, fewer still make it all the way to  $B$ .

### 1.2.1 Transition state theory

We discuss the treatment described in the works of Ref. [31], used subsequently also in the context of computational rate calculation methods [32–34]. The central approach is to relate macroscopic rates to the microscopic details of the system is to write the rate as the transport coefficient corresponding to a flux auto-correlation function, in the way of hydrodynamic transport coefficients [31]. In this representation, the rate  $k_{AB}$  is analogous to an average velocity with which trajectories started in  $A$  reach  $B$ . This rate has been shown to not vary with changes in ensemble and even across closed and open/dissipative systems. Further details on this will be set aside for now and discussed in Section 6.3. Briefly, in transition state theory the rate from  $A$  to  $B$  is written in the following way.

$$k_{AB}(t) = k_{TST}^{AB} \kappa(t) \quad (1.11)$$

The first term on the RHS is a static quantity which is the probability of being at the top of the barrier or transition state. The second quantity is a transmission co-efficient. The transmission coefficient is quantified in various ways. For example, as mentioned in [35]

$$k_{AB}(t) = \frac{1}{P_A} \left( \frac{P_{TST}}{\delta} \right) \langle v(t) \rangle \zeta \quad (1.12)$$

In the expression above,  $P_A$  is the probability of being in  $A$ ,  $P_{TST}$  is the probability of being at the transition state,  $\delta$  is the width of the transition state,  $\langle v \rangle$  is the average velocity (of the order parameter) at the transition state and  $\zeta$  is an indicator function that specifies the fraction of trajectories at the transition state which started at  $A$  and do finally end up in  $B$ .

In the work of Chandler [31] and in the subsequent transition path sampling formalism [32], the rate is written as the time derivative of the population correlation function

$$k_{AB}(t) = \frac{d}{dt} C(t) = \frac{d}{dt} \frac{\langle h_A(x_0) h_B(x_t) \rangle}{\langle h_A(x_0) \rangle} \quad (1.13)$$

In the expression above, the numerator is the time correlation of populations at  $A$  at  $t = 0$  and  $B$  at  $t$  and the ensemble is over paths connecting  $A$  and  $B$ . The denominator is the number of paths exiting  $A$ . Details are in Sec. 6.3.

In the treatments above, the rate  $k_{AB}$  is generally a time dependent quantity, with the transmission co-efficient and/or derivative of  $C(t)$ , having a time dependence. However, in the case of a steady state flux, the value can be shown to have a plateau

[31], which is treated as, and connected to the macroscopic phenomenological rate. The existence of such a plateau value over a reasonable timescale is a requirement of such a treatment.

### 1.2.2 Kramers' escape rate to model transitions

Kramers in 1940 [36] originally set out to find the rate at which a Brownian particle escapes from a potential well over a potential energy barrier. This representation has since then found a wide range of applications, particularly in the modelling of reactions or transformations where an analogy can be drawn between the potential energy landscape and the free energy landscape and as well, between the position of the Brownian particle and the collective variable or reaction coordinate that describes the reaction. In essence, the trajectories in Fig. 1.2 are modelled as Brownian swimmers executing a random walk, with a finite probability of crossing the barrier from  $A$  to  $B$  stochastically.

This analogy is most used with the important assumption that the equation of motion governing the movement of the Brownian particle is written in the limit of high friction or zero inertia (infinite mass). Another assumption that is made here is that the reaction that we wish to model can be described by a reaction coordinate (vector or scalar) that constitutes the the most slowly varying degrees of freedom for the system. All other degrees of freedom are thus assumed to relax to their equilibrium distributions nearly instantaneously, allowing us to describe the motion of the reaction coordinate as a Brownian particle in a lower dimensional space.

The probability distribution of diffusing Brownian particles is given by the Fokker-Planck equation. In the limit of high friction, the Fokker-Planck equation is modified to give the Smoluchowski equation in Eq. 1.14. We use this framework to derive the mean first passage time which is the inverse of the rates. These quantities are defined here with a more detailed derivation in Appendix A.2 We can write:

$$\frac{dP}{dt} = D \frac{\partial}{\partial x} \exp(-U(x)/k_B T) \frac{\partial}{\partial x} [\exp(U(x)/k_B T) P]. \quad (1.14)$$

This is called the *Smoluchowski equation*, which describes diffusion in an external potential. Note that  $D$  is the diffusion coefficient as given by the Einstein formula with the notation relating diffusion coefficient  $D$  to friction  $\zeta$  as,  $D = \frac{k_B T}{\zeta}$ . We can

re-write this in terms of a drift term and a diffusion term:

$$\begin{aligned}\frac{\partial P}{\partial t} &= -\frac{1}{\zeta} \frac{\partial}{\partial x} (U' P) + D \frac{\partial^2 P}{\partial x^2} = \mathcal{D}P \\ P(x, 0) &= \delta(x - x_0), \quad P(x, t) = 0 \text{ on } \partial V\end{aligned}\tag{1.15}$$

Here,  $\partial V$  denotes the surface on sub-volume  $V$ . We represent a Fokker-Planck operator  $\mathcal{D}$  which also accounts for the boundary conditions applied. We can re-write the time evolution as

$$P(x, t) = e^{t\mathcal{D}} \delta(x - x_0)\tag{1.16}$$

The operator,  $D$  is the Smoluchowski operator, giving us,

$$\begin{aligned}\mathcal{D} &= \frac{\partial}{\partial x} D(x) e^{-\beta U(x)} \frac{\partial}{\partial x} e^{\beta U(x)} \\ \mathcal{D}^* &= e^{\beta U(x)} \frac{\partial}{\partial x} D(x) e^{-\beta U(x)} \frac{\partial}{\partial x}\end{aligned}\tag{1.17}$$

The second equation follows from considering the adjoint of the differential operator and noting that the operator  $\mathcal{D}$  is of the Sturm-Liouville type (see Appendix A.2), which is self-adjoint.

The mean first passage time can be calculated by considering trajectories that explore phase space between a reflecting boundary  $a$  and an absorbing boundary  $b$ . The locations of the boundaries are chosen to coincide with the initial metastable state  $A$  and the final state  $B$  respectively. The mean first passage time is then written as the solution of the adjoint equation (see Appendix A.2 for details):

$$\begin{aligned}e^{\beta U(x)} \frac{\partial}{\partial x} D(x) e^{-\beta U(x)} \frac{\partial}{\partial x} \tau(x) &= -1 \\ \tau(x) &= \int_x^b dy \frac{1}{D(y)} e^{\beta U(y)} \int_a^y e^{-\beta U(z)} dz\end{aligned}\tag{1.18}$$

In Kramers' formulation, the rate is related to the inverse mean first passage time to the absorbing boundary  $b$ , as  $k_{AB} = 1/\tau(b)$ . In order to compute the rate, the following approximations are made:

- The integral over  $z$  is dominated by  $U$  near the minimum of the basin at  $A$ . We can expand  $U(z)$  in the following way:

$$U(z) = U_{\min} + \frac{1}{2} \omega_{\min} (z - z_{\min})^2\tag{1.19}$$

- Similarly, the integral over  $y$  is dominated by the value at the top of the barrier, where the following approximation is made:

$$U(y) = U_{\max} - \frac{1}{2}\omega_{\max}(y - y_{\max})^2 \quad (1.20)$$

In both approximations, the surface is subjected to a harmonic approximation with curvature  $\omega_{\min}$  or  $\omega_{\max}$ . The mean first passage time then reduces (assuming constant  $D$  here for simplicity) to,

$$\tau(x) = \frac{1}{2D} \frac{2\pi k_B T}{\omega_{\min}\omega_{\max}} e^{\beta\Delta U} \quad (1.21)$$

where  $\Delta U = U_{\max} - U_{\min}$ .

### 1.2.3 Computing rates from simulations

Methods such as umbrella sampling [37], forward flux sampling [38,39], transition interface sampling [40] and metadynamics [41] were devised with the aim to facilitate reversible sampling in an otherwise irreversible process. While methods such as forward flux sampling provide expressions for the rate, other methods enhance sampling near the rarely visited barrier to give estimates of the barrier height and rely on the relation between the barrier height and the rate [32].

The mean first passage time method of Reguera and co-workers [42–44] uses unconstrained molecular dynamics runs to compute both the rate and the free energy profile, but has the important requirement, along with some of the other methods mentioned, that there be only one “tunnel” of reactions that connect the metastable and the stable state.

Rates are typically determined by a calculation of the reversible probability of being at the top of the barrier, followed by a calculation of “success” rates from the barrier-top, or by calculating the mean first passage time and inverting it to get a phenomenological rate.

### 1.2.4 Order parameters

When representing the ensemble of transition paths, or constructing the Landau free energy surface, one needs to specify the collective variable or order parameter that will be used. Another important quantity is the reaction coordinate, which is

defined as the vector or scalar quantity along which the transformation proceeds. The true reaction coordinate is that which drives the reaction and quantifies the extent to which the transformation has progressed. This quantity is difficult to define, as will be discussed in slightly more detail in Chapter 4, and what is often used as order parameters is at best an approximation to whatever the true reaction coordinate might be. One can define, however, a number of different collective variables which serve the purpose of mapping the many-dimensional system (the liquid has  $3N - 6$  degrees of freedom) to a lower dimensional subspace that captures the essential differences between the two states. A good choice of such a collective variable will serve as an effective proxy to the reaction coordinate.

If the transition is between a disordered and an ordered state, for example in crystallisation or ferromagnetic ordering, it is often the case that these collective variables are called “order parameters”. The choice of order parameter has important implications, as one can imagine, in the results of free energy calculations will depend heavily on this choice. We discuss this in greater detail in subsequent chapters, with a focus on crystallisation. Another important quantity is the committor surface. Briefly, the committor for a given point in order parameter space is the probability that the system, when starting from that point, ends up in the stable state vs the probability it end up in the metastable parent state. Along each user-defined order parameter, one can calculate the committor function along other collective variables. The set of values for which the committor is half, is the transition state. Our specific interest in this thesis is to perform calculations of the Landau free energy, which allows us to calculate the barrier between the metastable and the stable state at a given state point.

In the context of supercooled network-forming liquids such as silicon, the choice of order parameters has been driven by the need to, on the one hand, distinguish effectively between liquid and crystal [16, 29], and, on the other hand, between the two possible metastable liquid forms [45]. A single order parameter that distinguishes all 3 has not been found. It is therefore common practice to use two order parameters. We will discuss in greater detail, the considerations that go into choosing a crystallinity order parameter later in the chapter. Different ways in which the two possible liquids might be distinguished is discussed in Chapter 4.

Some key facts that serve as consistency checks are the following:

- A global order parameter that distinguishes ordered crystalline states from disordered states will still have small but finite values for the disordered state.

However, the value for the disordered state will decrease as  $N^{-1/2}$ , where  $N$  is the system size, while remaining unchanged for the crystalline state.

- For two co-existing phases with macroscopic phase separation and an interface separating the two, the free energy barrier as a function of the order parameter will display a barrier. Note that this barrier is distinct from the barrier to growth of local fluctuations of one phase in the other. The barrier discussed here is a function of a global order parameter. The barrier itself will scale as  $N^{2/3}$ .

In the context of crystallisation, the importance of describing a local order parameter has been discussed in the literature [46, 47]. This will be discussed in greater detail in Chapter 3 and Chapter 4. In the context of the LLPT, the two putative liquids are known to differ in the degree of local tetrahedral ordering [1] and local density. We explore these aspects to identify the appropriate quantitative measure.

## 1.3 The crystallisation transition

At this point, we turn our attention more firmly to the study of the crystallisation transition. In general, the first order phase transition from the metastable to the stable state is driven by the change in the free energy per particle that transforms from the old, metastable state to the new, stable state.

The free energy per particle is in fact the chemical potential and the change in free energy when one particle of the parent phase is transformed to the new phase is the *supersaturation*.

$$\Delta\mu = (G_{old} - G_{new})/N \quad (1.22)$$

At co-existence,  $G_{old} = G_{new}$  and the parent phase is said to be *saturated*. At temperatures where the parent phase is metastable, the free energy difference drives the transformation from the old state to the new state.

We note that since  $\mu$  is difficult to obtain, it is often related to other, more accessible quantities, such as the heat capacity to determine the degree of *supercooling* that the metastable parent phase has undergone. Details of this are in Appendix A.3.1. We next determine the work required for the phase transition to occur, noting that a finite free energy barrier exists between the metastable parent phase and the stable new phase.

### 1.3.1 Classical nucleation theory

In general, many paths in phase space may take the metastable parent phase to the stable new phase. Each of these paths will have a different barrier that needs to be crossed. The preferred path is expected to be that along which the barrier is lowest, i.e., requiring least work. In general, one can always make the following distinction. Consider an order parameter that describes the phase transition of interest, for example the density for the case of droplet nucleation from vapour. One can consider two cases here. The first is where the density changes uniformly as the substance changes from vapour to liquid. In this case, the work required to enact the transformation is proportional to the number of particles in the system,  $N$ , as  $N\Delta\mu$  and is quite large. The second case is where local fluctuations of size  $n$  in the density occur, with fluctuations of a certain size  $n^*$  being sufficient to cross the barrier. If such a path exists, the energy cost,  $n^*\Delta\mu$  will always be less than the energy cost for the uniform change. In fact, it is found that first order phase transitions are most often driven by local fluctuations where *nuclei* or clusters of the new phase are formed. Theories that consider this picture of how phase transitions proceed have been categorised under the broad umbrella of the nucleation approach. An alternate, more recent framework of quantifying the effect of these fluctuations, called *density functional theory* has also been developed. In Fig. 1.3, we have a cartoon depicting the nucleation picture. Clusters of the globally stable phase form and disintegrate stochastically, with a nucleation event occurring when one of them is big enough, i.e., post-critical. The formation of the new phase implies that an interface exists between metastable old phase and the new phase. This interface is assumed to have a finite non-zero lengthscale, and the work required to form it represents the excess free energy in Eq. A.50.

We focus here on the nucleation approach. In this approach, the work to form the new phase is first written in terms of the work required to form a localised cluster of size  $n$ , of the new phase. Since the new phase has a lower chemical potential, it is expected to lower the free energy. An excess free energy cost related to the formation of an interface between old and new phases is also present.

$$W(n) = -n\Delta\mu + G_{ex}(n) \quad (1.23)$$

A more detailed discussion is present in Appendix A.3.2. The excess free energy comes from the formation of an interface, and is thus a *surface term*. The typical



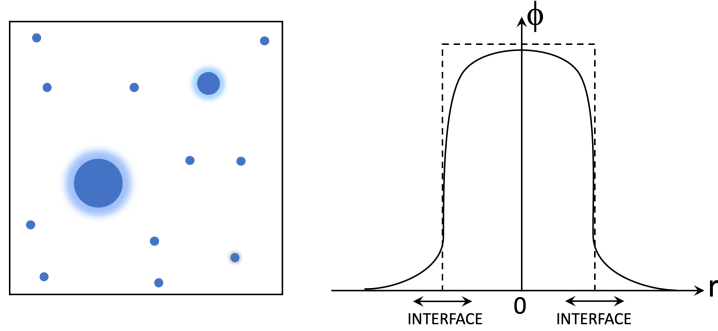


Figure 1.3: (*Left*) Cartoon depicting the formation of clusters of the globally stable new phase in the metastable old phase. Large clusters are rarer. A nucleation event occurs when a cluster crosses the critical size. The critical cluster size acts as the transition state  $\phi^*$  in Fig. 1.2. The halo around each cluster depicts the interface. (*Right*) The value of the order parameter,  $\psi$ , which differentiates the metastable phase from the globally stable phase, as a function of distance from the centre of a cluster. The change is not discontinuous, indicative of the interface of a finite lengthscale.

form, assuming a regular shaped spherical/polyhedral compact nucleus is:

$$\begin{aligned} G_{ex}(n) &= \phi(V_n) \\ G_{ex}(n) &= c\sigma V_n^{2/3} \end{aligned} \quad (1.24)$$

We use a shape factor,  $c$ , and a surface free energy per particle  $\sigma$ , which we treat here as constant. In general their variation accounts for the different surface areas of different shapes and different size dependence of the surface free energy. Details and generalisations are present in Appendix A.3.3.

### Critical size and barrier height

We consider the equations, obtained by taking the derivative of  $\beta\Delta W(n)$  with respect to  $n$ .  $n^*$  is the value for which this derivative is 0, indicating a maximum or minimum value. Considering a spherical nucleus, we get:

$$\beta\Delta W^* = \frac{16\pi}{3} \left( \frac{v'\sigma^{3/2}}{-\Delta\mu} \right)^2 \quad (1.25)$$

$$n^* = \frac{32\pi}{3} \left( \frac{(v')^{2/3}\sigma}{-\Delta\mu} \right)^3 \quad (1.26)$$

This tells us that  $\ln(\beta\Delta G^*)$  should scale with  $\ln(-\Delta\mu)$  with a slope of  $-2$  while  $\ln(n^*)$  should scale with  $\ln(-\Delta\mu)$  with a slope of  $-3$ . Here,  $\Delta\mu$  is the chemical potential difference between crystal and metastable liquid at a given state point. We test this by calculating the chemical potential of the crystal and of the liquid with respect to the reference at the melting pressure for a set of isotherms. At the melting point, the chemical potential is 0.

### Equilibrium cluster distribution

Following the description in [48], the equilibrium cluster distribution can be obtained by considering the work required to form a cluster of size  $n$ . This work can be shown to depend on the chemical potential/ free energy difference, and is related to the equilibrium probability of observing a cluster of size  $n$ :

$$-W(n) = k_B T \ln [N(n)/N(0)] \quad (1.27)$$

An extended derivation is in Appendix A.3.5, where we begin by treating the metastable liquid as a multi-component mixture of different  $n$ -mers and use the excess chemical potential of each component to arrive at an expression relating their concentration to the free energy cost and therefore the work.

### 1.3.2 General derivation of the rate expression

The general approach to calculating the nucleation rate is to construct a master equation that describes the time evolution of the number (or concentration) of clusters of size  $n$  [48, 49]. We make some key assumptions:

- Assume that the clusters are localised and clusters of all sizes are possible.
- Finite non-zero rates with which clusters of size  $n$  become clusters of size  $m$ . This can in general be time-dependent,  $f_{nm}(t)$ .
- All clusters of size  $n$  are equivalent, at least on average, allowing us to simplify our treatment and not worry about shape dependent interconversion rates,  $f_{nm}(t)$ .
- The clusters are otherwise non-interacting.
- The concentration of clusters of size  $n$  at time  $t$ ,  $N(n, t)$ , is assumed to be spatially uniform and homogeneous in the volume.

In general, the rates  $f_{nm}(t)$  need to be known to use this approach to calculate the full rate with this microscopic description. Moreover, the dependence of these rates on conditions  $(T, P, \Delta\mu)$  also need to be known.

The master equation can be written as

$$\frac{d}{dt}N(n, t) = \sum_{m=1}^{M(t)} [f_{mn}(t)N(m, t) - f_{nm}(t)N(n, t)] + K(n, t) - L(n, t) \quad (1.28)$$

$M(t)$  is the total number of available molecules at  $t$ , or the largest possible cluster size.  $K(n, t)$  and  $L(n, t)$  are respectively the probabilities of a cluster of size  $n$  appearing out of thin air at time  $t$  and disappearing into thin air at time  $t$ . In steady state, the rate of formation of nuclei of size  $n$  and  $n - 1$  are related to  $d/dtN(n, t)$  with

$$j_n - j_{n-1} = \frac{d}{dt}N(n, t) \quad (1.29)$$

Some manipulation relates this to the full rate of crystallisation:

$$J^{-1} = \sum_{n=1}^{n=\Lambda} \frac{1}{\beta A(n) p_{eq}(n)} \quad (1.30)$$

Based on this expression, knowing the equilibrium cluster distribution tells us the rate. This equilibrium distribution can be calculated by considering the minimum work required to form a cluster of size  $n$  as derived in Eq. A.68. Further, the rate  $J$  is related to the inverse mean first passage time as discussed in Section 1.2.2.

### 1.3.3 Crystal growth rate

Weinberg *et al* [50] describe a kinetic equation for the crystal growth (or shrinkage) rate based on a gain-loss master equation. They assume a large spherical cluster and write the growth rate as:

$$\frac{dR}{dt} = \left(\frac{v}{36\pi}\right)^{1/3} k_n^+ n^{-2/3} \left(1 - \frac{k_n^-}{k_n^+}\right) \quad (1.31)$$

Here,  $R$  is the radius,  $v$  is the volume per atom,  $k_n^+$  is the rate of formation of clusters sized  $n$  and  $k_n^-$  is the rate of disappearance. Next, by invoking detailed balance on the equilibrium cluster distribution, which is related to the free energy,

and sticking to the CNT approximation of a large spherical cluster, one can write

$$\frac{dR}{dt} = \left(\frac{v}{36\pi}\right)^{1/3} k_n^+ n^{-2/3} \left(1 - \exp\left[\beta\Delta G_{cl} \left(\frac{R^*}{R} - 1\right)\right]\right) \quad (1.32)$$

Here,  $R^*$  is the critical cluster radius and  $\Delta G_{cl}$  is the bulk free energy difference between liquid and crystal. Thus, the growth rate depends on the chemical potential difference between the liquid and crystal since  $\Delta\mu_{cl} = \Delta G_{cl}/N$  and not on the surface tension. Moreover, crystal growth rate slows down with supercooling regardless of the dynamics, which is a striking result [51].

### 1.3.4 Non-classical nucleation

The description of crystallisation detailed above revolved around the idea of nucleation. Small crystalline clusters form and disintegrate due to fluctuations until a post-critical nucleus forms. This nucleation event is local in nature and drives the change in phase from liquid to crystal. In computing both the free energy barrier and the rates, a number of assumptions and approximations have been made. Key among those is that of independently forming, rare and non-interacting clusters. One other is that the critical nucleus is considered large, approximately spherical. Finally, increase and reduction in size of the crystalline cluster is through mechanisms of attachment and detachment, which for simplicity are considered both size and time-independent.

In the context of the liquid-gas phase transition, Cahn and Hilliar made prominent efforts to understand the nature of the transition through a density functional approach near the spinodal stability limit of the liquid [52,53]. Analogous questions can be asked regarding the limit of stability of the liquid with respect to crystallisation [54,55]. The density functional approach has also been applied to the study of freezing at deep supercooling, with notable works including that of Ramakrishnan and Yussouff [56–59]. The key idea is to consider the fluid as non-uniform and to then write the free energy as a functional of the order parameter. Here, considering density we can write [57,60]:

$$F[\rho(\mathbf{r})] = F_{id}[\rho(\mathbf{r})] + F_{ex}[\rho(\mathbf{r})] \quad (1.33)$$

The free energy is written as a functional of the order parameter, i.e., integrated over all space. The ideal (*id*) contribution comes from considering a system without

interparticle interactions, while the excess part (*ex*) comes from the interactions.

$$\beta F_{id} = \int d\mathbf{r} \rho(\mathbf{r}) (\ln(\rho(\mathbf{r})\Lambda^d) - 1) \quad (1.34)$$

We have considered a  $d$  dimensional system above, and the constant  $\Lambda$  relates to the integral over the kinetic energy part of the Hamiltonian in the usual way. The excess part is usually written considering the number density fluctuations/ordering and two, three and many-body correlations.

$$\begin{aligned} \beta F_{ex}[\rho(\mathbf{r})] = & \text{const.} + \int d\mathbf{r} g^{(1)}(\mathbf{r}) (\rho(\mathbf{r}) - \rho_0) \\ & + \int d\mathbf{r} \int d\mathbf{r}' g^{(2)}(\mathbf{r}, \mathbf{r}') (\rho(\mathbf{r}) - \rho_0) (\rho(\mathbf{r}') - \rho_0) + \dots \end{aligned} \quad (1.35)$$

Typically the second order correlations are considered while the rest are truncated. The structure factor, obtained from the Fourier transforms of the correlation functions, is the order parameter whose fluctuations differentiate the isotropic liquid from the ordered crystal. Free energy studies at deep supercooling have in fact found unexpected features, such as a “flat” barrier profile [61, 62]. This could be indicative of a line of surface tension, due to a “crystalline edge”, whose contribution to the free energy becomes prominent for small clusters which are poorly approximated by spheres. Another possible contribution is that the formation of crystalline clusters are no longer uncorrelated events.

The other interesting phenomenon in this context is the existence of a metastable intermediate state, in which case nucleation becomes a two-step process [63]. The role of enhanced fluctuations and the formation of a wetting layer, which can sometimes facilitate the transition, have both been studied extensively [51, 64–68]. The pathway to nucleation and the final state when there are many possible polymorphs are other aspects that have been considered [58, 69–73]. An important question that has generated interest recently is what the free energy barriers to crystallisation look like in a two-step scenario. In particular, a two-step process need not imply a well-defined second metastable phase. A distinct intermediate state will alter the free energy profile, with a second phase appearing as a limiting case [74–76].

### 1.3.5 Studies of crystallisation

The earliest computational evidence of crystallisation was found at large densities for simulated hard spheres. This was a striking result, showing that crystal

formation could occur in the absence of attractive forces and could be purely entropy driven [77, 78]. At the time and for a while after, studying the liquid to solid transition close to co-existence proved to be challenging, in a variety of model systems such as the Lennard-Jones system [46, 79], colloidal proteins [80, 81] and soft spheres [82].

A number of early studies focussed on the *dynamics* of crystallisation. The work of Hoover and Ree was one of the earliest to identify the melting transition, where too the focus was on the role of entropy [83]. A subsequent study by Hoover *et al* studied the thermodynamics of various crystalline structures through simulations of the lattices. One of the prominent early works in which homogeneous nucleation was observed in simulations was that of Mandell *et al* [79].

In these simulations, the issues arising from crystallisation events being exceedingly rare close to co-existence were persistent. An important early study where the enhanced sampling protocol of Torrie and Valleau [37] was leveraged to obtain estimates of crystallisation rates and free energies close to co-existence was that of van Duijneveldt and Frenkel [82]. In this work, the bias parameter used to sample the crystallinity axis was the global  $Q_6$ , which has since then been found to not be ideal in certain circumstances [46].

Additionally, the role of system size (particle number  $N$ ) was poorly understood. Many early works used small system sizes due to resource constraints and found an increase in the barrier to nucleation with system size. This gave the impression of a system size dependence of the nucleation barrier before the effects of correlations beyond immediate neighbours became apparent [82]. At deep supercooling, sluggish dynamics due to the proximity to the glass transition also posed a challenge. One of the earliest large system size runs ( $10^6$  particles) was by Swope and Andersen [84], where it was established that beyond a particular system size, the results were not sensitive to  $N$ . With enhanced sampling simulations enabling investigations close to co-existence, one key question was whether the mechanism of crystallisation was the same at deep supercooling as it was close to co-existence. Ostwald proposed a step rule because of the observation that the rates of transitions were much faster at deep supercooling than at moderate supercooling [85]. The suggestion was that the phase that forms first need not be the most stable thermodynamically but rather that closest in free energy to the melt. This was coupled with Gibbs' insight that the formation of a new phase requires work to be done [86], and thus that a drastic change in work may be due to the formation of an intermediate phase with intermediate surface tension between the initial metastable and final phases. The role of

surface tension was given prominence by Becker and Döring and what is commonly known as Classical Nucleation Theory [49]. The role of surface tension as requiring work to be overcome was related to the idea that the state with the lowest free energy barrier to crystallisation would be the first to form, such as BCC precursors in the freezing transition to FCC [87, 88]. In fact it was found that the pathway to crystallisation was qualitatively different at deep supercooling, with metastable intermediates forming in the process, and changes also in the characteristics of the bulk stable phase [89].

Since the early work using enhanced sampling simulations with  $Q_6$ , the question of what order parameter best describes the kinetics and thermodynamics of crystallisation gained prominence. The size of the largest crystalline cluster was suggested as being superior to  $Q_6$  with the argument that a local measure best captures the formation of a critical nucleus – an inherently local event [46]. The necessity to study the transition from the point of view of multiple order parameters gained traction given the complexities arising from multiple polymorphs and metastable states and associated increase in the magnitude of fluctuations [47, 51, 64, 65, 68, 89–92]. Additionally, the role of changes in the local order in the liquid is thought to be as important, if not more, than enhanced fluctuations [93, 94]. In the context of silicon, computer simulation studies of crystallisation with the SW potential include those of Beaucage [95] and Romano *et al* [96, 97].

Related questions arise regarding the formation of different polymorphs of the crystalline state [97–100] or precursors [67, 68, 101]. These are relevant to the discussion for silicon where the possibility of a second liquid phase, or at least the changes in the structural properties of the metastable liquid have a bearing on crystallisation.

In addition to umbrella sampling, a number of other advanced sampling techniques have been developed and applied to the problem of crystallisation. The kinetic reconstruction from the mean first passage time [42–44] is a method which samples the steady state distribution and the mean first passage time to obtain the free energy and does not rely on any enhancement of sampling through the application of constraints. Another important family of methods is the forward flux sampling method [33, 38]. This method works by placing milestones along the transition path with which one can “save your progress” along the transition (like in a third person RPG for those familiar) and restart any number of independent simulations from to enhance the flux over the barrier. Any single simulation would

be unlikely to cross a high free energy barrier successfully but this method of ratcheting can enhance the sampling of the barrier drastically. An added benefit is that the order parameter along which milestones are placed need not be the reaction coordinate; any order parameter that distinguishes liquid from crystal will do. In order to obtain the free energy, one needs to also spawn an equal number of “backward” simulations [39]. Methods have been developed to circumvent this additional computational requirement, such as coupling the method to the mean first passage time method [102] and reweighting trajectories appropriately [103]. A multi-order parameter variant has also been developed though, to the best of the author’s knowledge, no expression for the free energy is derived [104]. One consideration when using this method is that it is typically assumed, as in the kinetic reconstruction from the mean first passage time, that the order parameter trajectories are continuous and Markovian. This is addressed in the work of Haji-Akbari [105]. A similar class of methods using milestoning are the Transition Interface Sampling [40] and the Transition Path Sampling [32] methods. The work of Filion *et al* [106] compares results from forward flux sampling with umbrella sampling results for the case of hard sphere crystal nucleation. Both the rates and the transition path, studied by characterising the composition of pre-critical nuclei, are found to be the same across methods.

A recent and effective method to study nucleation processes and the role of the interfacial free energy is the seeding method [107, 108]. This method works, as the name suggests, by implanting seed crystals in the liquid, of different sizes, and studying the subsequent time evolution.

The method of metadynamics has also been applied to the context of crystallisation [41, 109]. This is a powerful method that has been used in a wide range of contexts and works by the iterative addition of a time-dependent bias potential in regions of order parameter space that are frequently sampled. This process eventually “fills” the metastable minimum the system is trapped in and allows the system to escape to and explore other minima, until they are filled as well. This time-dependent potential converges and the converged value is the negative of the free energy. This method needs to be applied carefully when considering cases with large  $\Delta\mu$  differences, especially since the free energy  $\Delta G = N\Delta\mu$  is extensive and escaping minima can then become an inefficient process. Nevertheless, it has been applied successfully to the study of nucleation [110] and the LLPT [111], but with the caveat that exploring the crystal free energy basin is challenging because  $\Delta G$



is negative with large magnitude. In Ref. [110], an artificial energy penalty is imposed on large values of the crystallinity order parameter to avoid sampling that region. The literature on this method is vast; the original paper [41] and a recent review [109] are mentioned here for the reader.

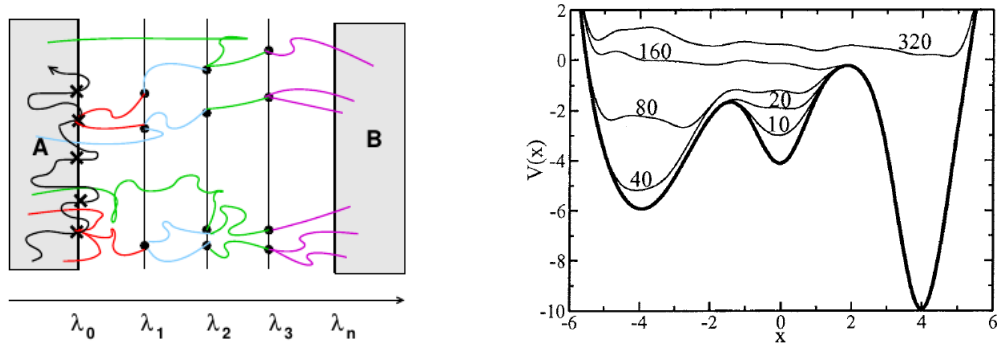


Figure 1.4: (*Left*) The milestoning procedure for Forward Flux Sampling and Transition Interface Sampling schemes with the order parameter  $\lambda$  separating the two states,  $A$  and  $B$ . Progress along the order parameter is preserved and the estimates of the transition rate are improved by saving configurations that cross successive milestones and using them to restart simulations. From Allen *et al* [33] with permission. (*Right*) The free energy function and the time-dependent bias potential at different iterations for the metadynamics procedure. As time progresses, the more frequently sampled basins are “filled up” by the bias potential. The converged bias potential at long times is the negative of the free energy. From Laio and Parrinello [41] with permission.

## 1.4 Studies of the LLPT

In this section we will briefly discuss the vast body of literature on thermodynamics in the specific context of anomalous, network-forming liquids. As mentioned briefly earlier, experimental studies in this context have proven to be difficult over the years because the behaviour of interest is often observed deep in the supercooled region of the phase diagram; crystallisation proves to be a hurdle [4, 16]. Experimental verification of the LLPT is a significant challenge, and is yet to be achieved insofar as experimental evidence has only been obtained under special conditions as opposed to observations for the bulk liquid.

Theoretical predictions regarding the nature and origin of the anomalies in these liquids have also been made, a significant portion of which have focussed on a two-state formulation to describe the liquid. This will be discussed in greater detail

later in Sec. 1.5.3. Numerical studies are advantageous in that a combination of small system sizes and advanced sampling techniques can be used. However, the findings from numerical studies can only be connected to our expectations for real liquids if (i) the model potential used to describe the substance is accurate and (ii) the assumptions under which the thermodynamic relations used to calculate the relevant properties (such as free energy) are applicable. In simulations as well, rapid crystallisation remains a hurdle. However, one can track changes in the system and study responses to various perturbations without the physical limitations that apply to experiments, perform simulations in different ensembles, including in constrained ensembles, and use smaller system sizes since the total rate of formation of critical nuclei increases with volume. In this section we will focus on the broad category of classical simulation studies that disregard quantum effects. A discussion of first principles or *ab initio* simulation studies will be included in the final section of this chapter.

We will briefly describe the different ways in which this question has been approached in the past.

### 1.4.1 Silicon

The earliest experimental studies of supercooled liquid silicon found a discontinuity (by extrapolation) in the Gibbs free energy when comparing the amorphous state and the high temperature metallic liquid [6, 7, 112, 113]. In particular, Donovan *et al* [112] performed calorimetric experiments and measured the heat capacity. The heat capacity was integrated to give the entropy ( $\Delta S = \int \frac{C_P}{T} dT$ ) and the enthalpy ( $\Delta H = \int C_P dT$ ), and finally the Gibbs' free energy ( $\Delta G = \Delta H - T\Delta S$ ). While considering the possibility of a glass transition, Aptekar made the connection to a possibility of a LLPT based on a two-state description of the overall liquid [8]. Experimental verification of the LLPT has proved difficult [4, 5, 16], but simulation studies have shown that the low density state is not a glass, but in fact a liquid with slower dynamics [1]. Given the use of silicon in electronics, and the change in electronic properties of silicon when going from high temperature (metallic) to low temperature amorphous (semiconductor), a large number of both experimental and first principles simulation studies have focussed on the electronic properties of the amorphous state. We briefly review some of these.

## Experiments

In addition to the experimental works of Kim *et al* [19] and Beye *et al* [20], more recent electrostatic levitation experiments have found evidence of a first order transition with associated latent heat below the melting temperature [114]. Experiments also report finite and persistent fractions of covalent bonding in the high temperature liquid, suggesting a mechanism by which a transition might occur at lower temperatures [115]. Notably, none of the experiments have probed the conditions at which the LLPT is expected at  $P = 0$  GPa, which is around  $T = 1060\text{K}$  [1, 2]. However, in experiments the phase transition is expected to occur at higher temperatures of  $T \sim 1400\text{K}$  [21]. Owing to the difficulties of conducting experiments on liquid silicon at these temperatures, as well as the difficulties in avoiding crystallisation [19, 20, 114–119], simulation studies have driven investigations into this question.

## Ab initio simulation studies

A number of simulation studies, including some of the most recent investigations in this area, employ *ab-initio* methods and identify liquid-liquid and liquid-solid transitions based on changes in the electronic structure reminiscent of those found in experiments; silicon is a semiconductor in the solid-state, a semi-metal in the low density liquid state and a metallic liquid in the high temperature, high density liquid state [21]. Morishita did an early study identifying a sharp change in the coordination number at low temperatures [120]. Jakse and Pasturel [22, 121] and independently Ganesh and Widom [23, 122] performed extensive studies identifying drastic changes and hysteresis in the density of the liquid and the density of states (which changed from metallic to having a pseudo-gap at the Fermi level), and significant differences from crystal structure of the LDL [22, 23, 121, 122]. Ashwin *et al* [21] used an empirical pseudopotential to study changes in the electronic structure with temperature using liquid configurations obtained from classical MD simulations of SW silicon. Fig. 1.5 shows the electronic density of states obtained by Ashwin *et al* [21] and the equation of state obtained by Ganesh and Widom [23]. Subsequent studies have investigated other aspects such as the hybridisation for the different amorphous states [123]. Zhao *et al* [124] found that evidence of a LLPT with *ab-initio* studies, with the critical point nearly coinciding with the liquid-gas spinodal. This results in the liquid-gas spinodal effectively acting like a re-entrant, curving upwards into the HDL spinodal (with respect to the LDL).

Other recent studies with different functionals identify a transition as well [125], with one recent study reporting 3 distinct LLPTs for a particular treatment of the density functional [24]. Deringer *et al* have recently performed simulations with machine-learning based quantum mechanical computations identifying co-existing amorphous states [126].

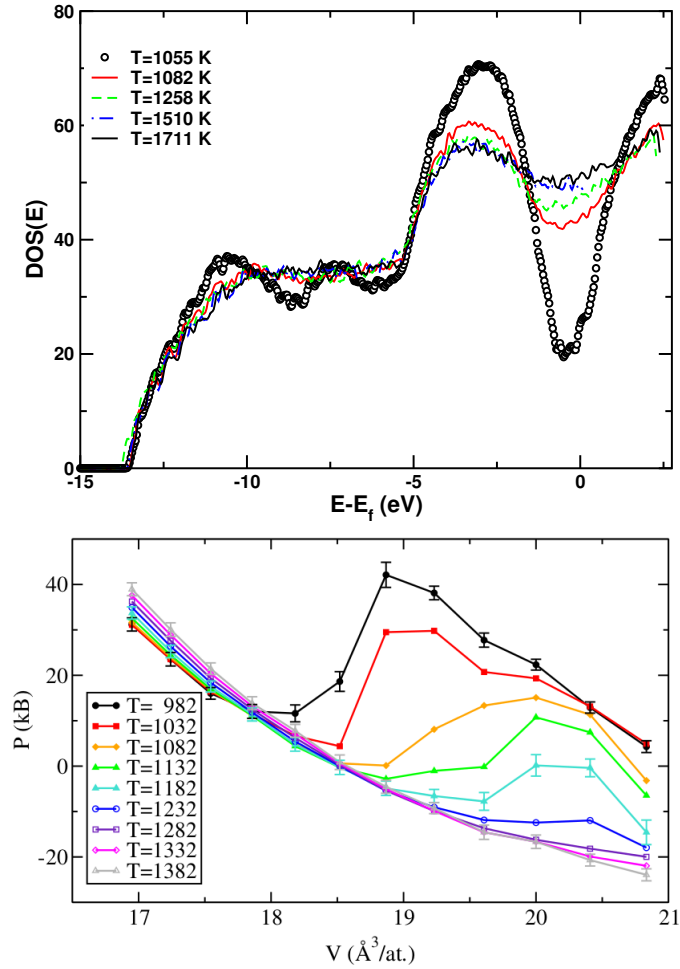


Figure 1.5: (*Left*) The electronic density of states showing the pseudo-gap at the Fermi level for the low temperature liquid. The high temperature liquid is metallic by contrast. [From Ashwin *et al* [21] with permission]. (*Right*) The equation of state showing a discontinuous change in the  $P - V$  isotherms at low temperature from *ab initio* simulations. [From Ganesh and Widom [23] with permission].

### Stillinger-Weber silicon

The classical empirical SW model is the most widely used model, and the model used in the work described in this thesis [25]. A description of the model is contained

in Chapter 2 but in brief, the interaction has both two-body and three-body terms. The three-body terms induce the tetrahedral ordering that is seen in real silicon. This model potential is known to reproduce the qualitative features of the phase diagram well. Additionally, early MD simulations showed that this model reproduced a range of anomalies that were known to be exhibited in water [127]. Early Monte Carlo simulation studies looked at high temperature behaviour [128]. Broughton and Li [129] performed thermodynamic integration of isobars and isotherms, as well as using the Frenkel-Ladd method [130] for the crystal, to identify liquid-solid co-existence. Some of the earliest computational investigations were equation of state studies by conducting molecular dynamics simulations at different state points. Sastry and Angell in 2003 [1] found a discontinuous change in the enthalpy, with evidence of hysteresis, below the melting temperature from constant pressure-constant enthalpy simulations, suggesting a phase transition between two liquids for SW silicon. This work determined that the low density phase was not a glassy phase by measuring the diffusivity and relaxation of the intermediate scattering function. The distribution of local bond orientational order confirmed the relatively more prominent tetrahedral arrangement in the low density liquid. Vasisht *et al* [2] found evidence of a critical point and mapped the different anomalies on the phase diagram. Their work found a van der Waals loop in the equation of state from isobars and isotherms, indicative of a phase transition between the two liquids. They made measurements of the compressibility from both the variance in volume and from analytical differentiation of the equation of state fit to a polynomial. From this, they found compressibility maxima of increasing magnitude, indicative of approach to a critical point at negative pressures. This work also identified the temperatures of density maxima and minima from the equation of state data. Subsequent work studied the thermodynamic anomalies in greater detail [131] and the effect of tuning parameters of the potential on the nature of the anomalies [132].

More recently, Angell and Kapko also studied the effect of tuning the potential on the location of the critical point [133]. The work of Limmer and Chandler [18] and of Ricci *et al* [30] called into question the evidence in favour of a LLPT obtained from equation of state studies with molecular dynamics trajectories. They performed free energy calculations which suggested that the second liquid state was in fact slowly, but spontaneously, crystallising in a barrier-less manner. Addressing the contradictions between the equation of state results and the subsequent free energy calculations is a principal motivation of the work in this thesis.

Other work of note on SW silicon include studies on the thermodynamics of

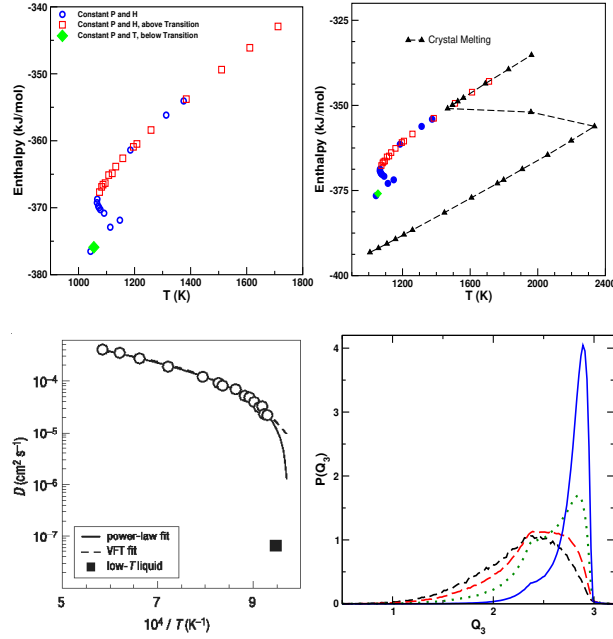


Figure 1.6: (*Top left*) The discontinuous change in enthalpy as temperature is decreased, indicative of a first order phase transition. (*Top right*) The change in enthalpy occurs at conditions below the melting temperature, suggesting a phase transition between two metastable states (*Bottom left*) The diffusivity change across the temperature. The low temperature liquid has a finite diffusivity, albeit much lower than that of high temperature liquid. This shows that both metastable states are liquid and can be equilibrated) (*Bottom right*) The distribution of  $Q_3$  for liquids at different temperatures. At the lowest temperature of  $T = 1055\text{K}$ , (blue curve) the distribution is sharply peaked at a high value similar to that of the crystal. [Adapted with permission from Sastry and Angell [1].]

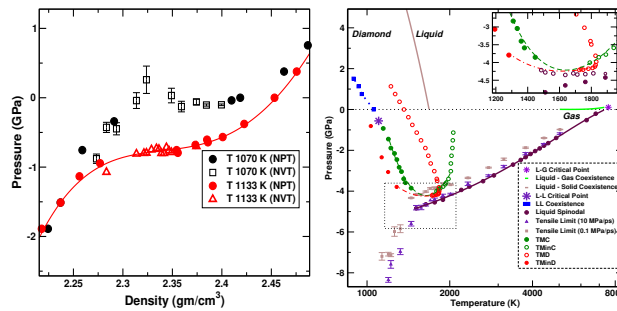


Figure 1.7: (*Left*) The equation of state isotherms from simulations at constant pressure and constant temperature (solid symbols), as well as constant volume, constant temperature (hollow symbols). The discontinuous change in the low temperature isotherm indicates a phase transition, with the constant volume simulations showing a van der Waals loop. (*Right*) The phase diagram showing the location of the critical point, LLPT line, the loci of maximum and minimum density (TMD, TMinD) and the loci of maximum and minimum compressibility (TMC, TMinC). [Adapted from Vasisht *et al* [2] with permission.]

nucleation [95], the role of changes in liquid coordination number of crystallisation [134, 135], studies of changes in the dynamics and in particular of the onset of hopping-like relaxation mechanisms and dynamical heterogeneity [136, 137], studies on quasi-2D, confined and sheared silicon [138–141] and studies contrasting changes in local entropy brought about by changes in the amorphous state vs changes brought about by crystallisation [142].

### 1.4.2 Water

As is the case with the majority of LLPT literature, the most well-studied case is that of water. Here, early attempts to explain the well-known anomalies (anomalous expansion on cooling) led to the stability limit conjecture of Robin Speedy [13]. Computational investigations into the predictions made by Speedy led instead to the detection of approach to a second critical point for supercooled water modelled with the ST2 potential [14]. A number of free energy calculations have since shown two liquids for ST2 water [111, 143–146]. The left panel of Fig. 1.8 shows free energy calculations by Poole *et al* [146] with two minima corresponding to the two liquids. A long debate ensued following findings by Limmer and Chandler suggesting that the apparent LLPT was instead slow, spontaneous crystallisation [18, 28]. Since then, however, it was conclusively shown by Palmer *et al* that ST2 water did indeed have a LLPT, with reversible sampling performed to obtain the free energy surface showing two liquid and the crystalline state [29]. The middle panel of Fig. 1.8 show free energy minima corresponding to the two liquid and the crystalline phase from the work of Palmer *et al* [29]. It was also determined that the discrepancy in results was due to an incorrect sampling protocol employed by Limmer and Chandler in their hybrid Monte Carlo simulations, leading to the angular velocities sampling a different distribution than the one corresponding to the bath temperature [147].

Monoatomic models of water include the isotropic two-scale ramp Jagla potential [148–150], which has been shown to exhibit a dynamical crossover and a liquid-liquid transition. Notably, the slope of the LLT is positive for the Jagla model, unlike the case for other model liquids displaying water-like anomalies [150]. The mW monoatomic model, which is a re-parameterisation of the SW potential, has also been studied in this context. Studies show that in this model an LLT does not occur and that crystallisation occurs on faster timescales than the liquid can equilibrate at the conditions of interest [68, 151, 152]. The work of Holten *et al* suggests that a structural change does underlie the observed anomalies and that

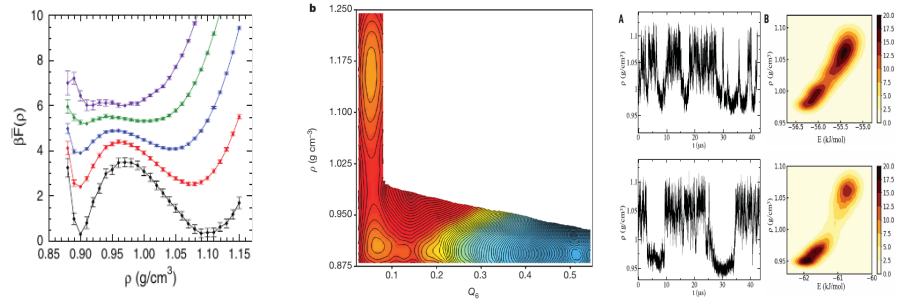


Figure 1.8: (*Left*) Contracted free energy surface as a function of density measured close to the critical point for a variant of the ST2 model of water. [From Poole *et al* [146] with permission.] (*Centre*) The free energy surface as a function of density and  $Q_6$  from umbrella sampling simulations of ST2 water, showing two liquid minima and the globally stable crystalline state. [From Palmer *et al* [29] with permission.] (*Right*) The density histogram from molecular dynamics simulations of TIP4P/2005 water close to the critical point. The bimodal distribution is indicative of two co-existing phases. [From Debenedetti *et al* [45] with permission.]

the spontaneous, slow crystallisation picture is not consistent with the observed trends [55].

The molecular TIP4P model has also been studied with predictions of a LLPT based on thermodynamic data [153]. The TIP4P model is known to display the expected structural and dynamical anomalies [154] and recent microsecond long molecular dynamics simulations of two TIP4P variants have found bimodal density distributions, indicative of phase separation in the vicinity of the expected critical point at  $T = 170\text{K}$ ,  $P \sim 0.2\text{ GPa}$  [45]. The right panel of Fig. 1.8 show a bimodal distribution of the density for TIP4P water close to the critical point and the difference between the two states in terms of potential energy and density. TIP5P and adaptive force matching potentials that closely mimic experimental behaviour have also been studied, showing LLPT-like behaviour [155].

Recent experiments to study the LLPT in real water have broadly followed two strategies.

The first is nanopore confinement, where low ambient temperatures ( $T = 150 - 210\text{K}$ ) are possible with no heterogeneous ice formation because of hydrophobic ice walls, but discrepancies in the behaviour of the samples compared to extrapolated expectations from the bulk [156]. Questions remain as to whether the confined water is liquid, amorphous or even crystalline, or whether such distinctions are meaningful at such small lengthscales [157]. Further, the conditions of confinement are argued to correspond to a situation of strong stretching  $P = -100\text{ MPa}$  [158].



The second is to use a small droplet and pulsed X-rays [159]. With this setup, low temperatures of  $227 \pm 1\text{K}$  can be reached [159, 160]. Such experiments have shown a peak in compressibility, consistent with the expected thermodynamic anomaly and samples have been shown to not crystallise over microsecond timescales. These researchers conclude that the evidence points to the LLPT based on the fact that (i) they observe a persistent temperature dependence in the structural properties of the liquid, ruling out spontaneous crystallisation, (ii) they observe a large increase in degree of tetrahedrality and correlated hydrogen-bonding, at odds with the singularity free scenario [3] where hydrogen bonding between neighbours is treated as independent and uncorrelated, and (iii) the critical-point-free scenario would require a drastic change in structure at ambient pressure across the transition, whereas their results suggested a nearly continuous change, indicative of proximity to a critical point.

A more recent experiment by Kringle *et al.* [161] study the structure of supercooled water from the infrared spectrum. These authors studied reversible changes in quasi-2D thin films of water with rapid heating and cooling cycles using nanosecond laser pulses. These techniques allow the authors to study the microscopic structure of the liquid at temperatures in the range of 160 – 245K while avoiding crystallisation. The authors note a sharp change in the fraction of high/low density particles across the Widom line, however, given that their measurements are made across the supercritical regime, no direct claim is made about a phase transition. The authors do note that the liquid can be described as a non-ideal mixture of two states, suggesting phase separation. The mixture-model perspective will be discussed in detail in Section 1.5.3. Kim *et al.* [162] used a combination of ultrafast femtosecond isochoric laser heating of a high density amorphous ice sample and femtosecond x-ray pulses to observe the subsequent resultant volume change. The expansion occurred an order of magnitude faster than crystallisation. This discontinuous change in the structural properties of the liquid prior to crystallisation is one of the most recent experimental indications of a liquid-liquid phase transition in water.

### 1.4.3 Silica

Early molecular dynamics studies of silica, using the BKS model found thermodynamic anomalies similar to those found earlier for a model of water [163, 164]. Additionally, the identification of a bimodal distribution in local order suggested

the possibility of two liquid states or local structures. Earlier work had compared other aspects of silica to water [165]. The prediction of an LLT also came from

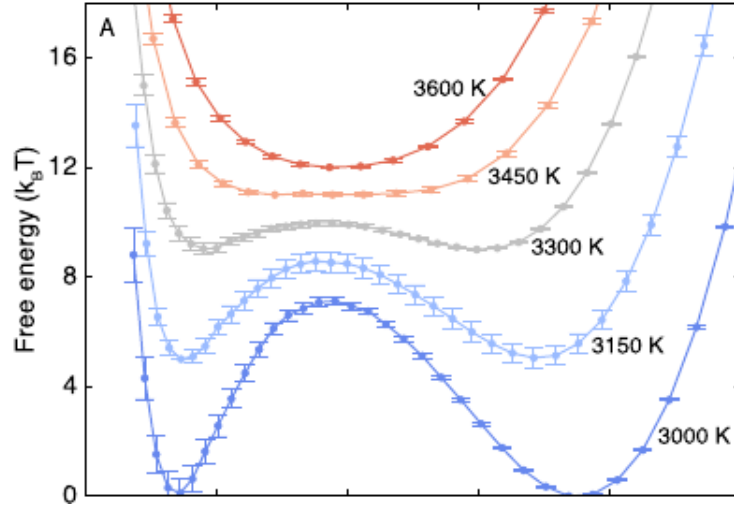


Figure 1.9: Contracted free energy as a function of density for the WAC silica model from umbrella sampling simulations close to the critical point. [From Chen *et al* [166] with permission.]

computational investigations using classical molecular dynamics for two different models [167]. The prediction came from fitting available thermodynamic data obtained from simulations to an equation of state, following the procedure in [60], and predicted a LLPTs at lower temperatures. Simulations performed at the conditions where phase separation was predicted showed a bimodal distribution of the distance to the fifth neighbour ( $g_5(r)$ ), suggesting two distinct phases. Since then, efforts to identify the critical point have met with little success given the proximity of the expected critical point to the glass transition temperature around which equilibrating the liquid becomes impossible [168]. Free energy studies of silica at these deeply supercooled conditions have established that the liquid remains a well-defined metastable state with respect to crystallisation even at these low temperatures [169, 170]. More recent free energy studies show clear signatures of an LLPT for the WAC model of silica with a bimodal density distribution and two free energy minima corresponding to a HDL and an LDL and a critical point at  $T = 3600\text{K}$ ,  $P = -0.02\text{ GPa}$  [166, 171]. Fig. 1.9 show results from the free energy calculations in Ref. [166].

#### 1.4.4 Phosphorus

The earliest indications of a LLPT in atomic phosphorus were from X-ray diffraction studies. The pair correlation function and static structure factors showed a drastic change across  $P = 1$  GPa and  $T > 900$ K, with a higher degree of correlation in the second shell, indicative of a transition from the  $P_4$  tetramer to a polymeric liquid [172]. Monaco *et al.* studied a larger range of temperatures, confirming a negative slope of the transition line for temperatures as high as  $T = 2000$ K [173]. Interestingly, the melting line for phosphorus is re-entrant, in that it has a maximum temperature as a function of pressure [172]. First principles molecular dynamics simulations showed that the  $P_4$  tetramer had small orbital overlap and was non-metallic, as opposed to the metallic polymeric liquid [174].

#### 1.4.5 Carbon

Togaya found indications of an LLPT from a discontinuous change in the slope of the melting line and in the electrical resistivity for carbon [175]. This melting point maximum was later confirmed along with observations of 2, 3 and 4-coordinated liquid structures [176]. However, consensus on the existence of the LLT in carbon is elusive, with first principles molecular dynamics confirming the change in slope of the melting line [177] but finding no clear evidence of LLT [177, 178]. Some recent work has found evidence of an LLT with decreasing temperature for quasi-2D carbon films [179]. Notably, changes in local coordination in the metastable liquid have been shown in simulations to affect the propensity to nucleate diamond [93]. This has sparked interest in the general question of the interplay between coordination in the metastable liquid and facilitation of nucleation.

#### 1.4.6 Sulphur

Sulphur has recently been shown to have a LLPT. Interestingly, this occurs under conditions where the liquid is in equilibrium, rather than being metastable [180]. This enables a more thorough characterisation of the LLPT since crystallisation is not an issue. In fact, Henry *et al.* [180] found a liquid-liquid critical point at  $T = 1100 - 1200$ K and  $P = 2.1 - 2.2$  GPa. The high density liquid is polymeric, and notably, sulphur displays a  $\lambda$  transition at lower pressures.

### 1.4.7 Triphenylphosphine

Interest in studying the liquid polymorphism of triphenylphosphite (TPP) started with the interesting observation that if TPP was quenched to 213 – 223K, and then annealed, it avoided turning glassy and instead formed a distinct glacial phase. This possible LLT is of interest since it does not occur at deeply supercooled conditions. Extensive experimental studies have been conducted [181] with a characterisation of both a nucleation-growth type transition and a spinodal-decomposition transition close to the respective limits of stability [182]. Studies into the nature of the transition have sought to confirm that it is first order [183]. However, there is a suggestion that the glacial phase is composed of nano-crystals, with the possibility of slow-coarsening [16]. A recent study claims to both confirm the LLT and describe its role in facilitating crystallisation [51].

### 1.4.8 Solutions and biological water

A successful method of deterring crystallisation is to study solutions of water with both polar and non-polar molecules. Early works studied the effect on crystallisation and behaviour at deep supercooling [184, 185]. An important point is that LLPTs can also occur without phase separation of the two component liquids, such as water and glycerol [182, 186]. In other words, a transition occurs between two mixture phases, both with the same composition (in water+solute), but with different densities. The addition of the second liquid works in some cases as a means to increase the pressure, deter hydrogen bond formation and also shift the melting point to lower temperatures [16]. In other cases the solute can form hydrogen bonds with water. The key quantity is the difference in chemical potential between water in the mixture and pure water at the same temperature and pressure.

Nanopore confinement is another of the primary ways in which water has been studied experimentally at deep supercooling. The small sample sizes allow measurements before crystallisation takes place and the nature of confinement plays a role as well [16]. This has been studied both through simulations [187] and experimentally [156, 188].

An interesting analogue of this is the behaviour of hydration water in the vicinity of proteins and other biological micromolecules. Proteins have been observed to display a drastic slow down in conformational changes at supercooled conditions. Studies have shown that the temperature dependence of the mean square fluctuations in

conformation change at a specific temperature  $T_P$  for different macromolecules in water. This temperature is found to be strongly correlated with the temperature,  $T_x$ , at which the dependence diffusivity of the surrounding water changes from non-Arrhenius to Arrhenius [189, 190]. Moreover, the maximum in the heat capacity of the system (including both protein and surrounding water), occurs at a temperature  $T_w$  which is also strongly connected to the above two temperatures. The finding that these three temperatures are nearly the same across systems has generated interest in the role of water in protein dynamics and conformational stability. Such behaviour has been observed in experiments as well [191, 192].

While the conditions of consequence in biological contexts do not correspond to those where phase separation is observed, the effect of crossing the Widom line, across which both the static and the dynamic properties of the liquid change significantly but continuously, has been noted in the works mentioned above.

## 1.5 Phenomenology of the LLPT

The existence of different disordered (amorphous) forms of a single-component fluid phase – most interestingly when there is a phase transition between the fluid phases – is known as fluid polyamorphism [16, 193, 194]. A wide variety of systems show fluid polyamorphism, as discussed in earlier sections. The connection in some, but not all, cases to the presence of thermodynamic anomalies, and other shared commonalities, have motivated researchers to try and understand the underlying mechanism through models of varying degrees of abstraction. In addition to those liquids which display signatures of a LLPT under relatively easily accessible conditions [51, 150, 181, 195–197], there are those for which the conditions are extremely challenging to produce to make reliable measurements [4, 29, 45].

In this section we will briefly review some of the prominent efforts to model LLPT phenomenology and make connections across systems.

One of the earliest attempts was in the context of silicon. Aptekar [8] and also Rapoport [198] and Ponyatovsky [199, 200] discussed a two-state non-ideal mixture model to explain the differences in the melting curves for amorphous silicon shown in experiments [6, 7] and suggested a metastable liquid-liquid critical point. Aptekar's two state model had the following form:

$$G_l = G_1(1 - \omega) + G_2\omega + W(1 - \omega)\omega + Nk_B T [\omega \log(\omega) + (1 - \omega) \log(1 - \omega)] \quad (1.36)$$

This form, that includes a mixing entropy and a non-ideality term, is very similar to the other two-state models that will be discussed later in this section. Franzese *et al.* discussed a general mechanism for LLPTs, studying experimental data in the context of the tetramer phosphorous liquid [201]. The model considered here was an isotropic model with one attractive and two repulsive lengthscales – a model known to mimic the behaviour of liquid metals [195, 196]. Notably, this work discussed the conditions under which an LLPT would be coupled to the associated thermodynamic anomalies. The LLPT need not generally result in accompanied thermodynamic anomalies. Similar work by Buldyrev *et al.*, where the model potential was two-scale isotropic repulsive with a hard core and a soft core repulsion, also discussed this in both 2D and 3D [202].

Briefly, one considers the following thermodynamic relation

$$\left(\frac{\partial V}{\partial T}\right)_P = \left(\frac{\partial S}{\partial P}\right)_T = \left(\frac{\partial S}{\partial V}\right)_T \left(\frac{\partial V}{\partial P}\right)_T \quad (1.37)$$

Noting the stability criteria  $\left(\frac{\partial V}{\partial P}\right)_T < 0$ ,  $\left(\frac{\partial V}{\partial T}\right)_P < 0$ , one can infer that  $\left(\frac{\partial S}{\partial V}\right)_T < 0$ . This can be connected to the Clausius-Clapeyron equation

$$\left(\frac{dP}{dT}\right)_{LLPT} = \frac{\Delta S}{\Delta V} \quad (1.38)$$

to relate the slope of the transition line to changes in the entropy and the volume. For a transition with a positive slope in the  $P$ – $T$  plane, the higher entropy phase has a lower density (higher volume), while in the case of a negatively sloped transition, the low density high volume phase in fact has a lower entropy – giving rise to the density anomaly and the other related anomalies [131].

Following the early studies of Speedy [13] and Poole *et al.* [14] on the anomalies of water, numerous other efforts have been made to model the thermodynamic behaviour of water. Part of these efforts was in developing interaction potentials that could be studied to understand the role of factors such as bond angle, bond flexibility and local density on macroscopic behaviour such as thermodynamics. A prominent study was that of Smallenburg *et al.* [203, 204] studying tetrahedral patchy colloids. By tuning the flexibility of bond angles, the authors showed that a variety of regimes could be accessed including, strikingly, a regime where the liquid-liquid coexistence was under conditions of thermodynamic stability, rather than metastability with respect to the crystalline state. Similar work studying the role of the degree of tetrahedrality on observed anomalies was done by Russo *et*

*al.* [205]. In this work, a two-state thermodynamic model was applied to the SW potential with the degree of tetrahedrality being tuned. By making arguments to quantify the loss of entropy in switching from the high density structure to the low density structure, they arrived at an equation describing the fraction of tetrahedrally structured particles. The study found using this construction that tuning the degree of tetrahedrality to lower values brought about a re-entrant spinodal, along the lines suggested by Speedy [13] for water.

The isotropic two-scale Jagla ramp potential [148] shows a LLPT with positive slope, along the lines of the work by Franzese *et al.* [201]. Here the two repulsive lengthscales give rise to a high density and a low density liquid. Contrary to other models of water, this model has a positive slope for the liquid-liquid coexistence line, suggesting the high density liquid has lower entropy [201,206] and that the low density liquid therefore does not have any tetrahedral ordering.

Two-state models similar to that of Aptekar have been used to both make predictions and explain the observations related to the LLPT for numerous models [16, 55, 194, 206, 207]. In particular, efforts have been made recently towards unifying the proposed thermodynamic scenarios, which will be discussed subsequently [16, 194].

Ising-like and lattice gas constructions that incorporate the effect of hydrogen bonds have also been studied, both analytically and with Monte Carlo simulations [3, 26, 208–211]. These will also be briefly discussed in the coming sections.

### 1.5.1 Thermodynamic scenarios

A number of thermodynamic scenarios have been proposed to explain first the observed anomalies in water, and the subsequent observations of a LLPT and a critical point. Given the difficulty in probing this question directly, both in experiments and in simulations, there has been both the need for and the room for the development of arguments, based on both thermodynamics and the microscopic details like hydrogen bonding and valency, which have been used to make predictions. These arguments are summarised below.

#### The stability limit conjecture

The work by Speedy [13] was motivated by experimental evidence of a locus of maximum density temperatures for water as well as the apparent divergence of

the isothermal compressibility below the melting temperature. The divergence of the compressibility is a signature of approach to a limit of stability, but of what? Speedy argues that this is liquid-gas spinodal. This is done in the following way:

$$dV = \left( \frac{\partial V}{\partial T} \right)_P dT + \left( \frac{\partial V}{\partial P} \right)_T dP \quad (1.39)$$

We should be able to write along any path  $x$ , in this case the l-g spinodal  $s$ .

$$\left( \frac{\partial V}{\partial T} \right)_x = \frac{dV_s}{dT} = \left( \frac{\partial V}{\partial T} \right)_P + \left( \frac{\partial V}{\partial P} \right)_T \frac{dP_s}{dT} \quad (1.40)$$

Replacing appropriately gives us

$$\alpha = \frac{dV_s}{dT} \frac{1}{V_s} + \frac{dP_s}{dT} K_T \quad (1.41)$$

Since the slope of the spinodal is always finite, as is the volume,  $K_T \rightarrow \infty$  implies  $\frac{\alpha}{dP_s/dT} \rightarrow \infty$ .

A temperature of maximum density is one where  $\alpha = 0$  with a sign change across it. This implies a change in the sign of  $dP_s/dT$  as well (see Fig. 1.10).

The data on the locus of density maxima at the time was available for positive pressures, the extrapolation to negative pressures with a negative slope was assumed. Since then, other works have investigated where such a scenario might be realised [208,212] with different model equations of state.

### The two critical point scenario

Poole *et al.* [14] conducted molecular dynamics simulations with the ST2 model of water to find the spinodal and verify the change in slope predicted by Speedy. A further aim was to test the assumption of the continuing negative slope of the locus of density maxima. What they found was

- The slope of the spinodal did not change sign
- The slope of the locus of temperatures of maximum density changed sign instead, and did not intersect the l-g spinodal.
- $P - V$  curves showed maxima in  $K_T$  suggesting approach to a critical point, but no clear divergence.



This scenario is called the two critical point (LLCP) scenario (see Fig. 1.10). A related possibility of a LLPT where the critical point was hidden beyond the liquid-gas spinodal at negative pressures was proposed by Angell [27]. The phase transition thus terminates at the l-g spinodal.

### The singularity free scenario

Sastry *et al.* [3] argued that the anomalies observed in water could be explained without the requirement of a critical point or the approach to a spinodal. Begin by noting that the slope of the TMD changes sign. We can then show that a locus of extremal compressibility can be determined without any divergence (see Fig. 1.10).

$$d\alpha_P = \left( \frac{\partial\alpha_P}{\partial T} \right)_P dT + \left( \frac{\partial\alpha_P}{\partial P} \right)_T dP \quad (1.42)$$

Along a line of constant density,  $d\alpha_P = 0$ , giving us

$$\left( \frac{dP}{dT} \right)_{d\alpha_P=0} = \frac{\alpha_P^2 - (1/V)(\partial^2 V/\partial T^2)}{K_T \alpha_P + (1/V)(\partial^2 V/\partial P \partial T)} \quad (1.43)$$

Along the locus of the TMD,  $\alpha_P = 0$ , allowing us to write:

$$\left( \frac{\partial K_T}{\partial T} \right)_{P,TMD} = \frac{1}{V} \frac{\partial^2 V/\partial T^2}{(dP/dT)_{TMD}} \quad (1.44)$$

- This means that the slope of the TMD locus and the slope of the  $K_T$  locus need to have the same sign.
- One notes that at high T,P,  $(\frac{\partial K_T}{\partial T})_P$  is positive, while at the TMD,  $(\frac{\partial K_T}{\partial T})_P$  is negative. This implies that there exists a locus of minimum  $K_T$ .
- One next considers  $(\frac{\partial K_T}{\partial T})_P$  near the spinodal, where it is positive. Reminding ourselves that at the TMD,  $(\frac{\partial K_T}{\partial T})_P$  is negative, one gets a locus of  $(\frac{\partial K_T}{\partial T})_P = 0$

The singularity free scenario predicts two states with no free energy cost to mixing [194]. Such a situation arises if the Hydrogen-bond formation is uncorrelated, allowing the intermixing of Hydrogen-bonded and non-bonded molecules [3,26,159].

It should be noted that two distinct liquid states can exist without phase separation and that data for some models is consistent with a sharp but continuous change in the properties of the liquid. Notably, the mW model displays such behaviour [55]. Aqueous solutions, where the solute effectively increases the pressure, changing the

phase diagram without increasing the propensity to crystallise (for non-polar solutes like glycerol) show experimental signatures of two liquid states for water without phase separation [182]. Analysis of thermodynamic data for TIP4P water [153], and recent results from  $\mu s$  long molecular dynamics simulation find phase separation to be weak [45], though these measurements were made close to the expected critical point.

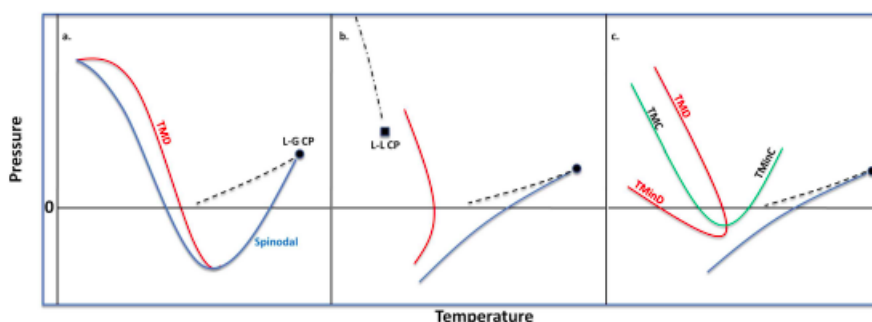


Figure 1.10: Schematic depiction of the stability limit conjecture (a), the two critical point scenario (b) and the singularity free scenario (c). The stability limit conjecture shows the liquid-gas spinodal curving upwards as it meets the locus of density maxima. The two critical point scenario shows the LLPT line ending at the LLC. The singularity free scenario shows the loci of density and compressibility extrema but without any phase transitions or critical points. This case can be understood as a situation where the LLC is at  $T = 0K$ . [From Vasisht and Sastry [4] with permission.]

## Spontaneous crystallisation

Another scenario that seeks to explain the apparent LLPT was first put forward by Limmer and Chandler who argued that the evidence from EOS studies pointed instead to spontaneous, slow crystallisation [18, 28]. They argued that the molecular dynamics runs were not equilibrated, and that this fact was obscured by the relaxation time of the degree of crystallinity being much larger than the relaxation time of the density. Their findings showed that the global bond orientational order, which was their measure of crystallinity, had a relaxation time at least two orders of magnitude greater than density. Based on this, and on umbrella sampling simulations, they argued instead for the slow coarsening of ice as the underlying cause of the apparent low density liquid. Since then, it has been shown that the relaxation timescales for  $Q_6$  and density are in fact similar [29, 30]. Notably, Limmer and Chandler noted that crystallisation could proceed without a growth in  $Q_6$ , and

despite constraining it with a bias potential. While their conclusions from this were in the direction of slow crystallisation, this instead foreshadowed some of the issues with  $Q_6$  as a measure of crystallinity that will be discussed in detail in this thesis.

In addition to Limmer and Chandler, the work of Moore and Molinero on mW water, also pointed to slow crystallisation rather than a second liquid [68]. Their work identified a temperature of maximum crystallisation rate below which the liquid crystallises faster than it can be equilibrated. This was argued, as also in the work of Limmer and Chandler, to be indicative of a lower limit of *thermodynamic* metastability of the liquid. In the context of silica, free energy calculations have highlighted the difference between the temperature of maximum crystallisation rate and the loss of thermodynamic stability of the liquid [169, 170].

The work of Holten *et al.* studied the available data on the mW model in depth and considered the possibility of weak, but spontaneous, crystallisation [55]. They applied a mean field theory to the fluctuations in short ranged translational order (measured from the static structure factor), fitting the available data to the expected form. In addition, they extrapolated data on the surface tension to estimate where it goes to 0, indicative of barrier-less crystallisation. From these analyses, they predicted that the thermodynamic limit of stability, where crystallisation is barrierless and spontaneous, is far below the temperature of maximum crystallisation rate, where the barrier is small but finite. Nevertheless, the (equilibrium) fluctuations in degree of crystallinity do increase, and their effect on the observed thermodynamic anomalies cannot be ruled out. This scenario argues that the low density phase will demonstrate finite ordering at all system sizes.

Ricci *et al.* found similar results for SW silicon, with umbrella sampling runs suggesting (i) no metastable LDL and (ii) loss of thermodynamic metastability of the liquid with respect to crystallisation [30]. Understanding their results is of core interest to this thesis.

In summary, this scenario is characterised by a gradual increase of the crystallinity order parameter which manifests in a barrier-less free energy profile. It is important to note that at low temperatures, both the barrier and the crystal growth rate are simultaneously low [50, 51]. Spontaneous crystallisation does not imply fast crystallisation in absolute time. This does not pertain to the existence of the anomalies directly but in this scenario, the formation of open, low-coordinated structures acts as a precursor to crystallisation. No distinct phase comprising of the low-coordinated particles exists. These arguments were made on the basis of

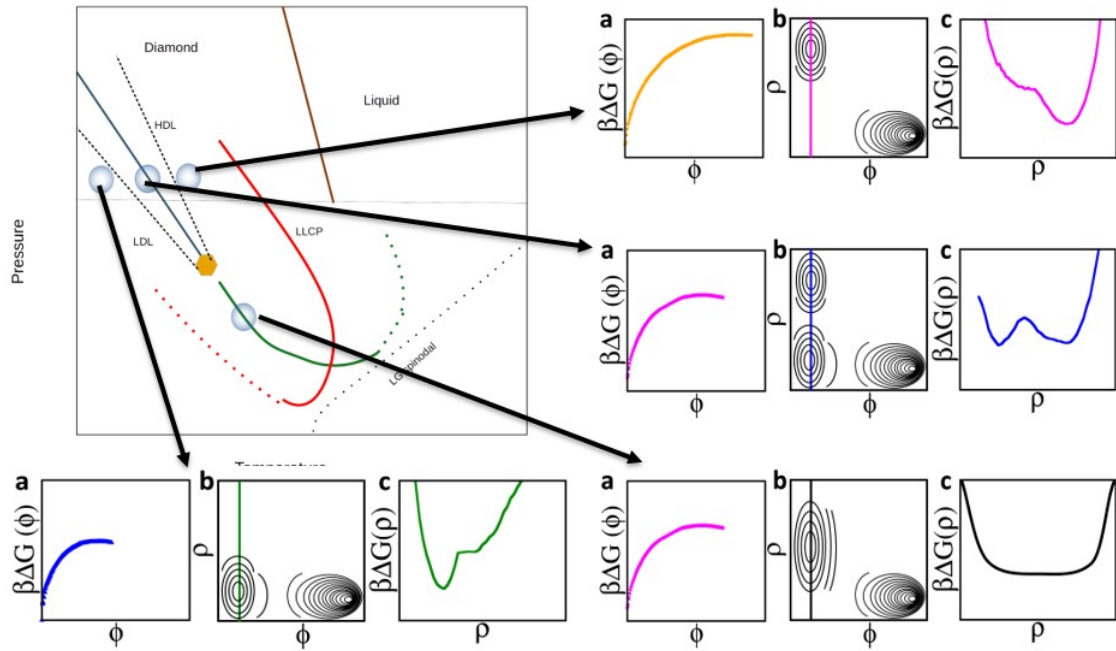


Figure 1.11: An annotated cartoon phase diagram, modelled on the one in Vasisht *et al.* [2]. The loci of extremal compressibility are in green while the loci of extremal density are in red. Dashed red/green are minima while solid red/green are maxima. The LLCP and the LGCP are shown as solid gold hexagons. The LDL-HDL coexistence limits are shown as dashed lines emanating from the LLCP to positive pressures. The LLPT is shown as a solid black line ending at the LLCP. The panels show (a) the expected nucleation barrier, (b) the two order parameter free energy profile (indicative contours), (c) the contracted free energy as a function of density. Each of the four panels is a representation of expected behaviour at the respective state points on the phase diagram. The four points are in the HDL region, on the LLPT coexistence line, in the LDL region and on the Widom line in the supercritical region.

reversible free energy calculations which are expected to give conclusive results for thermodynamics. Important considerations arise on the choice of order parameter which are discussed further in Chapter 3 and Chapter 4.

In Fig. 1.11, we show the expected results from free energy calculations based on the phase diagram reported from the equation of state studies of Vasisht *et al.* [2]. The spontaneous crystallisation scenario will instead show no barrier to crystallisation, while the singularity free scenario will not show phase separation and co-existence. The critical point free scenario will not show the continuous change in the liquid upon crossing the  $\kappa_T$  locus.

### 1.5.2 Microscopic lattice models

Prominent efforts to produce lattice models that display thermodynamic anomalies use the Ising lattice model as a baseline. Here, one includes additional variables to account for the role of hydrogen-bonding (in the case of water) as a microscopic driver of the presence of anomalies. Thus, in addition to defining a lattice site as occupied or empty, one has an additional variable for occupied lattice sites, specifying orientation – like in the Potts model [208].

Here, we need to satisfy some physical requirements

- The low temperature (presumed ground) state is an *open* structure. It has low density, low entropy and a lowered energy due to a stable hydrogen bond.
- The hydrogen-bond forms only if the requirements of open (more on this later) and orientation are met, thus the added orientation variable.
- Finally, the high density phase is also high energy, lacking the added stabilisation of a hydrogen bond but allowed more freedom of orientation in the lattice (in reality also translation) and thus greater entropy.

The lattice can be considered as two inter-penetrating sub-lattices  $A$  and  $B$  so that openness is now defined by whether for any given site  $i$  on sub-lattice  $A$  (say), there are no neighbours on sub-lattice  $B$  (open) or there are (closed) [208]. A schematic is provided in Fig. 1.12. The Hamiltonian can be written as, with  $XX$  meaning  $i, k$

neighbours on same sub-lattice and  $XY$  meaning different

$$H = -2\epsilon \sum_i^N \left( \sum_k \langle XX \rangle n_i n_k + \sum_j \langle XY \rangle n_i n_j \right) - 2J \sum_i^N \sum_j \langle XY \rangle n_i (1 - n_j) \delta_{\sigma_i, 1} \quad (1.45)$$

Such a Hamiltonian associates an additional energy benefit for no neighbours of  $i$  on the other sub-lattice and  $i$  being the correct orientation, specified by the orientation variable  $\sigma_i$  being the correct value, here written as 1. The partition function used here is the grand canonical partition function and with the mean field approximation one obtains expressions for the equilibrium density and equation of state.

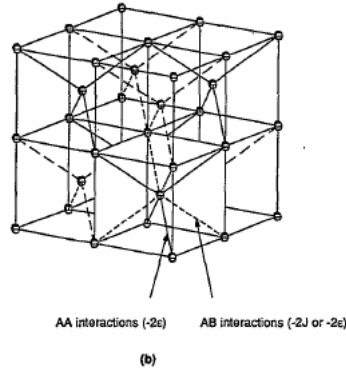


TABLE I. (a) Possible  $AA$  pair configurations and their interaction energies. (b) Possible  $AB$  pair configurations and their interaction energies.

$n_i$	$n_j$	Energy
1	0	0
0	1	0
0	0	0
1	1	$-2\epsilon$

$n_i$	$\sigma_i$	$n_j$	Energy
1	$\neq 1$	0	0
0		0	0
0		1	0
1	Any	1	$-2\epsilon$
1	1	0	$-2J$

Figure 1.12: Schematic of the inter-penetrating lattices (*Left*) and a table describing the interactions (*Right*). [From Sastry *et al.* [3] with permission.]

One can go a step further and write the Hamiltonian as sum of hydrogen-bonded and non-hydrogen-bonded contributions [3]. With this one gets

$$H = H_{NHB} + H_{HB} = -\epsilon \sum_{ij} n_i n_j - J \sum_{ij} n_i n_j \delta_{\sigma_i, j, \sigma_j, i} \quad (1.46)$$

Here we define orientation of  $i$  with respect to  $j$  and vice-versa. A choice needs to be made about whether the orientation of  $i$  with respect to  $j$ , which corresponds to formation or not of a hydrogen bond, specifies the orientation of  $i$  with some other  $k$ , or whether they can vary independently. For the calculation in [3], it was treated as independent to demonstrate the singularity free scenario.

Next, writing a description of the microscopic volume as  $b_{ij} = b$  if NHB and

$b_{ij} = b + \delta b$  if HB, where we have specified that hydrogen bonding results in increased volume, we have an expression for the total volume

$$V = \sum_{ij} b_{ij} = \sum_{ij} (b + \delta b n_i n_j \delta_{\sigma_{i,j}, \sigma_{j,i}}) \quad (1.47)$$

The control variables in this case are  $P, \mu, T$ , giving a Boltzmann weight of  $H + PV - \mu N$  and thermodynamic potential  $U - TS + PV - \mu N$  which is exactly 0 everywhere. The mean field approximation is used again to write the equation of state for the number density as a function of pressure  $P$  and so on. This calculation was used to verify conditions under which the singularity free scenario could be observed [3, 26]. La Nave *et al.* [213] performed such a calculation on the Bethe lattice with exact expressions for the free energy. Similar calculations have since been done, notably by Stokely *et al.*, incorporating the effects of hydrogen bond cooperativity [210]. These researchers find that tuning the energy benefit of hydrogen bonding and the constraints on orientation produced both phase-separation-like and singularity free behaviour.

### 1.5.3 Two-state thermodynamic models

The underlying framework is to use the equation of state for a mean field description like the van der Waals equation or the lattice gas equation. One then constructs a two-state analogy of the one-component liquid, invoking the free energy of mixtures. The known thermodynamic anomalies give one a benchmark of behaviour to expect and reproduce. An important point is that in these descriptions, the liquid is considered to be composed of particles which can be in one of two **states** (rather than a mixture of two liquids, or a mixture of two permanent local structures). These states are characterised by a free energy  $G_A$  and  $G_B$ , for the two states  $A$  and  $B$ . Many questions remain as to whether they are truly independent, how they depend on conditions and so on. The background free energy for the fluid equation of state needs to be included - allowing us to put liquid-vapour and LLPTs on one phase diagram.

**How do we now incorporate liquid polyamorphism?** At a given  $P, T$ , one can define the Landau free energy as a function of some order parameter  $\phi(\mathbf{r})$ .

$$L(\phi) = k_B T f(\phi(\mathbf{r})) - h\phi(\mathbf{r}) \quad (1.48)$$

The vector  $\mathbf{r}$  is the set of positions of a configuration. The quantity  $\phi(\mathbf{r})$  is a scalar, vector or tensor collective variable that serves to distinguish the disordered state (for which  $\phi = 0$ ) from the ordered state (for which  $\phi$  is finite).

If we use this to now construct the full free energy  $G(P, T, \phi)$ , which includes the background free energy describing the fluid equation of state, we get

$$G(P, T, \phi) = G_0(P, T) + k_B T f(\phi) - h\phi \quad (1.49)$$

We can ask the question of which regions of phase space  $\mathbf{r}$  are stable or metastable at a given  $P, T$  by considering solutions of  $\partial L / \partial \phi = 0$  which are solutions of  $\partial f / \partial \phi = h$ .

### Free energies for two-state models

At this point, we need to make arguments for the form of  $f(\phi)$  and of  $h$ . We mentioned before that we will consider the one-component fluid to be one with two inter-convertible states. The order parameter  $\phi$  can naturally be chosen as the reaction coordinate,  $x$  which is the fraction of particles/molecules in state  $B$ . Consider the single-component fluid as being composed of two interconvertible states  $A \rightleftharpoons B$  with reaction equilibrium (assuming Arrhenius rate with same kinetic prefactor) given by  $k_B T \ln(K(P, T)) = k_B T \ln(k_{AB}/k_{BA}) = -G_{BA}(P, T) = -h$ . We further argue that the one-component fluid with two states can be treated as a two-component mixture. This gives us  $f(\phi) = G_{\text{mix}}$ . The free energy of mixing can be written as

$$G_{\text{mix}} = k_B T (x \ln(x) + (1 - x) \ln(1 - x)) + \omega x(1 - x) \quad (1.50)$$

which we will quickly derive.

The general free energy expression as a function of  $P, T, x$  will be given by

$$G(P, T, x) = G_A(P, T) + x G_{BA}(P, T) + k_B T (x \ln(x) + (1 - x) \ln(1 - x)) + \omega x(1 - x) \quad (1.51)$$

The first term is the background free energy of the pure fluid, where the fluid of all  $A$  is considered the parent fluid. The second term is the free energy change when a switch occurs from  $A$  to  $B$  - more on this later. The remaining terms come from the mixing free energy. Other works have also investigated a two-state description of the liquid [16, 193, 209, 210]. The background fluid is typically described by a



standard equation of state such as the van der Waals equation or the lattice gas equation [194].

### Gibbs energy of mixtures

$$G_{\text{mix}} = H_{\text{mix}} - TS_{\text{mix}} \quad (1.52)$$

The entropy of mixing can be derived in a number of ways. Easiest to consider the Boltzmann definition

$$S = -k_B \sum_i p_i \ln(p_i) \quad (1.53)$$

Here,  $p_i$  is the probability of being in state  $i$ . If we have a two-state mixture,  $A, B$  where a fraction  $x$  is in state  $B$  then we get

$$S_{\text{mix}} = -k_B(x \ln(x) + (1 - x) \ln(1 - x)) \quad (1.54)$$

An ideal mixture is one where  $G_{\text{mix}} = -TS_{\text{mix}}$ . However, a non-ideal mixture will involve an enthalpy of mixing

$$H_{\text{max}} = \omega(P, T)x(1 - x) \quad (1.55)$$

For the rest of the discussion we consider  $\omega$  to be constant. Later, we will revisit the implications of this assumption. The dependence of  $\omega$  on state variables  $P, T$  depends on whether (i) the non-ideality of the solution is heavily dependent on entropy, i.e., the possible positions of  $A$  and  $B$  types are heavily dependent on  $T$  meaning - size differences or geometric constraints matter. (ii) The non-ideality of the solution is heavily dependent on enthalpy, i.e., the energy difference between  $AA, AB$  and  $BB$  arrangements dominate over size-differences. This means  $P$  is the dominant variable.

Consider expanding the free energy change when switching as a polynomial expansion in  $P$  and  $T$ .

$$G_{BA}(P, T) = k_B(\lambda + \alpha P + \beta T + \gamma PT + \delta T^2 + \epsilon P^2) \quad (1.56)$$

This is to say that a state switch from  $B$  to  $A$  has an accompanying change in energy,  $\lambda$ , change in volume given by  $\alpha$ , change in entropy given by  $\beta$ , expansion coefficient,  $\gamma$ , heat capacity  $\delta$  and compressibility  $\epsilon$ . In the discussion that follows, only the linear terms are included, however, different truncations to the series have

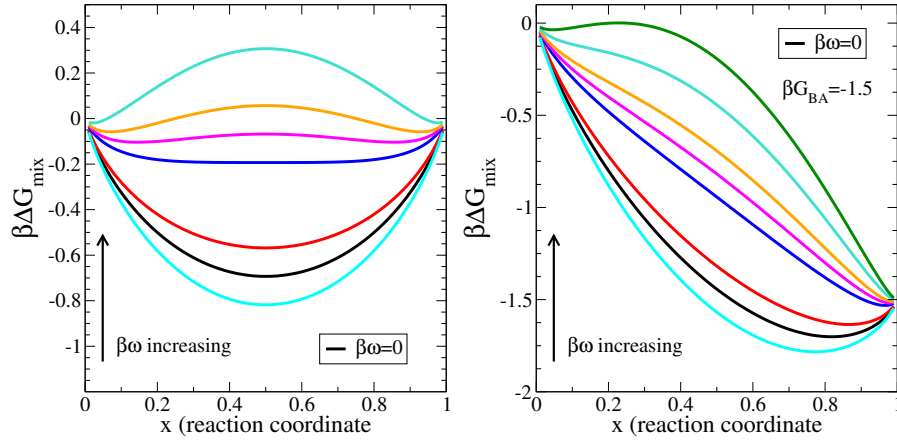


Figure 1.13: Compare the solutions of  $\frac{\partial\beta\Delta G_{\text{mix}}(x)}{\partial x} = 0$  as we change the enthalpy of mixing (*Left*) and add a free energy difference between the  $B$  state and  $A$  state.

been proposed, either based on physical arguments or as first order approximations [16, 55, 153, 194, 206]. The implications of the approximation made are serious, as is the assumption that  $G_A$  and  $G_B$  vary independently with  $P$  and  $T$ .

$$G_{BA}(P, T) = k_B(\lambda + \alpha P + \beta T) \quad (1.57)$$

The locus of  $G_{BA}(P, T) = 0$  gives us the critical point and line of phase transitions.

## Critical point and phase transition line for two-state models

Consider the case where the Hamiltonian has no asymmetry wrt states,  $A$  or  $B$ , i.e.,  $G_{BA}(P, T) = 0$ . In this case, the solutions for  $x$  of  $\frac{\partial\beta\Delta G_{\text{mix}}(x)}{\partial x} = 0$  give us extrema of  $G_{\text{mix}}$ . We are interested in minima, i.e., stable solutions indicated by the intersections of the two functions (see Fig. 1.14).

Solutions satisfy the equation

$$k_B T \ln\left(\frac{x}{1-x}\right) = \omega(1-2x) \quad (1.58)$$

The locus of  $G_{BA}(P, T) = 0$  is the line of phase transitions with the critical temperature dependent on the non-ideality of the mixture by the relation

$$T_c = \frac{\omega}{2k_B} \quad (1.59)$$

At  $T < T_c$  we have two phases with different concentrations of  $B$ . For  $T > T_c$ , the

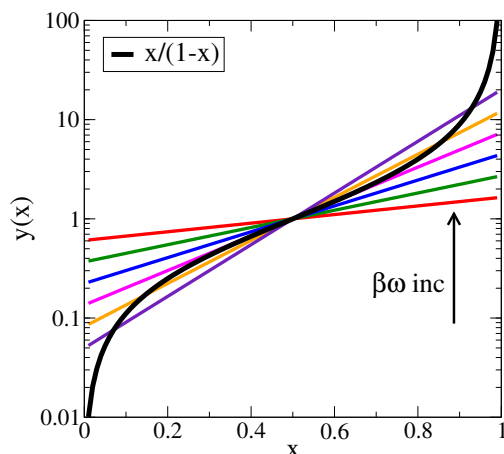


Figure 1.14: Intersections of  $\frac{x}{1-x}$  with  $\exp(\beta\omega(2x-1))$  are shown. As we cross  $\beta\omega = 2$  from higher  $T$  (lower  $\beta$ ) we go from one stable solution at  $x = 0.5$  to two stable solutions on either side of  $x = 0.5$  with the  $x = 0.5$  solution becoming an unstable solution.

only stable solution is the mixed phase with  $x = 0.5$ . The transition pressure,  $P_c$  is the value of  $P$  that satisfies  $G_{BA}(P, T_c) = 0$ . The asymmetric case has only one solution, depending on the sign of  $G_{BA}$ .  $G_{BA}(P, T)$  needs to be continuous across the transition line. If it changes sign across the line we go from a stable  $A$  phase to a stable  $B$  phase.

### The role of inter-conversion timescales on phase equilibrium

- If we consider the reaction  $A \rightleftharpoons B$  to be fast wrt the observation timescales, then we can assume a reaction equilibrium case.
- If this reaction is slow, then the value of  $x$  is static and a free parameter. We cannot then look for solutions of  $\frac{\partial \beta \Delta G_{\text{mix}}(x)}{\partial x} = 0$ .
- This reaction doesn't have to be a chemical reaction involving the breaking of bonds, simply a well-defined change in state of the components, on a fast timescale compared to the observation time

### 1.5.4 Characterising the liquid-liquid critical point

The LLPT is expected to belong to the Ising 3D universality class [214, 215]. For us to understand what this means we need to find analogues to the fields and to the order parameter in the Ising system. What plays the role of magnetisation,

$M$ , magnetic field,  $h$ , and temperature,  $T$ ? We also need to define the relevant susceptibilities.

In general, one can write a thermodynamic potential,  $\Psi$ , which is a free energy corresponding to the relevant ensemble. Two fields are then defined, with which one associates the order parameters, and Legendre transforms to other thermodynamic potentials [215–217]. If we call these fields  $h_1$  and  $h_2$ , and the respective parameters  $\phi_1$  and  $\phi_2$ , we can write the following equation of state:

$$\Psi = \phi_1 dh_1 + \phi_2 dh_2 \quad (1.60)$$

Here, one field is the “ordering field” while the other is the “thermal field”. The respective order parameters are “strongly fluctuating” and “weakly fluctuating. Consider for a moment the liquid-gas transition. It may seem that the ordering field is the pressure and the corresponding parameter some function of density, such as  $(\rho - \rho_c)/\rho_c$ , where  $\rho_c$  is the density at the critical point. However, in reality the fields  $h_1$  and  $h_2$  are linear combinations of temperature, pressure and other state control variables, depending on the ensemble.

Close to the critical point ( $h_1 = 0, h_2 = 0$ ), the equation of state has an asymptote of the form:

$$\Psi = |h_2|^{2-\alpha} f^\pm \left( \frac{h_1}{|h_2|^{2-\alpha-\beta}} \right) \quad (1.61)$$

Here,  $\alpha$  and  $\beta$  are critical exponents, and an additional exponent,  $\gamma$  can be related as  $\gamma = 2 - \alpha - 2\beta$ .  $f^\pm$  can vary in general depending on whether  $h_2 < 0$  or  $h_2 > 0$  [217].

Of course, the exponents  $\alpha, \beta, \gamma$  are the well-known exponents for heat capacity, order parameter dependence on the temperature field in the sub-critical regime, and the susceptibility respectively. Their values are determined by the universality class of the phase transition, and for Ising 3D their values are  $\alpha = 0.110, \beta = 0.3265, \gamma = 1.237$ .

The fields  $h_1$  and  $h_2$  are defined differently depending on whether the system is a lattice gas [217], liquid-liquid co-existence [207, 215, 218, 219], liquid-vapour or a binary mixture [216, 217, 220, 221].

We will use the example of liquid-liquid co-existence to illustrate the connection between the fields and thermodynamic state variables. Consider the scaled pressure and temperatures,  $\Delta P = \frac{(P-P_c)}{\rho_c N k_B T}$ ,  $\Delta T = \frac{T-T_c}{T_c}$ . If the slope of the co-existence line

$(d\Delta P/d\Delta T)_{LLPT} = \tan\theta$ , then the field is given by [215]:

$$\begin{aligned} h_1 &= \Delta P \cos(\theta) - \Delta T \sin(\theta), \\ h_2 &= \Delta T \cos(\theta) + \Delta P \sin(\theta). \end{aligned} \quad (1.62)$$

In the two-state model described earlier, recall that the rate constant governing interconversion between states  $A$  and  $B$  was defined  $\ln K(P, T) = -\beta G_{BA}(P, T)$ .  $\phi_1$  is the order parameter differentiating  $A$  and  $B$ . We then have  $h_1 = \ln K$  and  $h_2 = 2 - W$ , where  $W$  is the non-ideality in the two-state scheme [207]. Note that the fields are defined differently for other cases, and that even for the LLCP, arguments can be made for a non-linear or inhomogeneous definition of  $h_1$  and  $h_2$  in terms of the state variables.

In general, the ordering variable follows  $\phi_1 = \pm B_0 |h_2|^\beta$  close to the critical point for  $h_2 < 0$ .  $B_0$  is an amplitude that depends on the system being studied. It quantifies the degree to which the two phases differ in the value of  $\phi_1$ . The thermal variable, to which the entropy also contributes, follows  $\phi_2 = A_0 h_2^{-\alpha}$ .

The susceptibilities are given by

$$\chi_{ij} = \frac{\partial \phi_i}{\partial h_j} \quad (1.63)$$

where  $i, j$  are indexed over the two fields and variables. The free energy  $\Psi$  can also be written in the mean-field limit in the Landau form. Following through these lines of analysis provides predictions for both the degree and nature of differences between the two phases based on thermodynamic consistency. One also can define the Widom line as earlier, the locus of  $\ln K(T, P) = 0$  for  $h_2 > 0$ . The loci of the maxima of the response functions asymptotically approach the Widom line close to the critical point [215].

### 1.5.5 Connecting simulations to phenomenological models

A comparison of the macroscopic trends, the exponents and amplitudes discussed in the preceding sections with simulation results for a system such as silicon would be a challenging task. Extensive simulation studies would need to be performed at precise and challenging conditions. The other challenge is to identify the order parameters and ordering fields that do exhibit Ising-like fluctuations.

Such an analysis, while challenging, can address some important questions. In

the discussion in this section and also in Sec. 1.5.3, the locus of co-existence is approximated to various simple forms. The equation for the locus has deep implications for the predictions that are subsequently generated. Thus, having reliable data on the locus of co-existence is a key step towards leveraging the ability of these models to classify and/or generalise the phenomenology observed in different systems. Other questions that can be addressed by simulations are whether there is in fact a clear separation into two states, or whether there is a continuous spectrum. Is the treatment of the relative free energies of the two states used in the models of Sec. 1.5.3 justified? The singularity free scenario is realised when hydrogen-bonding is allowed to occur in an uncorrelated manner between different neighbours. Is such a scenario observed for any real or model liquid?

## 1.6 Scope of the thesis

Chapter 2 will summarise the model potential, simulation methods and methods to calculate various quantities and common order parameters that have been used in this work, each of which are also described in the literature.

Chapter 3 will discuss the crystallisation transition in the deeply supercooled liquid. The goal is to determine whether there is a free energy barrier to crystallisation. We find through two independent methods that there is.

Chapter 4 will contain a detailed discussion of different order parameters, their merits and demerits, and as well focus on the role of choice of order parameter in earlier work suggesting spontaneous crystallisation. A discussion of other relevant order parameter definitions is also included.

Chapter 5 will describe results from the investigation into the LLPT. We find through extensive simulations that there are two distinct liquid states and that we can identify conditions of co-existence.

Chapter 6 will describe a novel method to conduct free energy calculations and demonstrate results when applied to a toy model. The method described here is one that can be used to reconstruct free energy profiles of multiple order parameters from unconstrained crystallising simulations.

Chapter 7 will contain concluding remarks as well as directions of future study.

# Chapter 2

## Model and methods

### 2.1 The Stillinger-Weber potential

The Stillinger-Weber potential, employed here, is the most widely used classical potential of silicon. It consists of a two-body term and a three-body term,  $U_2$  and  $U_3$ , respectively. [25]

$$U_{SW} = \sum_{j>1}^N U_2(r_{ij}) + \sum_{i<j<k}^N U_3(\mathbf{r}_i, \mathbf{r}_j, \mathbf{r}_k) \quad (2.1)$$

The vectors,  $\mathbf{r}_i, \mathbf{r}_j, \mathbf{r}_k$ , are position vectors for atoms  $i, j, k$  and  $r_{ij}$  is the distance between the  $i^{th}$  and  $j^{th}$  atoms.  $N$  is the total number of atoms in the system.

$$U_2(r_{ij}) = \begin{cases} \epsilon A \left( \frac{B}{r_{ij}^4} - 1 \right) e^{\frac{1}{r_{ij}-r_c}} & \text{if } r < r_c \\ 0 & \text{if } r \geq r_c \end{cases} \quad (2.2)$$

The three-body interaction term is defined by

$$U_3(\mathbf{r}_i, \mathbf{r}_j, \mathbf{r}_k) = h(r_{ij}, r_{ik}, \theta_{jik}) + h(r_{ij}, r_{jk}, \theta_{ijk}) + h(r_{ik}, r_{jk}, \theta_{ikj}) \quad (2.3)$$

In turn,

$$h(r_{ij}, r_{ik}, \theta_{jik}) = \begin{cases} \epsilon \lambda [\cos\theta_{jik} + \alpha]^2 e^{\frac{\gamma}{r_{ij}-r_c} + \frac{\gamma}{r_{ik}-r_c}} & \text{if } r_{ij}, r_{ik} < r_c \\ 0 & \text{if } r_{ij} \text{ or } r_{ik} \geq r_c \end{cases} \quad (2.4)$$

The constants used in the equations above are listed in the table below:

Symbol	$A$	$B$	$r_c$	$\lambda$	$\alpha$	$\gamma$
Value	7.04955	0.60222	1.80	21.0	1/3	1.20

An in-house code was used for the Umbrella Sampling Monte Carlo simulations that used an efficient double-sum implementation of the three-body Stillinger Weber potential described in Saw *et al* [222] and in [128]. Umbrella sampling is described later on in this chapter. Table 2.1 lists the conversions from reduced units to standard units.

Observable	Factor (Unit)
Length	$r^* \times 2.0951$ (Å)
Energy	$E^* \times 209.5$ (kJ/mol)
Mass	$m^* \times 28.0855$ (gm/mol)
Temperature	$T^* \times 25173$ (K)
Pressure	$P^* \times 37.776$ (GPa)
Density	$\rho^* \times 5.0571$ (gm/cm <sup>3</sup> )
Time	$t^* \times 76.6$ (fs)
Diffusivity	$D^* \times 0.005730345$ (cm <sup>2</sup> /s)
Viscosity	$\eta^* \times 0.029060146$ (poise)

Table 2.1: Conversion factor for various observables calculated from the Stillinger-Weber model potential for silicon.

## 2.2 Molecular dynamics

Molecular dynamics simulations of silicon have largely been performed in the  $NVT$  and  $NPT$  ensemble using the LAMMPS simulation package [223]. The equations of motion are integrated with the commonly used velocity Verlet scheme and a timestep of 0.3830  $fs$ . Very briefly, one integrates positions and velocities with the following pair of equations in the  $NVE$  ensemble.

$$\begin{aligned}
 \mathbf{r}_i(t + \Delta t) &= \mathbf{r}_i(t) + \Delta t \mathbf{v}_i(t) + \Delta t^2 \frac{\mathbf{F}_i(t)}{m_i} \\
 \mathbf{v}_i(t + \Delta t) &= \mathbf{v}_i(t) + \Delta t \frac{\mathbf{F}_i(t) + \mathbf{F}_i(t + \Delta t)}{2m_i}
 \end{aligned}
 \tag{2.5}$$

For constant pressure, constant temperature simulations, the Hoover equations are used which incorporate additional degrees of freedom to implement the temperature



control and for the adjustable volume [224]. It should be noted that the underlying Hamiltonian is therefore modified from the canonical

$$H = U(\{\mathbf{x}_i\}) + \frac{1}{2m} \sum_i \mathbf{p}_i^2$$

The resulting modified equations of motion are

$$\dot{\mathbf{r}}_i = \frac{\mathbf{p}_i}{m_i} + \frac{p_\epsilon}{W} \mathbf{r}_i, \quad (2.6)$$

$$\dot{\mathbf{p}}_i = \mathbf{F}_i - \frac{p_\epsilon}{W} \mathbf{p}_i - \frac{p_\xi}{Q} \mathbf{p}_i. \quad (2.7)$$

$$\dot{V} = \frac{d V p_\epsilon}{W}, \quad (2.8)$$

$$\dot{p}_\epsilon = d V (P_{int} - P_{ext}) - \frac{p_\xi p_\epsilon}{Q}, \quad (2.9)$$

$$\dot{\xi} = \frac{p_\xi}{Q}, \quad (2.10)$$

$$\dot{p}_\xi = \sum_{i=1}^N \frac{\mathbf{p}_i^2}{m_i} + \frac{p_\epsilon^2}{W} - (N_f + 1) k_B T \quad (2.11)$$

The variable that defines the volume is  $\epsilon = \ln(V/V_0)$ .  $\xi$  is the thermostat position while  $p_\xi$  is the thermostat momentum.  $p_\epsilon$  is the barostat momentum.  $N_f$  is the number of degrees of freedom,  $3N$  in 3D.  $P_{int}$  is the ‘‘internal’’ pressure calculated from the virial and the kinetic energy of the system, and  $P_{ext}$  is the external, imposed pressure.  $W$  is a piston-like pressure damping factor while  $Q$  is a temperature damping factor. The forces  $F$  are obtained from the gradient of a continuous, differentiable interaction potential. The values of the damping coefficient used in the simulations of silicon were  $Q = 100$  and  $W = 1000$  across all cases.

$$P_{int} = \frac{1}{dV} \left[ \sum_{i=1}^N \frac{\mathbf{p}_i^2}{m} + \sum_{i=1}^N \mathbf{r}_i \cdot \mathbf{F}_i \right] \quad (2.12)$$

Note that this form does not include the corrections related to long-range interactions [224]. The LAMMPS package uses optimised, modified versions of this scheme [225, 226].

## 2.3 Monte Carlo

Monte Carlo (MC) simulations are performed to compute equilibrium properties and averages in multiple ensembles. The MC scheme uses a non-physical probabilistic trial move and a Boltzmann weighted acceptance criterion to sample phase space. As a result, dynamical quantities are not accessible, though timescales can be mapped in some cases.

In a MC simulation a series of configurations are generated such that the distribution of these configurations will be proportional  $\exp(-\beta H(\{\mathbf{r}\}))/Z$ , where  $H(\{\mathbf{r}\})$  is the Hamiltonian of the system and  $Z$  is the partition function. Thermodynamic averages can be calculated in such an importance sampling scheme as  $\langle A \rangle = \frac{1}{N} \sum_{i=1}^N A(\{\mathbf{r}\})$ , where  $N$  total number of configurations. The Metropolis method defines the probability of a move from state  $o$  to state  $n$  as

$$P(o)\pi(o \rightarrow n) = P(n)\pi(n \rightarrow o) \quad (2.13)$$

where  $\pi(o \rightarrow n)$  is the transition probability (from  $o$  to  $n$ ) and  $P(o)$  is the probability of the system being in state  $o$ . The transition probability is the product of a trial probability  $\alpha(o \rightarrow n)$  and an acceptance probability  $\text{acc}(o \rightarrow n)$ . In all our simulations we assume  $\alpha$  is symmetric i.e.,  $\alpha(o \rightarrow n) = \alpha(n \rightarrow o)$ . Hence we get

$$\begin{aligned} P(o)\text{acc}(o \rightarrow n) &= P(n)\text{acc}(n \rightarrow o) \\ \frac{\text{acc}(o \rightarrow n)}{\text{acc}(n \rightarrow o)} &= \frac{P(n)}{P(o)} = \exp(-\beta[E(n) - E(o)]) \end{aligned} \quad (2.14)$$

Finally, we use an acceptance probability of the form

$$\begin{aligned} \text{acc}(o \rightarrow n) &= \exp(-\beta[E(n) - E(o)]) \quad \text{if } E(n) > E(o) \\ &= 1 \quad \text{if } E(n) < E(o). \end{aligned} \quad (2.15)$$

In the constant pressure, constant temperature NPT ensemble, the acceptance ratio is

$$\begin{aligned} \text{acc}(o \rightarrow n) &= \min(1, \exp(-\beta[E(n) - E(o) + P(V_n - V_o) \\ &\quad - (N + 1)\beta^{-1} \ln(V_n/V_o)])) \end{aligned} \quad (2.16)$$

where energy  $E$  is a function both coordinates and volume,  $P$  is the applied pressure. In the NPT ensemble, trial moves include trial changes in the (logarithm of) the volume, with particle positions accordingly rescaled. The umbrella sampling and parallel tempering schemes are built on the Monte Carlo scheme and will be discussed in Section 2.8 and Section 2.8.1.

## 2.4 Structural parameters - Radial distribution function and static structure factor

The radial distribution function belongs to the family of  $n$ -particle correlation functions of the number density. In the liquid state, the expected behaviour of such correlation functions has been studied extensively for various model liquids, those with purely repulsive interactions and those with both repulsive and attractive interactions. Specifically, the radial distribution function,  $g(r)$ , is the  $n = 2$  instance of the number density correlations, hence also known as the pair correlation function. It serves as an extremely useful first quantity to look at in the context of supercooled liquids which may display structural changes. Moreover, for the crystalline state, which has long ranged order, one observes a distinctive  $g(r)$ , sharply peaked at the lattice positions and low (or zero elsewhere).

$$g^{(2)}(\mathbf{r}_1, \mathbf{r}_2) = \frac{V^2}{N^2} \frac{N!}{(N-2)!} \frac{\int \cdots \int e^{-\beta U_N} d\mathbf{r}_3 \cdots d\mathbf{r}_N}{Z_N} \quad (2.17)$$

In simulations,  $g(r)$  is obtained by populating a histogram of interparticle distances.

$$g(r) = \frac{V}{N^2} \left\langle \sum_i \sum_{j \neq i} \delta(|\mathbf{r}| - \mathbf{r}_{ij}) \right\rangle. \quad (2.18)$$

The static structure factor, for a wave vector  $k$  is defined as

$$\begin{aligned} S(k) &= \frac{1}{N} \left\langle \delta\rho(\vec{k}) \delta\rho(-\vec{k}) \right\rangle \\ S(k) &= \frac{1}{N} \left\langle \frac{1}{N_k} \int_{\mathbf{r}} d\mathbf{r} \rho(\mathbf{r}) e^{i\mathbf{k}\cdot\mathbf{r}} \rho(\mathbf{r}) e^{-i\mathbf{k}\cdot\mathbf{r}} \right\rangle \end{aligned} \quad (2.19)$$

where  $N$  is the total number of particles and  $\delta\rho(\vec{k})$  is the fluctuation in local density in Fourier space. The structure factor is related to the isothermal compressibility

$K_T$  of the system at temperature  $T$ , by

$$\lim_{k \rightarrow 0} S(k) = \rho k_B T \kappa_T \quad (2.20)$$

where  $k_B$  is the Boltzmann constant.

## 2.5 Dynamical quantities

The mean square displacement (*MSD*) is a measure of the average distance a particle travels in a given time interval and is defined as:

$$\langle \mathbf{r}^2(t) \rangle \equiv \frac{1}{N} \left\langle \sum_{i=1}^N |\mathbf{r}_i(\mathbf{t}) - \mathbf{r}_i(\mathbf{0})|^2 \right\rangle \quad (2.21)$$

where  $N$  is the total number of particles. The angular bracket represents average over different time origins. Typically the MSD has three regimes of dynamics. (i) The short time ballistic regime (no collisions) where the MSD is proportional to  $t^2$  as with motion at constant velocity. (ii) An intermediate ‘‘caging’’ timescale can be identified when particles begin to collide with their neighbours. At dense packings or deep supercooling, the caging timescale can be long with a clear plateauing of the MSD. At even longer timescales the particles escape their cages and diffusive motion sets in where the MSD is proportional to  $t$ . One can infer the diffusivity from the MSD with:

$$D = \lim_{t \rightarrow \infty} \frac{\langle \mathbf{r}^2(t) \rangle}{6t} \quad (2.22)$$

At very deep supercoolings where the cage breaking time extends to infinity, the metastable liquid is said to have fallen out of equilibrium – marking the onset of glassy dynamics.

### 2.5.1 Time auto-correlation functions

In this section, we introduce correlation functions that describe time, space, or frequency dependent responses in the system. A time correlation function between two quantities  $A$  and  $B$  is generally defined as follows:

$$C_{AB}(t) = \langle A(t_0)B(t_0 + t) \rangle_{t_0;eq}$$

where we have taken an equilibrium average. For systems in equilibrium, the time-correlation function has no initial time dependence, and is symmetric with respect to time-reversal. The correlation function where  $A = B$  is the auto-correlation function, and gives a measure of the time required for memory-loss or equilibration to occur. We define  $\Delta A(t) = A(t) - \langle A \rangle$  and use the following normalised expression:

$$\begin{aligned} C_A(t) &= \frac{\langle \Delta A(t) \Delta A(0) \rangle}{\langle A^2 \rangle - \langle A \rangle^2} \\ &= \frac{\langle A(t) A(0) \rangle - \langle A \rangle^2}{\langle A^2 \rangle - \langle A \rangle^2} \end{aligned} \quad (2.23)$$

**The integrated auto-correlation time** is obtained from the self auto-correlation as

$$g = 1 + 2 \left[ \sum_{t=1}^{T-1} \left( 1 - \frac{t}{T} \right) C_{AA}(t) \right] \quad (2.24)$$

This quantity gives a measure of the timescale separating decorrelated observations in a trajectory or time series. It is of relevance in performing equilibrium sampling.

### 2.5.2 Self-intermediate scattering function

**Van Hove function:** It is defined as the probability density of finding a particle  $i$  in the vicinity of  $r$  at time  $t$  given that the particle  $j$  was in the vicinity of origin at time  $t = 0$ .

$$\begin{aligned} G(\mathbf{r}, t) &= \frac{1}{N} \langle \rho(\mathbf{r}, t) \rho(0, 0) \rangle \\ &= \frac{1}{N} \left\langle \sum_j \sum_i \delta(\mathbf{r} - \mathbf{r}_j(t) + \mathbf{r}_i(0)) \right\rangle \end{aligned} \quad (2.25)$$

$G(\mathbf{r}, t)$  has two parts as described below.

$$G(\mathbf{r}, t) = G_s(\mathbf{r}, t) + G_d(\mathbf{r}, t) \quad (2.26)$$

$$\begin{aligned} G_s(\mathbf{r}, t) &= \frac{1}{N} \left\langle \sum_i \delta(\mathbf{r} - \mathbf{r}_i(t) + \mathbf{r}_i(0)) \right\rangle \\ G_d(\mathbf{r}, t) &= \frac{1}{N} \left\langle \sum_i \sum_{j \neq i} \delta(\mathbf{r} - \mathbf{r}_j(t) + \mathbf{r}_i(0)) \right\rangle \end{aligned}$$

**Intermediate scattering function:** The Fourier transform of  $G(\mathbf{r}, t)$  is called the intermediate scattering function  $F(\mathbf{k}, t)$  defined as the following.

$$\begin{aligned} F(\mathbf{k}, t) &= \int d\mathbf{r} G(\mathbf{r}, t) \exp(-i\mathbf{k}\cdot\mathbf{r}) \\ &= \frac{1}{N} \langle \rho(\mathbf{k}, t) \rho(-\mathbf{k}, 0) \rangle \end{aligned} \quad (2.27)$$

Where

$$\rho(\mathbf{k}, t) = \int d\mathbf{r} \rho(\mathbf{r}, t) \exp(-i\mathbf{k}\cdot\mathbf{r}) \quad (2.28)$$

$F(\mathbf{k}, t)$  can be also be divided into self part and distinct part :

$$F(\mathbf{k}, t) = F_s(\mathbf{k}, t) + F_d(\mathbf{k}, t)$$

$$F_s(\mathbf{k}, t) = \int d\mathbf{r} G_s(\mathbf{r}, t) \exp(-i\mathbf{k}\cdot\mathbf{r})$$

$$F_d(\mathbf{k}, t) = \int d\mathbf{r} G_d(\mathbf{r}, t) \exp(-i\mathbf{k}\cdot\mathbf{r}) \quad (2.29)$$

The self-intermediate scattering function,  $F_s(k, t)$  is calculated at a  $k$  value corresponding to the first peak of structure factor  $S(k)$ . The alpha relaxation time ( $\tau_\alpha$ ) is obtained usually as the time at which the  $F_s(k, t)$  decays by a factor of  $e$ .

The self diffusion coefficient or the diffusivity  $D$  is also obtained from the velocity auto-correlation function using the Green-Kubo formula

$$D = \frac{1}{3} \int_0^\infty \langle \vec{v}(t) \cdot \vec{v}(0) \rangle dt. \quad (2.30)$$

## 2.6 Order parameters

The order parameters that distinguish the different phases will be discussed in this section. The ordered crystalline configurations typically have high degrees of orientational ordering. The bond orientational order parameters are used as a result. The low temperature liquid differs significantly from the high temperature liquid in the degree of orientational ordering, specifically tetrahedral ordering. As will be discussed in more detail in Chapter 4, there are significant implications to whether a local or a global measure of crystalline ordering is used. We will define both global and local bond orientational order and the prescription to identify bulk

crystalline particles which can then be grouped together into clusters based on a distance criterion.

### 2.6.1 Bond orientational order

The thermodynamics of whether the liquid is metastable with respect to crystallization at a given temperature and pressure is determined by constructing the Landau free energy as a function of an order parameter. The order parameter(s) is chosen such that it distinguishes the liquid from the crystalline state sufficiently well. Here the strategy that is used is to identify crystalline particles and calculate the free energy cost to the growth of crystalline clusters of different sizes. Such an approach is broadly in consonance with Classical Nucleation Theory [48, 227] where the transition from the metastable liquid to the crystalline state occurs through rare fluctuations that generate crystalline clusters of different sizes. These clusters have a lower free energy in the bulk than the surrounding liquid, whereas the formation of an interface between the liquid and the solid induces a free energy cost. The bond orientational order parameters of Steinhardt and Nelson, [228]  $q_l$  serve to distinguish local crystalline structures from disordered liquid ones.

Specifically, the local analogue of these order parameters can be used to distinguish the neighbourhoods of individual particles and classify them as being ordered or disordered. In terms of

$$q_{lm}(i) = \frac{1}{n_b(i)} \sum_{j=1}^{n_b(i)} Y_{lm}[\theta(r_{ij}), \phi(r_{ij})], \quad (2.31)$$

the order parameter  $q_l$  is obtained by summing over  $m$ 's:

$$q_l(i) = \left[ \frac{4\pi}{(2l+1)} \sum_{m=-l}^l |q_{lm}(i)|^2 \right]^{1/2} \quad (2.32)$$

In the present work, we use  $q_3(i)$  [1], noting that using  $q_6(i)$  is equally feasible, and gives very similar results [15, 131]. The number of neighbours,  $n_b(i)$ , is taken to be the atoms within the first coordination shell of the pair-correlation function, i.e., atoms within a cut-off of  $2.95 \text{ \AA}$  from the reference atom. Other works have considered other definitions, such as considering only the four nearest neighbours. However, when there are more than four atoms at similar distances from the reference atom, certain artefacts arise such as the apparent decrease of tetrahedral

ordering with density or an increase with pressure [131]. We therefore employ a distance-based cut-off to specify nearest neighbours.

The global bond order parameters have been used in some work to distinguish the crystalline state from the disordered liquid [18, 28–30]. These are defined as

$$Q_{lm} = \frac{1}{N_b} \sum_{i=1}^N \sum_{j=1}^{n_b(i)} Y_{lm}[\theta(r_{ij}), \phi(r_{ij})] \quad (2.33)$$

Here,  $n_b(i)$  is the number of bonds for the  $i^{\text{th}}$  particle.  $Y_{lm}$  is the spherical harmonic and  $N_b$  is the total number of bonds. The limits of the neighbourhood are defined by the first minimum of the radial distribution function.

The global bond orientational order can now be expressed in terms of  $Q_{lm}$

$$Q_l = \sqrt{\frac{4\pi}{(2l+1)} \sum_{m=-l}^l |Q_{lm}|^2} \quad (2.34)$$

One often encounters a modified equation for the global order

$$Q_l^i = \sqrt{\frac{4\pi}{(2l+1)} \sum_{m=-l}^l \left| \frac{1}{N_b(i)} \sum_{j=1}^{N_b(i)} Y_{lm}[\theta(r_{ij}), \phi(r_{ij})] \right|^2} \quad (2.35)$$

$$Q_l = \frac{1}{N} \sum_{i=1}^N Q_l^i. \quad (2.36)$$

Written in this way, the main difference is that the global order for odd  $l$  does not vanish. In Eq. 2.34, the global order for odd  $l$  vanishes due to the  $-1^l$  parity of the bond orientational order parameter.

### 2.6.2 Defining crystalline particles

To identify crystalline particles, we compute the correlations in the local orientational order of neighbouring atoms, following the prescription described in the literature [46, 63, 82]. Atoms with correlated neighbourhoods of high local orientational order are classified solid-like particles.



Quantitatively, this correlation is given by the quantity, [63, 96, 229]

$$Re(q_3(i).q_3(j)) = Re\left(\sum_{-3}^3 q_{3m}(i)q_{3m}^*(j)\right) \quad (2.37)$$

A particle  $i$  and a particle  $j$  are considered to be “bonded” if  $Re(q_3(i).q_3(j)) < -0.23$ . We note here the significance of the the cut-off value of  $-0.23$  which demands that the crystal structure formed is diamond cubic, to the exclusion of the diamond hexagonal crystal structure which also has local tetrahedral ordering [96]. Crystalline particles have a  $q_3 > 0.6$  and are ”bonded” to at least 3 neighbours. Further, crystalline particles within the SW-cutoff distance of each other belong to the same cluster. In this study we consider both the size of the largest cluster,  $n_{\max}$  and the full distribution of cluster sizes  $P(n)$ .

The distributions of  $q_3$ ,  $Re(q_3(i).q_3(j))$  and number of bonded neighbours for the differently labelled particles are shown in Fig. 2.1. The distribution for the liquid at  $T = 1055K$ ,  $P = 0$  GPa is obtained from a non-crystallising MD trajectory of 90  $ns$  and system size of  $N = 512$ . The distribution for the liquid at  $T = 1100K$ ,  $P = 0$  GPa is obtained from a non-crystallising MD trajectory of 10  $ns$  and system size of  $N = 512$ . We observe that using  $q_6(i).q_6(j)$  to identify crystalline particles gives nearly identical results when the appropriate cut-off is chosen [131], shown in Fig. 2.2. The choice of cut-off will depend on whether a normalisation factor is included in the definition [30]. Bulk crystalline particles that are within a chosen cut-off distance of each other are said to belong to the same crystalline cluster. The size of such connected clusters,  $n$ , and the size of the largest such cluster,  $n_{\max}$  are used as order parameters in this work. In Chapter 4, we will discuss an alternate connectivity criterion for crystalline particles which also takes into account the lattice orientation of neighbouring bulk crystalline particles. With this method, one can identify “crystallites”, which are made up of particles sharing both ordering and lattice orientation. One can also naturally identify the “grain boundaries” separating two connected but misoriented crystallites, analogous to domains in ferromagnets.

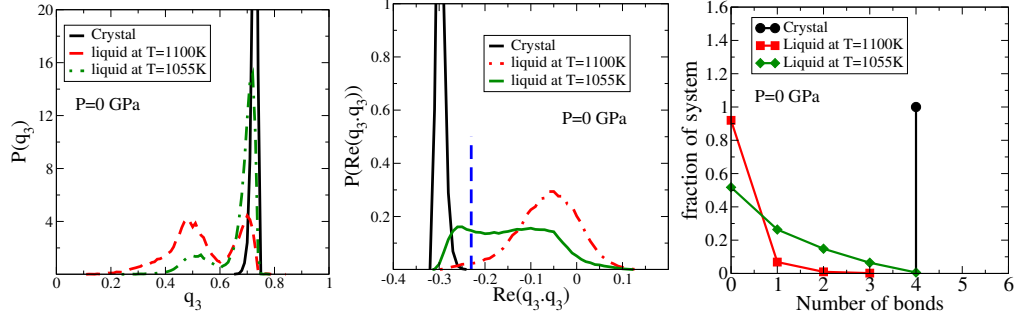


Figure 2.1: (*Left*) Distribution of  $q_3$  for different types of configurations, high density liquid, crystal at  $T = 1260\text{K}$  and a non-crystallised, low density liquid (LDL) configuration. (*Centre*) Distribution of  $\text{Re}(q_3(i) \cdot q_3(j))$  for different types of configurations, high density liquid, crystal at  $T = 1260\text{K}$  and a non-crystallised, low density liquid (LDL) configuration. The blue vertical line at  $-0.23$  marks the cut-off defining solid particles. (*Right*) Typical distribution of number of connections per atom in high density liquid, low density liquid and in the pure crystalline phase.

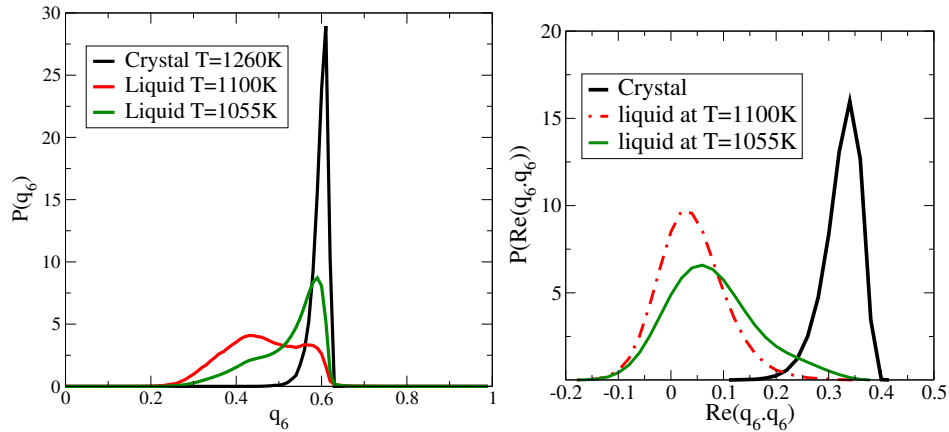


Figure 2.2: (*Left*) Distribution of  $q_6$  for different types of configurations, high density liquid, crystal at  $T = 1260\text{K}$  and a non-crystallised, low density liquid (LDL) configuration. (*Right*) Distribution of  $\text{Re}(q_6(i) \cdot q_6(j))$  for different types of configurations, high density liquid, crystal at  $T = 1260\text{K}$  and a non-crystallised, low density liquid (LDL) configuration.

## 2.7 Kinetic reconstruction of the free energy from the mean first passage time

The work here follows the method developed and described by the group of David Reguera where the kinetics of nucleation from a large number of free MD runs is utilised to obtain the free energy barrier to nucleation from the mean first passage time (MFPT) [42–44].

The quantity that is often of most interest in the context of crystallisation is the

crystallisation rate. For activated processes, which involve the crossing of a free energy barrier, the rate of crossing depends heavily on the height of the free energy barrier. In terms of a general reaction coordinate,  $x$ , this can be written as [48]

$$J_{cross} = \frac{1}{2}k e^{-\beta\Delta G(x^*)} \quad (2.38)$$

where  $x^*$  is the value of the order parameter where the free energy  $\beta\Delta G(x^*)$  is maximum and  $k$  is a kinetic pre-factor.

In Classical Nucleation Theory, this free energy function is understood to have a dependence on the order parameter,  $x$  in the following way:

$$\Delta G(x) = -\Delta\mu x + \sigma x^{2/3} \quad (2.39)$$

Here,  $\Delta\mu$  is the difference in chemical potential between the bulk crystal and the bulk liquid and  $\sigma$  is a term that describes the free energy cost due to the growth of the interface. Note that, when written in this form, the order parameter,  $x$ , is in fact the size of clusters and this equation describes the work of formation of different clusters of size  $x$ . Whereas the applicability of the form of  $\Delta G(x)$  described above is debated, the work of formation is still broadly understood to include a net free energy gain in the bulk crystalline phase and a free energy cost to the growth of the interface between liquid and crystal, thus implying (under metastable conditions) that the free energy has a maximum. In the description that follows, our goal is to calculate the free energy cost to the growth of clusters of size  $x$ ,  $\beta\Delta G(x)$ . However, rather than to use the form described above, which requires the calculation of the chemical potential and the interfacial free energy, we use a method that relies on the kinetics of the process alone, without assumptions about the specific form of the free energy barrier.

One can write the rate of crossing the nucleation barrier, assuming a diffusive crossing of an energy barrier which can be modelled using the Smoluchowski equation in one dimension, as follows. The process is described by the Smoluchowski equation

$$\begin{aligned} \frac{\partial P(x,t)}{\partial t} &= \frac{\partial}{\partial x} \left[ D(x)e^{-\beta\Delta G(x)} \frac{\partial}{\partial x} (P_{st}(x)e^{\beta\Delta G(x)}) \right] \\ &= \frac{-\partial J(x,t)}{\partial x} \end{aligned} \quad (2.40)$$

where  $J(x,t)$  is the current,  $D(x)$  is the order parameter dependent diffusivity,

$\Delta G(x)$  is the free energy function and  $P(x, t)$  is the time dependent distribution function of the order parameter. In the steady state, with  $P(x, t) = P_{st}(x)$  we can write the expression for the rate of barrier crossing [230] as:

$$J = -D(x)e^{-\beta\Delta G(x)} \frac{\partial}{\partial x} (P_{st}(x)e^{\beta\Delta G(x)}). \quad (2.41)$$

In cases where the free energy  $\Delta G(x)$  is not known, one can rearrange and arrive at

$$\beta\Delta G(x) = -\ln P_{st}(x) - J \int \frac{dx'}{D(x')P_{st}(x')} + C \quad (2.42)$$

One can also write the mean first passage time for a trajectory starting at  $x_0$ , to reach  $x$ , with a reflecting boundary condition  $a$ , and absorbing boundary at  $b$  [230]:

$$\tau(x; x_0, a) = \int_{x_0}^x \frac{1}{D(y)} dy e^{\beta\Delta G(y)} \int_a^y dz e^{-\beta\Delta G(z)} \quad (2.43)$$

One can also write this in the following way:

$$\frac{\partial^2 \tau}{\partial x^2} = \left[ \frac{\partial \beta\Delta G(x)}{\partial x} + \frac{\partial D(x)}{\partial x} \right] \frac{\partial \tau}{\partial x} + \frac{1}{D(x)}$$

This equation can be re-arranged and one can substitute  $A(x) = \partial\tau(x)/\partial x$  to get,

$$\frac{\partial \ln(A(x)D(x))}{\partial x} = \frac{1}{D(x)A(x)} + \frac{\partial \beta\Delta G(x)}{\partial x} \quad (2.44)$$

Further, one can write  $B(x) = A(x)D(x)$  to get

$$\beta\Delta G(x) = \ln(B(x)) - \int \frac{dx'}{B(x')} + C \quad (2.45)$$

From here, using  $J = 1/\tau(b)$  (where  $\tau(b)$  is the mean first passage time at which the absorbing boundary at  $b$  is reached), Eq. 2.44 can be combined with Eq. 2.42 to get

$$\frac{\partial(B(x)P_{st}(x))}{\partial x} = P_{st}(x) - \tau(b) \frac{\partial \tau(x)}{\partial x} \quad (2.46)$$

Integrating this equation gives us,

$$\beta\Delta G(x) = \beta\Delta G(x=1) + \ln\left(\frac{B(x)}{B(1)}\right) - \int_1^x \frac{dx'}{B(x')} \quad (2.47)$$

$$B(x) = -\frac{1}{P_{st}(x)} \left[ \int_x^b P_{st}(x') dx' - \frac{\tau(b) - \tau(x)}{\tau(b)} \right] \quad (2.48)$$

Eq. 2.47 and Eq. 2.48 are the equations used to reconstruct the free energy from the MFPT and the steady state probability. For the case of crystal nucleation,  $x$  can be replaced with  $n_{\max}$ , the size of the largest crystalline cluster, while  $n_{\max} = 1$  is taken to be the second bin from the reflecting boundary condition.  $\beta\Delta G(x = 1)$  (or  $\beta\Delta G(n_{\max} = 1)$ ) is an unknown constant at this point. Fig. 2.3 is indicative of the nature of the steady state probability and the mean first passage time. For a

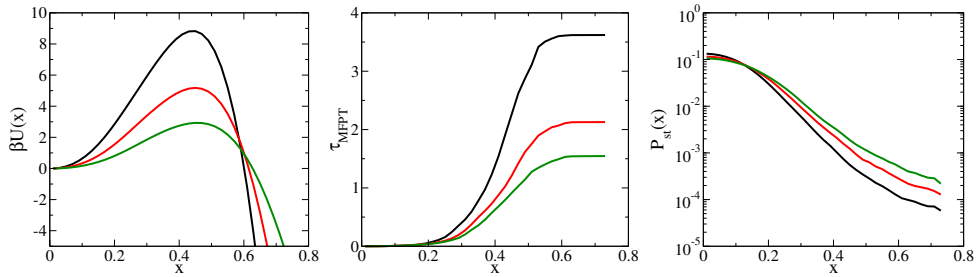


Figure 2.3: (*Left*) The dimensionless potential/free energy function as a function of some general coordinate  $x$ , with three barrier heights depicted. (*Centre*) The corresponding mean first passage times as a function of  $x$  and (*Right*) the steady state sampling probabilities as a function of  $x$ .

sufficiently high barrier, the mean first passage time,  $\tau(x)$ , is sigmoidal in form and can be used to extract information regarding the steady-state nucleation rate, the critical cluster size and the curvature at the top of the barrier, also known as the Zeldovich factor. In the general case, this method does not make any assumptions about the diffusivity of the order parameter,  $D(x)$  or the shape of the energy barrier,  $\beta\Delta G(x)$ , beyond the overall framework of a diffusive barrier crossing in which the expression for  $\tau(x)$  is written (see Chapter 1).

Note that the small  $n_{\max}$  behaviour of  $P(n_{\max})$  involves special consideration. We will discuss this issue and describe how the constant is determined in Chapter 3, Section 3.3.4. The use of this method requires that the size of the largest cluster,  $n_{\max}$  (defined in Section 2.6.2), be tracked in each of an ensemble of MD trajectories. From this, the steady state probability,  $P_{st}(n_{\max})$ , and the mean first passage time, hereafter labelled  $\tau_{MFPT}(n_{\max})$ , is calculated. Each of the trajectories is extended till an absorbing boundary conditions is reached. An important practical aspect of using this method is that the ensemble of MD runs should preferably start from configurations with no crystalline ordering to effectively sample  $\tau_{MFPT}(n_{\max})$  and  $P_{st}(n_{\max})$  for the smallest possible  $n_{\max}$  values. This is especially important when

one does not have the guarantee that unconstrained MD runs will fully sample the order parameter space starting from configurations with any arbitrarily chosen starting value of the order parameter. More details of the MD simulations performed for this method are given below in Section 3.3.1. This method has been used in a number of studies of nucleation [94, 140, 231, 232].

## 2.8 Umbrella sampling

The other technique used to determine the free energy cost to the growth of crystalline clusters is the umbrella sampling scheme which facilitates the reversible sampling of cluster sizes that are otherwise rarely sampled. In Chapter 5, Section 5.1.2, we discuss the extension to multiple order parameters. Here, we consider the application of this method to the single order parameter case, where the order parameter in question is a measure of crystallinity. The free energy cost to the growth of crystalline clusters of size  $n$ ,  $\beta G(n)$  is obtained (up to an additive constant) from the equilibrium probability density of sampling clusters of size  $n$ , with (see Chapter 1)

$$\beta \Delta G(n) = -\ln(P(n)) + \text{const.} \quad (2.49)$$

Umbrella sampling is performed with NPT Monte Carlo simulations [37, 233] to sample the desired range of order parameters effectively. An in-house code was used for the umbrella sampling simulations that used an efficient double-sum implementation of the three-body Stillinger Weber potential described in Ref. [222] and Ref. [128]. A standard Metropolis scheme is used for the Monte Carlo (MC) simulations with an MC step consisting of either  $N$  single particle trial displacements or a trial change in the volume.

The general expression for the Hamiltonian under application of bias is given by:

$$H_C = H + W(n_{\max}) \quad (2.50)$$

where  $W(n_{\max})$  represents the bias potential and  $H$  is the original Hamiltonian. In the first instance, a harmonic bias of the form

$$W(n_{\max}; n_{\max}^0, k_{n_{\max}}) = \frac{1}{2} k_{n_{\max}} (n_{\max} - n_{\max}^0)^2 \quad (2.51)$$

is used to enhance sampling around a desired value of  $n_{\max}$ , labelled  $n_{\max}^0$ . The sampling of different values of  $n_{\max}$  is enhanced by running multiple simulations with each independent simulation having a different bias centre,  $n_{\max}^0$ , or bias potential  $W(n_{\max}; n_{\max}^0)$ , thus sampling different windows of  $n_{\max}$  values.

In order to address the complications arising from the choice of a harmonic bias on the order parameter [169],  $n_{\max}$ , we also consider a different bias protocol for the umbrella sampling scheme when attempting to measure the free energy barrier at deep supercooling. Here, the Hamiltonian is modified by adding a constraining potential of the hard wall form rather than a harmonic bias, as described by Saika-Voivod et al [169]. The hard wall bias strictly constrains the size of the largest cluster to be between  $n_{\max}^l$  and  $n_{\max}^u$  as described in Eq. 2.52. Different independent simulations constrain sampling within different bounds. The full cluster size distribution is also used, from which we can calculate free energy using Eq. 2.49. For the purposes of comparison, the free energy as a function of  $n_{\max}$  is also calculated from simulations with the hard wall bias.

The corresponding bias potential then takes the form:

$$W = \begin{cases} 0 & n_{\max}^l \leq n_{\max} < n_{\max}^u \\ \infty & \textit{otherwise} \end{cases} \quad (2.52)$$

To improve equilibration, we perform parallel tempering, wherein simulations at different temperatures or for different bias potentials ( $n_{\max}^0$  or  $[n_{\max}^l, n_{\max}^u]$  values) are run in parallel, and configurations for distinct temperatures or bias potentials (with adjacent values of  $n_{\max}^0$  or  $[n_{\max}^l, n_{\max}^u]$ ) are swapped periodically, using the parallel tempering Metropolis scheme.

Short segments of the trajectory of 50 MC steps are generated with the unbiased Hamiltonian. These are then accepted or rejected with a probability,

$$P_{\text{accept}}(o \rightarrow n) = \min\{1, \exp[-\beta(W_n - W_o)]\} \quad (2.53)$$

In this case, the  $o$  and  $n$  configurations refer to those at the beginning of the trajectory segment and at the end, respectively. Note that for the case of the hard wall bias,  $W_n - W_o$  is either 0 or  $\infty$ .

These simulations are used to generate a distribution of  $n_{\max}$  values  $P_b(n_{\max})$ , where the subscript  $b$  refers to sampling in the biased ensemble. One can obtain the

unbiased distribution of  $n_{\max}$  (up to normalisation) using the relation

$$P(n_{\max}) = P_b(n_{\max})e^{\beta W(n_{\max})} \quad (2.54)$$

where  $P(n_{\max})$  is the frequency with which the largest cluster samples a size,  $n_{\max}$ . From the unbiased distribution, one obtains the Landau free energy as a function of  $n_{\max}$  as:

$$\beta\Delta G(n_{\max}) = -\ln(P(n_{\max})) + \text{const.} \quad (2.55)$$

From Eq. 2.55, we wish to identify the constant the yields  $\beta\Delta G(0) = 0$ . The estimates are obtained from simulations with different  $n_{\max}^0$  or  $[n_{\max}^l, n_{\max}^u]$  bounds and sample different but overlapping windows of  $n_{\max}$ . Here, we make a distinction between the free energy calculated at high temperatures, where the critical cluster is expected to be large, and free energies calculated when the critical cluster is expected to be small. In the former case, the missing constant in each independent simulation, specified by index  $d$ , is obtained by fitting  $\beta\Delta G_d(n_{\max})$  to a single polynomial of  $n_{\max}$ . This is done by a least square fit, by minimising

$$\chi_{US} = \sum_{d=1}^{N_{sim}} \sum_{n_{\max}=n_{lo}^d}^{n_{hi}^d} \left[ \beta\Delta G_d(n_{\max}) + a_0 n_{\max} - a_1 n_{\max}^{2/3} - \sum_{i=2}^p (a_i n_{\max}^i) - b_d \right]^2 \quad (2.56)$$

where  $N_{sim}$  is the number of independent simulations and  $n_{lo}^d$  and  $n_{hi}^d$  are respectively the lower and upper bounds within which  $n_{\max}$  is sampled in the simulation indexed  $d$ . The index  $d$  runs from 1 to  $N_{sim}$ .  $p$  is the order of the polynomial with coefficients  $a_i$ , and  $b_d$  will give us the missing constants. The CNT expression  $\beta\Delta G(n) = -a_0 n + a_1 n^{2/3}$  can be expected to be valid for sufficiently large critical clusters and high free energy barriers. Hence a polynomial of the form  $a_0 n + a_1 n^{2/3} + a_2 n^2 + a_3 n^3 \dots$  is used.

Where the critical cluster is expected to be small, we make no assumption of a CNT-like polynomial fit. The overlap between  $\beta\Delta G(n_{\max})$  obtained from different simulations sampling adjacent bounds is maximised by identifying the appropriate constant for each independent simulation,  $b_d$ . This is done by minimising the following quantity:

$$\chi_{HW} = \sum_{d=1}^{N_{sim}} \sum_{n_{\max}=n_{lo}^d}^{n_{hi}^d} \left[ \beta\Delta G_d(n_{\max}) - \beta\Delta G_{d+1}(n_{\max}) - b_d \right]^2 \quad (2.57)$$

$N_{sim}$  is the number of independent simulations and  $[n_{lo}^d, n_{hi}^d]$  is the range of  $n$



over which adjacent simulations overlap. The index,  $d$ , runs over each independent simulation, starting from  $d = 1$  to  $d = N_{sim}$ . This procedure yields the free energy,  $\beta\Delta G(n_{\max})$ , up to an unknown constant as given in Eq. 2.55. As mentioned for the reconstruction of  $\beta\Delta G(n_{\max})$  through the MFPT approach, as well as umbrella sampling, the procedure used to determine this remaining unknown constant is described in Section 3.4.1.

The umbrella sampling runs using the hard wall bias are also used to obtain  $\beta\Delta G(n)$ .  $\beta\Delta G(n)$  can also be obtained from  $N(n)$  from umbrella sampling runs with a harmonic bias, which we do not do here. The unbiased expectation value of  $N(n)$  (the number of clusters of size  $n$ ) can be written as:

$$\langle N(n) \rangle = \frac{\langle N(n)e^{\beta W} \rangle_C}{\langle e^{\beta W} \rangle_C} \quad (2.58)$$

The expectation subscript  $C$  is the sampled probability from the simulation under the modified Hamiltonian.

The un-biasing described in Eq. 2.58 simplifies since  $W = 0$  or  $W = \infty$  depending on the size of the largest cluster. For the case of the hard wall bias potential, one can thus replace  $\langle N(n) \rangle = \langle N(n) \rangle_C$  within the constrained region.

We compute  $\beta\Delta G(n)$  from  $-\ln(N(n))$  up to an unknown constant, within the window in which we perform biased sampling. We use the equilibrium data of  $P(n) = N(n)/N(0)$  at small  $n$  and demand that  $P(n)$  from simulations sampling other values of  $n$  sequentially match these, as described by Eq. 2.59. From a set of independent simulations, each indexed by  $d$  and having distinct but adjacent bounds, one obtains the free energy differences  $\beta\Delta G_d(n)$  up to an undetermined constant,  $b_d$ . The constants,  $b_d$ , are obtained by minimising the error described in Eq. 2.59,  $\chi_{HW}$ , sequentially between overlapping data points from simulations with adjacent bounds.

$$\chi_{HW} = \sum_{d=1}^{N_{sim}} \sum_{n=n_{lo}^d}^{n_{hi}^d} [\beta\Delta G_d(n) - \beta\Delta G_{d+1}(n) - b_d]^2 \quad (2.59)$$

This is done in the same way as in Eq. 2.57, but subject to the constraint  $\beta\Delta G_d(0) = 0$  if  $n_{lo}^d = 0$ .

Note that unlike the procedure in Eq. 2.57 for  $\beta\Delta G(n_{\max})$ , the added constraint in Eq. 2.59 that  $\beta\Delta G_d(n = 0) = 0$  if  $n_{lo}^d = 0$  does not leave behind an undetermined additive constant. Another important point here is that no assumption to fit the

CNT form is made;  $\beta\Delta G(0) = 0$  as a consequence of how quantities have been defined. The steps involved in obtaining free energies from constrained simulations is shown in Fig. 2.4 for both the harmonic and the hardwall bias.

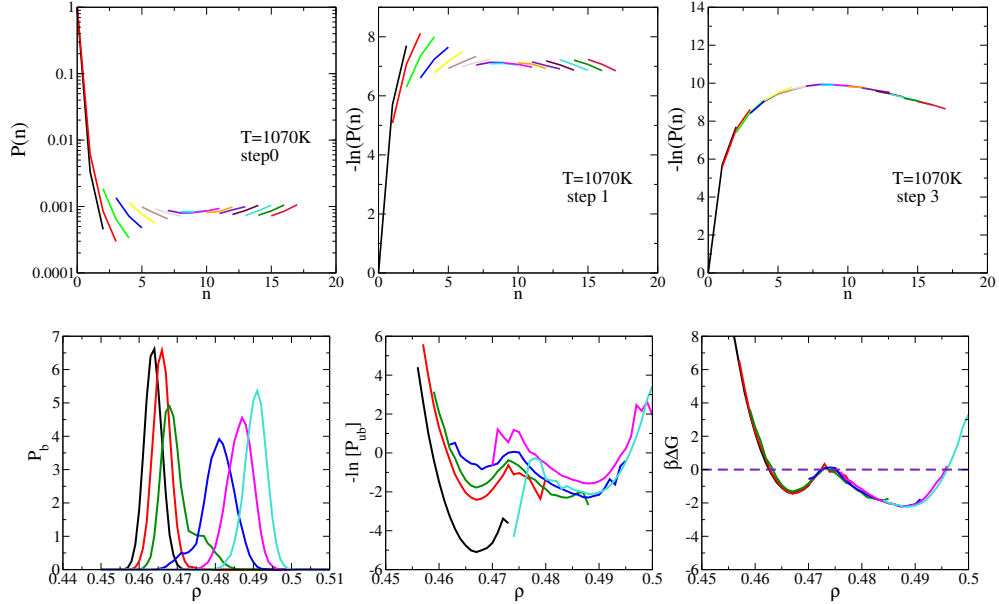


Figure 2.4: Reconstruction of the free energy from umbrella sampling for  $n$  (or  $n_{\max}$ ) from HWUS MC (*Top*) and for density,  $\rho$ , with harmonic bias USMC (*Bottom*). From left to right we have the biased sampling probability, the negative log of the unbiased sampling probability and the free energy as a function of the order parameter. Note that for the harmonic bias, large errors are present in the unbiased probability at the edges. Thus, some well-chosen number of entries are pruned from the edge of each bias window.

### 2.8.1 Parallel tempering

The general expression for probability of acceptance of parallel tempering swaps in the NPT ensemble between simulations indexed  $i$  and  $j$  is given by

$$P_{\text{accept}} = \min \left( 1, \exp \left[ \left[ (E_i - E_j) + P(V_i - V_j) \right] (\beta_i - \beta_j) \right] \right. \\ \left. \exp \left[ -\beta_j W_i(n_{\max_j}) - \beta_i W_j(n_{\max_i}) \right] \right. \\ \left. \exp \left[ \beta_i W_i(n_{\max_i}) + \beta_j W_j(n_{\max_j}) \right] \right) \quad (2.60)$$

The details of parallel tempering are as follows:

- Consider  $N$  independent simulations run in parallel - different temperatures or different bias potentials.
- To ensure better sampling of the phase space  $\mathbf{r}(\mathbf{t})$  and consequently of the order parameter, we swap adjacent configurations periodically.
- Two types of swaps are performed, one type where simulations with different temperatures but the same bias potential exchange configurations and one type where simulations at the same temperature but different bias potentials exchange configurations.
- A swap between adjacent simulations indexed  $i$  and  $j$ , at different temperatures,  $1/\beta_i$  and  $1/\beta_j$ , but with the same bias potential is executed with a probability of
 
$$\min\left(1, \exp[(E_i - E_j) + P(V_i - V_j)](\beta_i - \beta_j)\right)$$
- For cases where  $\beta$  is the same but the bias potential varies, the probability is  $\min(1, \exp[\beta(W_N - W_O)])$
- Here, the term  $W_N - W_O$  represents the sum of the bias potentials after the swap minus the sum of the bias potentials before the swap (the sum being over the bias applied on the two runs in consideration).

$$\begin{aligned} W_N &= W_j(n_{max_i}) + W_i(n_{max_j}) \\ W_O &= W_i(n_{max_i}) + W_j(n_{max_j}) \end{aligned}$$

For the hard wall bias, the swap is accepted with probability 1 if the  $n_{max_i}$  and  $n_{max_j}$  are both within the new constraints after the swap and rejected otherwise.

Parallel tempering can also be performed between simulations at different pressures. The acceptance criteria associated with such a swap move is given by

$$\begin{aligned} acc((1, \beta_1, P_1), (2, \beta_2, P_2) \rightarrow (2, \beta_1, P_1), (1, \beta_2, P_2)) & \quad (2.61) \\ &= \min(1, \exp(\Delta(\beta P)\Delta V + \Delta\beta\Delta E)) \end{aligned}$$

where

$$\begin{aligned}\Delta(\beta P) &= \beta_2 P_2 - \beta_1 P_1 \\ \Delta V &= V(o)_2 - V(o)_1 \\ \Delta E &= E(o)_2 - E(o)_1\end{aligned}\tag{2.62}$$

The subscript 1 and 2 represent the systems at different temperature and pressure values. Note that in a NPT MC simulation, for each system, we also have to change the volume of the box and hence involves current volume and associated energy (represented by  $V(o)$  and  $E(o)$ ) and new trial volume and associated energy ( $V(n)$  and  $E(n)$ ). The above acceptance criteria is in terms of current volume and energy.

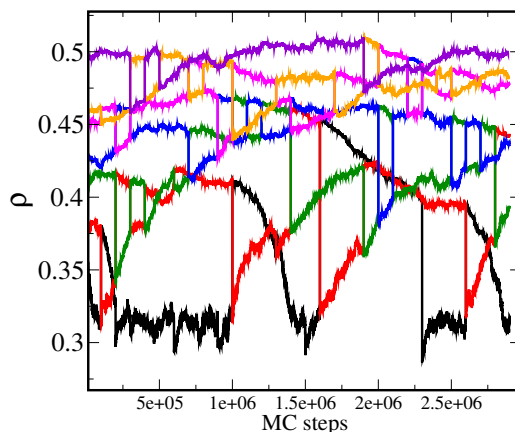


Figure 2.5: A representative image tracking the time series of the order parameter for simulations with different bias potentials in an umbrella sampling scheme. At each instance where a swap is accepted, the configurations (particle positions) between the two adjacent windows are exchanged and both windows evolved from the new configuration. The parallel tempering swaps between adjacent windows cause each independent simulation to explore a larger portion of the phase space than otherwise possible. Note that in a real simulation, swaps may be more or less frequent and simulations with adjacent bias windows may not be as separated. This figure is purely for representation.

## 2.9 Histogram reweighting

The weighted histogram analysis of Ferrenberg and Swendsen is used to stitch free energy estimates across bias windows or temperatures [234]. The final pair of equations that needs to be self-consistently solved [235] is:

$$p_0^{est}(Q) = \frac{\sum_{i=1}^N \langle H_i(Q) \rangle}{\sum_{i=1}^N \exp(-\beta(W_i - \Delta F_i)) M_i}$$

$$\Delta F_i = -k_B T \ln \left[ \sum_Q \exp(-\beta W_i) p_0^{est}(Q) \right]. \quad (2.63)$$

Here,  $\langle H_i(Q) \rangle$  is the histogram count for the state  $Q$  from simulation indexed  $i$ .  $M_i$  is obtained by summing over the histogram counts for all  $Q$  for simulation  $i$ .  $W_i$ , shorthand for  $W_i(Q)$ , is the weight factor to be determined for the simulation indexed  $i$  and is the free energy shift corresponding to  $i$ . In this sense, a summation  $\sum_{i=1}^N W_i(Q)$  is the sum of the bias potential at  $Q$  due to each window,  $i$ , i.e., the same  $Q$  experiences a different  $W_i(Q)$  for each  $i$ . The sum  $\sum_Q W_i(Q)$  is the sum of the bias potential in the window  $i$ , i.e., due to the bias potential  $W_i$  at each  $Q$  in the full range of  $Q$  values. Details of the derivation for the equations above are included in Appendix A.4. The integrated auto-correlation time can be incorporated to weight the histograms according to only the decorrelated samples [236]:

$$p_0^{est}(Q_1, Q_2) = \frac{\sum_{i=1}^N \langle H_i(Q_1, Q_2) \rangle}{\sum_{i=1}^N \exp(-\beta(W_i - \Delta F_i)) M_i}$$

$$\Delta F_i = -k_B T \ln \left[ \sum_{Q_1; Q_2} \exp(-\beta W_i) p_0^{est}(Q_1; Q_2) \right] \quad (2.64)$$

The term  $g_i$  is the integrated auto-correlation time for each simulation window, and is used to weight sampling according to the number of decorrelated samples obtained as a function of  $\mathbf{Q}$ . The error as a function of  $\mathbf{Q}$  is

$$\omega(\mathbf{Q}) = \left( \sum_{i=1}^N \frac{g_i}{\langle H_i(\mathbf{Q}) \rangle} \right)^{1/2} \quad (2.65)$$

### Temperature re-weighted histograms

A simpler temperature re-weight of histograms can be achieved by considering

the density of states,  $W(E)$ ,

$$H_0(E) = \frac{N}{Z_0} W(E) \exp(-\beta_0 E) \quad (2.66)$$

Here,  $H_0(E)$  is the histogram count for energy  $E$  when simulated at  $\beta_0$ . From this, we can write an estimate of the histogram  $W$  as

$$W(E) = \frac{Z_0}{N} H_0(E) \exp(\beta_0 E). \quad (2.67)$$

Knowing  $W(E)$ , we can write the distribution at any other temperature  $T_1$  as

$$P_1(E) = \frac{1}{Z_1} W(E) \exp(-\beta_1 E). \quad (2.68)$$

Substituting for  $W(E)$ ,

$$P_1(E) = \frac{Z_0}{N Z_1} H_0(E) \exp((\beta_0 - \beta_1)E). \quad (2.69)$$

We do not however know the normalization  $Z_0/Z_1$ . But this can be imposed by explicitly normalizing  $P_1$ . Thus,

$$P_1(E) = \frac{H_0(E) \exp[(\beta_0 - \beta_1)E]}{\sum_E H_0(E) \exp[(\beta_0 - \beta_1)E]}. \quad (2.70)$$

This will work when we consider  $T_0$  and  $T_1$  such that the region of sampling in the two cases overlap substantially. We can expect that when this is not the case, this method will not work so well. In such cases, we may employ methods for improved sampling, such as umbrella sampling. A more general set of expressions is used in Chapter 5, Section 5.1.2, for reweighting across  $\beta$ ,  $P$  and bias potential.

## 2.10 Thermodynamic integration

The chemical potential can be written as

$$\Delta\mu = \Delta G/N$$

Where,

$$V = \left( \frac{\partial G}{\partial P} \right)_{T,N}$$

Integrating this along an isotherm can give us

$$\Delta G_{21}/N = G_2/N - G_1/N = \int_1^2 V(P)/N dP = - \int_2^1 V(P)/N dP$$

We can integrate the equations of state of the liquid and the crystal to get  $\Delta G_{21;cry}$  and  $\Delta G_{21;liq}$  from the isotherms of each. Note that the free energy of crystal and liquid at state point 1 are the same if the pressure at state point 1 is the melting pressure for the given isotherm.

$$G_{1;cry} = G_{1;liq} \quad \text{if} \quad P_1 = P(T)_{melt} \quad (2.71)$$

## 2.11 Measuring compressibility

We calculate the compressibility  $\kappa_T$  from the EOS using:

$$\kappa_T = \frac{1}{\rho} \left[ \frac{\partial \rho}{\partial P} \right]_T \quad (2.72)$$

where  $\rho$  is the number density and  $P$  is the pressure. Polynomial fits to isotherms are used in calculating the derivatives. The polynomial is typically third order, keeping in mind the truncated Virial equation of state

$$P = Nk_B T \rho (A + B\rho + C\rho^2 + \dots) \quad (2.73)$$

We also calculate  $\kappa_T$  from fluctuations of volume  $V$  using:

$$\kappa_T = \frac{\langle V^2 \rangle - \langle V \rangle^2}{\langle V \rangle k_B T} \quad (2.74)$$

The latter method is computationally very demanding requiring sufficient sampling to obtain good measures of the variance in volume at constant pressure, and the comparison between the two reveals the degree to which sampling in equilibrium is satisfactory.

# Chapter 3

## Crystallisation in deeply supercooled Stillinger-Weber silicon

### 3.1 Introduction

The phase behaviour of liquid silicon is a subject of continuing interest due to the many anomalous properties it exhibits in the liquid state, reminiscent of water and of other tetrahedral liquids. Of particular interest is deeply supercooled silicon, i.e., the liquid cooled to temperatures significantly lower than the melting temperature. Here, as in water, anomalous behaviour such as a density maximum and the possibility of the existence of a first order phase transition between two metastable liquid states – a high density liquid (HDL) and a low density liquid (LDL) – has been the subject of numerous investigations that have approached the question from different directions [1, 2, 4, 8, 16, 19–24, 30, 138, 237]. The existence of a first order transition between “amorphous” and liquid states was first proposed based on experimental observations [6, 7, 112, 113] and the possibility of a liquid-liquid transition was suggested on the basis of a simple two state model by Aptekar [8]. Notable experimental works since then, probing the phase behaviour of deeply supercooled silicon include the work of Kim *et al* [19], where electrostatic levitation was used to prevent crystallisation induced by the container walls and temperatures as low as  $T = 1350\text{K}$  were probed. Subsequently, Beye *et al* [20] used ultra-fast pump probe spectroscopy to discern changes in the electronic structure to identify a two-step change in the melt from semi-conductor to semi-metal to a



high temperature metallic liquid.

Owing to the difficulties of conducting experiments on liquid silicon at these temperatures, as well as the difficulties in avoiding crystallisation [19, 20, 114–119], computer simulations have played a significant role in efforts to study the liquid-liquid transition in silicon [1, 2, 4, 16, 18, 22–24, 30, 138, 140, 237]. A number of simulation studies, including some of the most recent investigations in this area, employ *ab-initio* methods and identify liquid-liquid and liquid-solid transitions based on changes in the electronic structure reminiscent of those found in experiments; silicon is a semiconductor in the solid-state, a semi-metal in the low density liquid state and a metallic liquid in the high temperature, high density liquid state [21–24, 121–123, 125, 138].

Classical simulations using the Stillinger-Weber (SW) potential [25] have been performed extensively to probe relevant time scales whereby the metastable liquid phase can be studied in order to explore the possibility of a liquid-liquid transition [1, 2, 4, 5, 18, 30, 134, 138, 140]. At the relevant temperatures and pressures, the dynamics of the metastable liquid is sufficiently slow (relaxation times of tens of nanoseconds and longer) to make computer simulations challenging. On the other hand, crystal nucleation occurs on comparable time scales making experimental studies challenging. Employing simulations of SW silicon, Sastry and Angell [1] observed a discontinuous change in enthalpy below the melting temperature, suggesting a first order phase transition between two states that were identified to be liquid-like based on structural and dynamical properties. Vasisht *et al*, 2011 [2], identified a co-existence region and a transition line that ended at a critical point at negative pressures. These works estimated the transition temperature to be  $\sim 1060\text{K}$  at  $P = 0$  GPa. Vasisht *et al* [2] further illustrated the behaviour of important thermodynamic loci consistent with their observation of approach to a second critical point, similar to a number of models of water [14, 45, 147].

The question of the existence of two metastable liquid states for supercooled SW silicon has since been investigated through attempts to construct two dimensional free energy surfaces that may display distinct minima corresponding to the two liquid phases in addition to that corresponding to the stable crystal phase. Studies by Limmer and Chandler [18, 28] and by Ricci *et al* [30], evaluating the free energy surfaces, did not find any evidence of a metastable LDL. In fact, it was argued in these works that the metastable liquid was no longer stable with respect to crystallisation at the state points where earlier studies had found evidence of an LDL phase, and that crystallisation was spontaneous. In the context of water, a coarse-grained

model of water based on reparametrising the SW model was employed to argue that increased crystallisation rates precluded the possibility of a transformation to the low density liquid phase [68], consistently with the above arguments. Nevertheless, from simulations of more explicit multi-site models of water such as the ST2, TIP4P and TIP5P models, clear evidence of an LLPT ending at a critical point has been shown, notably in [29, 45, 150, 154, 229] among others.

In the case of SW silicon, the claim that no free energy barrier separates the liquid state from the crystal free energy minimum for state points in the vicinity of  $\sim 1060\text{K}$  at  $P = 0$  GPa is puzzling, given the long simulation times over which the simulated systems have been observed in the liquid state [1, 2, 131, 133]. A possible origin of such inconsistency is that the order parameters chosen to construct the free energy surfaces in [18, 28, 30] lead to artefacts in the presence of low barriers to crystallisation, as briefly discussed in [30]. In particular, the choice of a global order parameter ( $Q_6$ ) as a measure of the degree of crystalline order may not permit a reversible control of crystallisation with the bias potentials used in umbrella sampling simulations. Related considerations with respect to the use of the global order parameter ( $Q_6$ ) for evaluating free energy barriers have already been noted [46].

In this chapter, we address one aspect of the issues surrounding the possibility of a liquid-liquid transition in SW silicon. As the discussion above makes clear, crystal nucleation rates play a central role, and among the possibilities that cast doubt on the possibility of the liquid-liquid transition, the most extreme case is that the liquid is simply not stable in the relevant state points, and crystal nucleation is spontaneous, or barrierless. Thus, the first question that needs to be addressed is whether the liquid state is metastable, and hence finite free energy barriers to crystallisation exist, for the relevant state points. If the liquid state can be demonstrated to be metastable, one must address the separate question of whether two forms of the liquid exist, which we do not address in this work.

In order to reliably compute free energy barriers to crystallisation, we need to also demonstrate that no artefacts arise as a result of the choice of order parameters in constrained simulations such as umbrella sampling. To this end, at deeply supercooled conditions, we compute the free energy profile for crystallisation using two independent methods, namely, (i) kinetic reconstruction of the free energy from unbiased molecular dynamics (MD) runs in the constant temperature, pressure and number of particles (NPT) ensemble, using the method described by Wedekind *et al* [42–44] and (ii) Umbrella Sampling Monte Carlo simulations (USMC) in the NPT

ensemble [37], specifically, the prescription described by Saika-Voivod, Poole and Bowles, [169]. Both of these works have focused on cases of low free energy barriers and have discussed the specific considerations that become relevant to accurately measure them.

We find that finite free energy barriers and well-defined critical nuclei, albeit small, exist for all the state points we investigate. We also demonstrate that the free energy profiles obtained using two independent methods agree well with each other for the state points considered. Thus, our results rule out the possibility that the liquid state is not stable for the range of state points across which a liquid-liquid transition has previously been claimed to arise.

## 3.2 Defining crystalline particles

We use the prescription described in Section 2.6.2 to define crystalline particles and clusters of them. For the conditions studied here, the distributions and cut-offs are shown in Fig. 2.1, reproduced below for reference as Fig. 3.1. A particle

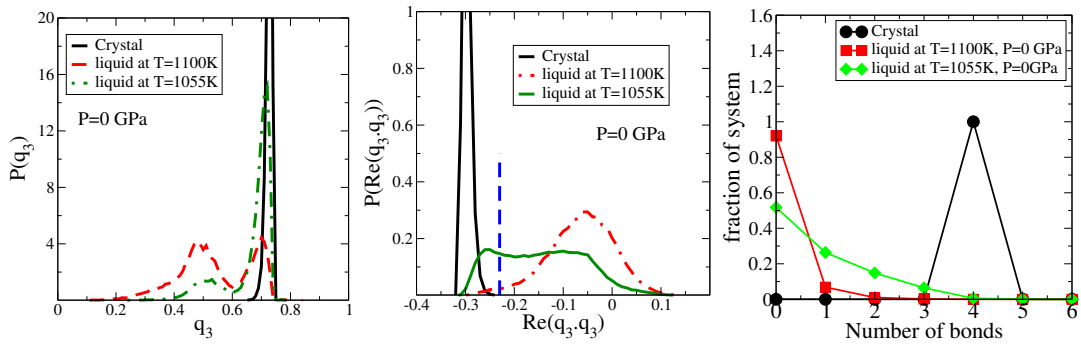


Figure 3.1: (*Left*) Distribution of  $q_3$  for different types of configurations, high density liquid, crystal at  $T = 1260K$  and a non-crystallised, low density liquid (LDL) configuration. (*Centre*) Distribution of  $\text{Re}(q_3(i) \cdot q_3(j))$  for different types of configurations, high density liquid, crystal at  $T = 1260K$  and a non-crystallised, low density liquid (LDL) configuration. The blue vertical line at  $-0.23$  marks the cut-off defining solid particles. (*Right*) Typical distribution of number of connections per atom in high density liquid, low density liquid and in the pure crystalline phase.

$i$  and a particle  $j$  are considered to be “bonded” if  $\text{Re}(q_3(i) \cdot q_3(j)) < -0.23$  (see Fig. 3.1). The histogram of number of bonded neighbours for the differently labelled particles is shown in Fig. 3.1. We note here the significance of the the cut-off value of  $-0.23$  which demands that the crystal structure formed is diamond cubic,

to the exclusion of the diamond hexagonal crystal structure which also has local tetrahedral ordering [96].

Crystalline particles have a  $q_3 > 0.6$  and are “bonded” to at least 3 neighbours. Further, crystalline particles within the SW-cutoff distance of each other belong to the same cluster. In this study we employ both the size of the largest cluster,  $n_{\max}$  and the full distribution of cluster sizes  $P(n)$ .

The distribution for the liquid at  $T = 1055K$ ,  $P = 0$  GPa is obtained from a non-crystallising MD trajectory of 90 ns and system size of  $N = 512$ . The distribution for the liquid at  $T = 1100K$ ,  $P = 0$  GPa is obtained from a non-crystallising MD trajectory of 10 ns and system size of  $N = 512$ . We note here that using  $q_6(i) \cdot q_6(j)$  to identify crystalline particles gives nearly identical results when the appropriate cut-off is chosen [15] (see Section 2.6.2, Fig. 2.2). The choice of cut-off will depend on whether a normalisation factor is included in the definition [30].

### 3.3 Simulation methods

Free energy reconstructions are performed using two independent methods at low temperatures, along the  $P = 0$  GPa isobar, in order to obtain reliable estimates of the free energy barriers. The first method we employ is a kinetic reconstruction using the mean first passage time (MFPT) from unconstrained MD runs [42–44]. In this method, the steady state probability of  $n_{\max}$ ,  $P_{st}(n_{\max})$ , as well as the mean first passage time,  $\tau_{MFPT}(n_{\max})$  are computed from a collection of independent, crystallising trajectories and used to reconstruct the free energy using Eq. 3.1 and Eq. 3.2, written in Chapter 2 as Eq. 2.47 and Eq. 2.48 for a general order parameter,  $x$ .

$$\beta\Delta G(x) = \beta\Delta G(x = 1) + \ln \left( \frac{B(x)}{B(1)} \right) - \int_1^x \frac{dx'}{B(x')} \quad (3.1)$$

$$B(x) = -\frac{1}{P_{st}(x)} \left[ \int_x^b P_{st}(x') dx' - \frac{\tau(b) - \tau(x)}{\tau(b)} \right]. \quad (3.2)$$

Here,  $x$  in this context is the size of the largest crystalline cluster,  $n_{\max}$ .  $b$  is the size of the largest crystalline cluster at which an absorbing boundary is imposed.  $\Delta G(x)$  is the free energy of forming a crystalline nucleus of size  $x$ . The equations are integrated with an Euler integration scheme which is appropriate since  $n_{\max}(x)$  takes integer values. In order to compute the free energy using this method, 600 independent NPT MD of  $N = 512$  particles simulations were started from disordered configurations with no crystalline particles and allowed to crystallise.

The MD runs are performed on the LAMMPS software suite using the velocity Verlet algorithm with a timestep of 0.3830 fs [223]. Thermostatting and barostatting are done with a Nosé-Hoover thermostat/barostat with time constants of 100 and 1000 steps respectively. The other technique used to construct the free energies is umbrella sampling Monte Carlo [37]. Simulations are performed in the NPT ensemble with constraints applied on the size of the largest crystalline cluster,  $n_{\max}$ . For results described in this chapter, a hard wall bias is used to constrain  $n_{\max}$  [169]. Parallel tempering swaps between simulations adjacent in temperature or bias potential are performed to speed up equilibration. We begin simulations by applying a harmonic bias potential for  $10^7$  MC steps before switching the bias potential. The auto-correlation functions of density ( $\rho$ ),  $Q_6$  and potential energy were monitored under the application of the hard wall bias and the relaxation time found to be similar and less than  $10^5$  MC steps for all the windows and for each of the three quantities considered. Keeping in mind a relaxation time of  $\tau = 10^5$  MC steps, we use an equilibration length, under application of hard wall bias, of  $50\tau$  and a production length of  $250\tau$ . We note here that the thermodynamic stability of the liquid is determined by whether there is a non-zero free energy cost to form small crystalline clusters which is maximum for some critical cluster size  $n^* > 0$ . We gather statistics on the number of clusters of size  $n$ ,  $N(n)$ . The quantity  $P(n) = N(n)/N(0)$  can be related to the free energy as  $\beta\Delta G(n) = -\ln(P(n))$  without the need to determine any additive constant since the way in which  $P(n)$  is defined applies the constraint that  $\beta\Delta G(n=0) = 0$ . To obtain statistics for the smallest cluster sizes, we perform simulations with a hardwall bias and use the full cluster size distribution to compute the free energy. When reconstructing the free energy using either umbrella sampling or the kinetic reconstruction with  $n_{\max}$  as the order parameter we additionally specify that the free energy as a function of the largest cluster size,  $\beta\Delta G(n_{\max})$  be equal to  $-\ln(P(n))$ , for small cluster sizes. By doing this, one obtains an estimate that can be meaningfully compared with  $\beta\Delta G(n)$ , the free energy from the full cluster size distribution. Similar techniques have been used in Ref. [44] and in Ref. [231]

We briefly describe the initial conditions for the simulations used for the kinetic reconstruction of free energy (Section 2.7) and the umbrella sampling simulations (Section 2.8).

### 3.3.1 Molecular dynamics simulations: Initial conditions

The initial ensemble of configurations for the MD runs at each temperature of interest, at zero pressure, was prepared by first running a simulation in the isobaric, isothermal (NPT) ensemble at a high temperature of  $T = 1400K$ ,  $P = 0$  GPa and system size  $N = 512$  for  $10$  ns. These configurations have a mean density of  $2.48g\ cc^{-1}$  with standard deviation of  $0.012g\ cc^{-1}$ . The relaxation time at these state points is of the order of  $0.01$  ns with diffusivities of the order of  $10^{-4}cm^2/s$  [4]. After ignoring an initial transient, 600 uncorrelated configurations were chosen as starting configurations. Energy minimisation was performed and the velocities were set to zero before being replaced with velocities corresponding to the target temperature. The length of the initial transient is chosen such that the liquid relaxes from the initial high temperature configuration. Subsequently, the liquid samples an initial metastable state corresponding to the target temperature, as discussed in the next section, Section 3.3.2. Each of the trajectories were simulated in the NPT ensemble using the velocity Verlet algorithm with the same timestep, thermostat and barostat at the target temperature at  $P = 0$  GPa till they crystallised. The first  $0.04$  ns were discarded and data gathered from the first time step after this where the total number of crystalline particles  $n_{tot} = 0$ . This is to ensure that at  $t = 0$  the configurations are highly disordered with no crystalline ordering. An absorbing boundary condition is applied so that data is gathered only until the absorbing boundary is crossed for the first time. Here, we emphasize that each of the independent trajectories needs to be extended till they reach the absorbing boundary.

### 3.3.2 Variation of the properties of the metastable liquid with temperature

The mean first passage time to different values of  $\rho$ , starting from an initial configuration with  $\rho = 2.48\ gcc^{-1}$  is shown in Fig. 3.2. The liquid samples a high density state on the timescale  $< 1$  ns before the density begins to drop (see Fig. 3.2). To understand the initial metastable state into which the liquid settles, we observe the change in the density profile of the metastable liquid, with temperature, during the first  $0.5$  ns. We ignore the first  $0.038$  ns initial transient during which the liquid is being quenched. In Fig. 3.3, we see a monotonic dependence of the density profile of the initial metastable state with temperature. To determine memory

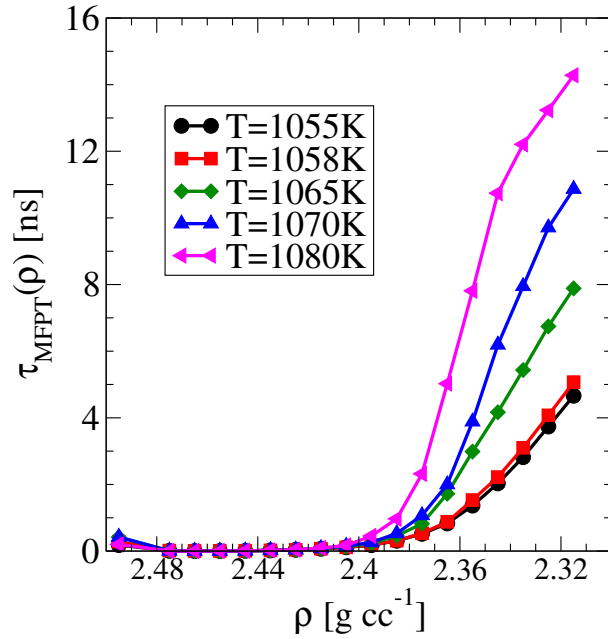


Figure 3.2: The mean first passage time to a given value of the density,  $\rho$ , for unconstrained NPT MD simulations starting from an initial condition with density  $2.48 \text{ gcc}^{-1}$ . At each temperature, 600 independent NPT MD runs were conducted at  $P = 0 \text{ GPa}$  and a system size of  $N = 512$ .

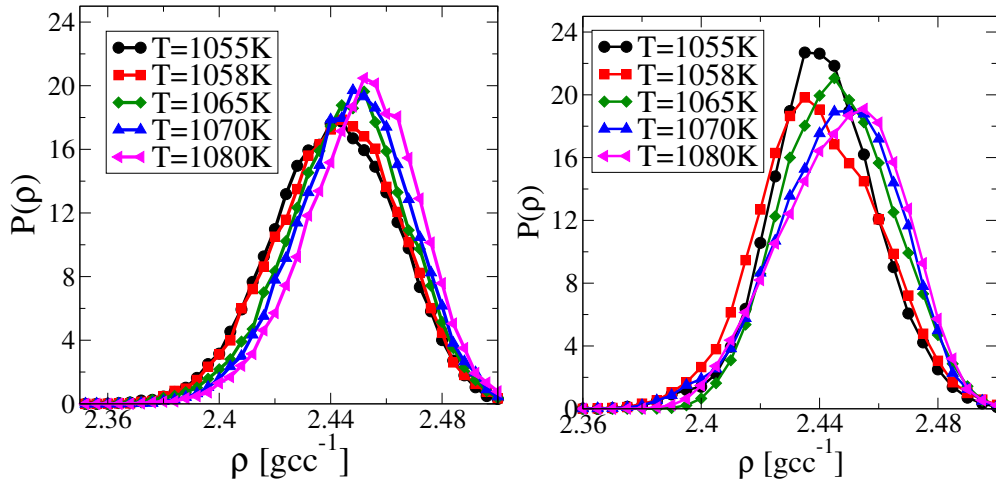


Figure 3.3: The density profile for the first  $0.5 \text{ ns}$  from a set of independent MD runs at five temperatures. At each temperature, 600 independent NPT MD runs were initialised from a high temperature quench (*Left*) and 8 independent NPT MD runs were initialised from a random initial configuration (*Right*). Simulations were conducted at  $P = 0 \text{ GPa}$  and a system size of  $N = 512$ . The initial  $0.038 \text{ ns}$  were discarded as the initial transient and the next  $0.5 \text{ ns}$  were used to aggregate the density profile at each temperature.

loss, we construct the density statistics in the same time window ( $0.038 - 0.5$  ns) for 8 trajectories started from initial configurations with randomly placed particles at a density of  $2.48$  gcc $^{-1}$ .

The dependence of the mean density on the temperature is compared, and the procedure is repeated for inherent structure energies as well. Given that the statistics are similar with a similar trend, this suggests that the sampled configurations are independent of starting configurations. Through this exercise, we are able to determine

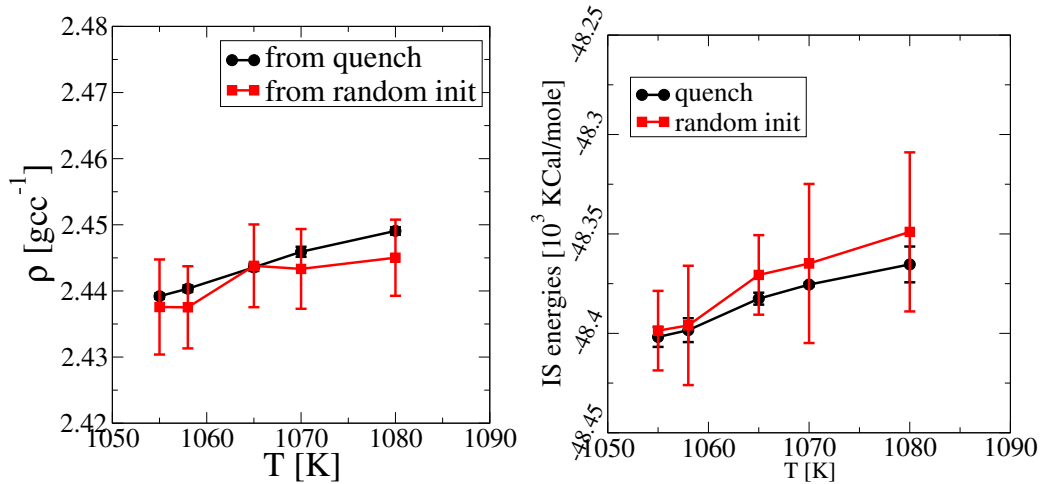


Figure 3.4: Average density (*Left*) and inherent structure energy (*Right*) vs temperature from two sets of starting conditions. The first  $0.5$  ns from a set of independent MD runs at five temperatures. At each temperature, 8 independent NPT MD runs were started from random initial configurations and 600 runs from the quench. Simulations were conducted at  $P = 0$  GPa and a system size of  $N = 512$ . The initial  $0.038$  ns were discarded as the initial transient and the next  $0.5$  ns were used to aggregate the density profile at each temperature. The error bars represent the uncertainty in the mean from different, equal-sized blocks.

that the liquid initially samples the metastable high density state corresponding to the target temperature post a transient. The liquid is therefore not stuck in a non-equilibrium state post the quench from the high temperature. The comparison of trends over temperature with the random initialisation further highlights this.

### 3.3.3 Umbrella sampling Monte Carlo simulations: Initial conditions

Umbrella sampling Monte Carlo simulations in the NPT ensemble were started by first randomly placing  $N$  particles in a box, taking care to prevent any two particles being too close so that large repulsive interactions are avoided. The initial box



size corresponded to a density of  $2.48g\text{ cc}^{-1}$ . For simulations at deep supercooling, where the hard wall bias is applied, simulations were initially equilibrated with a harmonic bias potential for  $10^7$  MC steps with a spring constant of  $k_{n_{\max}} = 0.01\epsilon$ . The harmonic bias was replaced with the hard wall bias after the initial equilibration under a harmonic constraint, taking care that the cluster size in each window be within the desired bounds. Thereafter,  $5 \times 10^6$  MC steps were performed with the hard wall bias before statistics were gathered for a subsequent  $2.5 \times 10^7$  MC steps. The auto-correlation functions of density ( $\rho$ ),  $Q_6$  and potential energy were monitored under the application of the hard wall bias and the relaxation time found to be similar and less than  $10^5$  MC steps for all the windows and for each of the three quantities considered. Thus, keeping in mind a relaxation time of  $\tau = 10^5$  MC steps, we use an equilibration length of  $50\tau =$  and a production length of  $250\tau$ .

Hard wall constraints are placed at  $(n_{\max}^l, n_{\max}^u) = [0, 2], [1, 3], [2, 4] \dots$  with parallel tempering swaps performed between simulations with adjacent and overlapping constraint, or adjacent temperatures, to speed up equilibration (see Section 2.8.1).

At state points where the free energy barrier is expected to be high, and the liquid is unambiguously metastable, a number of independent NPT MC simulations are initialised, each constraining  $n_{\max}$  in the vicinity of some  $n_{\max}^0$  with the use of a harmonic potential with spring constant  $k_{n_{\max}}$ . Each independent simulation is equilibrated for  $10^6$  MC steps or  $10\tau$ . The length of the production run over which the order parameters are sampled is determined in the following way. Each simulation is assigned a bias potential, specified either by the bias center or the bounds ( $n_{\max}^0$  or  $[n_{\max}^l, n_{\max}^u]$ ), as well as a temperature. The parallel tempering procedure should result in each simulation, with a “native” temperature and bias potential, “visiting” every other temperature or bias potential a finite number of times. We measure the time taken for the simulation with the lowest temperature or bias potential to visit the highest temperature or bias potential 10 times. The length of the production run is taken as the number of MC steps required for 10 such exchanges to happen, along each of the two axes, temperature and bias potential. An exception to this is when the number of MC steps taken for 10 exchanges to occur is less than  $10^7$  MC steps, in which case the production length is taken to be  $10^7$  MC steps.

At these state points, umbrella sampling with a harmonic bias is used, taking statistics on  $n_{\max}$ , to construct the free energy curves. Additional runs with a hard wall bias on  $n_{\max}$  are performed where statistics for  $P(n)$  are obtained for the smallest

cluster sizes. This is done to enhance sampling near  $n = 0$ , and to avoid the issues described below in the next section.

### 3.3.4 Consistency of free energy reconstructions at small cluster sizes

In computing the free energy barrier to nucleation, the size of crystalline clusters,  $n$ , is employed as the order parameter, and the equilibrium probability density of cluster sizes,  $P(n)$  is related to the free energy cost to the formation of a crystalline cluster of size  $n$ , by Eq. 2.49. Using Eq. 2.59 subject to the constraint that  $\beta\Delta G(0) = 0$  allows us to relate  $\beta\Delta G(n)$  to  $-\ln(P(n))$  without any unknown constants.

Often, (including parts of the present work) the order parameter,  $n_{\max}$ , and the corresponding distribution,  $P(n_{\max})$ , is used as a proxy to  $P(n)$ . The use of  $n_{\max}$  as the order parameter describing the crystallisation transition is appropriate only when  $P(n_{\max}) = P(n)$ . [44, 46, 169, 231, 238]. In a finite volume, the statistics of the largest cluster,  $n_{\max}$ , often show that configurations containing a small cluster (i.e., where the largest cluster is small) are more frequently sampled than configurations where there are no crystalline particles at all. This leads to the appearance of an artificial minimum in  $\beta\Delta G(n_{\max})$  at small values of  $n_{\max}$  as discussed at length in [44, 169, 231, 238, 239]. This effect is more pronounced at deeper supercooling and larger system sizes as shown (and later discussed) in Fig. 3.5 where the deviation between the largest cluster distribution,  $P(n_{\max})$ , and the full cluster size distribution,  $P(n)$ , is significant [44, 238].

For clusters larger than a size  $n_{low}$ , such that clusters of size  $n_{low}$  are rare,  $P(n_{\max}) = P(n) \forall n, n_{\max} \geq n_{low}$  [81, 169, 240]. Here, rare clusters are those for which the frequency with which clusters of size  $n_{low}$  are observed is well-approximated by the probability of observing one such cluster, and for which the formation of multiple such clusters can be considered independent events. In this limit,  $P(n_{\max})$  does not display system-size dependence, while for smaller clusters ( $n_{\max} < n_{low}$ ), system-size dependence is apparent. A different system size effect is evident when considering state points with large critical clusters whose diameter is greater than half the box length, thus inducing ordering across periodic images [15].

On the other hand,  $P(n)$  is independent of system size for all  $n$ . Given  $\beta\Delta G(n_{\max})$

up to an unknown additive constant, the question is how this relates to  $\beta\Delta G(n)$ . One uses the fact that  $\beta\Delta G(n) = -\ln(P(n))$ . However,  $P(n_{\max}) = e^{-\beta\Delta G(n_{\max})}$  is known to deviate from  $P(n)$  for small  $n$ , up to some (as yet unknown) cluster size  $n_{low}$ . For  $\beta\Delta G(n_{\max})$  obtained from umbrella sampling runs, we employ the procedure of using the equilibrium distribution  $P(n)$  to define our estimate of  $\beta\Delta G(n_{\max})$  up to an  $n$  value  $n_{hi} > n_{low}$ , and demanding that  $\beta\Delta G(n_{\max} = 0) = 0$ . In the case of the MFPT runs, we make the reasonable assumption that the steady state probability of observing clusters of size  $n$ ,  $P_{ss}(n) = \langle N(n)/N(0) \rangle$ , is equal to the equilibrium probability,  $P(n)$ , for  $n \leq n_{hi}$ . Here,  $n_{hi} \geq n_{low}$  is an as yet unknown upper limit up to which this assumption holds and the average is over an ensemble of independent, unconstrained MD trajectories. Note that  $P_{ss}(n)$  is not the steady state probability of sampling the largest crystalline cluster,  $P_{st}(n_{\max})$ . An explicit comparison is made in Fig. 3.5 to show that this approximation holds for some  $n_{hi}$ . On the other hand, for the umbrella sampling runs, we obtain  $P(n)$  from  $N(n)/N(0)$  as described before. This procedure is represented by the expression in Eq. 3.3 where we require that  $\beta\Delta G(n_{\max}) = -\ln(P(n)) \forall n_{\max} \leq n_{low}$  and make the demand that  $\beta\Delta G(n_{\max}) \approx -\ln(P(n))$  for  $n_{low} \leq n_{\max} \leq n_{hi}$ . The following error is then minimised:

$$\chi_c = \sum_{n, n_{\max}=n_{low}}^{n_{hi}} |\beta\Delta G(n_{\max}) + \ln(P(n)) + C| \delta_{n, n_{\max}} \quad (3.3)$$

Here, the sums are over  $n$  and  $n_{\max}$ , considering only those terms where  $n = n_{\max}$ . The unknown constant  $C$  that minimizes the difference between  $\beta\Delta G(n_{\max})$  and  $-\ln(P(n))$  within the range  $[n_{low}, n_{hi}]$  is determined. The choice of  $n_{low}$  and  $n_{hi}$ , as motivated by the discussion above, is determined by the deviation of  $P(n_{\max})$  from  $P(n)$  at small  $n$  or  $n_{\max}$ , as well as the limit up to which the equilibrium  $P(n)$  is well-approximated by  $P_{ss}(n)$ .

Similar methods have been used in Ref. [44] and Ref. [231]. The applicability of the procedure described in this section has limits if  $n_{low}$  itself shifts to values comparable to the critical size  $n^*$ . At lower temperatures, as  $P(n_{\max})$  and  $P(n)$  become progressively more different and the appropriate  $n_{low}$ , beyond which  $P(n_{\max}) \approx P(n)$ , shifts to larger values, this comparison between  $\beta\Delta G(n)$  and  $\beta\Delta G(n_{\max})$  becomes more difficult to the point that it is eventually no longer tenable.

## 3.4 Results

The results of free energy calculations performed at different state points are shown in this section, with a specific focus on temperatures across the previously reported LLPT at  $P = 0$  GPa [2]. At these temperatures, free energy calculations are performed using both the kinetic reconstruction from the MFPT and using umbrella sampling with a hard wall bias. The results for these state points are compared, showing a free energy barrier to the crystallisation transition at all the temperatures considered, demonstrating that crystallization is not spontaneous.

The rest of the results are subsequently presented showing the free energy cost to crystallization at other state points where the question of loss of metastability of the liquid does not arise. This includes free energy calculations performed at higher temperatures along the  $P = 0$  GPa isobar. Calculations at low temperatures along the  $P = 0.75$  GPa isobar are also performed. Along other isobars, the choice of state points is restricted to those understood to correspond to the high density liquid, based on the results in Ref. [2].

The free energy curves are also constructed along lines of constant coordination number,  $C_{NN}$ , and of constant isothermal compressibility,  $\kappa_T$ , in an attempt to understand the effect of density fluctuations and of the degree of tetrahedral ordering in the metastable liquid on the barrier to crystallisation. A further set of calculations is performed, crossing the line of maximum compressibility, known as the Widom line [149, 154], beyond the LLCPP reported in [2], where the two purported metastable liquids cease to be indistinguishable.

Results for the different sets of state points are now presented in turn, after first illustrating the methodology for the treatment of free energy profiles at small cluster sizes, and the MFPT method. We then discuss briefly the relationship between the free energy barrier and the critical nucleus size, and a comparison with the expectation based on CNT. Finally, for the low temperature  $T = 1055$ K at zero pressure, we consider whether the choice of the initial ensemble of configurations (HDL-like or LDL-like) will make a difference to the estimation of free energy barriers, and answer it in the negative.

### 3.4.1 Comparing results at small cluster sizes

The behaviour of supercooled liquid silicon is a matter of debate at deep supercooling, particularly in the vicinity of  $T = 1060$ K at  $P = 0$  GPa. To address the

question of whether crystallisation is spontaneous at these state points, the free energy barrier to the growth of crystalline clusters is calculated using the two methods described above.

We find that a clear and significant barrier to the growth of the crystalline phase exists at each of the state points considered and that the two methods give results that are in agreement, shown in Fig. 3.7. Mendez-Villuendaz *et al* [54], find that the largest cluster,  $n_{\max}$ , is the appropriate order parameter to determine the thermodynamic stability of the parent phase based on stronger coupling between the nucleation kinetics and the free energy profile as a function of  $n_{\max}$  in the context of supercooled gold nanoclusters in the liquid phase. As also in other work, [91, 239], a monotonically decreasing free energy as a function of  $n_{\max}$  is argued [54] to mark the loss of metastability of the liquid with respect to crystallisation. This conclusion is derived from the argument that  $n_{\max}$  is the order parameter that is best coupled to nucleation timescales. However, the thermodynamic stability of the metastable liquid is determined by the free energy cost to the growth of any cluster of size  $n$ ,  $\beta\Delta G(n)$ . In the present case, we point out that at all the state points we have considered, the free energy profile,  $\beta\Delta G(n_{\max})$ , is not monotonically decreasing with  $n_{\max}$  and displays a clear barrier.

Following the procedure described in Section 3.3.4, we make a comparison between  $\beta\Delta G(n)$  obtained from umbrella sampling runs with a hard wall bias to  $\beta\Delta G(n_{\max})$  obtained from both the kinetic reconstruction and umbrella sampling runs with a hard wall bias. At  $T = 1070\text{K}$ ,  $P = 0\text{ GPa}$  (see Fig. 3.5), using  $n_{\text{low}} = n_{\text{hi}} = 1$  gives nearly exact quantitative agreement between  $\beta\Delta G(n)$  and  $\beta\Delta G(n_{\max})$  at  $N = 512$  regardless of the method used to generate the curves. As expected, free energy curves constructed from USMC simulations using the equilibrium  $P(n)$  show no system-size dependence. In Fig. 3.5 (b),  $\beta\Delta G_{HW}(n_{\max})$  for small  $n_{\max}$  from umbrella sampling runs for  $N = 4000$  is obtained using  $n_{\text{low}} = 3$ ,  $n_{\text{hi}} = 5$  in Eq. 3.3. At lower temperatures, or even larger system sizes, as the appropriate value of  $n_{\text{low}}$  becomes larger a comparison between  $\beta\Delta G(n_{\max})$  and  $\beta\Delta G(n)$  can no longer be meaningfully made. The role of system size is evident when computing  $\beta\Delta G(n_{\max})$ , however,  $\beta\Delta G(n)$  does not show this effect at larger system sizes. A different finite size effect is evident when the critical cluster is large compared to the box length, and the cluster interacts with its own periodic image. This is discussed in more detail in Ref. [15]. Having described how to compare the free energy results using the two methods, a comparison is made at  $P = 0\text{ GPa}$  at temperatures where the crystallisation transition is of particular interest.

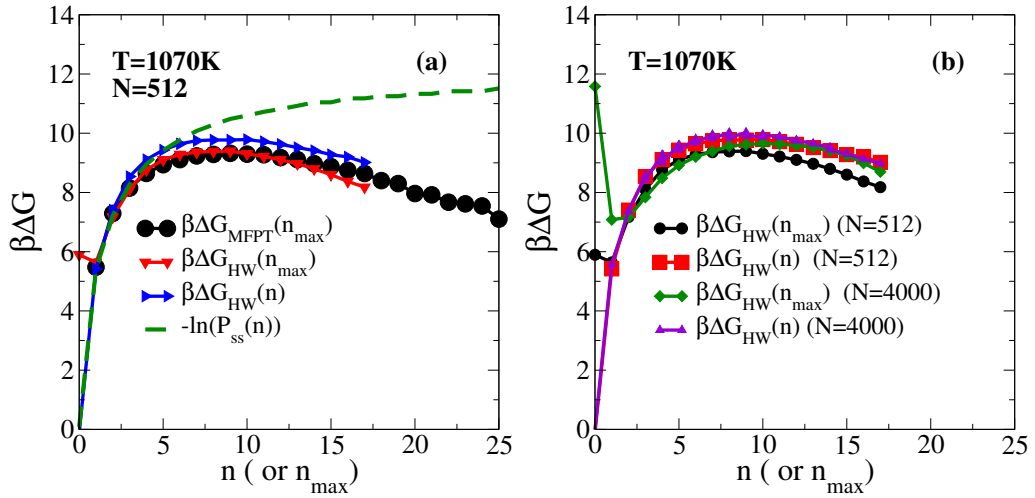


Figure 3.5: A comparison of free energy reconstructions at  $T = 1070\text{K}$ ,  $P = 0\text{ GPa}$  using both  $n$  and  $n_{\max}$  as order parameters at two system sizes,  $N = 4000$  and  $N = 512$ . (a) Comparison, at  $N = 512$ , of results from the MFPT method using  $n_{\max}$  as the order parameter with results from the hard wall bias umbrella sampling using either  $n$  or  $n_{\max}$  as the order parameter. (b) Comparison of results using either  $n$  or  $n_{\max}$  as the order parameter from the umbrella sampling simulations at two system sizes,  $N = 512$  and  $N = 4000$ . For the purpose of comparison of  $\beta\Delta G(n)$  with  $\beta\Delta G(n_{\max})$ , the error in Eq. 3.3 is minimised. For  $N = 4000$ , the error is minimised for  $1 < n \leq 3$ .

### 3.4.2 Kinetic reconstruction of free energy from MFPT

The two main ingredients to reconstruct the free energy using this method are the MFPT,  $\tau_{\text{MFPT}}(n_{\max})$ , and the steady state size distribution of the largest crystalline cluster,  $P_{\text{st}}(n_{\max})$ . These can be used as shown in Eqs. 3.1 and 3.2 to get the free energy with the largest cluster size as the order parameter,  $\beta\Delta G(n_{\max})$ . The MFPT and steady state probability are shown in Fig. 3.6 for the temperatures studied here. These results are generated from NPT MD runs of  $N = 512$  particles. Results using this method are produced at state points where the pressure is  $P = 0\text{ GPa}$  and the temperature is varied in a range from high temperatures where the liquid can be unambiguously sampled in equilibrium before nucleating ( $T = 1070\text{ K}$ ,  $1080\text{ K}$ ) to lower temperatures where the loss of liquid metastability with respect to crystallisation becomes a consideration ( $T < 1070\text{ K}$ ). The order parameter is the size of the largest cluster,  $n_{\max}$  and the absorbing boundary condition is placed at  $n_{\max} = 100$ . In Fig. 3.6, we see that the MFPT,  $\tau_{\text{MFPT}}(n_{\max})$ , shows a progressively decreasing sigmoidal character as we decrease the temperature from  $T = 1080\text{K}$  to  $T = 1055\text{K}$ . This suggests that the difference between the nucleation timescale and the timescale of cluster growth decreases. As discussed in the previous section, the steady state

probability  $P_{st}(n_{\max})$  shown in Fig. 3.6 (b) peaks at small values of  $n_{\max}$  ( which shows up as a minimum in  $-\ln(P_{st}(n_{\max}))$ ) and decays exponentially close to the absorbing boundary. At the higher temperature of  $T = 1080\text{K}$ , post-critical clusters grow rapidly. For this reason, we sample  $n_{\max}$  with a higher frequency to obtain smoother data for  $\tau_{MFPT}(n_{\max})$  that captures the post-critical growth phase well.

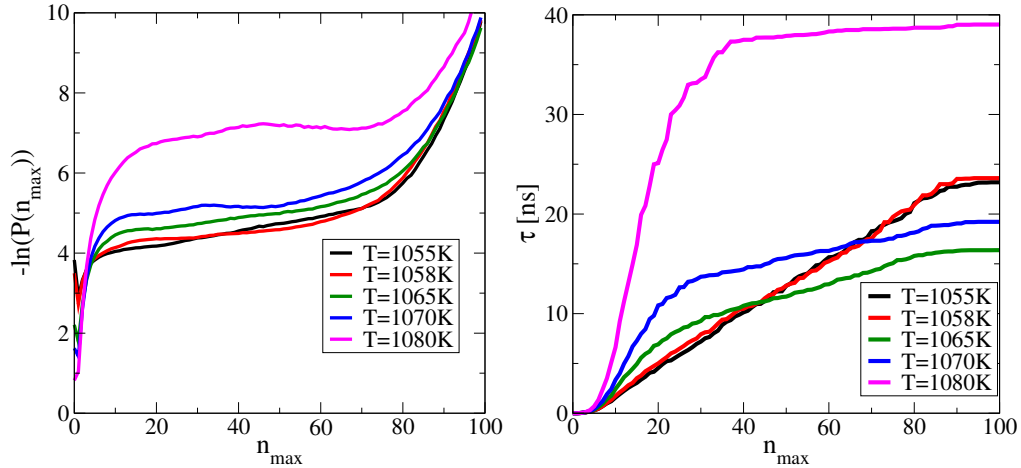


Figure 3.6: (a)  $-\ln(P_{st}(n_{\max}))$  plotted against  $n_{\max}$  for different temperatures. 600 NPT MD simulations at  $P = 0\text{GPa}$  were run with a system size of  $N = 512$ . (b)  $\tau_{MFPT}(n_{\max})$  plotted against  $n_{\max}$  from the same set of MD runs.

At  $T = 1055\text{K}$ ,  $1058\text{K}$ , we find that the difference between  $P(n_{\max})$  and  $P(n)$  (or between the corresponding steady state probabilities for the MFPT results,  $P_{st}(n_{\max})$  and  $P_{ss}(n)$ ) persists to larger values of  $n$  (or  $n_{\max}$ ) than at higher temperatures. It is worth noting that the comparison between  $P_{st}(n_{\max})$  and  $P_{ss}(n)$  is only meaningful for  $n$  or  $n_{\max}$  small enough that the steady state probabilities are good approximations to the equilibrium probabilities. When the difference between  $P(n_{\max})$  and  $P(n)$  persists to larger values, the only meaningful comparison between results from the two methods, umbrella sampling and the MFPT method, are those where the order parameter is the same, namely,  $n_{\max}$ . Notwithstanding the difficulty in making a satisfactory quantitative comparison with the free energy profiles obtained using the different methods at the lowest two temperatures, we close by pointing out two salient features of the results that are reported in Fig. 3.7, which are central to the main focus of the present study: (i) At all temperatures studied, a clear and significant free energy barrier is present for crystal nucleation, and the different estimates,  $\beta\Delta G_{MFPT}(n_{\max})$ ,  $\beta\Delta G_{HW}(n_{\max})$  and  $\beta\Delta G_{HW}(n)$  are in reasonable quantitative agreement. (ii) The free energy profiles  $\beta\Delta G_{MFPT}(n_{\max})$  and  $\beta\Delta G_{HW}(n_{\max})$ , obtained using the same order parameter  $n_{\max}$  are in very good

quantitative agreement at all temperatures, including the lowest two temperatures at which their comparison with  $\beta\Delta G_{HW}(n)$  is not very satisfactory. An important point needs to be made about the barrier heights that these investigations reveal. The resulting nucleation rates for  $N = 512$  (Fig. 3.7) are of the order of  $2.5 \times 10^7 s^{-1}$ . The corresponding nucleation rates for macroscopic or even nanoscopic droplets (e.g., sub-micron droplets) would be very large, and the liquid would be too short-lived to be probed under normal experimental conditions, and would require well-designed, ultrafast, measurements to detect [20]. In order to understand the significance of barriers of the order of  $10 k_B T$ , we consider the system size at which at least 1 critical cluster will be observed in the liquid in equilibrium. Along the lines suggested by the referee, we begin by writing:

$$\beta\Delta G(n) = -\ln \frac{N(n)}{N_{sys}} \quad (3.4)$$

where  $N_{sys}$  is the number of particles in the system. If we rearrange and consider that there is one critical cluster of size  $n^*$  with a barrier height of  $\beta\Delta G^*$ , we get

$$N_{sys}^* = (1)e^{+\beta\Delta G^*} = e^{10} \approx 22000 \quad (3.5)$$

The number on the RHS provides an upper bound on simulation sizes which can be used so that the liquid may be observed before crystallization occurs. This number is far smaller than typical macroscopic sample sizes relevant to most experimental contexts.

### 3.4.3 Free Energy profiles across the Widom line

We next evaluate the change in  $\beta\Delta G$  across the Widom line for the  $P = -1.88\text{GPa}$  isobar. Simulations are conducted for different isobars and, in addition to results shown in Ref. [15] are compiled together to demonstrate patterns and trends. The line of compressibility maxima, called the Widom line, that extends beyond the liquid-liquid critical point in water and related systems, has been the focus of several studies [149, 154, 229, 241, 242]. In these studies, sharp (if continuous) changes in various properties have been reported across the Widom line. We investigate whether crossing this line at constant pressures below the critical pressure reveals any indication of a marked change in the nucleation barriers. We first show the set



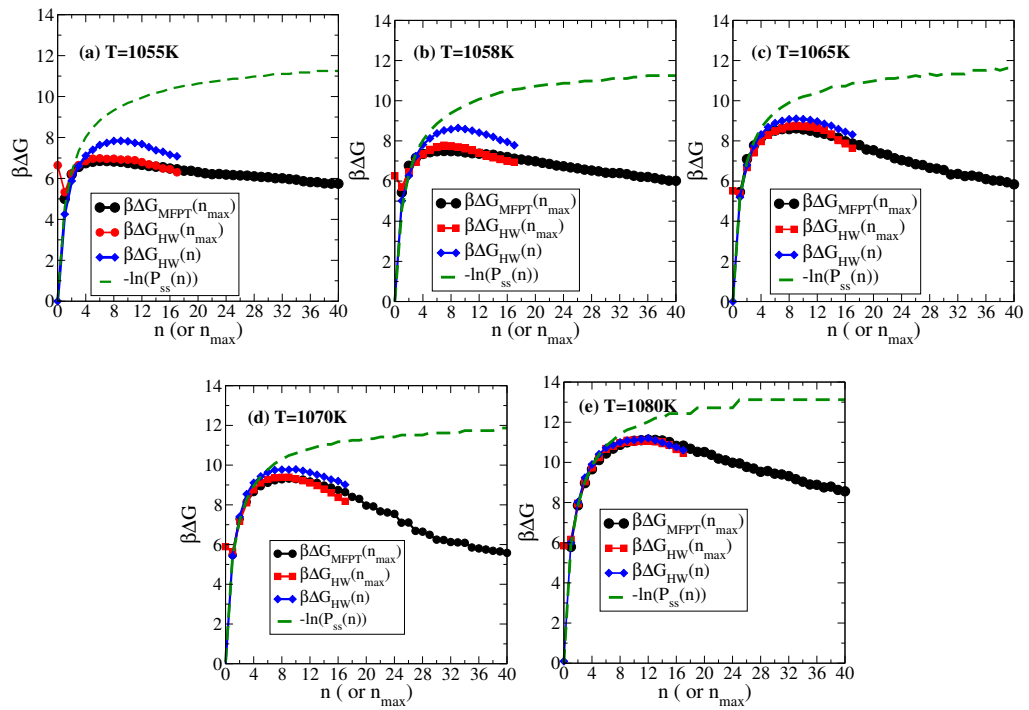


Figure 3.7: 1D nucleation barrier obtained using MFPT and HW bias methods at (a)  $T = 1055\text{K}$ , (b)  $T = 1058\text{K}$ , (c)  $T = 1065\text{K}$ , (d)  $T = 1070\text{K}$ , (e)  $T = 1080\text{K}$ . Curves are shifted such that  $\sum_{i=1}^3 |\beta\Delta G(n_{\max} - \ln(P_{st}(n_{\max} = 1)))|$  is minimised. MFPT free energy from 600 NPT MD runs of  $N = 512$  particles at  $P = 0$  GPa. The HW bias free energy from HW bias runs of  $N = 512$  particles at  $P = 0$  GPa.

of state points across which studies are conducted, indicated in Fig. 3.8, are calculated. The pressure is fixed at  $P = -1.88\text{GPa}$ , a value lower than the reported

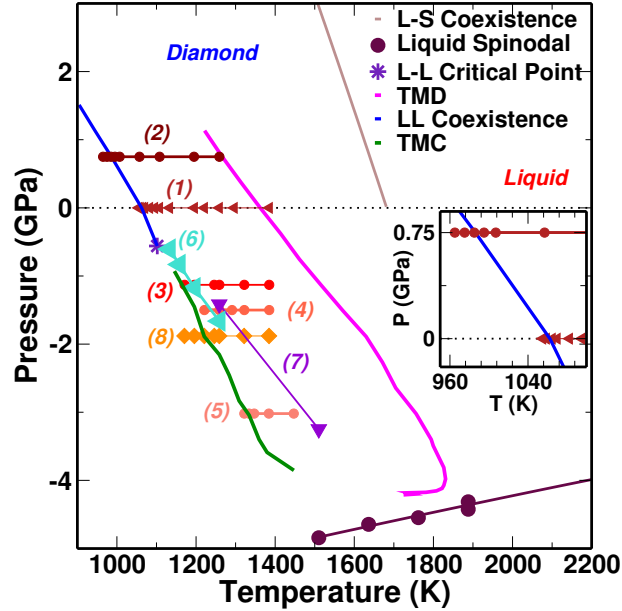


Figure 3.8: The phase diagram of SW silicon showing the loci of interest and the isolines along which free energy data is analysed in order to understand the relevant trends. Data along the following isolines. Each of the isolines is labelled, with the key as follows - (1)  $P = 0$  GPa isobar, (2)  $P = 0.75$  GPa isobar, (3)  $P = -1.13$  GPa isobar, (4)  $P = -1.5$  GPa isobar, (5)  $P = -3.02$  GPa isobar, (6) Line of constant coordination number  $C_{NN} = 4.66$  (7) Line of constant isothermal compressibility  $\kappa_T$ , (8)  $P = -1.88$  GPa isobar crossing the line of maximum isothermal compressibility. The free energy curves corresponding to lines (3), (4), (5), (6) and (7) are contained in Vishwas Vasisht's thesis [15] and are therefore not included here. *Inset* Zoomed in to the temperatures along the  $P = 0$  GPa and  $P = 0.75$  GPa isobars at which the free energy calculation is performed, showing the estimated liquid-liquid coexistence line in blue.

critical point, and the temperature varied from  $T = 1385\text{K}$  to  $T = 1171\text{K}$ . The compressibility maximum at  $P = -1.88$  GPa is at  $T \sim 1230\text{K}$ . The free energy barrier is found to decrease monotonically with temperature in Fig. 3.9. On the low temperature side of the reported Widom line, the free energy barrier changes by  $2k_B T$  for a 50K change in temperature while on the high temperature side, we find that for a similar change in temperature, the free energy barrier changes by  $> 10k_B T$ . Thus, our results indicate that indeed, a change in the temperature dependence of nucleation barriers occurs upon crossing the Widom line. Considering the critical nucleus size,  $n^*$ , we find a more striking change, with the critical nucleus size becoming nearly constant below the Widom line. While such a change

in temperature dependence is of interest, the presence of a free energy barrier to crystallization exists at state points above and below the Widom line, and points to the liquid retaining metastability at all these state points.

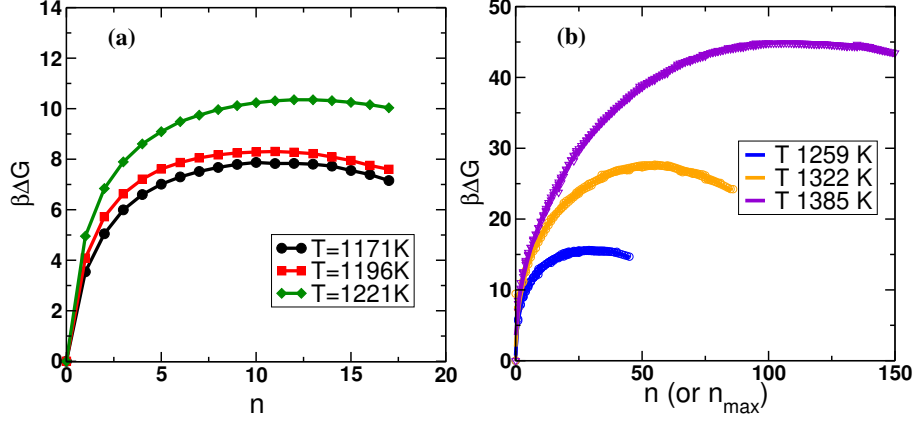


Figure 3.9: Free energy difference  $\beta\Delta G$  against the nucleus size obtained from NPT umbrella sampling MC simulation at  $P = -1.88\text{GPa}$ . (a) Low temperature side of Widom line,  $N = 512$  (b) High temperature side of Widom line,  $N = 4000$ . For the low temperature side in (a), the full cluster size distribution,  $P(n)$ , is obtained from runs with a hard wall bias on  $n_{\max}$  and used to construct the free energy curves. For the high temperature side, (b), [From PhD thesis of Vishwas Vasisht [15] with permission.] Umbrella sampling runs are performed with a harmonic bias on  $n_{\max}$ , and statistics of  $n_{\max}$  are gathered. Additional runs with a hard wall bias are performed, sampling  $P(n)$ , to improve statistics for small  $n$  (or  $n_{\max}$ ).

### 3.4.4 Dependence of barrier height and critical size on temperature

The Classical Nucleation Theory (CNT) expressions for the barrier height and critical size are

$$\beta\Delta G^* = \frac{16\pi}{3} \left( \frac{v'\sigma^{3/2}}{-\Delta\mu} \right)^2 \quad (3.6)$$

$$n^* = \frac{32\pi}{3} \left( \frac{(v')^{2/3}\sigma}{-\Delta\mu} \right)^3 \quad (3.7)$$

From this, one can infer a relation between the barrier height and the critical cluster size

$$\beta\Delta G^* = (n^*)^{2/3} \quad (3.8)$$

Trends in the critical cluster size  $n^*$  and the barrier height,  $\beta\Delta G^*$ , as a function of temperature along the  $P = 0$  GPa isobar are shown in Fig. 3.10 (a) and (b). Fig. 3.11 contains a parametric plot of the barrier height and the corresponding cluster size. Interestingly, one finds that a  $n^{2/3}$  scaling of the barrier height fits the data well at state points where  $n^*$  is large. This is in accordance with the CNT prediction. At deep supercooling where the critical cluster is small and poorly approximated to a sphere, the predictions from CNT are not expected to be obeyed given that a number of the assumptions made in CNT are not satisfied when  $n^*$  is small. Interestingly, we find that all the state points which show deviations from the CNT prediction fall on the lower temperature side of the liquid-liquid phase transition or the Widom line estimated in Ref. [2]. One further notes that the onset of deviations is not brought on by the crossing of some specific lower limit critical size(s) below which the CNT relation no longer holds. Instead, one finds that the deviations strongly correspond to the crossing of the Widom line, indicating the effect of a change in the microscopic structure of the liquid on the nucleation barrier. The free energy data from calculations performed in this thesis as well as from existing data [15] are compiled in order to understand changes in behaviour shown in Fig. 3.11.

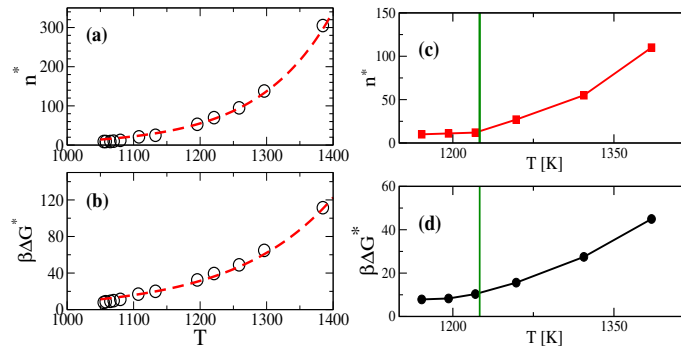


Figure 3.10: (a) The critical cluster size  $n^*$  and (b) the height of the free energy barrier,  $\beta\Delta G^*$  as a function of temperature at  $P = 0$  GPa. The dashed lines are guides to the eye. (c) The critical cluster size  $n^*$  and (d) the height of the free energy barrier,  $\beta\Delta G^*$  as a function of temperature at  $P = -1.88$  GPa.

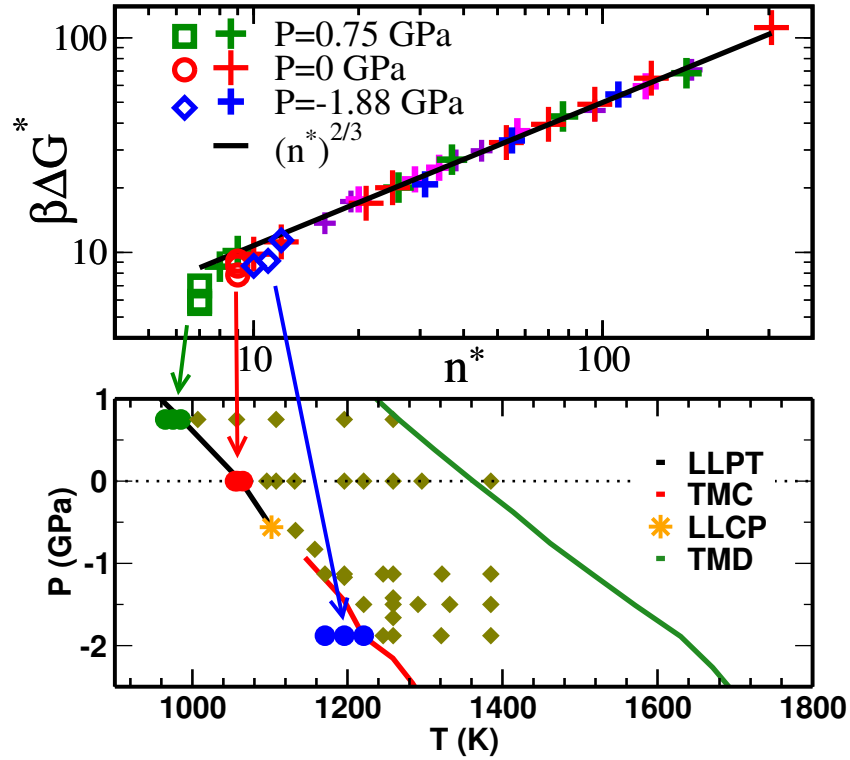


Figure 3.11: A parametric plot of the barrier height,  $\beta\Delta G^*$  and the corresponding critical cluster size,  $n^*$  obtained from different isobars combining data shown in this thesis as well as in Ref. [15]. The solid line corresponds to the  $n^{2/3}$  dependence of the free energy barrier expected according to CNT. Data points found to deviate from the scaling at low  $n^*$  are shown as open symbols in the top panel and the corresponding temperatures and pressures are marked as coloured circles in the bottom panel (with the colour denoting the isobar at which the measurement is made). The solid olive diamonds in the bottom panel are the state points for which the free energy barrier varies as  $n^{2/3}$ , which are shown as solid symbols in the main panel.

### 3.4.5 Microscopic structuring of the liquid around crystalline particles

A number of recent studies have investigated the microscopic transformations that underlie crystallisation [72, 76]. Questions that are of specific interest are the role of the low density phase in facilitating crystal nucleation and a possible two-step mechanism in crystal nucleation, which has been investigated for silicon in the past [15, 134]. In this section, we consider the neighbourhood of crystalline particles and how this changes as the cluster size changes. The figures below (Fig. 3.12, Fig. 3.13) illustrate the relative probability of observing HDL-like and LDL-like particles around crystalline nuclei of different sizes. These are produced from unconstrained MD simulations along the  $P = 0$  GPa isobar and the configurations are selected such that the size of the largest cluster is as mentioned in the legend. The radial distribution of particles is measured with respect to centre of mass of the largest crystalline cluster only. When multiple clusters have the same size as the largest cluster, one of them is arbitrarily labelled the largest. The radial distribution function is normalised with respect to the background HDL (or LDL) particle densities. LDL particles are identified as 4-coordinated liquid particles with local  $q_6(i) > 0.6$  but not bonded to 3 other such 4-coordinated particles. HDL particles are defined as 5-coordinated liquid particles with local  $q_6(i) < 0.6$  (see also Section. 5.1.1). Averaging is performed over  $\sim 10^4$  configurations at each temperature for each value of  $n_{max} < 10$  and  $\sim 100$  configurations for  $n_{max} \geq 10$ . Note the distinct difference in the distribution functions for  $n_{max} = 1$ , even at high temperatures of  $T = 1080K$ . The case of  $n_{max} = 1$  is also of interest in this context because it highlights the stark difference in the local neighbourhood of bulk crystalline monomers. The near absence of HDL-like particles in the neighbourhood of crystalline particles (probability lower than the background HDL density) suggests that the LDL-like state is a microscopic intermediate state even when the LDL phase is not macroscopically metastable. At larger cluster sizes, the distance with respect to the boundary of the cluster would be more interesting than the distance from the centre to counteract the effect of an irregularly shaped cluster on the radial distribution function.

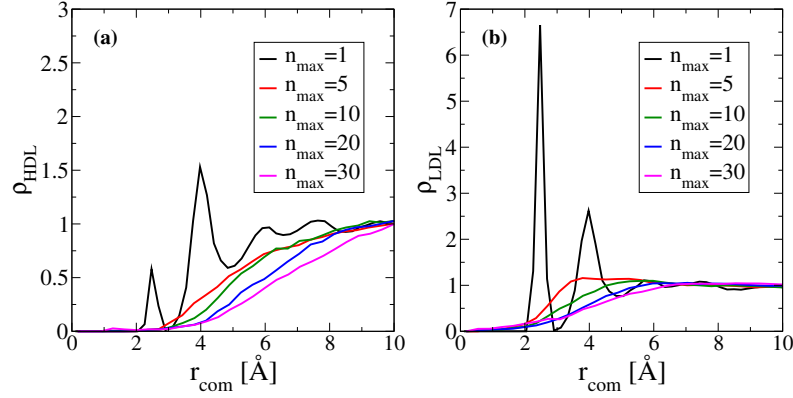


Figure 3.12: Radial distribution function of HDL-like particles (panel (a)) and LDL-like particles (panel (b)) around crystalline nuclei of different sizes as shown. Configurations are obtained from 600 unconstrained NPT MD simulations of  $N = 512$  particles at  $P = 0 \text{ GPa}$ ,  $T = 1055 \text{ K}$  where the largest cluster is of the size given in the legend. The radial distribution function is obtained by averaging over different uncorrelated configurations (separated by  $10^6$  MD steps).

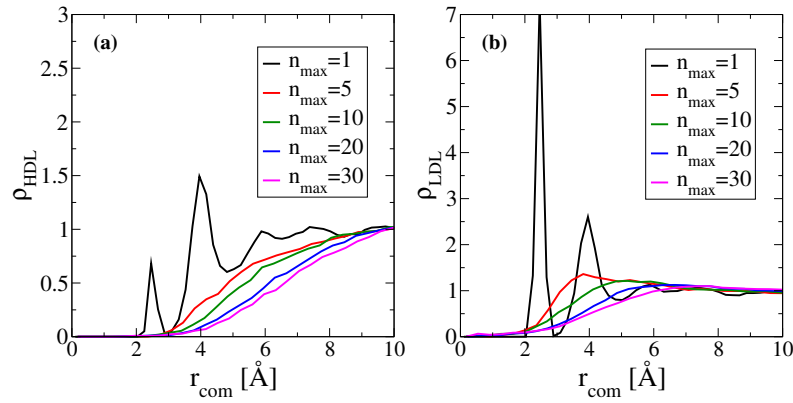


Figure 3.13: Radial distribution function of HDL-like particles (panel (a)) and LDL-like particles (panel (b)) around crystalline nuclei of different sizes as shown. Configurations are obtained from 600 unconstrained NPT MD simulations of  $N = 512$  particles at  $P = 0 \text{ GPa}$ ,  $T = 1080 \text{ K}$  where the largest cluster is of the size given in the legend. The radial distribution function is obtained by averaging over different uncorrelated configurations (separated by  $10^6$  MD steps).

### 3.4.6 Effect of changing the ensemble of starting configurations at $T = 1055\text{K}$

We compare the free energy curves produced when the ensemble of initial conditions is changed from the disordered liquid considered earlier to a liquid more typical of  $T = 1055\text{K}$ , noting the significant difference in the characteristics of the two at this temperature. One expects that if the sampling along other order parameters can be assumed to be complete, regardless of the set of starting configurations, then the two sets of results should be exactly the same. This is seen in the case of the umbrella sampling runs with the hard wall bias, shown in Fig. 3.14. We compare results when the starting configurations are of randomly place particles in a box corresponding to density  $2.48 \text{ gcc}^{-1}$  to those where the starting set of configurations are selected from MD runs at  $T = 1055\text{K}$ ,  $P = 0 \text{ GPa}$  satisfying the following criteria:

- $\rho \leq 2.37 \text{ gcc}^{-1}$
- $n_{\text{max}} \leq 5$
- $n_{\text{tot}} \leq 10$  where  $n_{\text{tot}}$  is the total number of crystalline atoms

For the kinetic reconstruction, we start a set of MD simulations at  $T = 1055\text{K}$ ,  $P = 0 \text{ GPa}$  from an ensemble of LDL-like configurations, produced from the earlier set at  $T = 1055\text{K}$ . In this case, we find that the assumption of full sampling along other order parameters is not valid, making a comparison more difficult.

### 3.4.7 Measuring the chemical potential from thermodynamic integration

We extend the melting line in Ref. [2] to low temperatures using a linear extrapolation. From this, we extract the  $P_{\text{melt}}$  for  $T = 1070\text{K}$ ,  $T = 1108\text{K}$ . The chemical potential can be written as

$$\Delta\mu = \Delta G/N$$

Where,

$$V = \left( \frac{\partial G}{\partial P} \right)_{T,N}$$



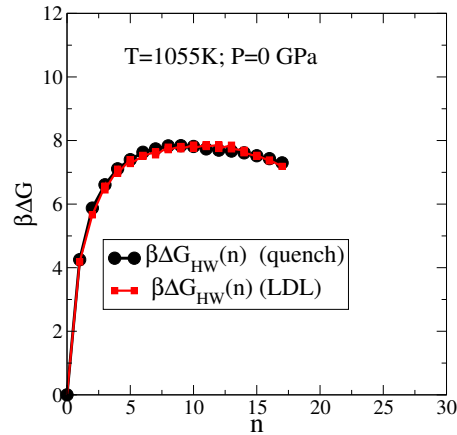


Figure 3.14: We compare the free energy reconstructions from two sets of umbrella sampling runs with the hard wall bias. Simulations are performed at  $T = 1055K$ ,  $P = 0$  GPa with a system size  $N = 512$ . The curve labelled "quench" is started from a set of randomly placed particles in a box such that the density is  $2.48 \text{ gcc}^{-1}$ . The curve labelled "LDL" is started from a set of configurations selected from MD runs at  $T = 1055K$ ,  $P = 0$  GPa with low density and low degree of crystallinity as discussed in the text.

Integrating this along an isotherm can give us

$$\Delta G_{21}/N = G_2/N - G_1/N = \int_1^2 V(P)/NdP = - \int_2^1 V(P)/NdP$$

We can integrate the equations of state of the liquid and the crystal to get  $\Delta G_{21;cry}$  and  $\Delta G_{21;liq}$  from the isotherms of each. Note that the free energy of crystal and liquid at state point 1 are the same if the pressure at state point 1 is the melting pressure for the given isotherm. The isotherms are shown in Fig. 3.15.

$$G_{1;cry} = G_{1;liq} \quad \text{if} \quad P_1 = P(T)_{melt} \quad (3.9)$$

We obtain the chemical potential by integrating the EOS for each isotherm from corresponding melting pressure to  $P = 0$ . The difference between the chemical potential of the crystal and the liquid at each temperature  $T$  is given by  $\Delta\mu_{cry}(T) - \Delta\mu_{liq}(T)$ . The dependence of barrier height and the extrapolation of the  $\Delta\mu$  curve (exponentially) to estimate the liquid-solid co-existence temperature at  $P = 0$  GPa (where  $\Delta\mu = 0$ ) is shown in Fig. 3.16. The results in Fig. 3.16 show that the barrier does follow the trend of  $1/(-\Delta\mu)^2$  along the  $P = 0$  GPa isobar, at least at higher temperatures. While the method to compute the chemical potential is approximate, the estimate of the melting temperature provides a useful benchmark. A similar analysis of the critical cluster size and of the dependence of the surface tension need

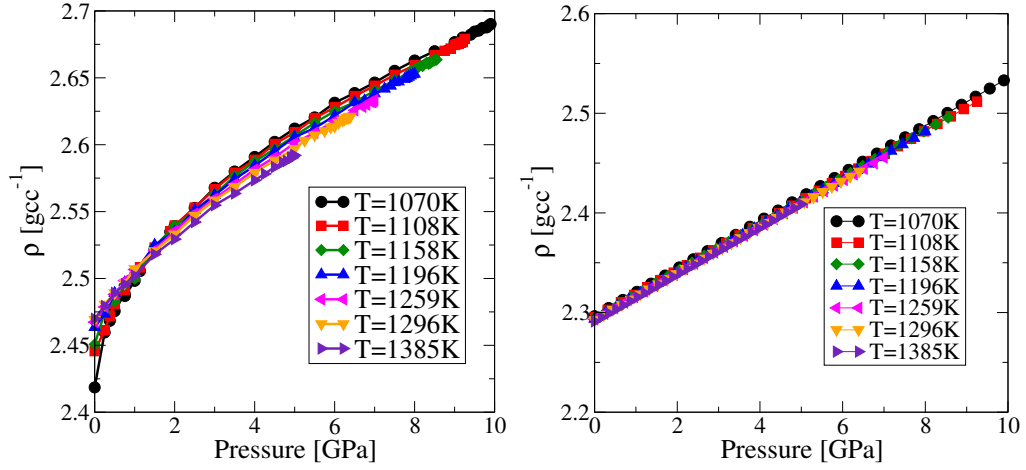


Figure 3.15: Isotherms (EOS) for the liquid (*Left*) and for the crystal (*Right*). For crystal the isotherms are calculated from  $P = 0$  GPa to  $P = 3$  GPa. This data is fit to a straight line and extrapolated till the corresponding  $P_{melt}$ .

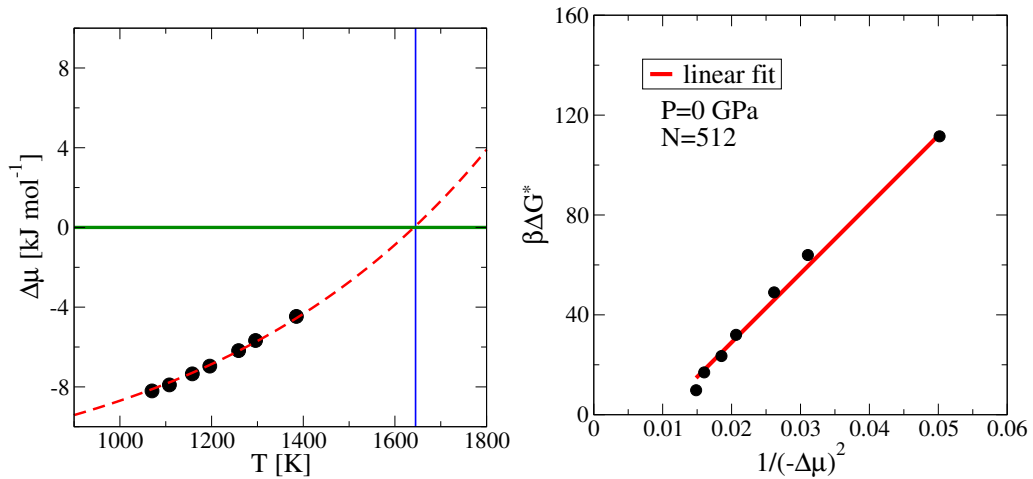


Figure 3.16: (*Left*) The difference in chemical potential is plotted vs temperature. An exponential extrapolation provides an estimate of the melting temperature at  $P = 0$  GPa. (*Right*) The barrier height along the  $P = 0$  GPa isobar is shown vs the corresponding value of  $1/(-\Delta\mu)^2$ .

to be performed to have a thorough understanding. The analysis performed here has some key limitations. Firstly, the thermodynamic integration scheme that has been used cannot be extended across a discontinuity such as a phase transition. Secondly, the thermodynamic integration of the equations of state is not the ideal choice to estimate the chemical potential of the crystalline state. The Frenkel-Ladd method [130] for example is the more standard approach. The analysis here is not able to provide an analogous observation to that in Fig. 3.11.

## 3.5 Discussion

In summary, we have investigated crystal nucleation barriers in Stillinger-Weber silicon for a wide range of state points, employing two distinct methods, namely umbrella sampling and the reconstruction of the free energy barriers through the computation of mean first passage times from unconstrained molecular dynamics simulations. In particular, we focus on state points close to the liquid-liquid transition that has previously been studied, although in the present work we do not directly address the liquid-liquid transition itself. Instead, we focus on the question of whether a free energy barrier to crystal nucleation exists at the relevant state points, since it has been suggested in some previous works that no such barrier exists and crystal nucleation occurs spontaneously [18, 28, 30]. Based on the two independent methods of estimating free energy barriers mentioned above, we consistently find that at all state points we investigate, finite free energy barriers to crystallisation are present. Thus, our results confirm the metastability of the liquid phase at state points that are relevant to the investigation of the liquid-liquid transition.

In addition to the low temperature state points at zero pressure that we focus on primarily, we compute the free energy barriers across a wide range of temperatures and pressures. We show that crossing the Widom line at constant pressure leads to a change in the temperature dependence of the free energy barrier and the critical nucleus size – both become slower functions of temperature – indicating a change in the character of the liquid across the Widom line.

Finally, we compare the dependence of the free energy barrier height,  $\beta\Delta G^*$  on the size of the critical nucleus,  $n^*$ , with the CNT prediction that  $\beta\Delta G^* \sim n^{*2/3}$ . Remarkably, we find that the CNT prediction is satisfied for the high temperature and pressure state points, that lie above the boundary defined by the liquid-liquid

transition line and the Widom line taken together, as estimated in Ref. [2], and one observes deviations from the CNT prediction for state points across this boundary. Clearly, a change in character of the liquid takes place across this boundary.

Our results thus clearly establish that finite barriers to crystal nucleation exist at state points across which a liquid-liquid transition have been argued to exist for Stillinger-Weber silicon by some previous works [2] and where the metastability of the liquid has been questioned in others [18, 28, 30]. They also point to changes in the nature of these barriers across state points which have been identified previously as corresponding to the liquid-liquid transition or the Widom line. These results do not directly address the existence of the liquid-liquid transition itself, but establish the necessary condition for questions about such a possibility to be meaningfully investigated. Ascertaining the existence of a liquid-liquid transition is the subject of Chapter 5.

# Chapter 4

## Order parameters

In Chapter 1 we discussed how phase transitions can be described as activated processes, with a barrier crossing describing the transformation from an initial metastable state to another, or to the final state. In this picture, one needs to describe the appropriate collective variable or order parameter, typically a static quantity which is a function of the large dimensional position vector,  $\phi(\{\mathbf{x}_i\})$ . This scalar or vector order parameter needs to be able to distinguish between the different states or phases of interest. Thus, the set of values that  $\phi$  takes for state  $A$  should be non-overlapping with the set of values for state  $B$  (in the case where we are describing the transformation from  $A$  to  $B$ ). Defining the correct order parameter, which closely describes the true reaction coordinate – the coordinate which directly captures the degree of progress of the transformation – becomes an important, and often challenging, task. The true reaction coordinate would be that for which the (scaled) value of the coordinate would map linearly onto the probability of completing the reaction if initiated at the said value of the coordinate. For a many-dimensional (but not  $3N$  dimensional) coordinate, one should be able to separate the reactant from the product by a series of hyperplanes along which the probability of completion of the reaction varies monotonically. The large number of possible combinations for a high dimensional system as well as gaps in the knowledge of the mechanism, even for a well-studied case such as crystal nucleation, make it hard to define such a quantity.

This is of even greater importance when the order parameter is used as a bias parameter in an enhanced sampling scheme (see Chapter 2, umbrella sampling) to promote the transformation or to enhance sampling in the vicinity of the barrier.

In Chapter 3, we mentioned how, in the specific case of crystallisation in deeply

supercooled silicon, an incorrect choice of bias or order parameter gives misleading results viz. the barrier. There, as in earlier work [46], the conclusion was that a local order parameter was more appropriate than a global order parameter such as global  $Q_6$  to describe crystallisation. In this chapter, we explain why and when  $Q_6$  is an inappropriate order parameter in the context of crystallisation. We will compare results with those shown in Chapter 3, wherever helpful. Briefly, the cause of discrepancy can be attributed to artefacts arising from applying a bias potential on  $Q_6$ , as done in umbrella sampling simulations. This is an interesting, if artificial phenomenon, and we describe the mechanism by which this occurs.

Subsequent to this, we discuss other order parameters which serve as candidates to distinguish the liquid from the crystalline phase, and also, the two putative liquid phases. Broadly, the set considered here are in the category of order parameters that try to quantify different types of local structures. A brief mention of other methods in the literature is also included.

## 4.1 Global vs local measures of crystalline ordering

We discuss why the choice of  $Q_6$ , which is the global bond orientational order parameter (Sec. 2.6.1 Eq. 2.34), is an inappropriate choice as a bias parameter in constrained sampling simulations such as umbrella sampling. The outline of the argument is as follows:

We identify the correlation between  $Q_6$  and the total number of crystalline particles from unconstrained simulations in the liquid state. Crystalline particles are as defined in Sec. 2.6.1. We then investigate how this correlation breaks down upon the imposition of bias potentials constraining  $Q_6$ . In order to understand the manner in which this correlation breaks down, we characterise the configurations sampled with and without bias. We find significant differences in the size and type of crystalline clusters sampled in the two cases. These differences help explain the discrepancy between free energy reconstructions using  $Q_6$  and using  $n_{\max}$  (or  $n$ ). Finally, we test whether  $Q_6$  is a suitable order parameter when used in a kinetic reconstruction of the free energy (Sec. 2.7). We find that the results can be shown to be consistent with results obtained using  $n_{\max}$ , however,  $Q_6$  is not an ideal choice, as will be discussed in more detail. We first identify non-crystallising runs at  $T = 1070\text{K}$ , at  $P = 0\text{ GPa}$  for two system sizes,  $N = 512, 4000$ . Molecular dynamics simulations at

this state point show this to be in the HDL regime with the relaxation time being much smaller than typical crystallisation times [2]. However, free energy studies using  $Q_6$  suggest that the liquid spontaneously crystallises at this state point [30]. This is therefore an ideal case for the purpose of comparison. We also consider  $T = 1055\text{K}$  at  $P = 0$  GPa. We characterise the liquid to the best of our ability, shown in Fig. 4.1, taking note of the typical  $Q_6$  for the liquid, and as well the total number of crystalline particles,  $n_{\text{tot}}$ , and the largest crystalline cluster size,  $n_{\text{max}}$ .

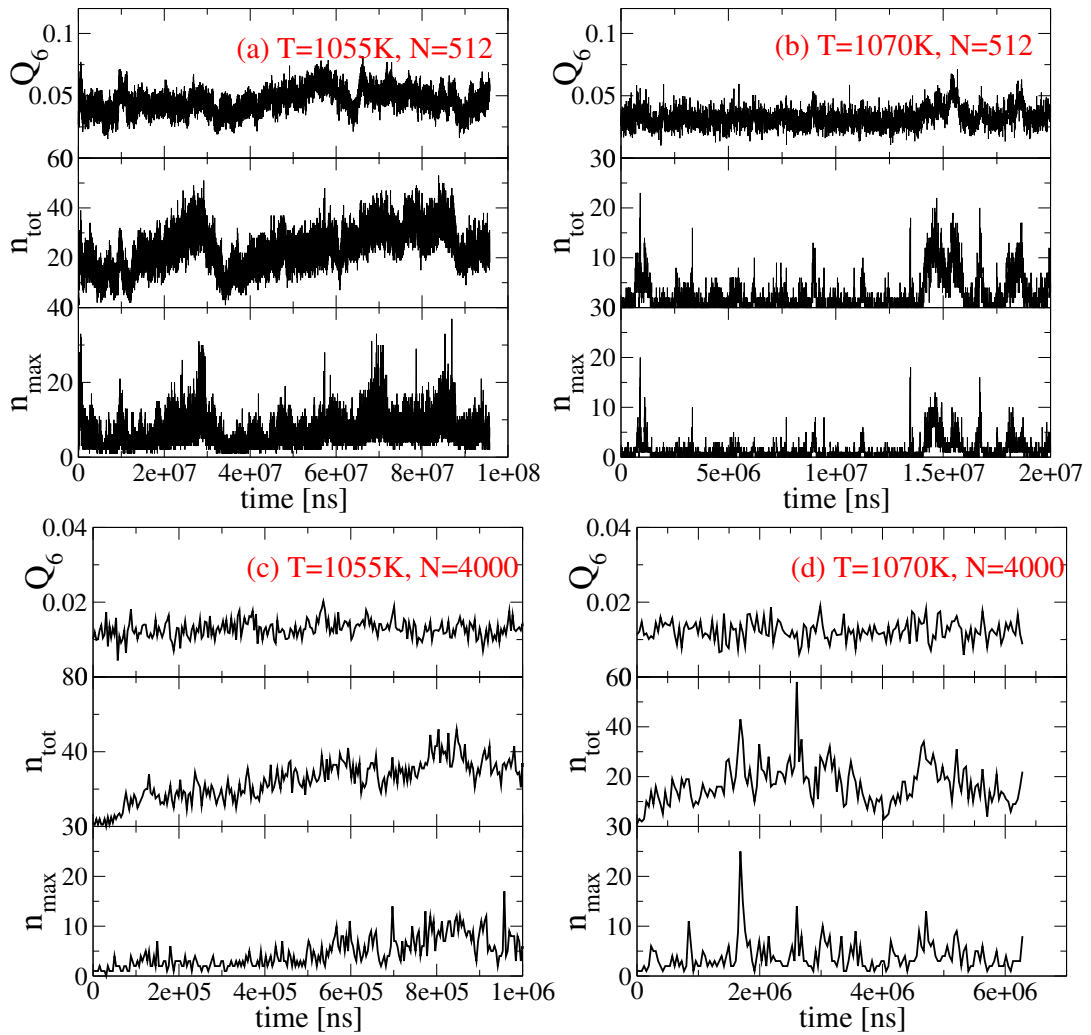


Figure 4.1: We consider non-crystallising trajectories at  $T = 1055\text{K}$ ,  $1070\text{K}$  at two system sizes,  $N = 512, 4000$  at  $P = 0$  GPa. These trajectory segments are used to characterise the typical distribution of  $Q_6$  and of cluster sizes for the corresponding liquid. It should be noted that for  $N = 4000$ , obtaining a long non-crystallising trajectory is difficult - we choose apparently suitable candidates.

### 4.1.1 $Q_6$ bias does not constrain the degree of crystallinity

We show that while in the unbiased case,  $Q_6$  and  $n_{\text{tot}}$  are correlated at two temperatures and two system sizes, when a bias is applied on  $Q_6$ , this correlation breaks down and the system can explore large  $n_{\text{max}}$  and  $n_{\text{tot}}$  values for demonstrably liquid-like  $Q_6$  values. We begin by evaluating the typical  $Q_6$  distribution for the liquid at a high temperature where the liquid is disordered at two system sizes. We choose an appropriate bias minimum  $Q_6^0$  that is within this distribution (see Fig. 4.2) and bias our simulations to study how the degree of crystallinity is affected by the presence of the bias on  $Q_6$ . One finds that in the absence of any constraints,

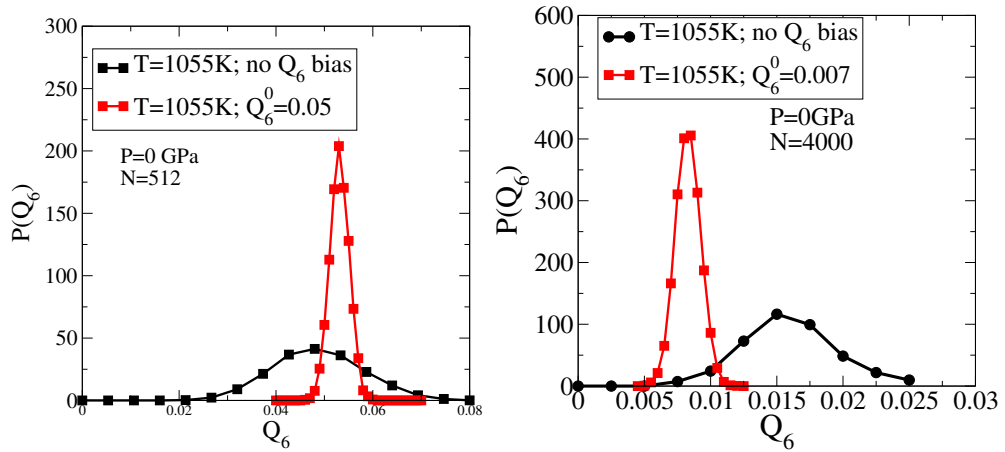


Figure 4.2: We compare the distribution of  $Q_6$  values for the liquid from unbiased MD runs with the distribution from biased USMC runs with the bias minimum at  $Q_6^0$  as shown. The spring constants for the harmonic bias potential were  $K_{Q_6} = 10000$  for  $N = 512$  and  $K_{Q_6} = 40000$  for  $N = 4000$ . The constrained MC runs were of  $6 \times 10^7$  MC steps. The initial  $4 \times 10^7$  MC steps were omitted as transient to equilibrate in the bias potential. These values of  $Q_6^0$  are used hereafter.

$Q_6$  and  $n_{\text{max}}$  are correlated as shown by the negative log of bivariate  $P(Q_6, n_{\text{max}})$  in Fig. 4.3. This correlation breaks down under the application of an umbrella bias on  $Q_6$ . The data in Fig. 4.3 are from unconstrained, crystallising MD simulations of  $N = 512$  particles in the NPT MD ensemble at  $P = 0$  GPa. Under application of a harmonic bias on  $Q_6$  this sampling probability changes drastically, with no correlation apparent, as shown in Fig. 4.4. In Fig. 4.5 we find that the largest cluster size distribution is qualitatively different and also that a constraint on  $n_{\text{max}}$  does not produce as large variability in  $Q_6$  as the bias on  $Q_6$  does on  $n_{\text{max}}$ .

In Fig. 4.6 we observe the  $n_{\text{tot}}$  vs  $Q_6$  correspondence showing a similar breakdown in correlation. In Fig. 4.7, we observe a similar breakdown in correlation under application of bias for a system size of  $N = 4000$ .



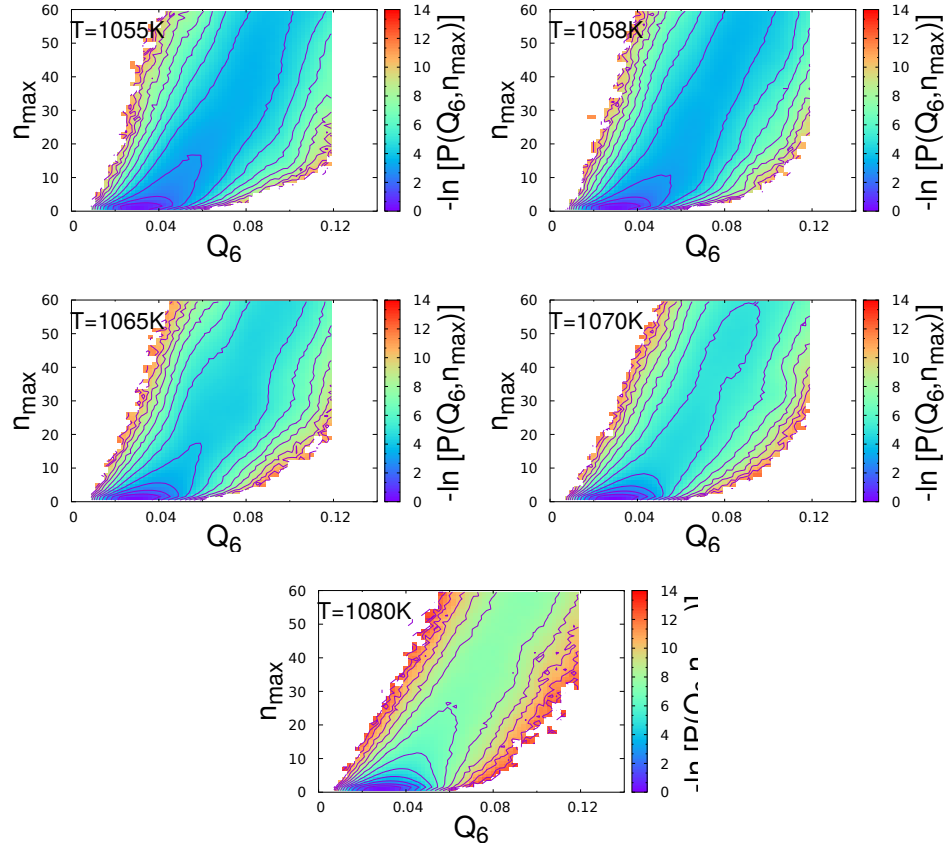


Figure 4.3: The negative log of the steady state  $P_{st}(Q_6, n_{\max})$  is shown here from the set of crystallising trajectories for 5 temperatures at  $P = 0$  GPa. Data is from 600 independent NPT MD simulations of  $N = 512$  particles. Each trajectory starts in a disordered configuration with  $n_{\max} = 0$  and proceeds till an absorbing boundary of  $n_{\max} = 100$  is reached.  $n_{\max}$  and  $Q_6$  are found to be correlated, with the most probable  $n_{\max}$  for a given  $Q_6$  increasing with  $Q_6$ . However, the low  $Q_6$  values of  $Q_6 = 0.03, 0.04$  still map to a large range of values of  $n_{\max}$  particularly at the low temperature.

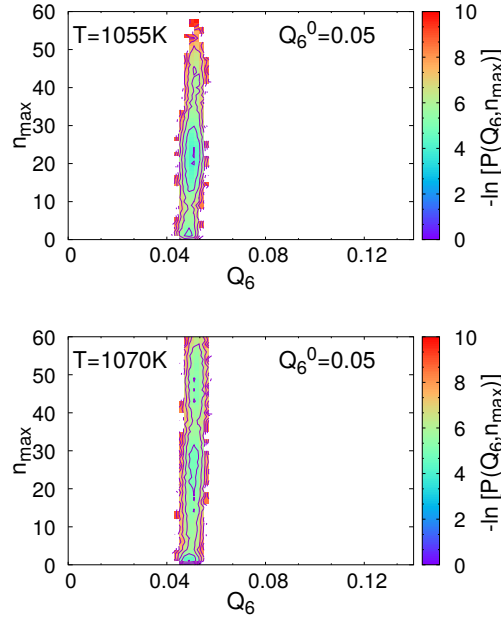


Figure 4.4:  $Q_6$  bias is applied at  $Q_6^0 = 0.05$ ,  $k_{Q_6} = 10^4\epsilon$  for  $N = 512$  particles at  $T = 1055\text{K}$  (*Top*) and  $T = 1070\text{K}$  (*Bottom*). Colourmap represents  $\ln(P(Q_6, n_{\max}))$  – red regions are frequently sampled.

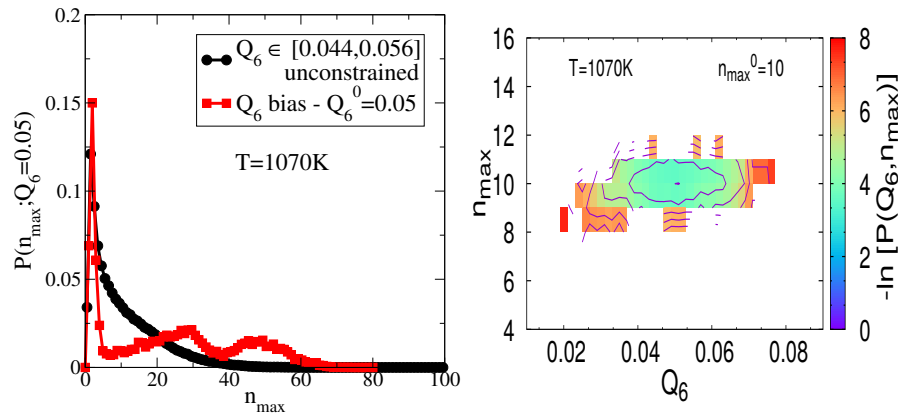


Figure 4.5: (*Left:*) Slice of  $P(n_{\max}; Q_6 = 0.05)$  compared for the unconstrained case vs the case of a constraint on  $Q_6$  at  $Q_6^0 = 0.05$ . In the former, this is done by taking a slice along  $Q_6 \in [0.044, 0.056]$  and plotting  $P(n_{\max})$  vs  $n_{\max}$ . Correlation breaks down upon application of bias on  $Q_6$  – all values of  $n_{\max}$  are nearly equiprobable for the same window of  $Q_6$  values when  $Q_6$  bias is applied. (*Right:*) A heat map showing the probability of sampling different  $Q_6, n_{\max}$  values when a harmonic bias is applied on  $n_{\max}$  at  $n_{\max} = 10$ .

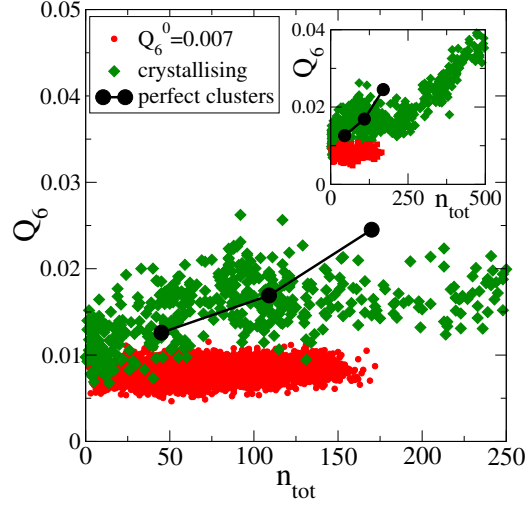


Figure 4.6: We look at  $Q_6$  vs  $n_{\text{tot}}$  for freely crystallising MD runs at  $T = 1055\text{K}$ ,  $N = 4000$  and for constrained MCUS runs at  $T = 1055\text{K}$ ,  $N = 4000$  of  $2 \times 10^7$  MC steps with a bias minimum at  $Q_6^0 = 0.007$  and spring constant  $K_{Q_6} = 40000$ . We also compare the dependence of  $Q_6$  on the degree of crystallinity,  $n_{\text{tot}}$ , when a pure crystal ( $T = 0\text{K}$ ) of given size is inserted in a bath of randomly placed liquid particles without overlap.

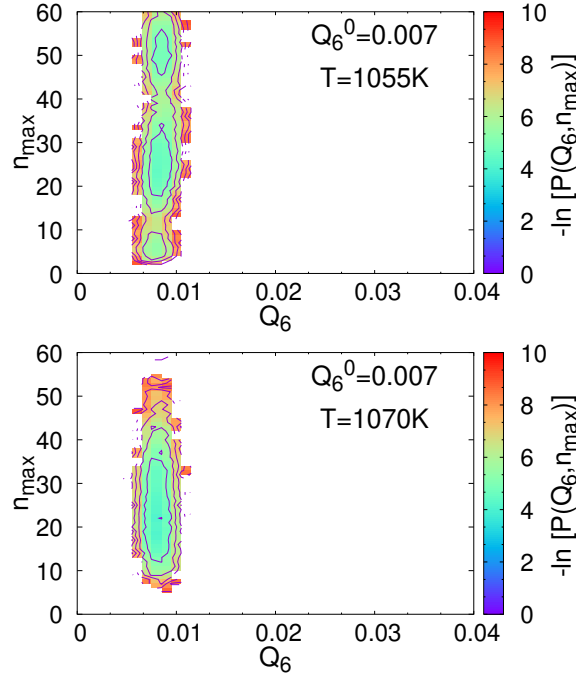


Figure 4.7: To understand the typical  $n_{\text{tot}}$  values that are sampled under the application of  $Q_6$  constraint. For  $N = 4000$ , with a  $Q_6^0 = 0.007$ ,  $K_{Q_6} = 40000$ , we look at the probability distribution  $P(Q_6, n_{\text{tot}})$  at two temperatures,  $T = 1055\text{K}$  (*Top*) and  $T = 1070\text{K}$  (*Bottom*).

### 4.1.2 Configurations sampled under $Q_6$ bias have higher degree of polycrystallinity

We attempt to understand how the configurations with a large degree of crystallinity (read large  $n_{\text{tot}}$  or  $n_{\text{max}}$ ) have a low  $Q_6$ . To do this, we first consider an array of 100 unit cells of the diamond cubic lattice, spaced far apart such that no neighbours are shared across unit cells. We rotate a fraction of these unit cells by an arbitrary angle and calculate the average global  $Q_6$  from a number of realisations of rotations of the given fraction. In Fig. 4.8, we observe the effect on global  $Q_6$  of varying the fraction of rotated unit cells. As the rotated fraction increases,  $Q_6$  decreases, despite all the particles being crystalline based on their neighbourhoods.

Having determined that crystalline clusters placed such that they are rotated with

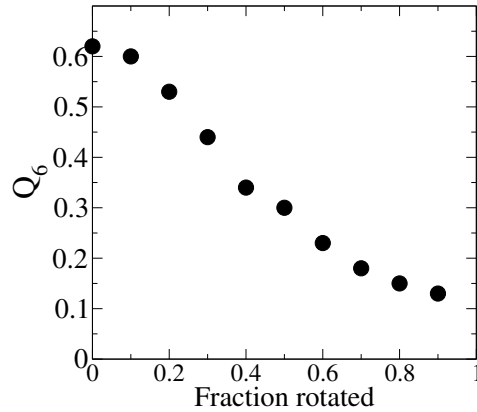


Figure 4.8: Average global  $Q_6$  from a number of realisations where a fraction of well-spaced diamond cubic unit cells are rotated about the  $y$  – axis through an arbitrarily chosen angle. The cosine of the angles sample a uniform distribution  $\in [-1, 1]$ . When no unit cells are rotated, the global  $Q_6$  is that of the diamond cubic structure. The global  $Q_6$  falls as a larger fraction is rotated. Note that the total degree of crystallinity stays constant throughout.

respect to each other (crystallites) have lower global  $Q_6$  even when not sharing an interface, we discuss how to identify such crystallites from configurations generated in MC or MD trajectories. Note that the clusters identified using the Frenkel criterion [46, 82], used also by Romano *et al* [96] and Ricci *et al* [30], do not consider the orientation of the unit cell when constructing clusters of crystalline particles, considering instead only the separation between the particles. This algorithm identifies the **grain boundaries** between misoriented crystallites. We describe the algorithm below:

### Algorithm to identify crystallites

1. Identify all crystalline particles of the system, as identified in Sec. 2.6.2.
2. Choose a random crystalline particle as the seed particle  $s$ .
3. Store the positions of its nearest neighbours as a template centred on the seed particle. An external reference frame needs to be used.
4. Proceed through the graph of nearest neighbour connected atoms – beginning with the nearest neighbours of  $s$ . For each such atom, which we label  $v$ , compare the positions of  $v$ 's neighbours with the template for  $s$  as described below. We label neighbours of a particle  $v$  as  $\{n(v)\}$
5. The comparison is carried out by measuring the root mean squared deviation of the positions of  $\{n(v)\}$  from the positions of  $\{n(s)\}$ . One should note that depending on how the neighbours are labelled, one obtains different values. There is no meaningful “corresponding” member of  $\{n(v)\}$  for each member of  $\{n(s)\}$ . We identify the combination that minimises the root mean square distance and use that minimum value. The form is detailed below.
6. For member  $i$  of  $\{n(v)\}$  and member  $j$  of  $\{n(s)\}$ , calculate  $(r_{iv} - r_{js})^2$ . Do for each  $i$  and  $j$  and find the average. Consider Fig. 4.9, where the nearest neighbour positions of a hypothetical particle  $v$  (red) are superposed on the nearest neighbour positions of  $s$  (blue). The green thick lines represent the distances that are calculated, for the minimum root-mean-squared distance:

$$d_v^{RMS} = \min \left( \frac{1}{2} \sqrt{\sum_i \sum_j (\mathbf{r}_{iv} - \mathbf{r}_{js})^2} \right) \quad (4.1)$$

7. If the deviation,  $d_v^{RMS}$ , is greater than some tolerance, the current atom is not of the same lattice as the original seed (but still is crystalline).

- Here one needs to take care to compare the neighbourhood of  $j$  with both the template as well as the template rotated through an angle of  $\pi/4$  about an axis connecting the mid-points of any two mutually exclusive pairs of atoms. This is because the diamond cubic lattice consists of alternating “upward” and “downward” tetrahedra. If this is not accounted for, alternate atoms of the diamond cubic lattice, in the sense of number of connections away from  $s$ , will have a high  $d_v^{RMS}$ . (see Fig. 4.11).

- In Fig. 4.12 we observe that “upward” and “downward” facing tetrahedra differ by a rotation of 90 degrees around any axis passing through the centre and one of the corners. In Fig. 4.13 we observe that this mapping is preserved even if a global rotation of reference frame is performed.

- Since the axis is oriented at an arbitrary set of angles  $(\theta, \phi)$ , quaternion rotations are best suited to describe the process simply. We identify the transformation required to rotate a vector  $\mathbf{v}$  an angle  $\theta$  about an axis  $\mathbf{u}$ . The following equation is used [243]:

$$L_q(\mathbf{v}) = \cos\theta.\mathbf{v} + (1 - \cos\theta)(\mathbf{u}\cdot\mathbf{v})\hat{\mathbf{u}} + \sin\theta.(\hat{\mathbf{u}} \times \mathbf{v}) \quad (4.2)$$

8. Once a deviant particle is identified in step 7, backtrack one edge/step on the graph connecting the current particle  $v$  to the seed  $s$ , and try a different neighbour.
9. Once backtracking has brought us back to the seed and all neighbours of the seed are visited, i.e., all boundaries of current cluster identified, find another seed, i.e, step 2. All the traversed atoms for which  $d_v^{RMS}$  is small belong to the same “crystallite”.
10. Proceed through steps 3-8 with the new seed. This should omit all atoms already identified with another crystallite, but one can check explicitly as a test.

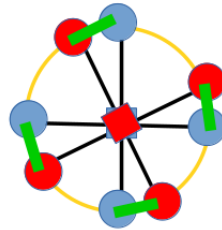


Figure 4.9: A schematic showing the positions of the four neighbours of a particle  $v$  (red), superposed on the template for the seed  $s$  (blue). The green solid segments represent the contributions to  $d_v^{RMS}$ , based on the combination that minimizes  $d_v^{RMS}$ . The central particles are represented by squares to indicate the orientation of their respective lattices.

In 2D one can get an idea of what this algorithm achieves from the application to Fig. 4.10.

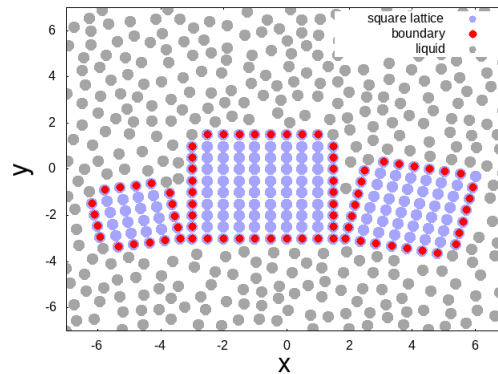


Figure 4.10: The algorithm to identify grain boundaries applied to a toy 2D case. The blue particles are bulk solid, having at least 3 neighbours in lattice positions, and the red particles are marked boundary. The grey particles are randomly placed imitating “liquid”. A connectivity criterion based on inter-particle distances would label all three square lattice box as one large cluster because of the connection at the bottom. The boundaries identified allow us to resolve the block into three misoriented crystallites. Note that the corner particles will not be identified as bulk crystalline because only two of their neighbours have lattice positions.

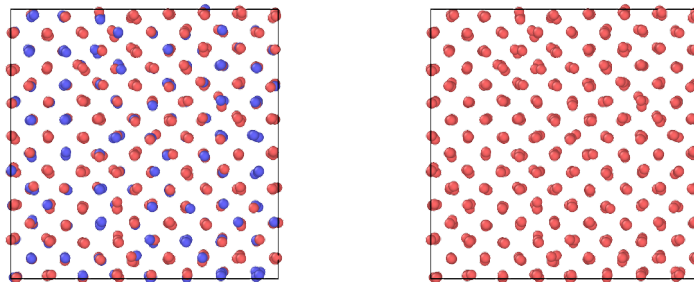


Figure 4.11: Left panel shows the identification of atoms with “upward” (red) and “downward” (blue) facing tetrahedrally arranged neighbours. Right panel shows the actual largest cluster of crystalline atoms. Image is a snapshot of an NPT MC simulation of SW Si starting from diamond cubic and simulated at  $T=1260\text{K}$ .

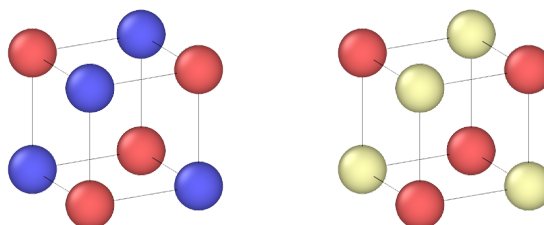


Figure 4.12: Consider a tetrahedron centered at the origin (red balls - left panel). The neighbours are situated at alternate corners of a regular cube. The corresponding “downward” tetrahedron sites are occupied by the blue balls (left panel). In the right panel, the white balls show the effect of rotating the positions of the red balls by 90 degrees around any axis as defined in the procedure above.

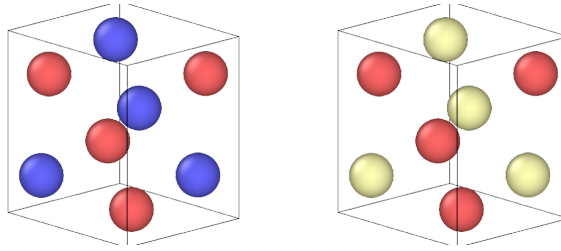


Figure 4.13: Consider a tetrahedron centered at the origin (red balls - left panel). The neighbours are situated at alternate corners of a regular cube. The corresponding “downward” tetrahedron sites are occupied by the blue balls (left panel). In the right panel, the white balls show the effect of rotating the positions of the red balls by 90 degrees around any axis as defined in the procedure above. Here, the original tetrahedron (red balls - left panel) have been rotated by 60 degrees around the z-axis and then by 60 degrees around the x-axis to demonstrate that the method is robust to any possible initial orientation of the tetrahedron to be rotated.

### Cluster size and crystallite size distributions

In Fig. 4.14 and Fig. 4.15 the distribution of clusters and crystallites are shown for unbiased simulations and for simulations where  $Q_6$  is constrained. Simulations are performed at  $T = 1055K, T = 1070K, P = 0$  GPa at two system sizes of  $N = 512$  and  $N = 4000$ . The choice of bias centering of  $Q_6$  is based on Fig. 4.2. The unconstrained simulations are characterised by configurations with comparable cluster size and crystallite size distributions. However, when a bias is applied on  $Q_6$ , the system samples configurations with larger clusters, but which are made of smaller crystallites. The resultant configurations have a low global  $Q_6$  as constrained by the bias. These results are shown in Fig. 4.14 and Fig. 4.15.



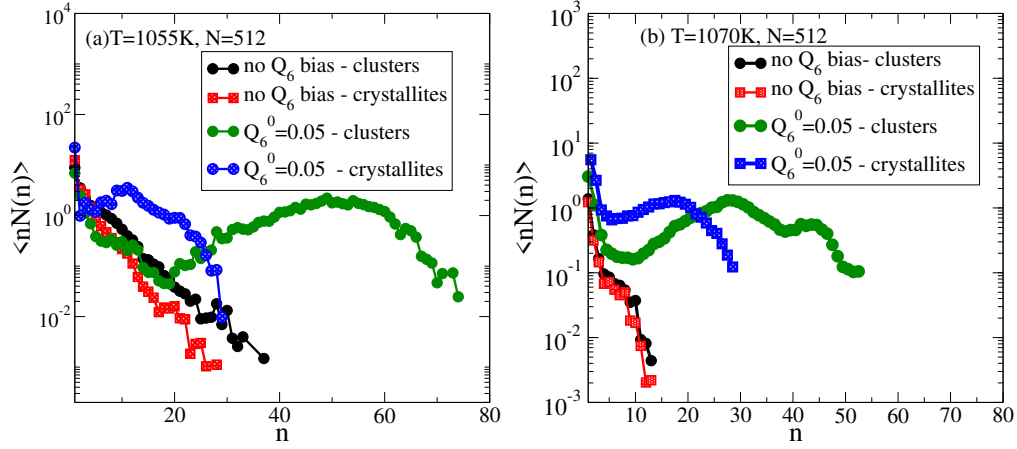


Figure 4.14: We compare the number of crystalline clusters of a given size,  $n$ , and of crystallites of size  $n$  for  $N = 512$  at two temperatures,  $T = 1055\text{K}$  and  $T = 1070\text{K}$  for both unconstrained liquid configurations (see Fig. 4.1) and for configurations from a biased ensemble with  $Q_6^0 = 0.05$  and  $K_{Q_6} = 10000$ . The comparison is made with the mass-weighted distribution of the sizes. We see that the number of large clusters is significantly higher under the application of bias. Moreover, we see a bigger separation between the largest cluster size and the largest crystallite size, suggesting that the large clusters are composed of smaller crystallites sharing an interface.

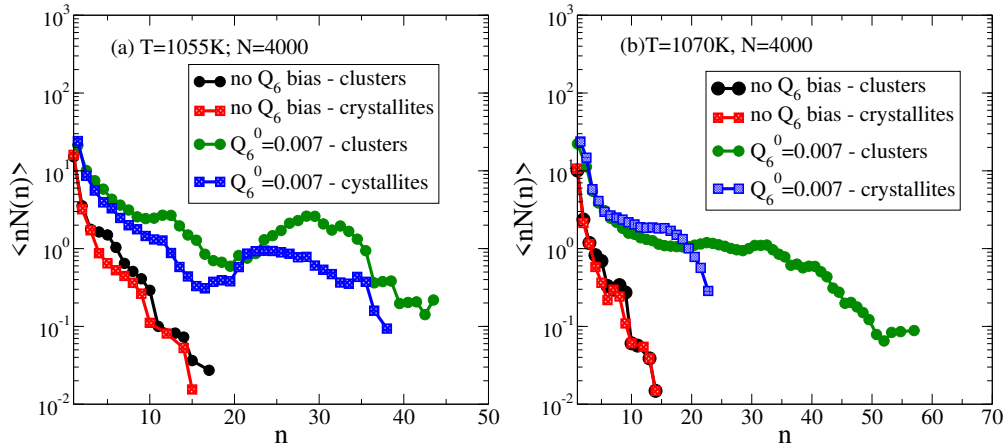


Figure 4.15: We compare the number of crystalline clusters of a given size,  $n$ , and of crystallites of size  $n$  for  $N = 4000$  at two temperatures,  $T = 1055\text{K}$  and  $T = 1070\text{K}$  for both unconstrained liquid configurations (see Fig. 4.1) and for configurations from a biased ensemble with  $Q_6^0 = 0.007$  and  $K_{Q_6} = 40000$ . The comparison is made with the mass-weighted distribution of the sizes. We see that the number of large clusters is significantly higher under the application of bias. Moreover, we see a bigger separation between the largest cluster size and the largest crystallite size, suggesting that the large clusters are composed of smaller crystallites sharing an interface.

### 4.1.3 Kinetic reconstruction of free energy as a function of $Q_6$ )

The free energy from the cluster size distribution ( $\beta\Delta G(n_{\max})$ ) is found in Chapter 3 to display a barrier to the growth of crystalline clusters at all the temperatures studied along  $P = 0$  GPa, with quantitatively consistent results when using either umbrella sampling or the kinetic reconstruction from unconstrained MD runs. Umbrella sampling runs using  $Q_6$  as the bias parameter show crystallisation to be spontaneous for  $T \leq 1070\text{K}$  at  $P = 0$  GPa [30].

The question arises, is the free energy produced from unconstrained runs, expressed as a function of  $Q_6$  ( $\beta\Delta G_{MFPT}(Q_6)$ ), similarly consistent with umbrella sampling results ( $\beta\Delta G_{US}(Q_6)$ )? Thereafter, we check if the free energy as a function of  $Q_6$  from the MFPT reconstruction is consistent with the free energy as a function of  $n$  (or  $n_{\max}$ ), by performing a mapping between order parameters. Ultimately, is there an issue with  $Q_6$  as an order parameter, and if yes, are these issues confined to the use of bias potentials? Finally, which order parameter best describes the transformation to the crystalline state? We perform a kinetic reconstruction with  $Q_6$  as the order parameter and measured the barrier, if any, to crystallisation. We then attempt to compare these results with the  $n_{\max}$  results with an appropriate variable transformation.

#### Kinetic reconstruction procedure

$\beta\Delta G(Q_6)$  is obtained through a kinetic reconstruction of the free energy (see Sec. 2.7) from unconstrained molecular dynamics simulations. 600 NPT MD trajectories of  $N = 512$  particles are simulated at  $P = 0$  GPa at a range of temperatures and allowed to crystallise. Trajectories are extended till an absorbing boundary condition of  $Q_6 = 0.12$  is reached –  $P_{st}(Q_6)$  and  $\tau_{MFPT}(Q_6)$  are constructed from the trajectories. Data is gathered starting from the first time at which  $Q_6 \in [0.029, 0.031]$  for each trajectory to construct the free energy using the MFPT method. This choice is made because the typical  $Q_6$  for the liquid is 0.03.  $Q_6$  bin width is set at 0.002. An important point is that short timescale fluctuations in  $Q_6$  may be larger than this value, however, the ideal choice of bin size should also provide resolution, hence a tradeoff. At each temperature, a number  $< 5\%$  of the trajectories do not reach  $Q_6 = 0.12$  (or  $Q_6 = 0.1$ ) and are therefore discarded

entirely. The longest trajectories are 285 *ns* long. In Fig. 4.16, the mean first passage time, the steady state probability and the reconstructed free energy profile are shown as a function of  $Q_6$ . The striking observation is that there is a barrier along  $\beta\Delta G(Q_6)$  at  $T = 1070\text{K}$ . However, this barrier is smaller,  $\sim 2k_B T$ , than the barrier for  $\beta\Delta G(n_{\max})$ , which is  $\sim 10k_B T$ . We next discuss how to quantitatively compare the two.

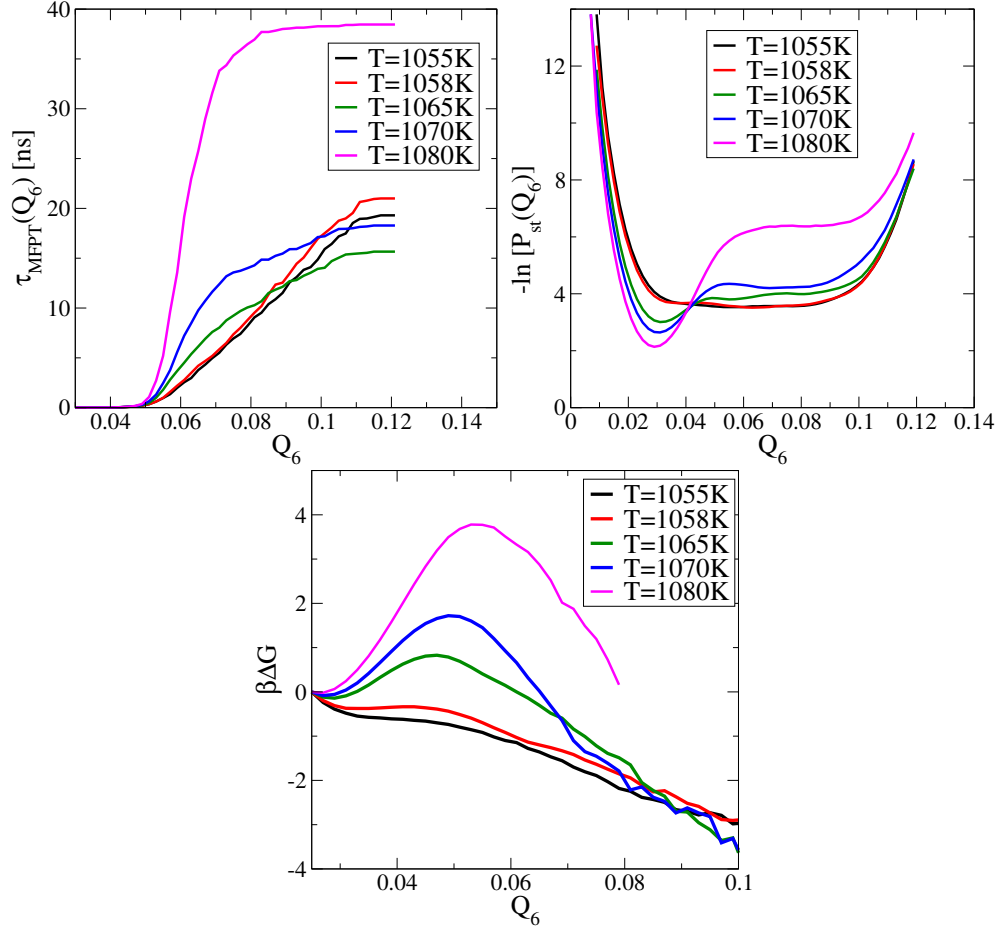


Figure 4.16: The MFPT,  $\tau_{MFPT}(Q_6)$  and the steady state probability  $P_{st}(Q_6)$  are shown.  $Q_6 < 0.02$  is almost never sampled with the probability decreasing rapidly for  $Q_6 < 0.03$ . At high temperature,  $T \geq 1070\text{K}$ ,  $\tau_{MFPT}(Q_6)$  has a sigmoidal nature which is not evident at lower temperatures. A reference of  $\beta\Delta G(Q_6 = 0.03) = 0$  is used. The free energy  $\beta\Delta G(Q_6)$  does not show a barrier for  $T < 1065\text{K}$ .

### Consistency between $\beta\Delta G(Q_6)$ and $\beta\Delta G(n_{\max})$

The question that arises here is whether  $\beta\Delta G(Q_6)$  and  $\beta\Delta G(n_{\max})$  are consistent. A comparison between  $\beta\Delta G(n_{\max})$  and  $\beta\Delta G(Q_6)$  requires a mapping between the

two order parameters. We consider the set of possible  $n_{\max}$  values for a given  $Q_6$ . This is described as the conditional probability at steady state,  $P_{st}(n_{\max}; Q_6)$ , represented by a slice of constant  $Q_6$  in the bivariate distribution  $P_{st}(n_{\max}, Q_6)$ .

Of specific interest are two parametric dependences, the average  $n_{\max}$  for a given  $Q_6$ , the average  $Q_6$  for a given  $n_{\max}$  and the corresponding values at first passage. The latter are obtained by noting the values of  $n_{\max}(Q_6)$  when a trajectory first attains a given  $Q_6$  ( $n_{\max}$ ). This is then averaged over the set of trajectories.

In order to quantitatively compare  $\beta\Delta G(Q_6)$  and  $\beta\Delta G(n_{\max})$  we consider the following relation, which can be used generally to relate distributions of different variables, but are written here considering the equilibrium sampling probabilities of  $Q_6$  and  $n_{\max}$ :

$$P_{eq}(Q_6)dQ_6 = P_{eq}(n_{\max})dn_{\max} \quad (4.3)$$

$$P_{eq}(Q_6) = P_{eq}(n_{\max}) \left| \frac{dn_{\max}}{dQ_6} \right| \quad (4.4)$$

$$-\ln(P_{eq}(Q_6)) = \beta\Delta G(Q_6) = \beta\Delta G(n_{\max}) - \ln \left[ \frac{dn_{\max}}{dQ_6} \right] \quad (4.5)$$

One can similarly write:

$$-\ln(P_{eq}(n_{\max})) = \beta\Delta G(n_{\max}) = \beta\Delta G(Q_6) - \ln \left[ \frac{dQ_6}{dn_{\max}} \right] \quad (4.6)$$

We attempt to identify the correct map between  $Q_6$  and  $n_{\max}$ . *A priori*, we can consider a few possibilities.

- We traverse through each trajectory and note at each point in time  $n_{\max}(t)$  for a corresponding  $Q_6(t)$ .
- $\langle n_{\max}(Q_6) \rangle$  is the average of the  $n_{\max}$  that corresponds to a given  $Q_6$  aggregated over all trajectories (see Fig. 4.17).
- We also do the reverse, computing  $\langle Q_6(n_{\max}) \rangle$ , the average  $Q_6$  that corresponds to a given  $n_{\max}$  (see Fig. 4.17).
- Finally, we store the  $n_{\max}$  value at the time of first passage to a given  $Q_6$ , averaged over all trajectories. This is denoted  $n_{\max}^{FP}(Q_6)$  (see Fig. 4.18).
- The corresponding reverse quantity is  $Q_6^{FP}(n_{\max})$ , the value of  $Q_6$  at the time of first passage to that  $n_{\max}$  value (see Fig. 4.18).

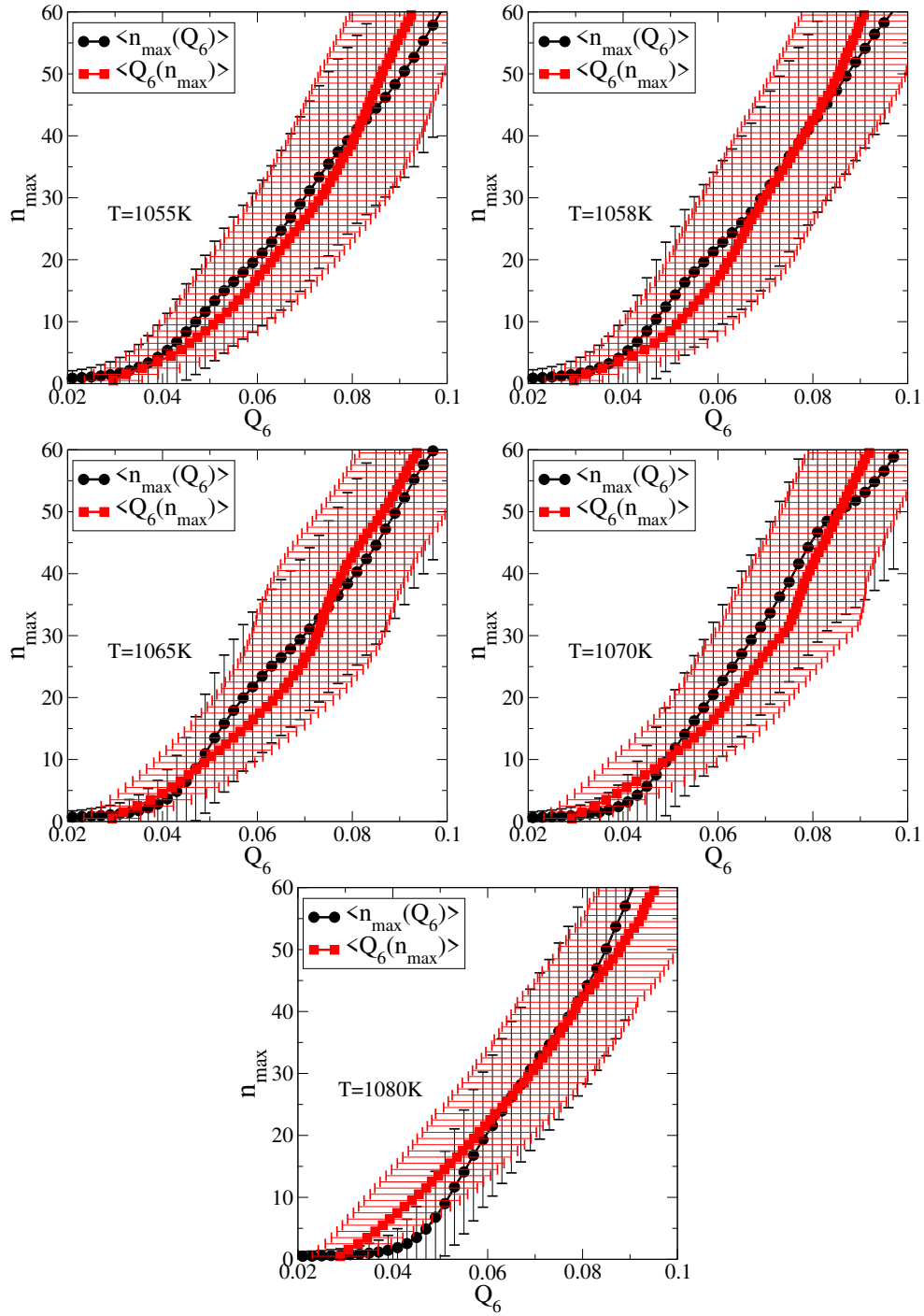


Figure 4.17: The average  $n_{\max}$  for a given  $Q_6$  and the average  $Q_6$  for a given  $n_{\max}$  are shown here. Error bars represent the standard deviation.  $\langle Q_6(n_{\max}) \rangle$  shows a larger standard deviation for small  $Q_6$  or  $n_{\max}$  than  $\langle n_{\max}(Q_6) \rangle$ .

Based on the results in Fig. 4.17 and Fig. 4.18, one should use the average values rather than the first passage values. The average values are subject to less noise, as evidenced by the error bars in both cases.  $\beta\Delta G(n_{\max})$  can be mapped to compare

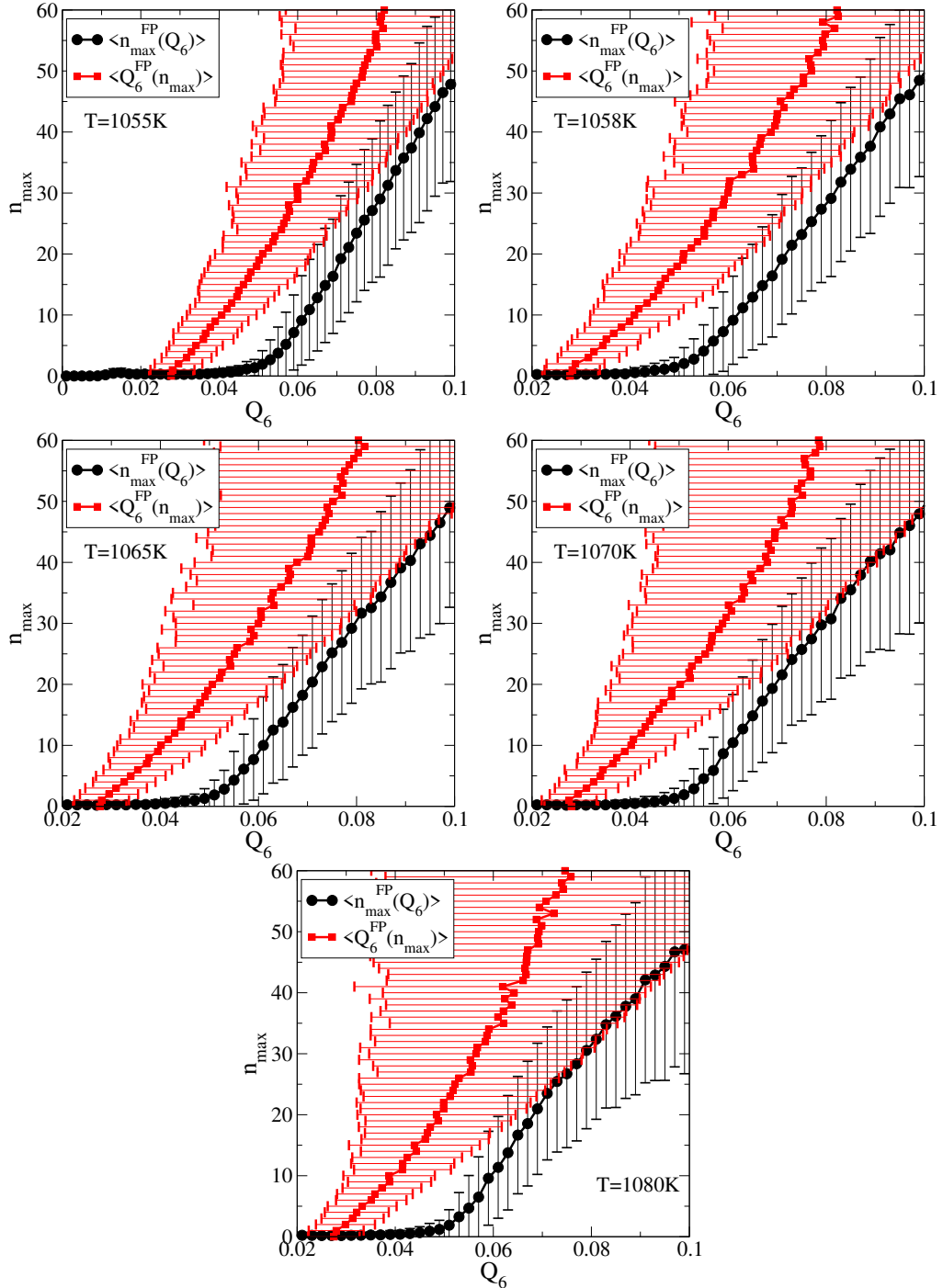


Figure 4.18: Error bars represent the standard deviations.  $n_{\max}^{FP}(Q_6)$  does not grow till  $Q_6 \geq 0.05$ .  $Q_6^{FP}(n_{\max})$  grows linearly with  $n_{\max}$  but shows larger deviations. The typical  $n_{\max}$  for a given  $Q_6$ , at first passage of that value of  $Q_6$ , is lower than the average  $n_{\max}$  for the same  $Q_6$ . The  $Q_6$  at first passage for a given  $n_{\max}$  is higher than the average  $Q_6$  for a given  $n_{\max}$ . A change in slope of  $n_{\max}^{FP}(Q_6)$  is observed at all temperatures.

directly with  $\beta\Delta G(Q_6)$  using the parametric dependence between  $n_{\max}$  and  $Q_6$  in two ways. The first is using  $\langle n_{\max}(Q_6) \rangle$  and the other using  $\langle Q_6(n_{\max}) \rangle$ . This is because the two parametric dependences are found to be different, as shown in Fig. 4.17. We use this to check for consistency between  $\beta\Delta G_{MFPT}(Q_6)$  and  $\beta\Delta G(n_{\max})$ , shown in Fig. 4.19 and Fig. 4.20.

$$\beta\Delta G_{map}^{(n_{\max}(Q_6))}(Q_6) = \beta\Delta G(\langle n_{\max}(Q_6) \rangle) - \ln \left[ \frac{d\langle n_{\max}(Q_6) \rangle}{dQ_6} \right] \quad (4.7)$$

In Eq. 4.7 the free energy for a given  $Q_6$  is obtained from the free energy of the average  $n_{\max}$  corresponding to that value of  $Q_6$  and using the numerical derivative of  $\langle n_{\max}(Q_6) \rangle$  vs  $Q_6$ . When  $\langle n_{\max}(Q_6) \rangle$  gives a fractional value, we use a linear interpolation between the adjacent integer values of  $n_{\max}$ .

$$\beta\Delta G_{map}^{(Q_6(n_{\max}))}(Q_6) = \beta\Delta G(n_{\max}) - \ln \left[ \frac{1}{\frac{d\langle Q_6(n_{\max}) \rangle}{dn_{\max}}} \right] \quad (4.8)$$

In Eq. 4.8, we use  $\beta\Delta G(n_{\max})$  for a given  $n_{\max}$  to get the free energy of the corresponding  $\langle Q_6(n_{\max}) \rangle$ , the average  $Q_6$  corresponding to that  $n_{\max}$ . Results from the procedures of Eq. 4.7 and Eq. 4.8 are shown in Fig. 4.19. Across the conditions studied, the optimal procedure appears to be to use Eq. 4.7.

One can similarly obtain  $\beta\Delta G(n_{\max})$  from  $\beta\Delta G(Q_6)$  as shown in Fig. 4.20, using a similar set of equations, Eq. 4.9 and Eq. 4.10.

$$\beta\Delta G_{map}^{(Q_6(n_{\max}))}(n_{\max}) = \beta\Delta G(\langle Q_6(n_{\max}) \rangle) - \ln \left[ \frac{d\langle Q_6(n_{\max}) \rangle}{dn_{\max}} \right] \quad (4.9)$$

In Eq. 4.9 the free energy for a given  $n_{\max}$  is obtained from the free energy of the average  $Q_6$  corresponding to it, linearly interpolating between adjacent  $Q_6$  bins and calculating the numerical derivative of  $\langle Q_6(n_{\max}) \rangle$  vs  $n_{\max}$ .

$$\beta\Delta G_{map}^{(n_{\max}(Q_6))}(n_{\max}) = \beta\Delta G(Q_6) - \ln \left[ \frac{1}{\frac{d\langle n_{\max}(Q_6) \rangle}{dQ_6}} \right] \quad (4.10)$$

In Eq. 4.10 we use the free energy of a given  $Q_6$  to determine the free energy of the average  $n_{\max}$  corresponding to it. The derivative of  $\langle n_{\max}(Q_6) \rangle$  is determined numerically and inverted.

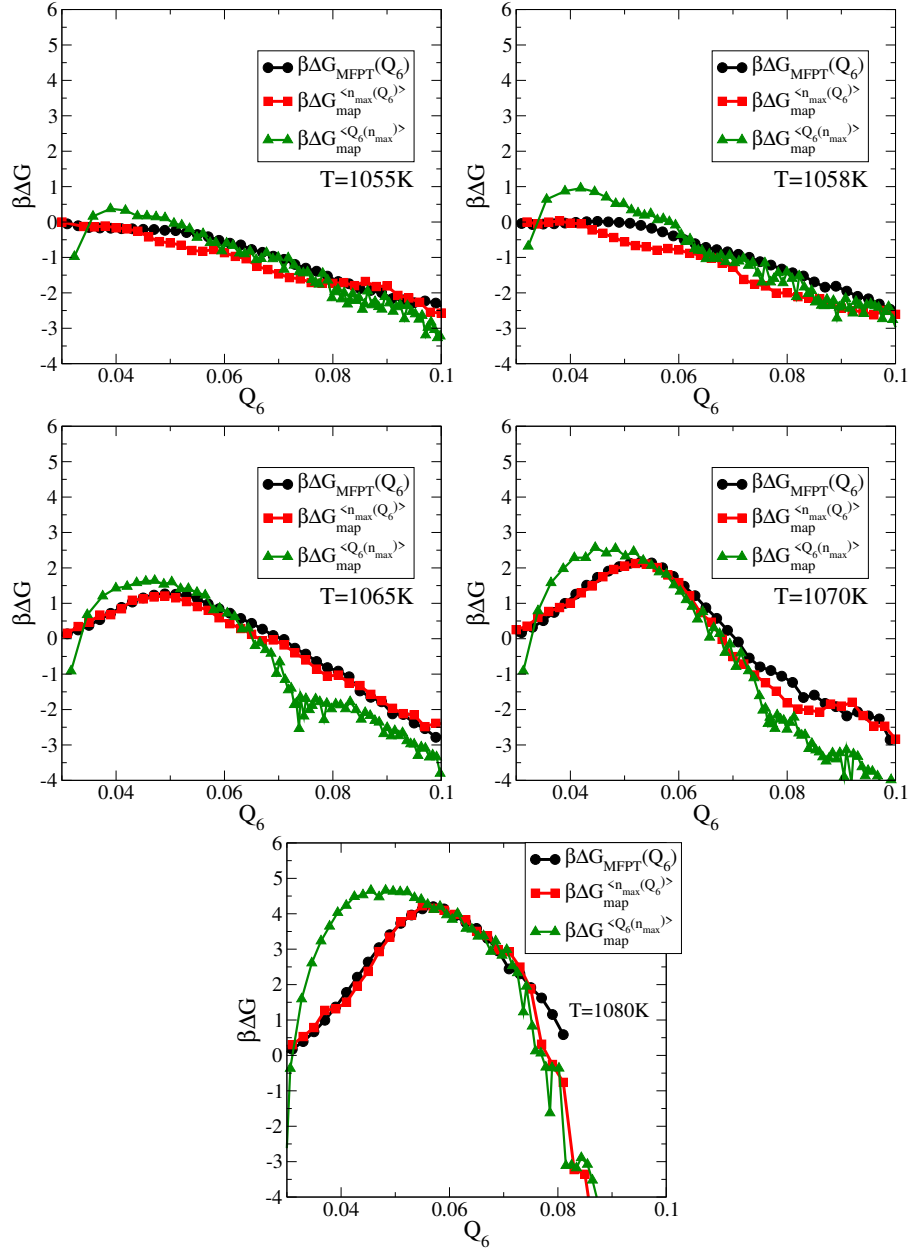


Figure 4.19: We numerically calculate the derivative  $dn_{\max}(Q_6)/dQ_6$  or  $dQ_6/dn_{\max}$  from each of the two parametric equations. We find that using  $\langle n_{\max}(Q_6) \rangle$  works better, in mapping  $\beta\Delta G(n_{\max})$  to  $\beta\Delta G(Q_6)$ . In calculating  $\beta\Delta G_{\text{map}}^{\langle n_{\max}(Q_6) \rangle}(Q_6)$ ,  $\beta\Delta G(\langle n_{\max}(Q_6) \rangle)$  is obtained by linearly interpolating  $\beta\Delta G(n_{\max})$  between the nearest integer values of  $\langle n_{\max} \rangle$ .



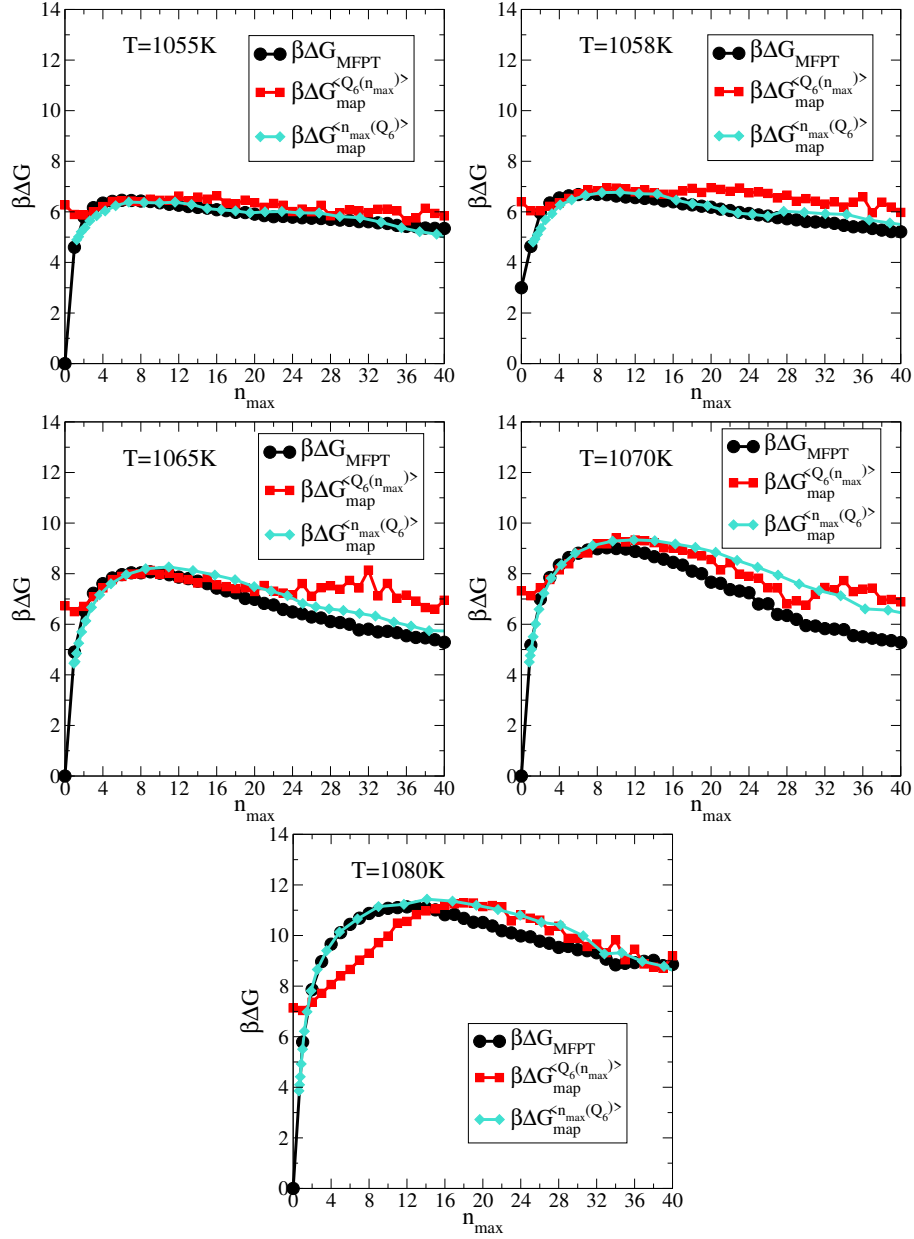


Figure 4.20: We numerically calculate the derivative  $dn_{\max}(Q_6)/dQ_6$  or  $dQ_6/dn_{\max}$  from each of the two parametric equations. We use  $\beta\Delta G(Q_6)$  to get  $\beta\Delta G_{\text{map}}(n_{\max})$ . In calculating  $\beta\Delta G_{\text{map}}^{<Q_6(n_{\max})>}(n_{\max})$ ,  $\beta\Delta G(<Q_6(n_{\max})>)$  is obtained by linearly interpolating  $\beta\Delta G(Q_6)$  between the nearest bins of  $Q_6$ . We find that using  $<n_{\max}(Q_6)>$  works better.

### Conclusion – mapping free energy through variable transformations

The errors at small  $n_{\max}$  for  $\langle n_{\max}(Q_6) \rangle$  give a better estimate of the derivative than other combinations. As a result, the mappings that work best (out of Eq. 4.7, Eq. 4.8, Eq. 4.9 and Eq. 4.10) are:

$$\beta\Delta G_{map}^{\langle n_{\max}(Q_6) \rangle}(Q_6) = \beta\Delta G(\langle n_{\max}(Q_6) \rangle) - \ln \left[ \frac{d\langle n_{\max}(Q_6) \rangle}{dQ_6} \right] \quad (4.11)$$

$$\beta\Delta G_{map}^{\langle n_{\max}(Q_6) \rangle}(n_{\max}) = \beta\Delta G(Q_6) - \ln \left[ \frac{1}{\frac{d\langle n_{\max}(Q_6) \rangle}{dQ_6}} \right] \quad (4.12)$$

This is apparent from the results of Fig. 4.19 and Fig. 4.20.

### Short time averages of trajectories

Trajectories represented in  $Q_6, n_{\max}$  space are averaged over a time window of  $10^6$  MD steps and overlaid on Fig. 4.3 to get Fig. 4.21. At the level of temporal coarse-graining used here, one finds that the degree of variability in  $Q_6$ - $n_{\max}$  mapping decreases. The majority of the trajectories pass through the central “tube” in Fig. 4.21. This suggests that the variability between  $Q_6$  and  $n_{\max}$  is a result of noise on a short timescale. Time averaging shows that typical trajectories pass through the “transition tube” one can identify in Fig. 4.3.

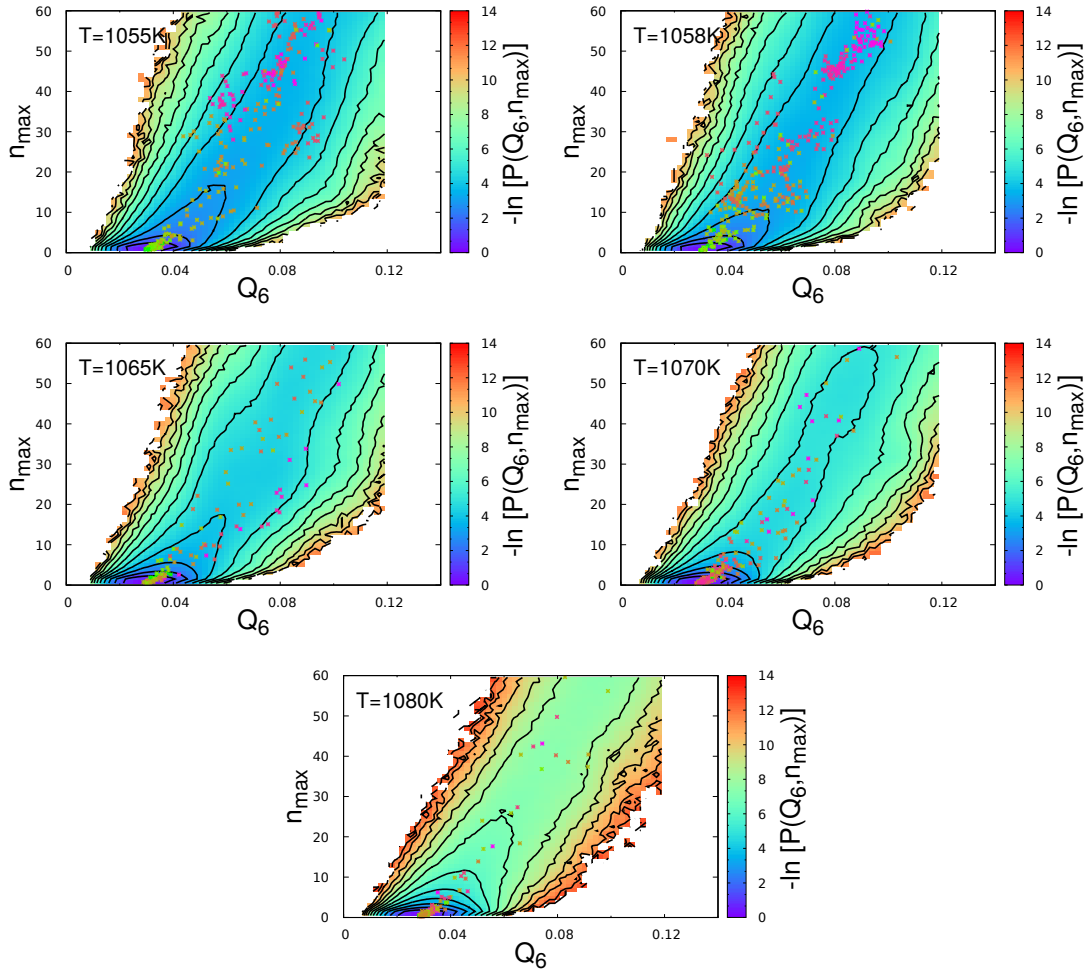


Figure 4.21: The negative log of the steady state  $P_{st}(Q_6, n_{\max})$  is shown here from a set of 10 crystallising trajectories for the lowest and the highest temperature, respectively. Short time averages of  $n_{\max}$  and of  $Q_6$  are taken over trajectory segments of  $1 \times 10^6$  MD steps ( 0.383 ns) and overlaid as a scatter. The green coloured points are from early stages of trajectories while the magenta points are from late stages of each trajectory.

#### 4.1.4 Umbrella sampling results with $Q_6$

We perform a free energy reconstruction from umbrella sampling simulations using  $Q_6$  as the order parameter. We compare with the results from kinetic reconstruction. This is done corresponding to the case of  $n_{\max}$  where we found qualitative agreement across the two methods. Results are shown in Fig. 4.23. Umbrella sampling runs with bias on  $Q_6$  show no free energy barrier at any of the temperatures where results using  $n$  or  $n_{\max}$  show a clear barrier. In Fig. 4.22, one observes that adjacent bias windows do not sample the same states. As a result, estimates from adjacent windows do not match in the way seen in Fig. 2.4. For example, simulations where  $Q_6$  is biased to be in the vicinity of the transition state value of  $Q_6^* = 0.05$  are shown to yield differing estimates of the dependence of  $\beta\Delta G(Q_6)$  for overlapping intervals of  $Q_6$ . This is a clear indication that the set of configurations being sampled by the differently biased NPT USMC simulations are different, despite their  $Q_6$  values being the same.

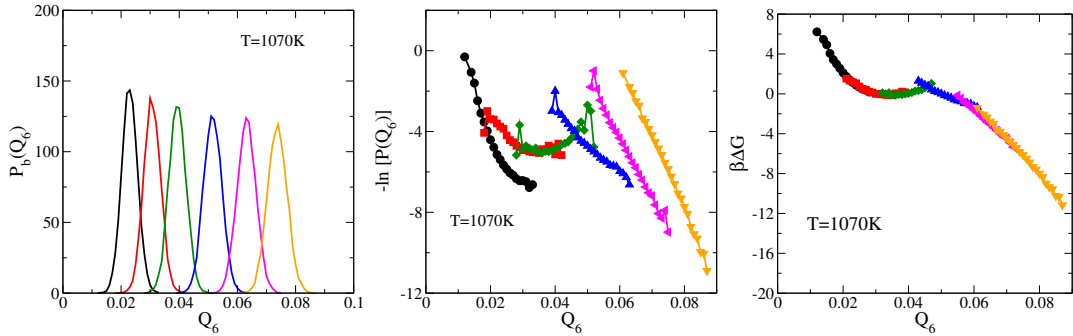


Figure 4.22: The raw histograms of  $Q_6$  under application of bias potential (*Left*), the negative log of the unbiased distributions (*Middle*) and the stitched free energy (*Right*) is shown at  $T = 1070K$ ,  $P = 0GPa$ . The 3 data points at either edge of each window are omitted in stitching the free energy.

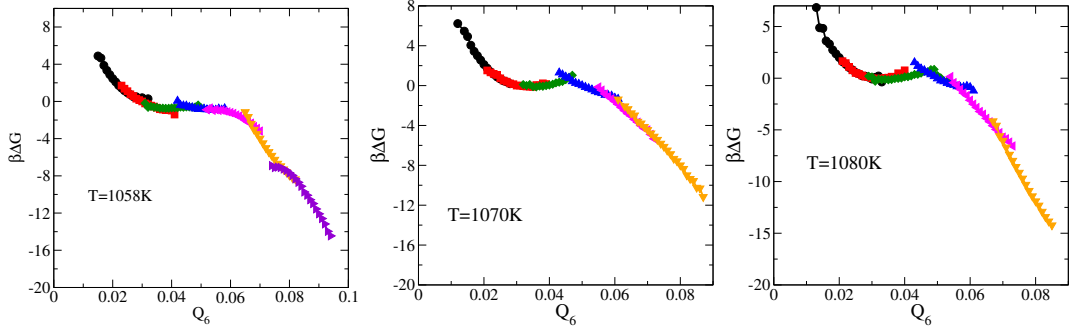


Figure 4.23: Free energy curves as a function of  $Q_6$  performed at 3 temperatures at  $P = 0$  GPa with  $N = 512$ . Equilibration is achieved by simulating for over  $1.5 \times 10^7$  MC steps and data generated over the next  $1.5 \times 10^7$  MC steps. Parallel tempering swaps occur every 5000 MC steps between adjacent temperatures and every 2000 MC steps between adjacent  $Q_6$  windows.  $K_{Q_6} = 4000\epsilon$ ,  $Q_6^0$  values are separated by 0.01. Auto-correlations decay to  $1/e$  for  $\rho$ ,  $Q_6$  and potential energy over a time-scale of  $5 \times 10^5$  MC steps to  $10^6$  MC steps.

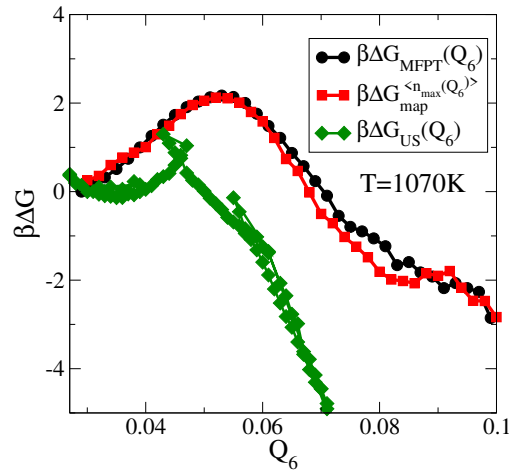


Figure 4.24: A comparison between the kinetic reconstruction using  $Q_6$ , umbrella sampling results for  $Q_6$ , and the mapping of kinetic reconstruction results from  $Q_6$  to  $n_{\max}$  using Eq. 4.12. The comparison is made at  $T = 1070\text{K}$ ,  $P = 0$  GPa for  $N = 512$  particles. The kinetic reconstruction results using  $n_{\max}$  can be mapped to those using  $Q_6$  to obtain agreement as shown. However, umbrella sampling results do not agree. As seen in Fig. 4.22, adjacent windows of  $Q_6$  bias do not match, and the sampling is therefore not correct.

## Summary

We find that in the straightforward case such as  $T = 1070\text{K}$ ,  $P = 0\text{ GPa}$  [2], a kinetic reconstruction of the free energy barrier to crystallisation gives finite barriers whether one uses  $Q_6$  or  $n_{\text{max}}$  or the full cluster distribution. A variable transformation that maps  $Q_6$  to  $n_{\text{max}}$  demonstrates that the results are consistent. The barrier as a function of  $Q_6$  is lower than that as a function of  $n_{\text{max}}$ . This is a result of a large set of  $n_{\text{max}}$  values corresponding to the same  $Q_6$  values. In concert with Fig. 4.3 and Fig. 4.21, this suggests that the cluster size is closer to the true reaction coordinate describing crystallisation than  $Q_6$ . For the general case where possibly multiple transition paths may exist, each with a corresponding saddle point separating the two states, there are two key questions. These are, (i) which saddle will be crossed? And, (ii), what order parameter to use to best represent the path? In the context of transition state theory, the transition path from the metastable state to the globally stable state is the one with the lowest saddle point [34]. When computing the barrier height for this lowest saddle, the free energy as a function of the reaction coordinate, i.e., along the saddle direction, will be the highest. All other order parameters, which are projections of the reaction coordinate, will display a lower barrier due to averaging out contributions from different values of the true reaction coordinate [34, 244]. On this basis, we argue that  $Q_6$  is not an optimal choice even for the kinetic reconstruction of the free energy.

One also finds that attempting to reversibly sample the degree of crystallinity through the use of an umbrella bias on  $Q_6$  does not work. The system samples configurations that have an artificially high degree of polycrystallinity, more than seen in unconstrained, crystallising MD simulations. In Fig. 4.14 and Fig. 4.15, we observe that for the unconstrained case, the typical crystallite size and the typical cluster size are roughly similar, as is their distribution. Under the application of bias on  $Q_6$ , for both system sizes and temperatures considered, the distribution changes to one of many small crystallites and larger clusters. The degree of polycrystallinity leads to a breakdown in the correlation between  $Q_6$  and  $n_{\text{max}}$  and free energy reconstructions as a function of  $Q_6$  display no barrier to crystallisation, implying spontaneous crystallisation. We are able to determine, through careful analysis, that these results are misleading, and that with the correctly chosen order parameter, one finds a finite free energy barrier under all the conditions of interest, regardless of sampling protocol or method.

## 4.2 Other order parameters to distinguish phases

One of the key challenges is to identify an appropriate order parameter to distinguish the different local structures that form in the supercooled liquid. The low temperature liquid is known to have a higher degree of tetrahedral ordering [131]. This is true also of other network-forming liquids that display such anomalies and/or a liquid-liquid phase transition [16]. The two liquids are expected to be composed of differing fractions of two distinct local structures, one of which may favour or facilitate crystallisation [16, 62, 68, 94].

The following sections describe various local structural measures which serve to distinguish the various putative phases. A number of other measures have also been described in the literature which will not be discussed in detail here. A brief description of some will be included at the end of this section.

### 4.2.1 Ring statistics

Another method of identifying local structures is to count the number of rings that are formed by neighbouring particles in the liquid. The ring construct is also relevant in the discussion of rigidity in amorphous solids [245, 246], hydrogen-bonded structures such as those found in water [247] and even directly as a structural order parameter [248]. Here, we describe the method of Franzblau, described in [249], which details an algorithm to uniquely identify shortest path rings. We follow a hierarchy of definitions:

- **Graph** :  $G = (V, E)$  consists of vertices  $V$  and edges  $E$ .
- **Vertex** : The particles/ smallest unit of interest. Connected to others via edges.
- **Edge** : An edge  $[x, y]$  connects the vertices  $x$  and  $y$  where they are necessarily adjacent.
- **Path** : Given vertices  $x$  and  $y$ , an  $x - y$  path of length  $k$  is a chain of  $k$  edges joining  $x$  and  $y$ , where at most two edges share any given vertex. Eg.,  $x, x_1, x_2, \dots, x_{k-1}, y$  with  $k$  edges in between.
- A **ring** of length  $k$  is simply a path of length  $k$  where the first and last vertices are the same. No loops and only one edge between two adjacent vertices, therefore, the shortest possible ring has length 3.

- $dist_G(x, y)$  is the minimum  $k$  such that there is a path  $x - y$  in graph  $G$ . The corresponding path is the shortest path  $x - y$  in  $G$ .  $dist_R(x, y)$  is the corresponding  $k$  for a given ring  $R$ .

The **diameter** of a graph is the largest possible  $dist_G(x, y)$  for any given  $x$  and  $y$  in the graph; likewise, the diameter of a ring. Note that for a ring of length  $k$ , the diameter is either  $k/2$  or  $(k - 1)/2$  (even or odd). Given a path  $P$  in a ring  $R$ , there exists a unique complementary path. Rings that cannot be decomposed, i.e., rings without shortcuts are the relevant structures of interest. The goal is to identify a set of rings that "covers" the graph and avoid over-counting rings.

### Shortest path rings, irreducibility criteria and the shortest path ring theorem

*Definition:* A shortest path ring contains a shortest path for each pair of vertices  $u, v$  in the ring. We can state this also as  $dist_G(u, v) = dist_R(u, v)$ .

*Definition:* Given a ring  $R$  and a path  $P$  contained in  $R$ ,  $R$  is  $P$ -irreducible if  $R$  is the shortest ring containing  $P$ .

*Definition:* Given a non-negative integer  $m$ ,  $R$  is  $m$ -irreducible if  $R$  is  $P$ -irreducible for every  $P$  of length  $m$ .

*Definition:* Given a ring of diameter  $d$ , with  $d^* = d$  or  $d + 1$  (if length of ring is even or odd),  $R$  is an SP ring if  $R$  is  $d^*$ -irreducible.

This satisfies some important properties:

- Every path connecting two vertices in a given ring is the shortest path possible path on the graph.
- Unless our distance criterion for adjacency leaves a particle with only one or fewer neighbours, all vertices belong to at least one ring.
- Every path of length  $d^*$  or greater belongs to at most one ring of diameter  $d^*$ .
- The number of rings per atom of a given size can be at most 1.

In order to implement an algorithm to count these shortest path rings, we use an important property, unimodality.

**Unimodality** is the property of a ring wherein, given a vertex  $z$  in a ring  $R$ , label each vertex  $u$  in  $R$  by  $dist_R(z, u)$ . The sequence of distances must be unimodal,



of the form,  $0, 1, 2, \dots, (k-1), k, (k-1), \dots, 1, 0$  (or  $0, 1, 2, \dots, (k-1), k, k, (k-1), \dots, 1, 0$  for an odd-length R). This feature will be exploited to identify the SP rings in a graph. However, to do so, we need a 2D array from which we can extract  $dist_G(i, j)$  to perform the check. To populate this array, we can use one of the following schemes

- Depth First Search (DFS)
- Breadth First Search (BFS)
- Dijkstra's algorithm for shortest paths (variant of BFS)
- Shortest path spanning tree algorithm (variant of DFS)

We use Dijkstra's algorithm in our implementation. In order to populate the set of rings on a graph, we need to find all rings of a given size that contain a given vertex of interest  $u$ . In turn, we need to find the SP rings of all sizes that contain  $u$ . We have found each SP ring containing  $u$  when for any neighbour  $v$  of  $u$ , the edge  $(u, v)$  belongs to an SP ring, or in other words,  $v$  belongs to an SP ring with  $u$  in it. To propagate our search, we use a last-in-first-out stack that contains at any given time, the shortest path from  $u$  to the last item in the stack. Whenever we arrive at a situation where none of the neighbours of the last item are suitable to complete the ring, we pop out the last item and try a different neighbour of its "parent" node - this process is usually referred to as *backtrack search*.

### Algorithm

For a given ring length  $m$  of interest, we start at some site  $u$  and propagate through one neighbour at a time, filling in the last-in-first-out stack. At each site, we try the following :

1. Close loop if the length of stack is  $m - 1$ .
2. find a vertex that increases stack length if current stack length is  $< m/2$ .
3. find a vertex that decreases stack length if current stack length is  $> m/2$ .
4. backtrack (pop out last element in stack and move to "parent" node) if desired option is unavailable.

Once we find all SP ring of length  $m$  that contains  $u$ , delete  $u$  and its connections from consideration and choose a new  $u$ . Since we find all the shortest path rings of a given size  $m$  passing through a site  $u$ , we can eliminate  $u$  from subsequent rounds and avoid any possible over-counting. The key feature we have exploited is that of *unimodality*, which gives a condition on whether or not to include a particle that is a given distance of  $d$  neighbours away (in shortest path terms) from our particle of interest,  $u$ .

## Results

For the case of silicon, we look at the statistics of both average ring length and the number of rings each particle participates in, on average, for the thermalised crystal, and the liquid at different temperatures, at  $P = 0$  GPa. The results are shown in Fig. 4.25. One observes that a useful criterion for identifying bulk crystalline particles emerges. For the diamond cubic configuration where the local geometry is tetrahedral, each crystalline particle participates in exactly 12 6-membered rings. Disordered liquid configurations are characterised by both shorter average ring lengths and a greater ring participation. One also finds that the low density liquid has a significantly larger average ring length and a significantly lower ring participation than the high density liquid. These measures have not been used extensively in the work of this thesis, however, the quantities here show interesting behaviour and are promising topics of future work.

### 4.2.2 Local average bond orientational order $q_l$

A measure of local bond orientational order is proposed here that calculates a scalar sum of the local Steinhardt-Nelson parameters of a particle and its neighbours upto a cut-off of choice; shown in Eq. 4.14 as  $\hat{q}_l^i$ . We begin by considering the definition of the standard local bond order parameters:

$$q_{lm}(i) = \frac{1}{n_b(i)} \sum_{j=1}^{n_b(i)} Y_{lm}[\theta(r_{ij}), \phi(r_{ij})],$$

$$q_l(i) = \left[ \frac{4\pi}{(2l+1)} \sum_{m=-l}^l |q_{lm}(i)|^2 \right]^{1/2} \quad (4.13)$$

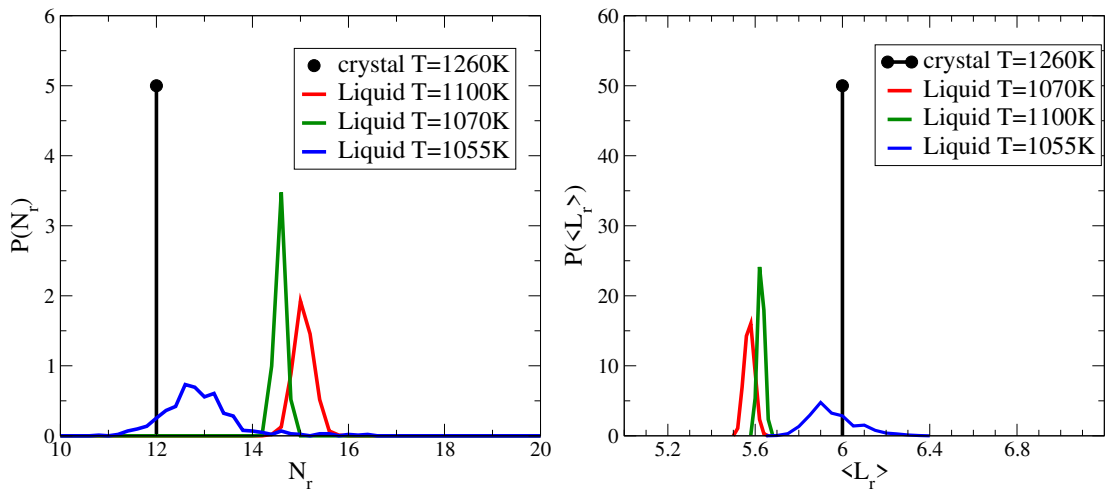


Figure 4.25: The distribution of number of rings each particle participates in (*Top*) and average ring length of the rings each particle participates in (*Bottom*) for the crystal and the liquid at different temperatures at  $P = 0$  GPa. Particles within the first neighbour shell are considered adjacent and potentially members of the same ring. The system size is  $N = 512$  particles and the configurations are obtained from NPT MD simulations of silicon. The crystal is initialised as a pure crystal and thermalised to the target temperature. The liquid is quenched to the target temperature before being relaxed over at least  $10\tau_\alpha$  at the target temperature. We monitor the trajectory to ensure that it is not crystallised by tracking the total number of crystalline particles,  $n_{\text{tot}}$ .

We define a local average on the scalar  $q_l(i)$  as follows:

$$\hat{q}_l^i = \frac{1}{N_b(i) + 1} \left[ \sum_{j=1}^{N_b(i)} q_l^j + q_l^i \right]. \quad (4.14)$$

Here, the summation is over  $i$  and all neighbours of  $i$ .  $N_b(i)$  is the number of neighbours of  $i$  plus one (for  $i$  itself); here too, an atom  $j$  is a neighbour of  $i$  if  $r_{ij} \leq r_{fs}$ . One can equivalently define an average where the contribution of nearby atoms is smoothed from a discontinuous 1-0 step function to a continuous function (see Eq. 4.16).

$$\hat{q}_l^i = \frac{\sum_j q_l^j f(r_{ij}) + q_l^i}{\sum_j f(r_{ij}) + 1}. \quad (4.15)$$

The switching function is given by,

$$f(r_{ij}) = \frac{1 - (r_{ij}/r_a)^6}{1 - (r_{ij}/r_a)^{12}}. \quad (4.16)$$

Since the averaging is performed after  $q_{lm}$  is calculated, for each particle, the disorder is similar in degree to the typical local  $q_l$ . What results is a distribution that is centered around the same value as  $q_l(i)$  but is narrower. With this narrowed distribution, one may better discern different types of particles. Notably, one may change the cut-off for performing the averaging, ( $r_a$  in Eq. 4.16). Taking into account farther neighbours further narrows the distribution by coarse-graining over a number of particles.

A similar prescription has been described in the literature [67]. In their local averaging procedure, the contributions of the second coordination shell neighbours would be taken into account via their ordering with respect to the first coordination shell neighbours in constructing  $q_{lm}(i)$ . The form of this order parameter looks like:

$$\bar{q}_l^i = \sqrt{\frac{4\pi}{(2l+1)} \sum_{m=-l}^l |\bar{q}_{lm}(i)|^2}, \quad (4.17)$$

where,

$$\bar{q}_{lm}(i) = \frac{1}{\bar{N}_b(i)} \sum_{k=0}^{\bar{N}_b(i)} q_{lm}(k). \quad (4.18)$$

Here, the sum over  $k$  includes all neighbours of  $i$  as well as  $i$  itself.  $\bar{N}_b(i)$  is one plus the number of neighbours of  $i$  where an atom  $j$  is a neighbour of  $i$  if  $r_{ij} \leq r_{fs}$

(plus one since  $i$  is also included). The definition of  $q_{lm}(k)$  is as in Eq. 4.13. Thus, in effect, this definition is a measure of the ordering of the neighbours and the neighbours of the neighbours of a given particle. An argument can be made for why the prescription in Eq. 4.14 estimates disorder to be less than Eq. 4.17. This has consequences for how easily one may differentiate ordered configurations from disordered ones. Further, given that the averaging over neighbours is not performed under the square root for Eq. 4.14, the calculation is  $O(N^2)$  rather than the  $O(N^3)$  computation required for Eq. 4.17.

### Comparing definitions

Let us define the following complex number for a given particle  $i$ ,

$$u_i = \frac{1}{n_b(i)} \sum_{j=1}^{n_b(i)} Y_{lm}[\theta(r_{ij}), \phi(r_{ij})]. \quad (4.19)$$

Here,  $j$  sums over the neighbours of  $i$  and  $n_b(i)$  is the number of neighbours of  $i$ .  $u_i$  can be explicitly written as  $u_i(l, m)$  but we choose to drop the parameters  $l, m$  henceforth. In this case, one can rewrite Eq. 4.18 as:

$$\bar{q}_{lm}(i) = \frac{1}{n_b(i)} \sum_{k=1}^{n_b(i)} u_k. \quad (4.20)$$

Here we have replaced  $\bar{N}_b(i)$  with  $n_b(i)$  reducing our consideration to the specific case when Eq. 4.18 is defined as the sum over nearest neighbours.

This gives, from Eq. 4.17,

$$\bar{q}_l^i = \frac{1}{1 + n_b(i)} \sqrt{\frac{4\pi}{(2l+1)} \left[ \sum_{m=-l}^l |u_i + \sum_{k=1}^{n_b(i)} u_k|^2 \right]}, \quad (4.21)$$

Similarly, substituting in Eq. 4.13 gives us,

$$q_l^i = \sqrt{\frac{4\pi}{(2l+1)} \sum_{m=-l}^l |u_i|^2}, \quad (4.22)$$

Eq. 4.14 can now be written as,

$$\hat{q}_l^i = \frac{1}{1 + n_b(i)} \sqrt{\frac{4\pi}{2l+1}} \left[ \sqrt{\sum_{m=-l}^l |u_i|^2} + \sum_{j=1}^{n_b(i)} \sqrt{\sum_{m=-l}^l |u_j|^2} \right]. \quad (4.23)$$

Our goal is to compare Eq. 4.23 (the proposed definition) with Eq. 4.21 (definition of Ref. [67]). Ignoring the preceding factors, one can now arrive at the following relation:

$$\sqrt{\sum_{m=-l}^l |u_i + \sum_{k=1}^{n_b(i)} u_k|^2} \leq \sqrt{\sum_{m=-l}^l |u_i|^2} + \sum_{j=1}^{n_b(i)} \sqrt{\sum_{m=-l}^l |u_j|^2},$$

*or,*

$$\sum_{m=-l}^l \left| \sum_{k'=1}^{n_b(i)+1} u_{k'} \right|^2 \leq \left[ \sum_{k'=1}^{n_b(i)+1} \sqrt{\sum_{m=-l}^l |u_{k'}|^2} \right]^2 \quad (4.24)$$

In order to understand Eq. 4.24, we square both sides and also rewrite the full sum using a new index  $k' = 1 + \sum_{k=1}^{n_b(i)}$ . We can state the following relation by applying the well-known Cauchy-Schwartz inequality piecewise for each value of  $m$ , i.e.,

$$\left| \sum_{k'=1}^{n_b(i)+1} u_{k'}(l, m) \right|^2 \leq \sum_{k'=1}^{n_b(i)+1} |u_{k'}(l, m)|^2 \quad \forall m \in [-l, l] \quad (4.25)$$

The Cauchy-Schwarz inequality says that for any sets of complex numbers (or vectors),

$u_1, u_2, \dots, u_n \in C$  and  $v_1, v_2, \dots, v_n \in C$ , the following relation holds:

$$\left| \sum_{i=1}^n u_i v_i \right|^2 \leq \sum_{i=1}^n |u_i|^2 \sum_{i=1}^n |v_i|^2. \quad (4.26)$$

Replacing the set of vectors,  $v_i$  with unity allows us to use this result in an unaltered form for our case.

The RHS of Eq. 4.25 is in turn less than the RHS of Eq. 4.24 since we know that,

$$\begin{aligned} \left[ \sum_{k'=1}^{n_b(i)+1} \sqrt{\sum_{m=-l}^l |u_{k'}|^2} \right]^2 &= \sum_{k'=1}^{n_b(i)+1} \sum_{m=-l}^l |u_{k'}|^2 \\ &+ \left[ \sum_{j'=1}^{n_b(i)+1} \sum_{k'=1}^{n_b(i)+1} \sqrt{\sum_{m=-l}^l |u_{k'}|^2} \sqrt{\sum_{m=-l}^l |u_{j'}|^2} \right] \end{aligned} \quad (4.27)$$

In Eq. 4.27, the second term on the RHS is positive definite, whereas the first term is identical to the RHS of Eq. 4.25. This completes the relation Eq. 4.24. Based on this, one expects that the distributions calculated using Eq. 4.17 would be

systematically shifted to the left when compared with those obtained from Eq. 4.14 or 4.15. Liquid silicon is characterised using the parameter defined in Eq. 4.14 for the liquid at different conditions and the thermalised crystal in Fig. 4.26. While the high temperature liquid is clearly distinguishable from the crystal, the low temperature liquid is not well-distinguished by either. This limits the utility of this definition in the context of liquid silicon.

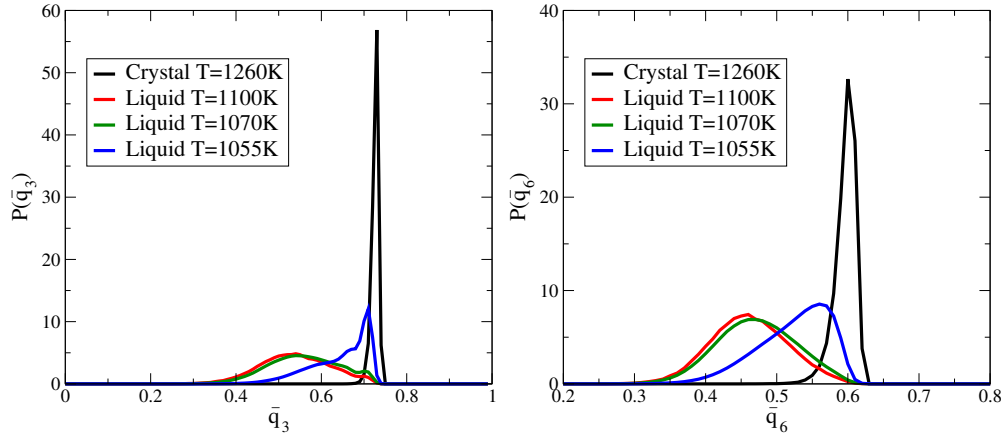


Figure 4.26: The distribution of  $q_3$  (*Top*) and  $q_6$  (*Bottom*) for the crystal and the liquid at different temperatures at  $P = 0$  GPa. The distributions are calculated from Eq. 4.14. The first neighbour shell is chosen as the particles within the first minimum of the pair-correlation function. The local averaging is performed over the nearest neighbours themselves. The system size is  $N = 512$  particles and the configurations are obtained from NPT MD simulations of silicon. The crystal is initialised as a pure crystal and thermalised to the target temperature. The liquid is quenched to the target temperature before being relaxed over at least  $10\tau_\alpha$  at the target temperature. We monitor the trajectory to ensure that it is not crystallised by tracking the total number of crystalline particles,  $n_{\text{tot}}$ .

### 4.2.3 Coordination number and fraction of 4-coordinated particles

The local  $q_l$  distributions display a bimodality in the liquid, suggesting two distinct liquid structures. These structures are strongly connected to the coordination number; particles with correlated neighbourhoods are predominantly 4-coordinated while those with disordered neighbourhoods are 5-coordinated. In Fig. 4.27, the distribution of  $q_3$  is resolved into contributions from 4-coordinated particles and contributions from 5-coordinated (5 or higher) particles. We can in fact define these 4-coordinated particles specifically as those with high local order but not

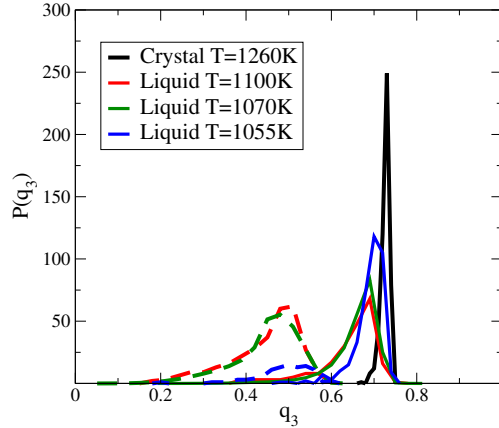


Figure 4.27: The distribution of  $q_3$  for the crystal and the liquid at different temperatures at  $P = 0$  GPa. The solid curves are for particles with 4 neighbours within the first shell and the dashed curves are for particles with 5 neighbours. The system size is  $N = 512$  particles and the configurations are obtained from NPT MD simulations of silicon. The crystal is initialised as a pure crystal and thermalised to the target temperature. The liquid is quenched to the target temperature before being relaxed over at least  $10\tau_\alpha$  at the target temperature. We monitor the trajectory to ensure that it is not crystallised by tracking the total number of crystalline particles,  $n_{\text{tot}}$ .

“bonded” to 3 of their neighbours according to the cut-off on  $Re(q_3(i).q_3(j))$ . These are therefore predominantly 4-coordinated particles with tetrahedral local geometry but not bulk crystalline. This distinction now allows a clear way to resolve 3 types of particles - bulk crystalline, disordered liquid with 5 or more neighbours and liquid with 4 neighbours in a tetrahedral local arrangement. In the PhD thesis of Vishwas Vasisht [15], the largest cluster of such 4-coordinated liquid particles is constructed, labelled the “Random tetrahedral network” (RTN). Changes in the fraction of such 4-coordinated particles with temperature and pressure are studied in greater detail in Chapter 5. Given a clear distinction between these two states, tetrahedral vs disordered 5-coordinated, rather than a continuous variation in states, the liquid can in fact be considered as a mixture of these two states as discussed in Chapter 1 Sec. 1.5.3. In this framework, the fraction of 4-coordinated liquid particles should be 0.5 at conditions of co-existence between two liquids, with a discontinuous change across the phase transition line.



## 4.3 Overview of the literature on order parameters

The most appropriate order parameter in the context of the putative metastable LLPT is the one that best quantifies the microscopic structural changes that occur in the liquid. These changes are known to arise from tetrahedral ordering, both experimentally [7, 20, 114, 120, 250] and in simulations [23, 95, 131, 134, 141] in silicon and in other liquids displaying water-like anomalies [16].

Some of the order parameters that have been proposed to capture the essential structural changes are described below. The orientational order of the second shell or next nearest neighbours rather than the nearest neighbours are found to correlate better with translational order in TIP5P water [251]. The topological cluster classification (TCC) algorithm described in [252] detects local structures from the topology of bonds with nearest neighbours. The bonds are identified from Voronoi tessellation. The tetrahedrality order parameter used in [16, 131] among other works quantifies the deviation from tetrahedral ordering in triplets of neighbouring particles. This is connected to bond orientational order but is specifically sensitive to tetrahedral ordering. Methods such as Common Neighbour Analysis identifies structures based on the number of shared neighbours, shared bonds and bond chains [253]. Centrosymmetry analysis measures whether a given particle is equidistant from two “opposite” neighbours [254]. An extensive review of these methods is contained in [255]. The use of Voronoi polyhedra to identify the crystal structure from local geometry or by matching templates is another method used in this context [256–258]. The local structure index used in the case of ST2 water and elsewhere quantifies the degree of favoured local ordering [29, 259]. Graph algorithms, similar to ring statistics are also used in such studies [260]. Even the Page Rank search algorithm has been retrofitted to this purpose [261]. A number of recent works suggest measures of local translational entropy [262, 263], such as that measured by the pair entropy,  $S_2$ . This has also been extended to orientational entropy [264]. It has also been argued that the relaxation timescales, which reveal the slowest modes, are the appropriate means to identify the best order parameter or combination of order parameters. This is discussed in the Spectral Gap Optimization of Order Parameters(SGOOP) method and its derivatives [265–267]. In recent times, a number of methods have sought to leverage the power of various machine learning schemes such as linear discriminant analysis [268] and deep

learning schemes [269, 270] to identify the slowest changing modes to identify appropriate order parameters. The body of literature in this topic is vast, and only a few examples known to the author have been mentioned. A large number of these order parameters, including some of the most frequently used, have been designed based on heuristics and an understanding of the structural changes underlying the phase transition being studied. However, a significant fraction of recent efforts have been devoted to the systematisation of order parameter definitions. Key concepts that have been used are the separation of timescales as in methods like SGOOP, relative magnitudes of fluctuations and the identification of one or more transition states intermediate to the phases of interest, as in the study of crystal nucleation. Another point worth noting is that changes in the structure that occur during a phase transition will reflect in changes across a number of quantities. As a result, many measures serve well as descriptive measures. However, the phase transformation itself is commonly understood to be driven by changes in one or a few key features. Identifying the correct quantity to directly represent this change, rather than a quantity that is only correlated with the underlying change, is one of the main challenges in defining order parameters.

## 4.4 Discussion

In this chapter, we discussed the implications of global vs local measures of crystalline ordering on reconstructing the free energy barrier to crystallisation. The issues with the global measure,  $Q_6$ , become apparent when one measures the degree of polycrystallinity resultant from applying an umbrella bias on  $Q_6$ . In order to do this, an algorithm was developed and coded to use a graph search procedure that identifies the boundaries between misoriented crystallites. One finds also that in unconstrained simulations that a finite barrier to crystallisation is found as a function of  $Q_6$  under conditions where umbrella sampling results suggest spontaneous crystallisation. This finite barrier can be shown to be consistent with the barrier as a function of  $n_{\max}$  using a variable transformation.

In the later portion of this chapter, we consider the issue of distinguishing the three possible local structures in the supercooled liquid, (i) the disordered, high density arrangement, (ii) the tetrahedral, low density arrangement, and (iii) the tetrahedral, crystalline arrangement with diamond cubic geometry. We briefly review the wide range of relevant order parameter definitions, and discuss the implementation of, and results from, a few interesting measures. These are the statistics of shortest

---

path rings [249] formed in the supercooled liquid and a minimally novel variant of a locally averaged bond orientational order described by Lechner and Dellago [67]. Finally we discuss the interplay of local orientational order and coordination number and the cluster of tetrahedrally ordered liquid-like particles [15].

## Chapter 5

# Metastable liquid-liquid phase transition in silicon

The existence of a first order phase transition between different liquid forms in single-component liquids has been vigorously investigated and widely debated. Liquid silicon is one such case, where a number of studies, both experimental and computational, have attempted to answer the question [4].

Silicon thus belongs to an extensive list of so-called network-forming liquids that demonstrate thermodynamic anomalies and in which, the existence of a liquid-liquid phase transition has been suggested [16]. The most prominent example is of course water, where early investigations attempting to understand the implications of the anomalous expansion upon cooling led to the discovery by Poole *et al.*, of a liquid-liquid phase transition line ending at a critical point for the ST2 model of water [14]. A number of studies reconstructing the free energy surface found two distinct minima in the free energy landscape corresponding to two different densities and low crystalline order [111, 143–146]. A subsequent study by Limmer and Chandler argued that these results were a misinterpretation of slow crystallisation, wherein the crystallinity order parameter, the global bond orientational order  $Q_6$ , was relaxing on slower timescales than the length of the simulations [18, 28]. This debate has since been resolved and the existence of the liquid-liquid phase transition confirmed for the ST2 models of water in a comprehensive study of the free energy surface by Palmer *et al.* [29]. On the other hand, for the monoatomic mW model of water, which is based on the SW potential, no evidence for an LLPT was found, while a lower limit of stability for the supercooled liquid was identified by Moore and Molinero based on the fact that crystallisation occurred on shorter

timescales than relaxation [68]. A study attempting to fit the available data to thermodynamic scenarios of “weak crystallisation” and of a mixture of two types of local ordering with weak phase separation found inconsistencies resulting from the “weak crystallisation” scenario [55]. For TIP4P water, an extensive study of non-crystallising molecular dynamics trajectories has found evidence of two distinct liquid states, with a small barrier between the two identified under the conditions studied therein [45]. For the case of silica, free energy reconstructions from constrained sampling simulations of the ionic WAC model [271] have shown two clearly distinct liquid states and behaviour reminiscent of ST2 water [166, 171]).

In the case of liquid silicon, the first suggestions of such a transition was based on experimental observations [6, 7] and on the basis of a two-state model by Aptekar in 1979 [8]. Experiments are challenging to perform, given the deeply supercooled conditions at which studies need to be conducted, at which avoiding crystallisation is difficult. Some recent experiments are those by Kim *et al* [19] and Beye *et al* [20]. Nevertheless, avoiding crystallisation remains a core issue in investigating this question [19, 20, 114–117, 119]. A number of *ab initio* studies by Ganesh and Widom and by others have also found evidence for a liquid liquid transition based on the electronic properties [22–24, 138, 140, 237]. Silicon is a metallic liquid at high temperature and a semi-metal at low temperature.

Classical molecular dynamics studies with the SW potential were first shown to demonstrate an LLPT in a study by Sastry and Angell [1]. Since then, Vasisht *et al* [2] explored the phase diagram of supercooled liquid silicon extensively and found a liquid-liquid critical point (LLCP) at negative pressures. Subsequent free energy studies by Limmer and Chandler [18] and by Ricci *et al* [30], using density and global bond orientational order,  $Q_6$ , as the order parameters did not find any evidence of an LLPT, arguing instead that the liquid loses thermodynamic metastability with respect to the crystal at the state points where an LLPT was earlier reported. Ricci *et al*, thus argued in favour of spontaneous, slow crystallisation as the cause of the apparent LLPT, though they do highlight some caveats arising from the use of  $Q_6$  as a measure of the degree of crystallinity. We saw in Chapter 3 that there was a finite free energy barrier to crystallisation at the conditions of interest, ruling out spontaneous crystallisation. In Chapter 4 we described how the use of  $Q_6$  leads to misleading results when used as a bias parameter, explaining the reason for the observation of barrier-less crystallisation in the work of Ricci *et al*. The use of global bond orientational order,  $Q_6$ , to constrain the system from crystallisation produces artefacts leading to incorrect estimates of the barrier to crystallisation.

Given that a well-defined metastable liquid state exists at the state points of interest, and that the changes in the microscopic structure of the liquid across the putative LLPT line reflect in changes in the temperature dependence of the free energy barrier to crystal nucleation, the relevant next question, which is the subject of this work, is the nature of the transition in the liquid state. Thermodynamic scenarios consistent with the nature of the anomalies observed in liquid silicon [131] are typically based on two-state thermodynamic models, which represent the metastable liquid as consisting of two distinct types of local order [55, 146, 194, 201, 206, 207]. These models, which have been able to explain available data to varying degrees of success, do not limit the possible sources of these anomalies to a liquid-liquid phase transition. Thermodynamic scenarios involving a sharp, but continuous change in the properties of the liquid have also been proposed [3, 26]. A free energy reconstruction that reversibly samples the metastable liquid under conditions of a low degree of crystalline ordering will determine whether a region of co-existence exists and the nature of the barrier between the two states. Such a study addresses the crucial obstacle of avoiding crystallisation, one that makes both experiments and measurements from standard molecular dynamics runs extremely challenging. In this work, we perform constrained simulations in a manner that reversibly samples both metastable liquid configurations as well as configurations with post-critical cluster sizes, conclusively addressing the question of the existence of the LLPT. We find a marked change in the density distribution of the metastable liquid across the putative LLPT line with a double-well in the reconstructed Landau free energy as a function of density – a feature characteristic of a liquid-liquid phase transition – at expected state points. Interestingly, we find that unlike in the case of ST2 water and silica, the typical density of both liquids show noticeable pressure dependence [146].

We perform umbrella sampling Monte Carlo [37] simulations of silicon modelled using the 3-body Stillinger-Weber potential [25] with a hard-wall umbrella bias that constrains the size of the largest crystalline cluster,  $n_{\max}$ , to different but overlapping windows [169]. Crystalline particles and clusters of connected crystalline particles are identified using the local analogue of the Steinhardt-Nelson bond orientational order parameters using the procedure described in [63, 82, 96] with cut-offs specific to SW silicon as used in Chapter 3. Parallel tempering swaps are performed between adjacent  $n_{\max}$  bias windows and adjacent temperatures to enhance sampling of different densities (see 2.1 for details). For comparison, umbrella sampling

runs where both density and  $n_{\max}$  biases are applied are also performed. Convergence of the simulations is checked by monitoring the decay of the auto-correlation functions of the density,  $Q_6$  and the potential energy. Further, visit and excursion statistics from the parallel tempering swaps are also monitored to determine the efficacy of sampling.

## 5.1 Methods

We construct the free energy landscape here using two methods, umbrella sampling with a hard wall bias potential and kinetic reconstruction using the mean first passage time. Both methods have been described in the literature and used in the past to construct the free energy profile for crystallisation in supercooled silicon at similar temperatures. Here we describe a prescription to extend these methods to the case of two order parameters and discuss the results obtained. We use the Stillinger-Weber potential described in Chapter 2.

### 5.1.1 Order parameters

We use the local bond orientational order parameters of Steinhardt and Nelson, [228] to identify both crystalline particles and 4-coordinated liquid particles, discussed in earlier chapters. To briefly recap:

$$q_{lm}(i) = \frac{1}{n_b(i)} \sum_{j=1}^{n_b(i)} Y_{lm}[\theta(r_{ij}), \phi(r_{ij})] \quad (5.1)$$

The corresponding order parameter, summed over  $m$ 's is

$$q_l(i) = \left[ \frac{4\pi}{(2l+1)} \sum_{m=-l}^l |q_{lm}(i)|^2 \right]^{1/2} \quad (5.2)$$

Here, we use  $q_3(i)$ , noting that using  $q_6(i)$  is equivalent and gives very similar results [131] (see Fig. 2.2). The number of neighbours,  $n_b(i)$  is taken to be the atoms within the first coordination shell of the pair-correlation function, i.e., atoms within a cut-off of  $2.95 \text{ \AA}$  from the reference atom. To identify crystalline particles, we look at the correlations in the local orientational order of neighbouring atoms, following the prescription described in the literature [46, 63, 82]. Atoms with correlated neighbourhoods of high local orientational order are classified solid-like particles.

Quantitatively, this correlation is given by the quantity, [63, 96, 229]

$$\text{Re}(q_3(i) \cdot q_3(j)) = \text{Re} \left( \sum_{-3}^3 q_{3m}(i) q_{3m}^*(j) \right) \quad (5.3)$$

A particle  $i$  and a particle  $j$  are considered to be "bonded" if  $\text{Re}(q_3(i) \cdot q_3(j)) < -0.23$ . We note here, the significance of the the cut-off value of  $-0.23$  which demands that the crystal structure formed is diamond cubic, to the exclusion of the diamond hexagonal crystal structure which also has local tetrahedral ordering [96]. Crystalline particles have a  $q_3 > 0.6$  and are "bonded" to at least 3 neighbours. Further, crystalline particles within the SW-cutoff distance of each other belong to the same cluster. In this study we consider both the size of the largest cluster,  $n_{\max}$  and the full distribution of cluster sizes  $P(n)$ .

LDL-like particles have a high  $q_3(i) > 0.6$ , showing high tetrahedral ordering, but have fewer than 3 "bonded" neighbours with similar ordering. Finally, HDL-like particles have disordered neighbourhoods with 5 or more neighbours and low  $q_3$ . The distributions used here and the cut-offs are shown in Fig. 2.1 in Sec. 2.6.2.

### 5.1.2 Umbrella sampling

USMC simulations were performed at the state points mentioned with a hard wall bias applied that strictly constrains the size of the largest cluster to be between  $n_{\max}^l$  and  $n_{\max}^u$  as described in Eq. 5.5. The full cluster size distribution is used to calculate the free energy using Eq. 5.15.

Parallel tempering swaps between adjacent windows are carried out to enhance sampling and speed up equilibration. The general expression for the Hamiltonian under application of bias is given by:

$$H_C = H + W_1(n_{\max}) + W_2(\rho) \quad (5.4)$$

where  $H$  is the original Hamiltonian,  $W_1(n_{\max})$  represents the bias potential on  $n_{\max}$ , and  $W_2(\rho)$  is the bias potential on  $\rho$ .

Here,  $W_1$  is defined by

$$W_1 = \begin{cases} 0 & n_{\max}^l \leq n_{\max} < n_{\max}^u \\ \infty & \text{otherwise} \end{cases} \quad (5.5)$$



For  $W_2$ , a harmonic bias of the form

$$W_2(\rho; \rho_0, k_\rho) = \frac{1}{2}k_\rho(\rho - \rho_0)^2 \quad (5.6)$$

is used to enhance sampling around a desired value of  $\rho$ , labelled  $\rho^0$ . We can write the constrained Hamiltonian as:

$$H_C = H + W_1(n_{\max}; n_{\max}^l, n_{\max}^u) + W_2(\rho; \rho_0, k_\rho) \quad (5.7)$$

The unbiased expectation value of some system property such as the density,  $\rho$  can be written as (in general for a bias applied on any combination of collective variables such as  $(n_{\max}, \rho)$ ):

$$\langle \rho \rangle = \frac{\langle \rho e^{\beta W_1 + W_2} \rangle_C}{\langle e^{\beta W_1 + W_2} \rangle_C} \quad (5.8)$$

The expectation subscript  $C$  is the sampled probability from the simulation under the modified Hamiltonian. Likewise,  $W_C$  is the bias potential that describes the constrained ensemble.

### Unbiased distributions for two-order parameter umbrella sampling

For simulations with both density and  $n_{\max}$  constrained, the free energy surfaces are stitched together with an in-house implementation of the WHAM equations. The scheme iterates the following calculations till convergence for biased simulation:

$$p_0^{est}(Q) = \frac{\sum_{i=1}^N \langle H_i(Q) \rangle}{\sum_{i=1}^N \exp(-\beta(W_i(Q) - \Delta F_i)) M_i}$$

$$\Delta F_i = -k_B T \ln \left[ \sum_Q \exp(-\beta W_i(Q)) p_0^{est}(Q) \right] \quad (5.9)$$

In order to determine both  $\beta \Delta G(\rho)$  and the unbiased shifted bi-variate distribution of density and potential energy,  $\beta \Delta G(\rho, PE)$ , one needs to simultaneously reweight for temperature and pressure, as discussed below.

**On-the-fly unbiasing**, i.e., storing the factor  $e^{\beta_i W_i}$  for each snapshot, is useful to obtain the un-biased distributions of all quantities, including other order parameters, under the given conditions of  $P, \beta$ .

Then, the histograms for each simulation of length  $T_i$  are given by

$$H_i(E, V, \phi) = \sum_{t=1}^{T_i} \delta(E_t - E) \delta(V_t - V) \delta(\phi_t - \phi) e^{\beta_i W_i(\phi)} \quad (5.10)$$

One can obtain the unbiased probability distributions, weighted on  $\beta$  and  $P$ , in the following way:

$$P_{ub}(E, V, \phi; \beta, P) = \frac{\Omega(E, V, \phi) e^{-\beta E} e^{-\beta P V}}{\sum_{\{E, V, \phi\}} \Omega(E, V, \phi) e^{-\beta E} e^{-\beta P V}} \quad (5.11)$$

An un-normalised histogram  $N_{ub}(E, V, \phi; \beta, P)$ , is then given by

$$\begin{aligned} N_{ub}(E, V, \phi; \beta, P) &= \Omega(E, V, \phi) e^{-\beta E} e^{-\beta P V} \\ N_{ub}(E, V, \phi; \beta, P) &= e^{-\beta E} e^{-\beta P V} \frac{\sum_{i=1}^R H_i(E, V, \phi)}{\sum_{i=1}^R N_i e^{-\beta_i E} e^{-\beta_i P_i V} e^{F_i}} \end{aligned} \quad (5.12)$$

An alternate form of the WHAM equations then gives us:

$$\begin{aligned} P_{ub}(E, V, \phi; \beta, P) &= e^{-\beta E} e^{-\beta P V} \frac{\sum_{i=1}^R H_i(E, V, \phi)}{\sum_{i=1}^R N_i e^{-\beta_i E} e^{-\beta_i P_i V} e^{F_i}} \\ e^{-F_i} &= \sum_{\{E, V, \phi\}} \Omega(E, V, \phi) e^{-\beta_i E} e^{-\beta_i P_i V} \\ &= \sum_{\{E, V, \phi\}} P_{ub}(E, V, \phi) e^{\beta E} e^{\beta P V} e^{-\beta_i E} e^{-\beta_i P_i V} \end{aligned} \quad (5.13)$$

The procedure is as follows:

- the histograms for each simulation of length  $T_i$  are given by

$$H_i(E, V, \phi) = \sum_{t=1}^{T_i} \delta(E_t - E) \delta(V_t - V) \delta(\phi_t - \phi) e^{\beta_i W_i(\phi)} \quad (5.14)$$

- The factors  $(\beta - \beta_i)E$  and  $(\beta P - \beta_i P_i)V$  are computed for each  $E, V$  given simulation  $\beta_i, P_i$  and target  $\beta, P$ .

- A tolerance of  $10^{-4}$  is set for the RMS convergence of  $\sqrt{\frac{1}{R} \sum_{i=1}^R (F_i - F_i^{old})^2}$
- The  $F_i$  are initialised to arbitrary non-zero values.

### Unbiased distributions for single order parameter umbrella sampling

The un-biasing described in Eq. 5.8 simplifies for the hard wall bias since  $W = 0$  or  $W = \infty$  depending on the size of the largest cluster.

For the case of the hard wall bias potential, one can replace, for the number of clusters of size  $n$ ,  $N(n)$ ,  $\langle N(n) \rangle = \langle N(n) \rangle_C$  within the constrained region. While the bias constraints are applied on  $n_{\max}$ , we track the full cluster size distribution because the approximation  $P(n_{\max}) \approx P(n)$  does not hold at deep supercooling when the size of the critical cluster is small (see Section 3.3.4). The free energy cost to the formation of a crystalline cluster of size  $n$  is given by

$$\Delta G(n) = -k_B T \ln(P(n)). \quad (5.15)$$

One can similarly obtain the bi-variate distribution,  $P(n, \rho)$  to obtain the full two-order parameter free energy  $\beta \Delta G(n, \rho)$ .

$$\Delta G(n, \rho) = -k_B T \ln(P(n, \rho)). \quad (5.16)$$

To obtain this, one first samples the following quantity:

$$P'(n, \rho) = \frac{1}{\tau_s} \sum_{t=0}^{\tau_s} \frac{N(n, t)}{N(0, t)} \delta(\rho(t) - \rho) \quad \text{if } n_{\max}^l \leq n \leq n_{\max}^u \quad (5.17)$$

We note here that  $P'(n, \rho)$  is not a probability since it is not normalised. We normalise it explicitly to get a probability  $P(n, \rho)$ .

$$P(n, \rho) = \frac{P'(n, \rho)}{\sum_n \sum_\rho P'(n, \rho)} \quad (5.18)$$

The free energy cost of formation of cluster sizes  $n$  in liquid of density  $\rho$  is given by

$$\beta \Delta G(n, \rho) = -\ln(P(n, \rho)). \quad (5.19)$$

One may also consider the free energy  $\beta \Delta G(n_{\max}, \rho)$  however, this would lead to the appearance of an artificial minimum at small  $n_{\max}$  [238, 239] (see also Section 3.3.4).

In order to obtain the full free energy landscape, we stitch together  $\beta\Delta G(n, \rho)$  from the different individual windows constraining sampling to slices in  $n_{\max}$ .

From a set of independent simulations, each indexed by  $d$  and having distinct but adjacent bounds in  $n_{\max}$ , one obtains the free energy differences  $\beta\Delta G_d(n, \rho)$  up to an undetermined constant,  $b_d$ . The constants,  $b_d$ , are obtained by minimising the error described in Eq. 5.20,  $\chi_{HW}$ , sequentially between overlapping data points from simulations with adjacent bounds.

$$\chi_{HW} = \sum_{d=1}^{N_{sim}} \sum_{n=n_{lo}^d}^{n_{hi}^d} [\beta\Delta G_d(n) - \beta\Delta G_{d+1}(n) - b_d]^2 \quad (5.20)$$

This is done subject to the constraint

$$\beta\Delta G(0) = - \int_{\rho_{low}}^{\rho_{high}} \exp(-\beta\Delta G(n, \rho)) d\rho = 0 \quad \text{if } n_{lo}^d = 0, \quad (5.21)$$

thus eliminating any additional additive constant.

The distribution of density subject to small  $n_{\max}$  is obtained from each of the individual windows and stitched together by summing over  $n_{\max}$ . Estimates across different windows are obtained by stitching together free energies (or equivalent distributions) as described in Eq. 5.20.

### Parallel tempering

The general expression for probability of acceptance of parallel tempering swaps in the NPT ensemble between simulations indexed  $i$  and  $j$  is given by

$$P_{accept} = \min \left( 1, \exp \left[ \left[ (E_i - E_j) + P(V_i - V_j) \right] (\beta_i - \beta_j) \right] \right. \\ \left. \exp \left[ -\beta_j W_i(n_{\max_j}; \rho_j) - \beta_i W_j(n_{\max_i}; \rho_i) \right] \right. \\ \left. \exp \left[ \beta_i W_i(n_{\max_i}; \rho_i) + \beta_j W_j(n_{\max_j}; \rho_j) \right] \right) \quad (5.22)$$

The details of parallel tempering are as given in Section 2.8.1. In all simulations replica exchanges are attempted across adjacent temperatures and bias windows. Thus, in simulations where both  $n_{\max}$  and  $\rho$  are constrained, parallel tempering

swaps are performed across  $T$ ,  $[n_{\max}^l : n_{\max}^u]$  and  $\rho_0$ . We note that in choosing whether to accept a swap based on a Boltzmann weight on  $W_N - W_O$ , these quantities are as defined below:

$$\begin{aligned} W_N &= W_j(n_{\max_i}; \rho_i) + W_i(n_{\max_j}; \rho_j) \\ W_O &= W_i(n_{\max_i}; \rho_i) + W_j(n_{\max_j}; \rho_j) \end{aligned}$$

For the hard wall bias, the swap is accepted with probability 1 if the  $n_{\max_i}$  and  $n_{\max_j}$  are both within the new constraints after the swap and rejected otherwise. For the harmonic bias, swaps are accepted based on the bias potential difference before and after the swap.

### 5.1.3 Convergence and sampling tests for umbrella sampling runs

The convergence of umbrella sampling runs is determined by measuring the decay of the auto-correlation times for various quantities in the bias window. Error estimates and the number of uncorrelated samples are obtained using the integrated auto-correlation time. **Integrated auto-correlation time and errors** are computed from the auto-correlation function of the order parameter,

$$C_Q(t) = \frac{\langle Q(t) - Q(0) \rangle - \langle Q \rangle^2}{\langle Q^2 \rangle - \langle Q \rangle^2} \quad (5.23)$$

The integrated auto-correlation time is obtained from the self auto-correlation as

$$g = 1 + 2 \sum_{t=1}^{T-1} \left(1 - \frac{t}{T}\right) C_x(t) \quad (5.24)$$

and is used to weight sampling according to the number of decorrelated samples obtained as a function of  $\rho$ . The error as a function of  $\rho$  is

$$\omega(\rho) = \left( \sum_{i=1}^{N_{sim}} \frac{g_i}{\langle H_i(\rho) \rangle} \right)^{1/2} \quad (5.25)$$

The WHAM equations are then modified as:

$$P_{ub}(E, V, \phi; \beta, P) = \frac{\sum_{i=1}^R g_i^{-1} H_i(E, V, \phi)}{\sum_{i=1}^R g_i^{-1} N_i e^{(\beta-\beta_i)E} e^{(\beta P - \beta_i P_i)V} e^{F_i}}$$

$$e^{-F_i} = \sum_{\{E, V, \phi\}} P_{ub}(E, V, \phi) e^{(\beta-\beta_i)E} e^{(\beta P - \beta_i P_i)V} \quad (5.26)$$

## 5.2 Results

In this section, we summarise the evidence for a liquid-liquid phase transition in silicon. Simulations are performed across the putative LLPT line for different isobars in both the sub-critical regime (where phase separation is expected to occur) and the super-critical regime, where the liquid changes continuously. The estimates for these conditions are based on the results of Vasisht *et al* [2]. We first focus on the  $P = 0.75$  GPa isobar, studying the convergence of sampling and the free energy profiles. Close to co-existence conditions, we resolve the liquid with two order parameter umbrella sampling, biasing both  $\rho$  and  $n_{\max}$ .

Far from the co-existence conditions, we use a scheme that biases only  $n_{\max}$  while enhancing sampling of the different densities with parallel tempering. This scheme does not work close to co-existence because the parallel tempering scheme is not effective in performing switches across the transition. As a result, correlations decay slowly at co-existence conditions, and sampling is subject to large errors. Convergence is shown for simulations far from co-existence with this scheme.

Other isobars are then studied after this, allowing us to trace the LLPT line. We study the fraction of 4-coordinated or LDL-like particles across the isobars, showing the change in sharpness of the transition across the critical point.

Finally, we study the scaling of the free energy barrier between the two liquids with system size at  $P = 0.75$  GPa at conditions close to co-existence.

The results for this study are organised in the following way:

- Results at  $P = 0.75$  GPa and  $N = 512$ . Convergence tests and free energy profiles.

- Matching free energy estimates obtained directly from USMC simulations with those obtained by using histogram reweighting.
- Bivariate distribution of density and potential energy for the two liquids.
- Results at other isobars.
- Fraction of 4-coordinated particles across the phase diagram.
- System-size scaling of the free energy barrier.

### 5.2.1 Results for $P = 0.75$ GPa

We begin by analysing the convergence of the two-order parameter umbrella sampling simulations. The free energy profiles are shown after that, with clear indications of the liquid-liquid phase transition.

#### Convergence tests for full two-order parameter umbrella sampling simulations

For simulations where umbrella bias is applied on both  $n_{\max}$  and  $\rho$ , at different bias minima,  $\rho_0$ , the autocorrelation functions for density and  $Q_6$  are shown in Panel A and Panel B of Fig. 5.1 and Fig. 5.2. The auto-correlation decay of density window index due to parallel tempering swaps is also shown in Panel C of Fig. 5.1 and Fig. 5.2. In Panel D of the same figures, the mean excursion length out of the “home” window or mean return time is shown for different density windows, indexed  $\rho_0$ , subject to the constraint of  $n_{\max} \leq 3$ .

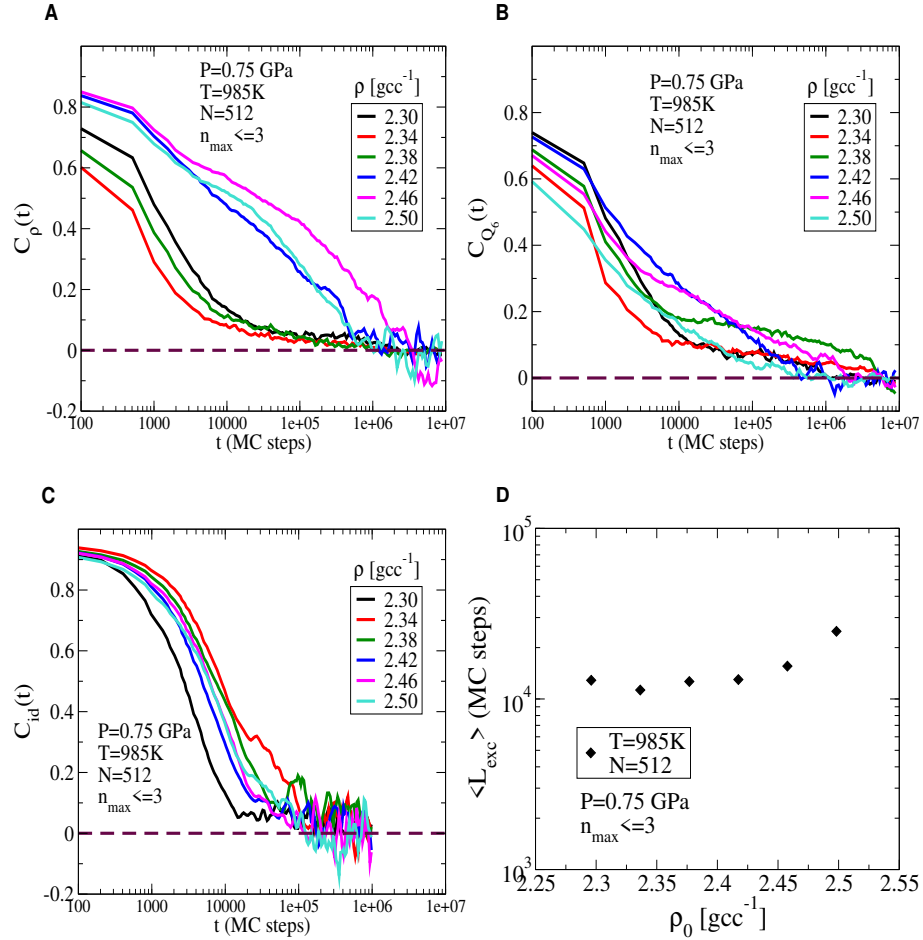


Figure 5.1: Decay of time auto-correlation function for density (Panel A),  $Q_6$  (Panel B), and for density window index (Panel C) for each of the density bias windows,  $\rho_0$ , subject to the constraint of  $n_{\max} \leq 3$  at  $T = 985$  K,  $P = 0.75$  GPa. Panel D shows the mean excursion length or return time as a function of  $\rho_0$  subject to the constraint on  $n_{\max}$ .



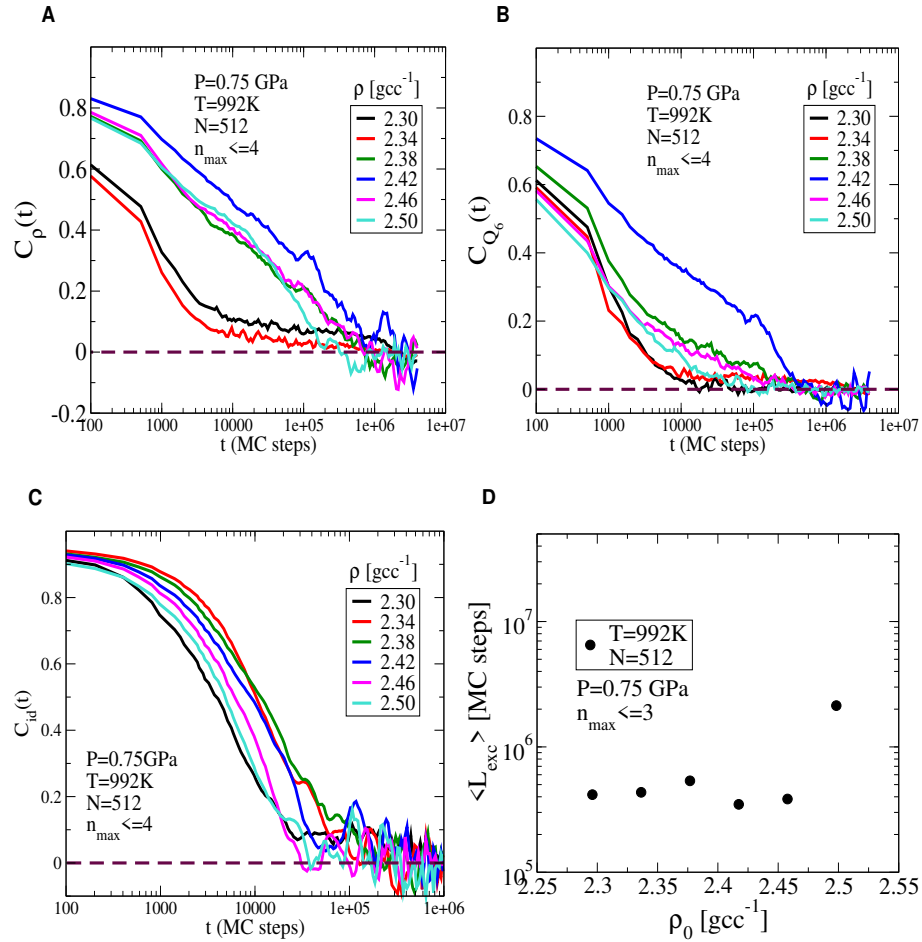


Figure 5.2: Decay of time auto-correlation function for density (Panel A),  $Q_6$  (Panel B), and for density window index (Panel C) for each of the density bias windows,  $\rho_0$ , subject to the constraint of  $n_{\max} \leq 3$  at  $T = 992$  K,  $P = 0.75$  GPa. Panel D shows the mean excursion length or return time as a function of  $\rho_0$  subject to the constraint on  $n_{\max}$ .

### Histogram reweighting at $P = 0.75$ GPa to test for equilibrium sampling

The histogram reweighting procedure in Eq. 5.27 is used to obtain the unbiased, reweighted, bivariate distribution  $P_{ub}(E, \rho; \beta, P)$  at the target conditions of  $T = 1/\beta$ ,  $P$ .

$$P_{ub}(E, \rho; \beta, P) = \frac{\sum_{i=1}^R g_i^{-1} H_i(E, \rho)}{\sum_{i=1}^R g_i^{-1} N_i e^{(\beta - \beta_i)E} e^{(\beta P - \beta_i P_i)N/\rho} e^{F_i}}$$

$$e^{-F_i} = \sum_{\{E, \rho\}} P_{ub}(E, V, \phi) e^{(\beta - \beta_i)E} e^{(\beta P - \beta_i P_i)N/\rho} \quad (5.27)$$

The distribution of density is then obtained as  $P_{ub}(\rho; \beta, P) = \sum_{-E_{\min}}^{E_{\max}} P_{ub}(E, \rho; \beta, P)$  and the free energy, shown in Fig. 5.3 and in Fig. 5.4 is given by  $\beta\Delta G(\rho; \beta, P) = -\ln(P_{ub}(\rho; \beta, P))$ . Note that changing the constraint on  $n_{\max}$  alters the coexistence temperature at a given isobar, however, the feature of coexistence remains and is robust to changes in the choice of  $n_{\max}$  less than the critical cluster size.

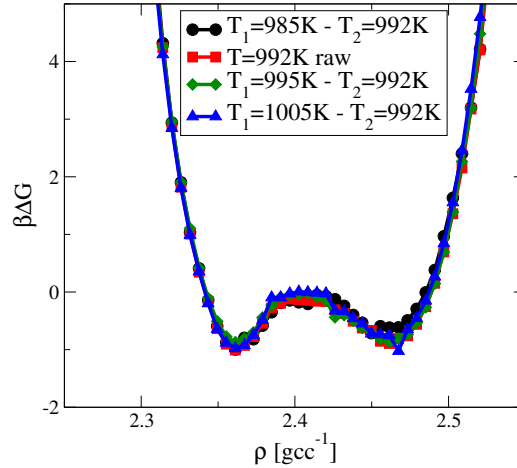


Figure 5.3: Raw and re-weighted free energies at three temperatures, for  $P = 0.75$  GPa,  $N = 512$ , with a constraint on  $n_{\max}$  at  $n_{\max} \leq 4$ . Note that for this constraint, the coexistence temperature is  $T = 992$ K.

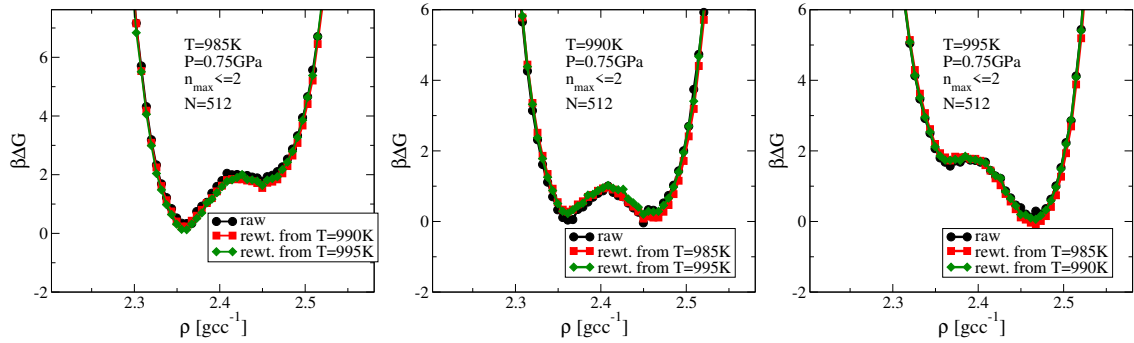


Figure 5.4: Raw and re-weighted free energies at three temperatures, for  $P = 0.75$  GPa,  $N = 512$ , with a constraint on  $n_{\max}$  at  $n_{\max} \leq 3$ . For this constraint of smaller  $n_{\max}$  (compared to Fig. 5.3), the coexistence temperature shifts to a lower temperature of  $T = 990$ K.

### Free energy reconstruction from constrained sampling

We perform umbrella sampling Monte Carlo simulations [37] of  $N = 512$  particles along the  $P = 0.75$  GPa isobar. The size of the largest crystalline cluster,  $n_{\max}$ , is constrained within overlapping hardwall constraints,  $[n^{lo}, n^{hi}]$ . The density is constrained with an additional harmonic bias on different bias centres  $\rho_0$  and a spring constant of  $2000\epsilon$  for  $N = 512$ .  $\epsilon$  is the energy scale associated with the Stillinger-Weber potential. Sampling is enhanced with parallel tempering swaps between adjacent windows and adjacent temperatures every  $2 \times 10^2$  MC steps ( $n_{\max}$ ),  $10^3$  MC steps ( $\rho$ ) and  $2 \times 10^3$  MC steps (temperature) respectively. The choice of temperatures is based on estimates of the LLPT line reported in [2], where the estimated transition temperature for  $P = 0.75$  GPa is  $T = 992$ K. In fig. 5.5(A), the free energy barrier to crystallisation is shown, with a finite free energy cost to the formation of crystalline clusters at each of the temperatures considered. We then construct the density distribution subject to the constraint  $n_{\max} \leq 3$ , integrating over the multivariate distribution to get

$$P(\rho) = \sum_{n_{\max}=0}^{n_{\max}=3} P(n_{\max}, \rho). \quad (5.28)$$

The corresponding free energies obtained from  $\beta\Delta G(\rho) = -\ln(P(\rho))$  are shown in Fig. 5.5(B), displaying a change in the typical density of the liquid across  $T = 992$ K, with a double-well at  $T = 992$ K, indicative of co-existence between two liquids. In Fig. 5.6, the two order parameter free energy surface is shown with cluster size on the  $x$ -axis and  $\rho$  on the  $y$ -axis. The cluster size is sampled up to the critical

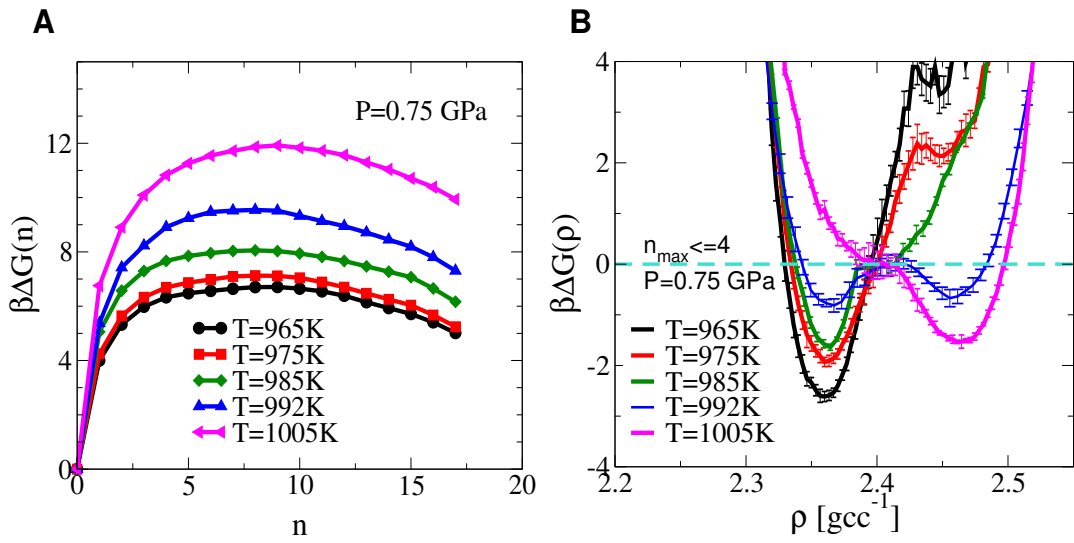


Figure 5.5: Panel (A) shows the free energy barrier to crystal nucleation from NPT US MC simulations of  $N = 512$  particles at  $P = 0.75$  GPa at the temperatures shown. The free energy is obtained from the full cluster size distribution using  $\beta\Delta G(n) = -\ln(P(n)) + \text{const.}$  with the condition  $\beta\Delta G(0) = 0$  fixing the value of the constant. The free energy barrier is finite at all temperatures, with the height at the lowest temperature being  $6 - 7k_B T$ . Panel (B) shows the free energy as a function of density, obtained from the negative log of the contracted distribution defined in Eq. 5.28, from the same simulations. Errors are obtained from estimates from overlapping bias windows. The double well feature at  $T = 992$  K is indicative of co-existence.

cluster size. In Fig. 5.7, the cluster size axis is truncated to  $n \leq 4$  to resolve the liquid states better.

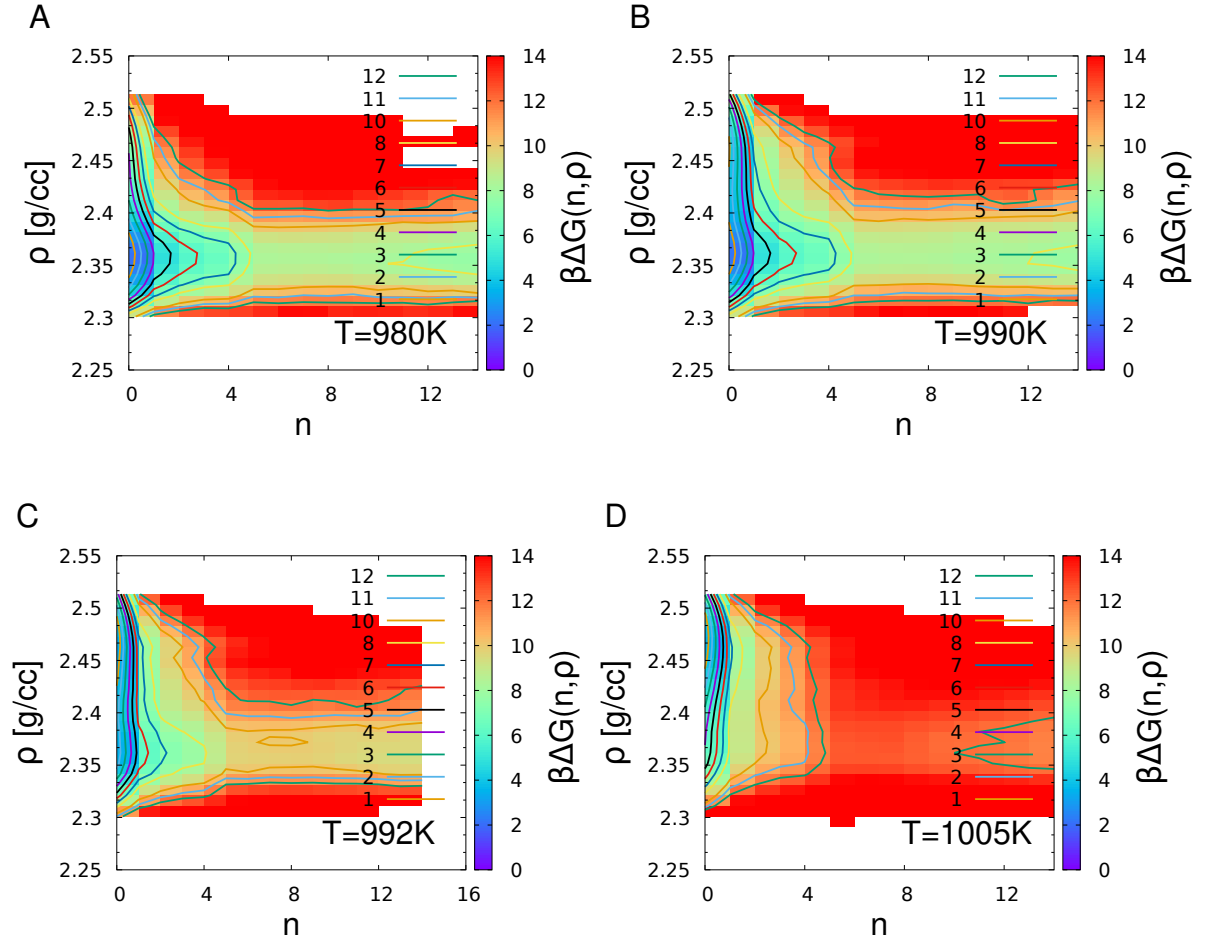


Figure 5.6: Two order parameter free energy surfaces along the  $P = 0.75$  GPa isobar from NPT USMC simulations of  $N = 512$  particles with both  $n_{\max}$  and  $\rho$  constrained. Parallel tempering swaps are performed across temperatures and across bias windows. Cluster sizes are sampled up to and including the transition state of  $n \sim 8 - 10$ .

In Fig. 5.6 (A), the low density liquid phase is found in the absence of any crystalline ordering.

### Energy and density differences between the metastable liquids

Results of histogram reweighting performed on the bivariate distribution of energy and density are shown in Fig. 5.8, where the reweighting is performed from temperatures above and below  $T = 992$ K to the target temperature of  $T = 992$ K

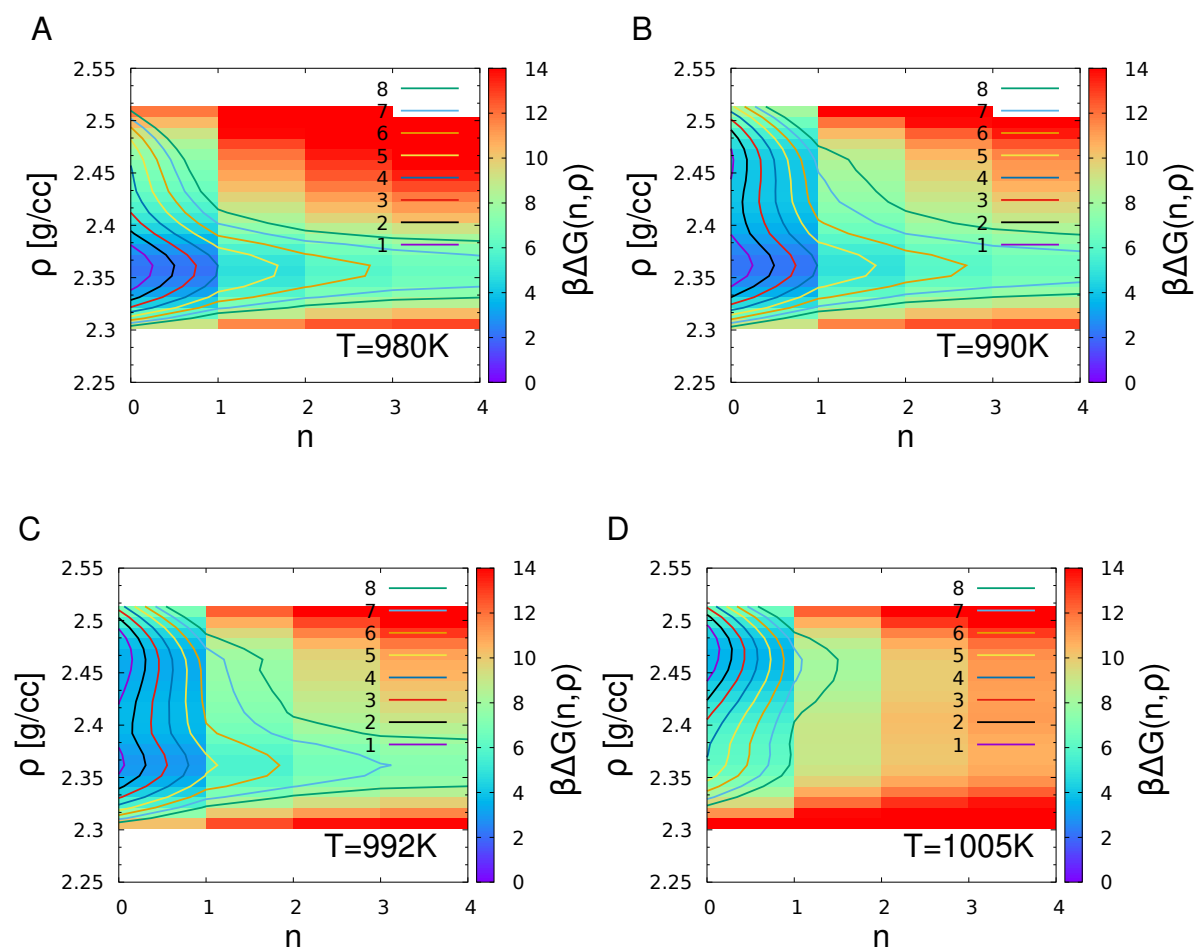


Figure 5.7: Two order parameter free energy surfaces along the  $P = 0.75$  GPa isobar from NPT USMC simulations of  $N = 512$  particles with both  $n_{\max}$  and  $\rho$  constrained. Parallel tempering swaps are performed across temperatures and across bias windows. Figure is truncated to focus on the region of  $n \leq 3$ .

and compared with the distribution obtained directly from USMC simulations at  $T = 992\text{K}$  (all for  $P = 0.75\text{ GPa}$ ). In Fig. 5.9, we show the multivariate distribu-

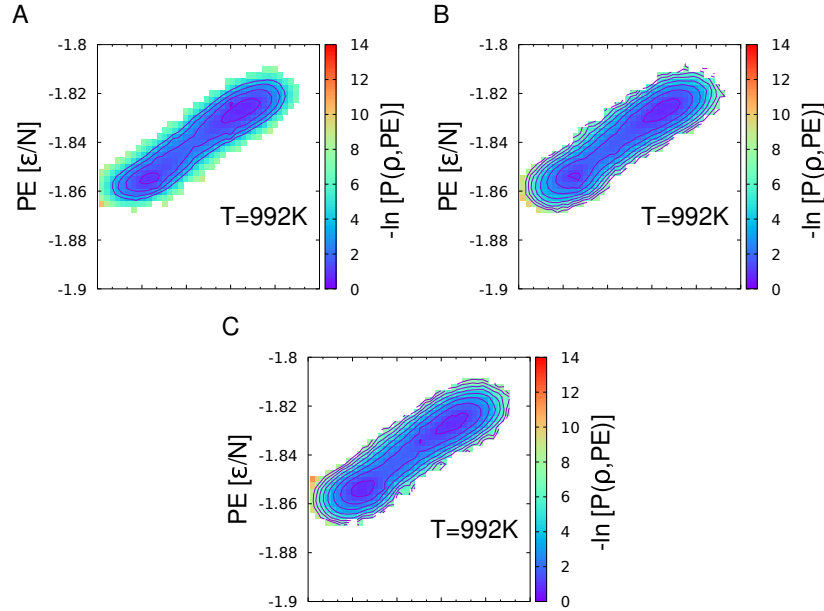


Figure 5.8:  $-\ln[P(\rho, PE)]$  at  $T = 992\text{K}$ ,  $P = 0.75\text{ GPa}$  from histogram reweighting at other temperatures across  $P = 0.75\text{ GPa}$ . (*Left:*) Re-weighted from  $T_1 = 985\text{K}$  to  $T_2 = 992\text{K}$ , (*Centre:*) raw, (*Right:*) re-weighted from  $T_1 = 995\text{K}$  to  $T_2 = 992\text{K}$ .

tion of density and potential energy per particle, subject to the same constraints as in Fig. 5.5(B). Here, one observes basins corresponding to the two liquids, a high energy-high density liquid and a low energy-low density liquid. The fact that the HDL has a higher energy and is more stable at the high temperature side of the transition, suggests that the LDL has a lower entropy or fewer favourable configurations. This behaviour is consistent with expectations derived from using the Clapeyron equation  $(dP/dT)_{LLPT} = Q/T\Delta V = \Delta S/\Delta V$  which relates the slope of the transition line to the difference in entropy and density between the two liquid phases. The implication of a negative slope for the transition line is that the lower density (higher volume) phase has a lower entropy.

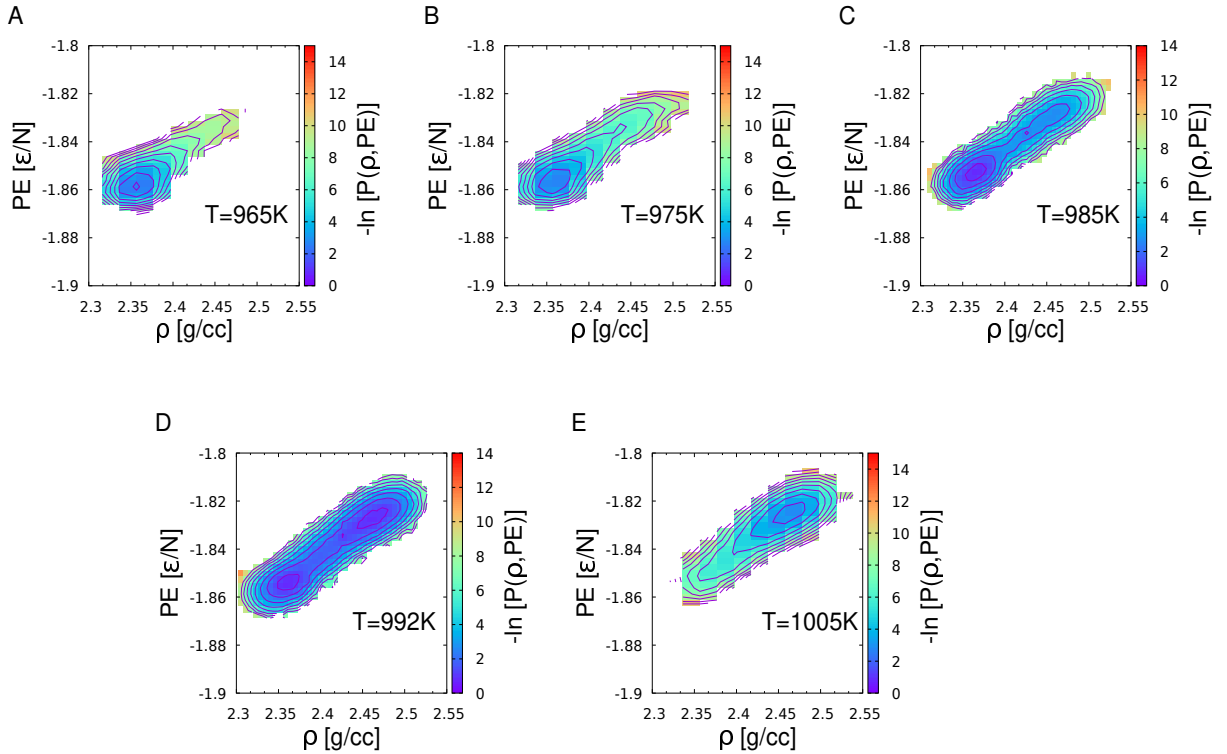


Figure 5.9: Negative log of the distribution of density and potential energy per particle obtained subject to the constraint of  $n_{\max} \leq 3$  along the  $P = 0.75$  GPa isobar at five temperatures,  $T = 965\text{K}$  (A),  $T = 975\text{K}$  (B),  $T = 985\text{K}$  (C),  $T = 995\text{K}$  (D) and  $T = 1005\text{K}$  (E). Data is obtained from NPT US MC simulations of  $N = 512$  particles. The two liquid phases differ both energetically and in density.

### 5.2.2 Convergence of simulations far from co-existence conditions

At conditions where only one liquid phase exists, i.e., away from co-existence conditions, simulations are performed with only hardwall bias on  $n_{\max}$ .

The auto-correlation functions of  $\rho$  and  $Q_6$  are shown in Figs. 5.10, 5.11, 5.12 and 5.13 for  $T = 965\text{K}$ ,  $T = 975\text{K}$ ,  $T = 1005\text{K}$  and  $T = 1015\text{K}$  at  $P = 0.75$  GPa and  $N = 512$  respectively. The decorrelation timescales are all found to be  $\tau \sim 5 \times 10^5$  MC steps and equilibration is performed, first with harmonic bias on  $n_{\max}$  for  $20 \times 10^6$  MC steps and then with hardwall bias on  $n_{\max}$  for  $60 \times 10^6$  MC steps which is equal to  $\sim 120\tau$ . Data is gathered over the subsequent  $80 \times 10^6$  MC steps.



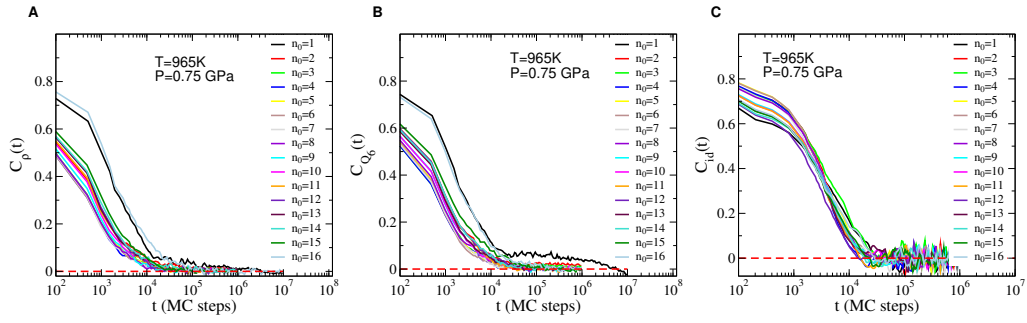


Figure 5.10: Autocorrelation of density,  $C_\rho(t)$  (Panel A),  $Q_6$ ,  $C_{Q_6}(t)$  (Panel B) and window index  $C_{id}(t)$  (Panel C) at  $T = 965\text{K}$ ,  $P = 0.75\text{ GPa}$  with  $N = 512$ .

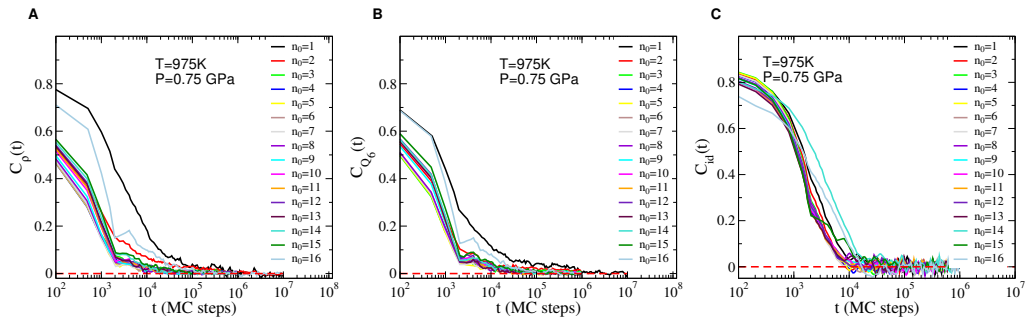


Figure 5.11: Autocorrelation of density,  $C_\rho(t)$  (Panel A),  $Q_6$ ,  $C_{Q_6}(t)$  (Panel B) and window index  $C_{id}(t)$  (Panel C) at  $T = 975\text{K}$ ,  $P = 0.75\text{ GPa}$  with  $N = 512$ .

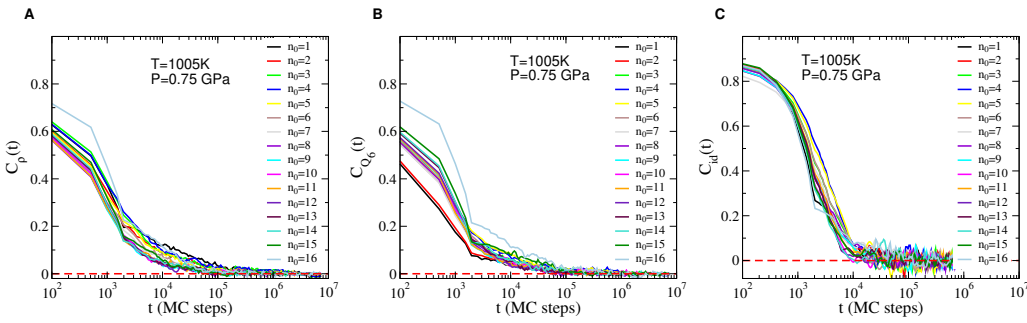


Figure 5.12: Autocorrelation of density,  $C_\rho(t)$  (Panel A),  $Q_6$ ,  $C_{Q_6}(t)$  (Panel B) and window index  $C_{id}(t)$  (Panel C) at  $T = 1005\text{K}$ ,  $P = 0.75\text{ GPa}$  with  $N = 512$ .

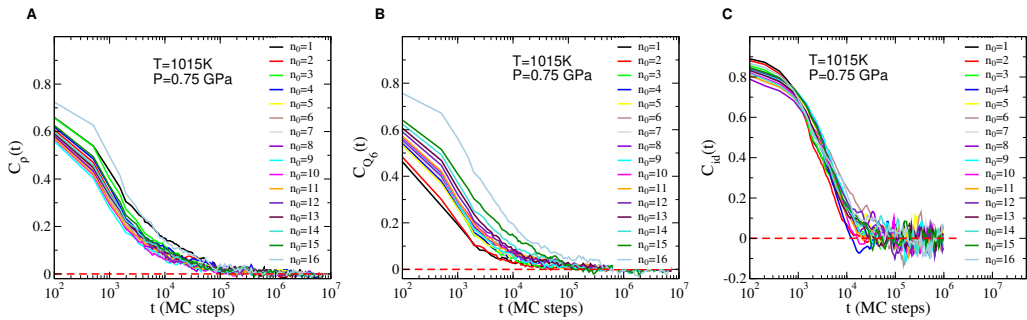


Figure 5.13: Autocorrelation of density,  $C_\rho(t)$  (Panel A),  $Q_6$ ,  $C_{Q_6}(t)$  (Panel B) and window index  $C_{id}(t)$  (Panel C) at  $T = 1015\text{K}$ ,  $P = 0.75\text{ GPa}$  with  $N = 512$ .

### 5.2.3 Equivalence of reconstruction methods far from co-existence

Away from the state points where two liquids co-exist, the two umbrella sampling schemes are expected to give the same results. Close to co-existence, the scheme of only performing parallel tempering swaps across temperature, without constraining the density, may or may not give converged estimates of the free energy on reasonable simulation timescales. This is because the temperature parallel tempering needs to effect a barrier crossing. In Fig. 5.14, we compare free energy reconstructions using both two order parameter umbrella sampling and one order parameter umbrella sampling with parallel tempering across temperature. The comparison is made either side of co-existence along the  $P = 0.75$  GPa isobar.

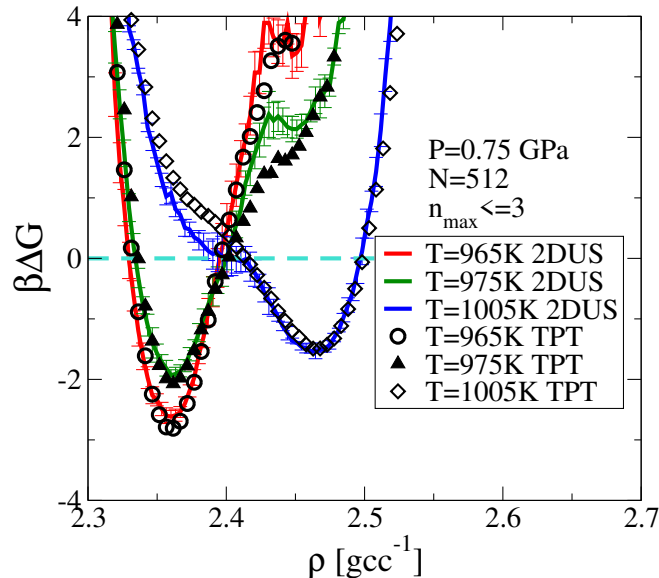


Figure 5.14: Comparison of  $\beta\Delta G(\rho)$  at different temperatures along the  $P = 0.75$  GPa isobar. The system size is  $N = 512$ . The curves labelled 2DUS are obtained from two order parameter umbrella sampling constraining  $n_{\max}$  and  $\rho$ . The curves labelled TPT are obtained from single order parameter umbrella sampling with only  $n_{\max}$  constrained. For these simulations, the sampling of density is enhanced by performing parallel tempering swaps across temperatures. All curves are shown for density histograms sampled subject to the constraint on  $n_{\max}$ .

#### Visit frequency and excursion statistics for parallel tempering swaps

Fig. 5.15 illustrates key characterisers of the parallel tempering protocol. The average length and number of excursions from each simulation window (temperature or

bias potential) as well as time spent in various states is quantified in order to understand the extent to which the exploration of order parameter space is enhanced.

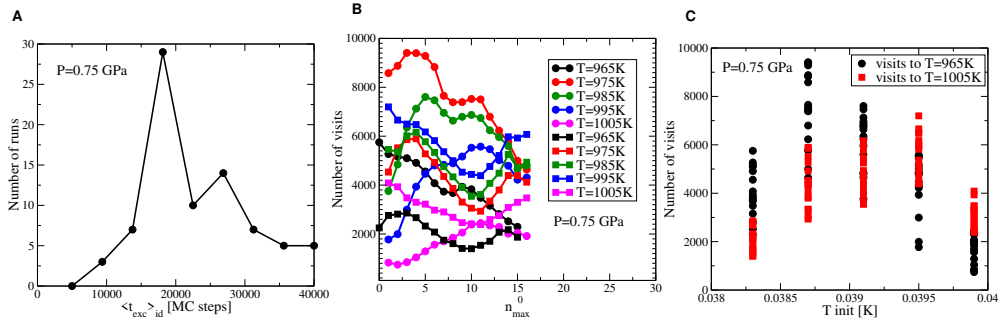


Figure 5.15: Panel A shows the average length of excursions away from the “home” temperature, before returning, for each independent simulation. Panel B shows the number of times that each independent simulation reaches either the lowest temperature (*black circles*) or the highest temperature (*red circles*). Panel C shows the number of visits to the lowest temperature (*solid circles*) or the highest temperature (*solid squares*) as a function of the  $n_{max}^0$  window index. Colours specify the “home” temperature index.

### 5.2.4 Results along other isobars

We perform a similar investigation along two other isobars in the sub-critical regime, finding that the liquid-liquid phase transition occurs at the expected state points in each case. Along one super-critical isobar, we find no evidence of a discontinuous change in the nature of the liquid. This is expected since the two liquids are expected to be indistinguishable in the supercritical regime. Fig. 5.16 and Fig. 5.17 show the autocorrelation functions and mean parallel tempering excursion lengths at state points close to co-existence for  $P = 0$  GPa and  $P = 1.5$  GPa respectively.

Co-existence conditions are also identified along the  $P = 0$  GPa and  $P = 1.5$  GPa isobars in Fig. 5.18 and Fig. 5.19. The free energy along density is shown subject to constraint on  $n_{max}$ . The  $\beta\Delta G(\rho)$  curves demonstrate the shift in the typical density of the liquid from high to low temperature and the conditions where the liquids co-exist.

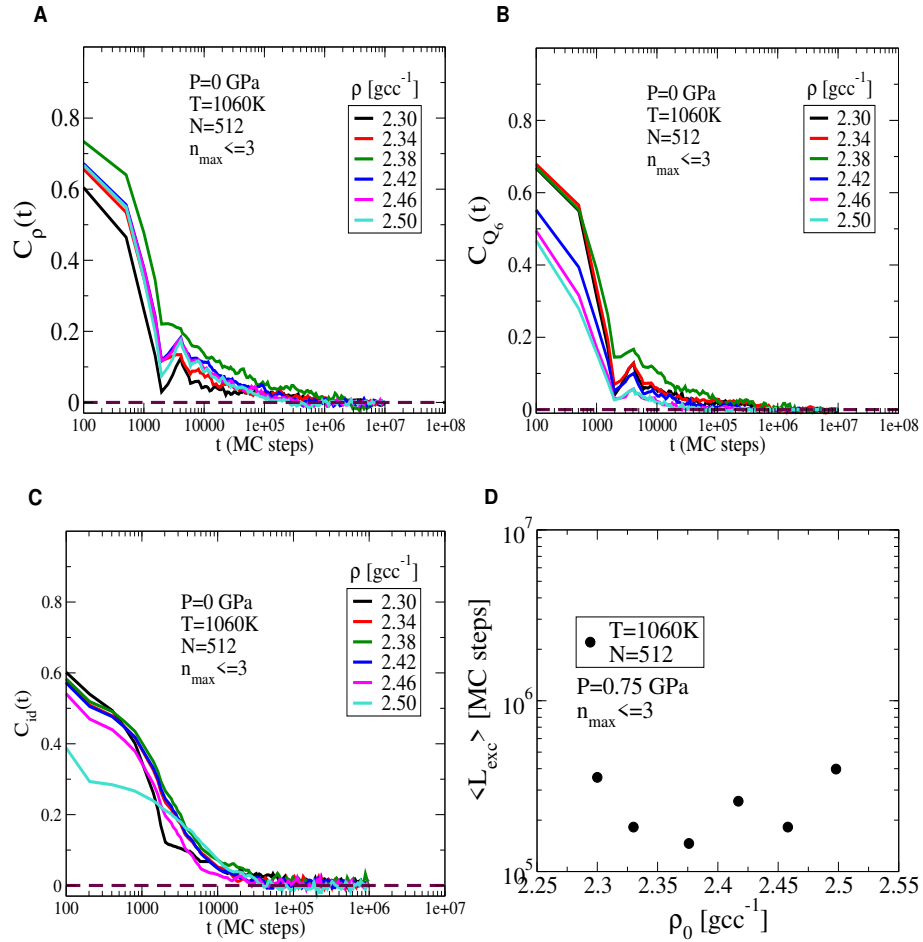


Figure 5.16: Decay of time auto-correlation function for density (Panel A),  $Q_6$  (Panel B), and for density window index (Panel C) for each of the density bias windows,  $\rho_0$ , subject to the constraint of  $n_{\max} \leq 3$  at  $T = 1060$  K,  $P = 0$  GPa. Panel D shows the mean excursion length or return time as a function of  $\rho_0$  subject to the constraint on  $n_{\max}$ .

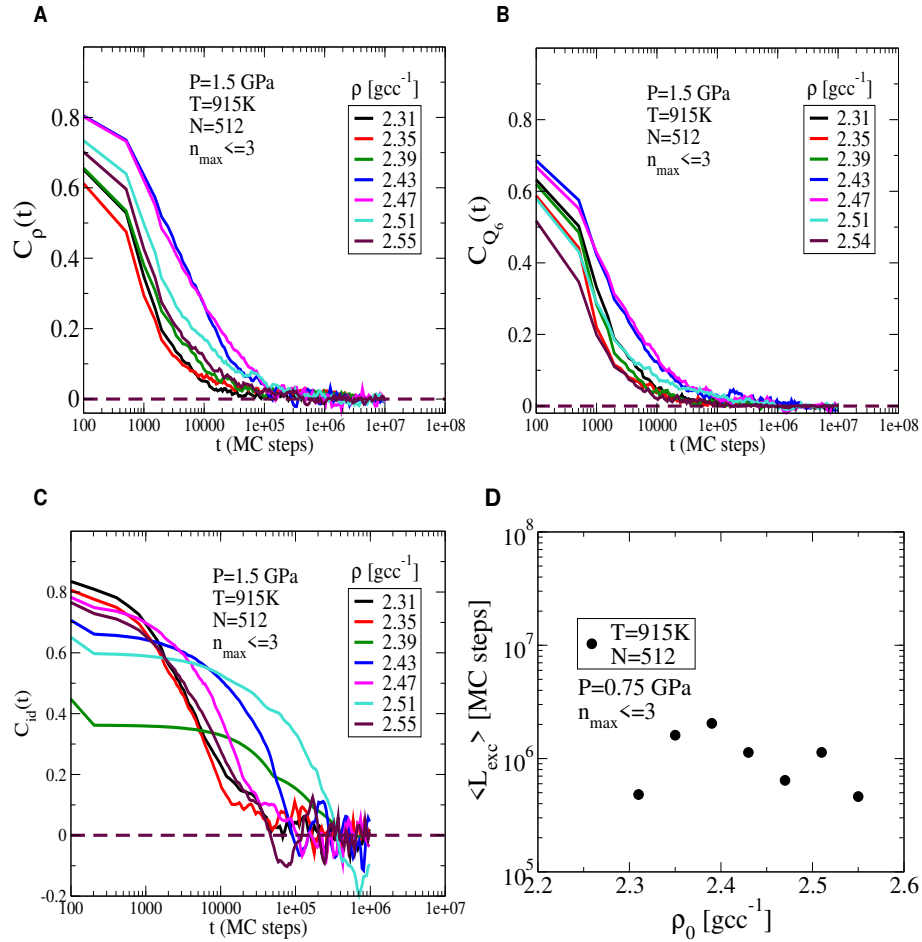


Figure 5.17: Decay of time auto-correlation function for density (Panel A),  $Q_6$  (Panel B), and for density window index (Panel C) for each of the density bias windows,  $\rho_0$ , subject to the constraint of  $n_{\max} \leq 3$  at  $T = 915$  K,  $P = 1.5$  GPa. Panel D shows the mean excursion length or return time as a function of  $\rho_0$  subject to the constraint on  $n_{\max}$ .

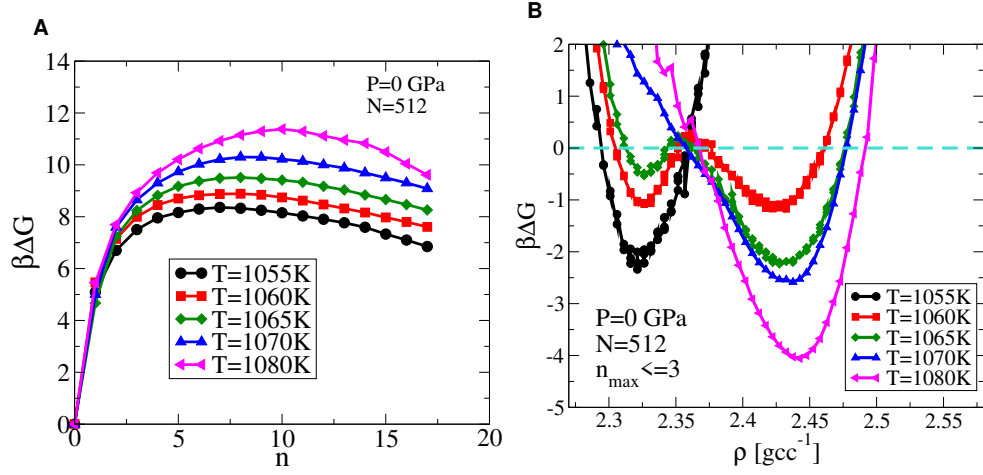


Figure 5.18: Free energy barrier to crystallisation along the  $P = 0$  GPa isobar (*Left*) and free energy as a function of density along the  $P = 0$  GPa isobar (*Right*). The free energy along density is obtained from the unweighted density distributions measured subject to constraint on  $n_{\max}$ .

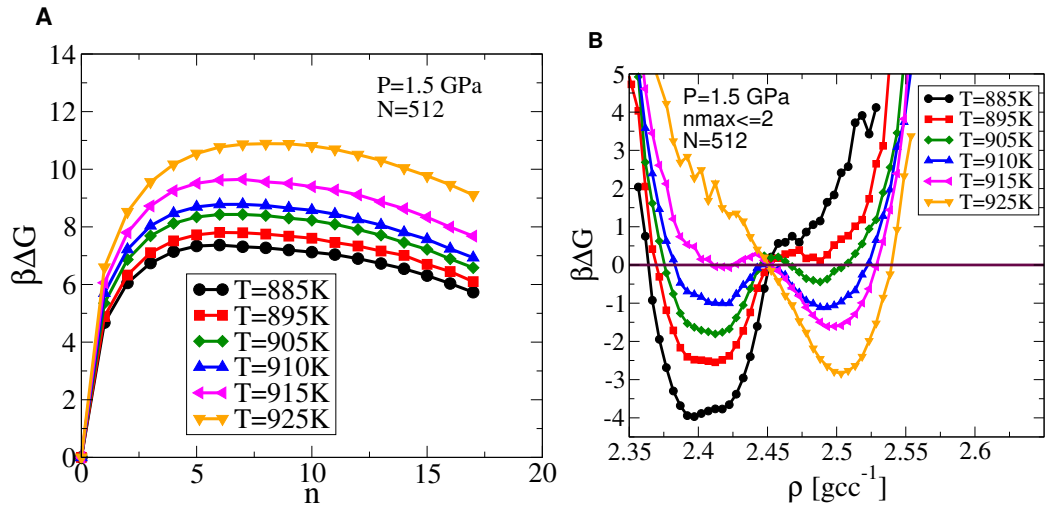


Figure 5.19: Free energy barrier to crystallisation along the  $P = 1.5$  GPa isobar (*Left*) and free energy as a function of density along the  $P = 1.5$  GPa isobar (*Right*). The free energy along density is obtained from the unweighted density distributions measured subject to constraint on  $n_{\max}$ .

### 5.2.5 Absence of bi-modality beyond the critical point

We perform similar US MC computations along different isobars crossing the LLPT line. From the equilibrium sampling distribution of the fraction of 4-coordinated particles,  $\phi_4$ , we extract the mean and standard deviation and plot as a function of temperature along isobars, shown in Fig. 5.20 (A). The fraction of 4-coordinated particles changes sharply across the LLPT line with larger fluctuations around a mean of 0.5 in the vicinity of the transition temperature. We perform USMC simulations at a negative pressure of  $P = -1.88$  GPa which is in the supercritical region of the phase diagram reported in [2]. At these state points, the putative LLPT line extends as the locus of maximum compressibility, also known as the Widom line. At these state points, no phase separation is expected to occur, though weak bi-modality may be observed at small system sizes when measured in close proximity to the critical point. In Fig. 5.20 (B), we show the equilibrium density distributions measured at different temperatures along the  $P = -1.88$  GPa isobar straddling the line of compressibility maxima. We find no hint of bimodality in the density distributions suggesting a fully continuous change in the character of the liquid across the LLPT line.

### 5.2.6 Free energy reconstructions at larger system sizes

In Fig. 5.25 we show the free energy profile as a function of density along the  $P = 0.75$  GPa isobar at four system sizes,  $N = 512$ ,  $N = 800$ ,  $N = 1000$  and  $N = 2000$ . For the case where the two liquids can have a stable interface between them, the barrier height between the two liquids is expected to scale as  $N^{2/3}$ . The barrier heights from either basin are compared with the  $N^{2/3}$  scaling to show this. The low density phase is a disordered phase, as shown by checking the scaling of  $Q_6$  in the low density basin with  $N$ . The decrease of  $Q_6$  as  $N^{-1/2}$  is indicative of a disordered phase, whereas ordered phases would have constant  $Q_6$  for all  $N$ . The autocorrelation functions are shown in Fig. 5.21, Fig. 5.22 and Fig. 5.23 for  $T = 992$  K,  $P = 0.75$  GPa. The free energy reconstruction is shown in Fig. 5.25.

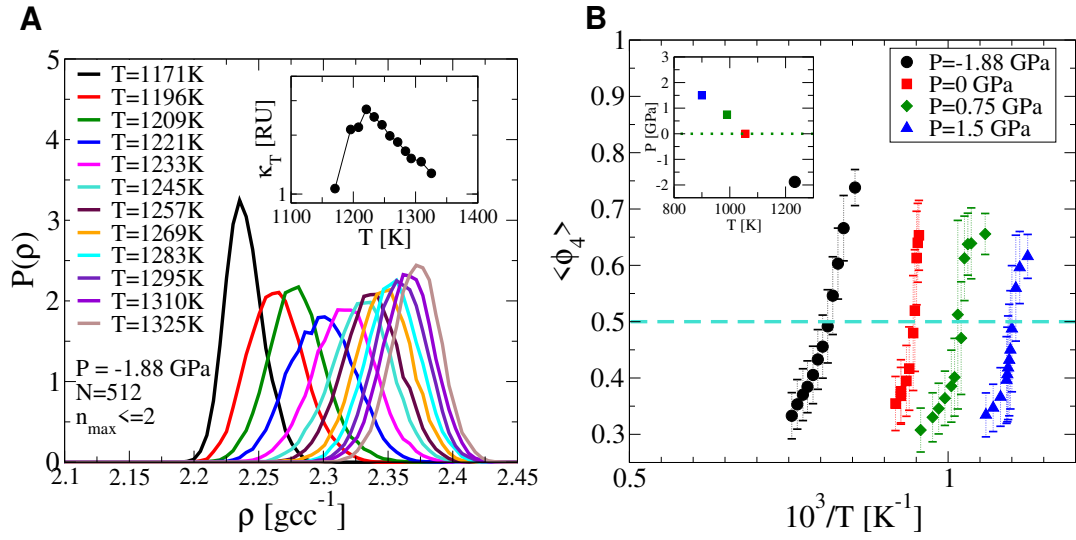


Figure 5.20: Panel (A) Equilibrium sampled density distributions from USMC simulations of  $N = 512$  particles along the  $P = -1.88$  GPa isobar. The distributions are unimodal throughout and show no hint of phase separation. *Inset* The compressibility measured for different temperatures along the  $P = -1.88$  GPa isobar showing a peak at  $T \sim 1230$  K, generally consistent with that reported by Vasisht *et al* [2]. Panel (B) The mean fraction of 4-coordinated particles from the equilibrium sampling probability measured subject to the constraint,  $n_{\max} \leq 2$  shown for 3 isobars below the critical point from NPT USMC simulations of  $N = 512$  particles.  $\phi_4$  is  $\sim 0.65$  at  $T = 965$  K,  $P = 0.75$  GPa. (*Inset*) The LLPT line obtained by estimating the point of crossing  $\langle \phi_4 \rangle = 0.5$  for each isobar. Estimates are found to be consistent with the equation of state data reported in [2].



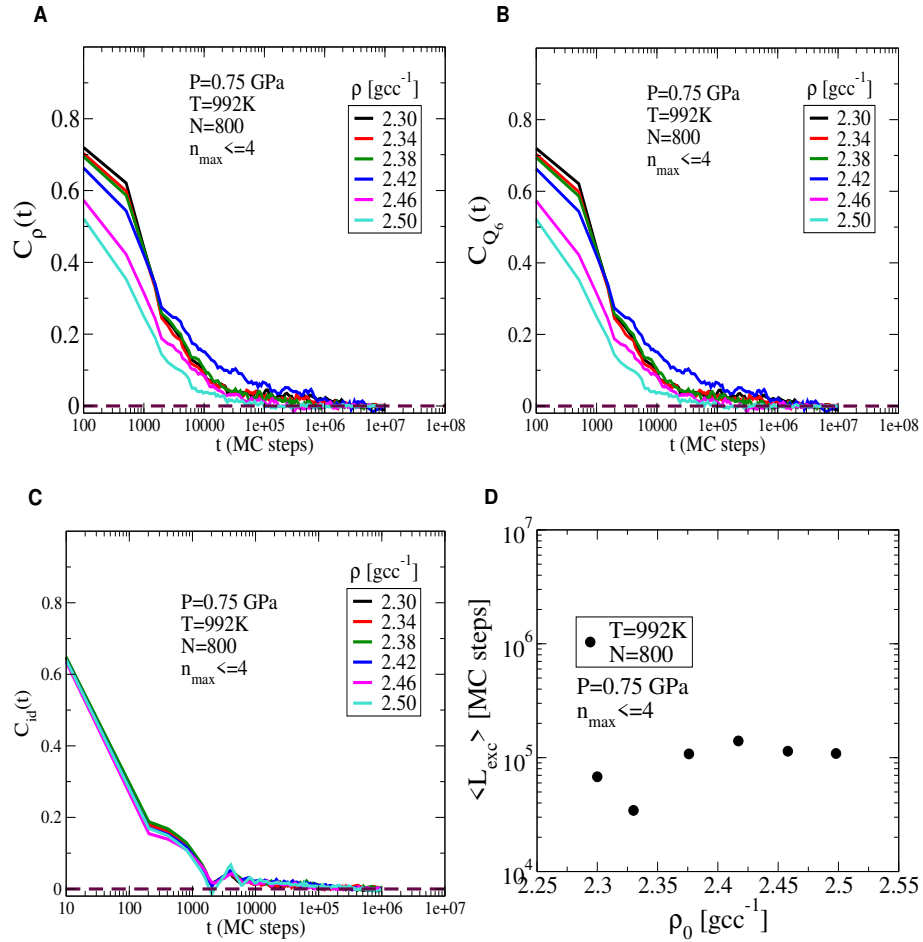


Figure 5.21: Decay of time auto-correlation function for density (Panel A),  $Q_6$  (Panel B), and for density window index (Panel C) for each of the density bias windows,  $\rho_0$ , subject to the constraint of  $n_{\max} \leq 4$  at  $T = 992$  K,  $P = 0.75$  GPa. Panel D shows the mean excursion length or return time as a function of  $\rho_0$  subject to the constraint on  $n_{\max} \leq 4$ .

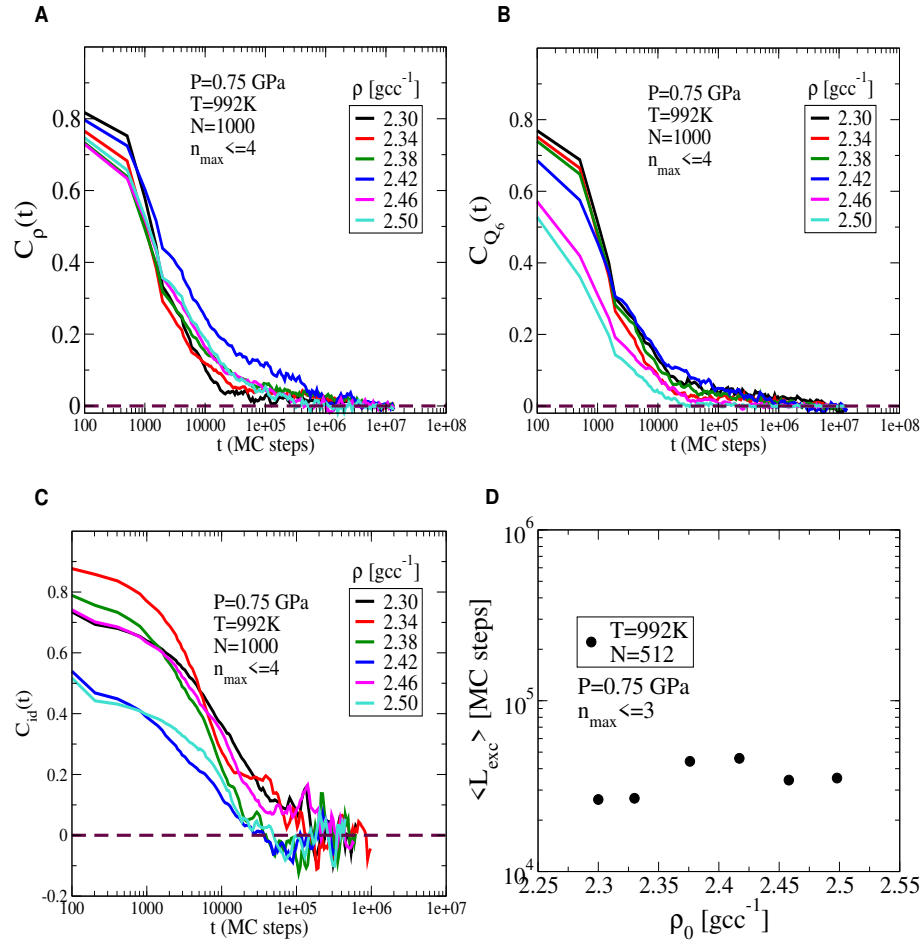


Figure 5.22: Decay of time auto-correlation function for density (Panel A),  $Q_6$  (Panel B), and for density window index (Panel C) for each of the density bias windows,  $\rho_0$ , subject to the constraint of  $n_{\max} \leq 4$  at  $T = 992$  K,  $P = 0.75$  GPa. Panel D shows the mean excursion length or return time as a function of  $\rho_0$  subject to the constraint on  $n_{\max}$ .

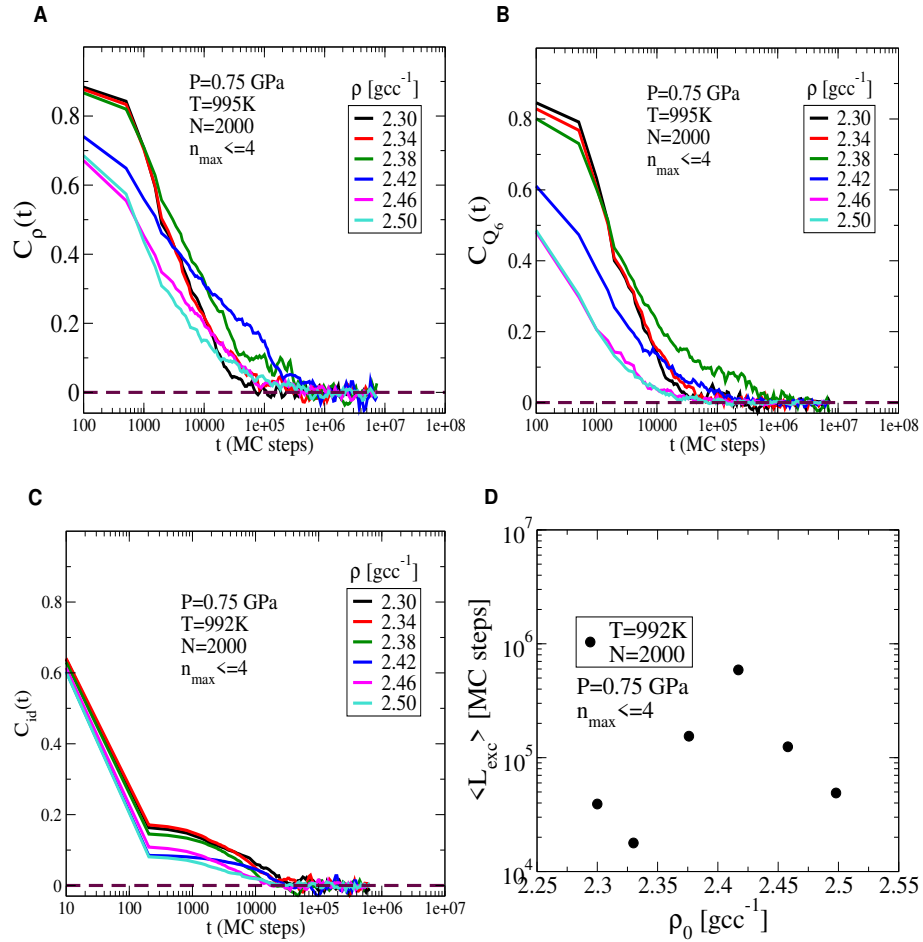


Figure 5.23: Decay of time auto-correlation function for density (Panel A),  $Q_6$  (Panel B), and for density window index (Panel C) for each of the density bias windows,  $\rho_0$ , subject to the constraint of  $n_{\max} \leq 4$  at  $T = 992$  K,  $P = 0.75$  GPa. Panel D shows the mean excursion length or return time as a function of  $\rho_0$  subject to the constraint on  $n_{\max}$ .

### Scaling of LDL basin depth with system size

Fig. 5.24 shows the decrease in basin depth as system size is increased, at  $P = 0.75 \text{ GPa}$ ,  $T = 985\text{K}$ .

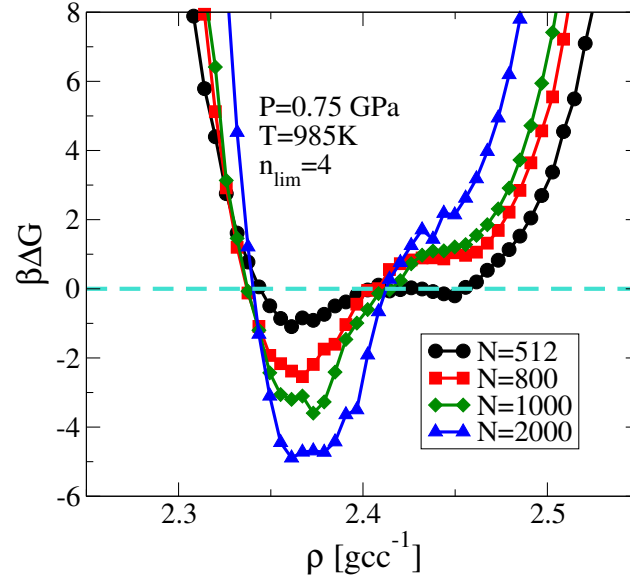


Figure 5.24:  $\beta\Delta G(\rho)$  at  $P = 0.75 \text{ GPa}$  and  $T = 985\text{K}$  from simulations and reweighting at 4 system sizes,  $N = 512, 800, 1000, 2000$ . These conditions correspond to a single stable LDL phase.

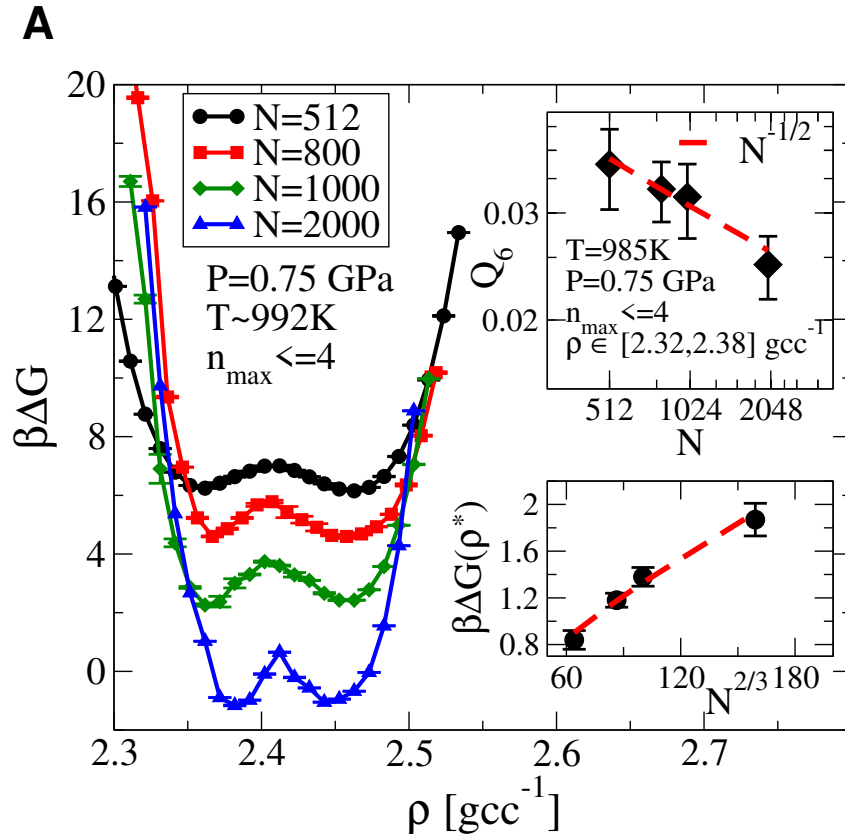


Figure 5.25:  $\beta\Delta G(\rho)$  from USMC simulations at  $T = 995$  K at  $N = 512, 800, 1000, 2000$  particles. Density is sampled subject to the constraint on  $n_{\max}$ . Bottom inset shows the height of the barrier from the LDL side (black) and the HDL side (red) as a function of system size. Both barriers scale with  $N^{2/3}$ , as expected when a stable interface can form between two phases. Top inset shows the scaling of  $Q_6$  with system size, when measured in the low density basin. The value of  $Q_6$  decreases with  $N$  as  $N^{-1/2}$ , demonstrating that the low density phase is macroscopically disordered.

$\beta\Delta G(n, \rho)$  at  $N = 800$

In Fig. 5.26 and Fig. 5.27, the two order parameter free energy,  $\beta\Delta G(n, \rho)$  is shown up to the critical cluster size and up to  $n \leq 4$ , respectively. The basin depths are greater because of the system size scaling, while  $\beta\Delta G(n)$  remains unchanged across system size.

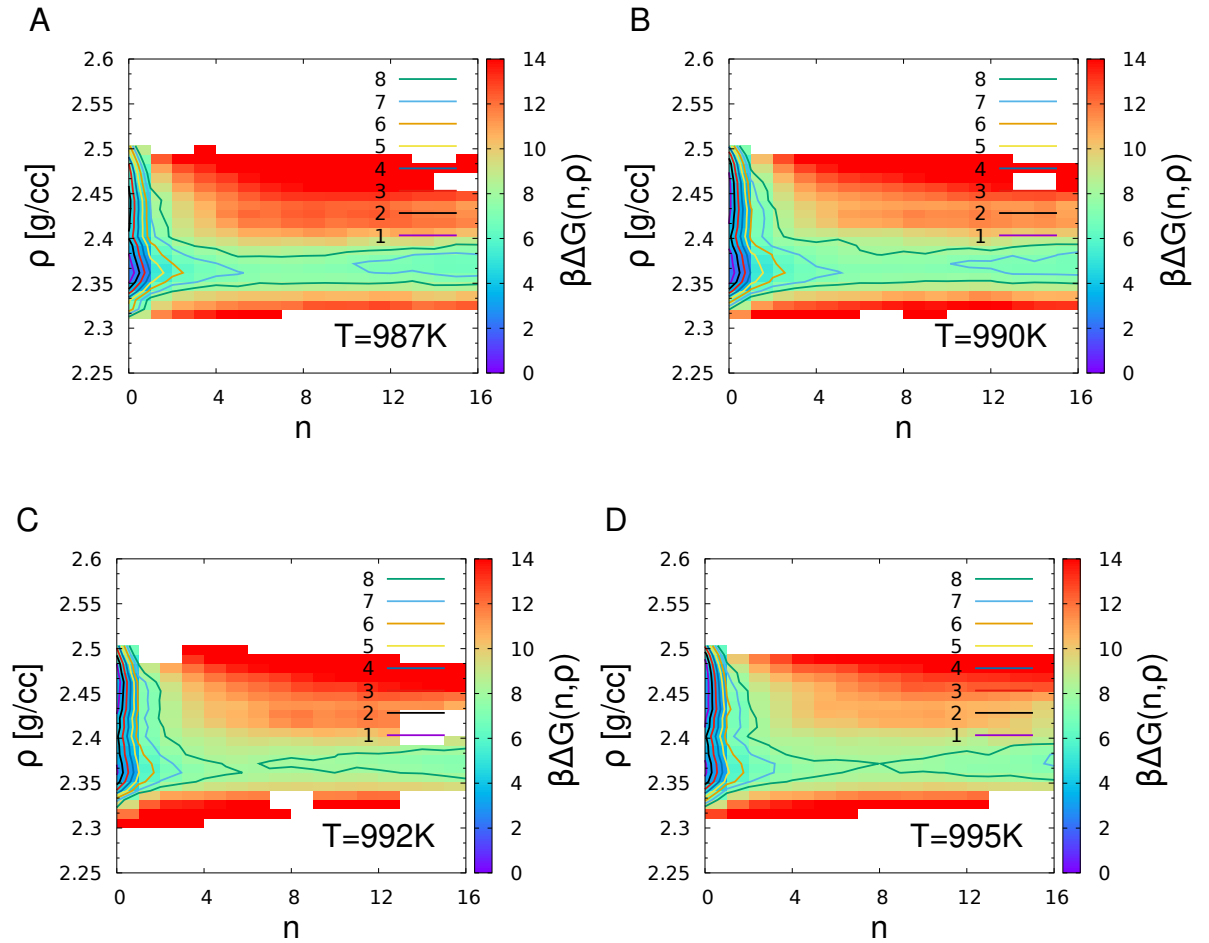


Figure 5.26: Two order parameter free energy surfaces along the  $P = 0.75$  GPa isobar from NPT USMC simulations of  $N = 800$  particles with both  $n_{\max}$  and  $\rho$  constrained. Parallel tempering swaps are performed across temperatures and across bias windows. Figure is truncated to focus on the region of  $n \leq 4$ .

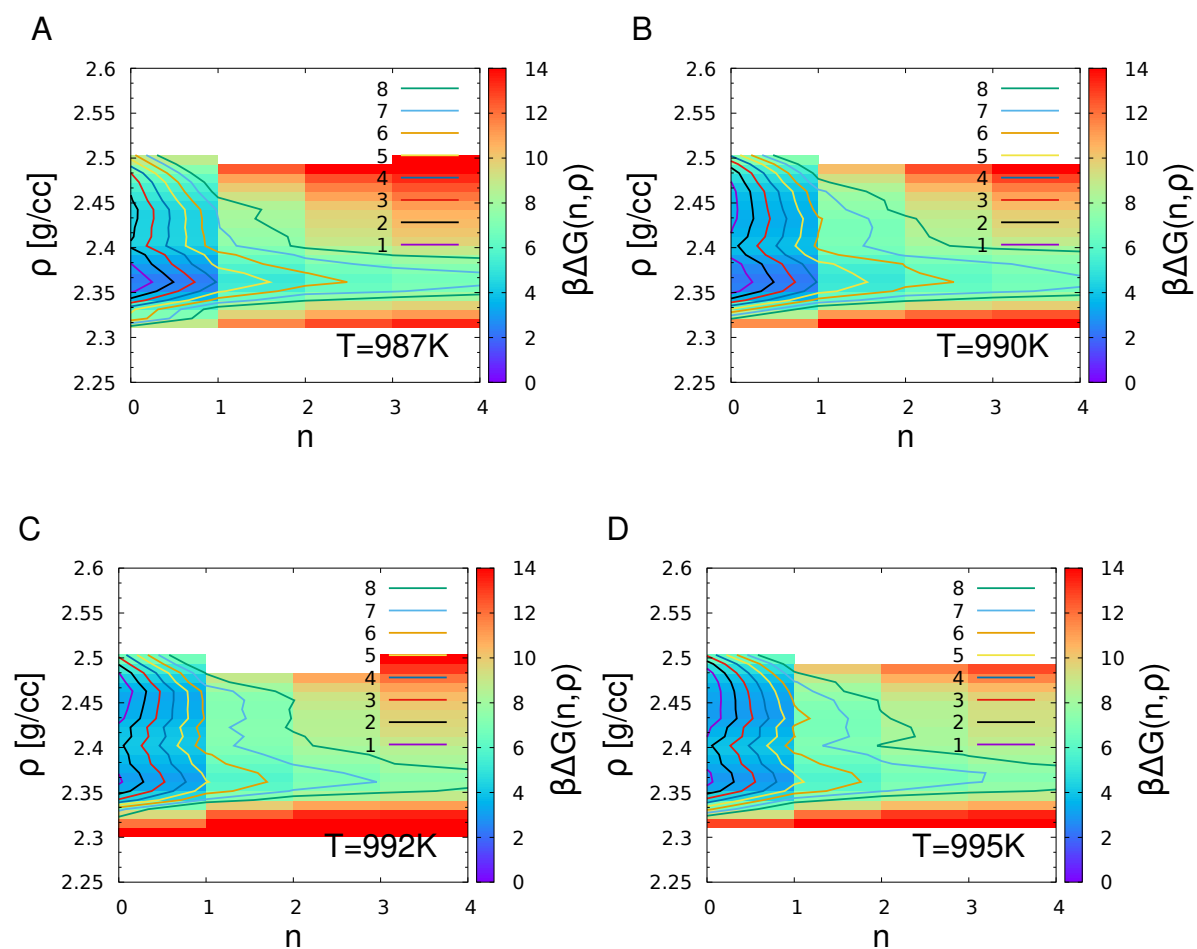


Figure 5.27: Two order parameter free energy surfaces along the  $P = 0.75$  GPa isobar from NPT USMC simulations of  $N = 800$  particles with both  $n_{\max}$  and  $\rho$  constrained. Parallel tempering swaps are performed across temperatures and across bias windows. Figure is truncated to focus on the region of  $n \leq 4$ .

### 5.2.7 Coexistence curves for the liquid-liquid phase transition

The free energy data in Fig. 5.5, Fig. 5.19 and Fig. 5.18 are combined to estimate the coexistence curves for the LDL-HDL transition in the  $T - \rho$  plane. The data in the subcritical region close to the critical point is the most interesting in this context because the value of the order parameter,  $M - M_c$  grows as  $|T - T_c|^\beta$  [272]. Thus, the difference in the density of the two liquid states grows fastest close to the critical point. This data is unfortunately not available, but with the free energy calculations performed so far, the estimated coexistence curves in the  $T - \rho$  plane are shown below in Fig. 5.28 with temperature pressure reweighting being performed to obtain estimates closer to the critical point (see Fig. 5.29) at  $T = 1080K$ ,  $P = -0.3776 GPa$  and  $T = 1087K$ ,  $P = -0.51 GPa$ . The basins corresponding to the LDL and HDL states are approximately identified and the data compiled in Fig. 5.28.

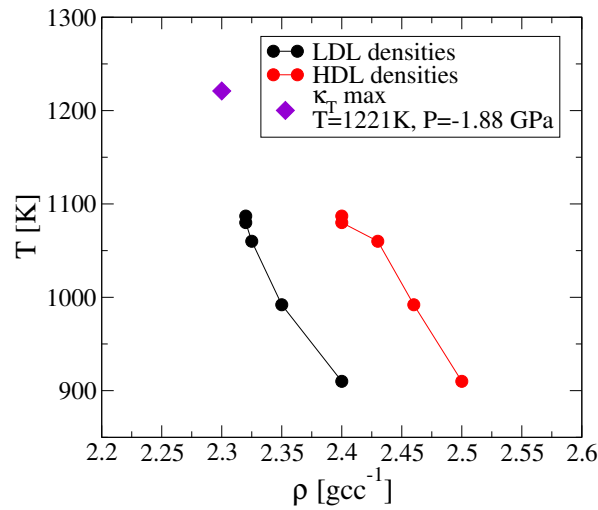


Figure 5.28: LDL and HDL densities identified from free energy calculations at coexistence conditions along the  $P = 0 GPa$ ,  $0.75 GPa$  and  $1.5 GPa$  isobars. Further data at  $P = -0.3776 GPa$  and  $P = -0.51 GPa$  is obtained by performing temperature-pressure reweighting on data from the  $P = 0 GPa$  isobar. The coexistence conditions are identified using Fig. 5.29. At  $T = 1221 K$ ,  $P = -1.88 GPa$ , the compressibility is found to be maximum (see Fig. 5.20 (A) in the thesis) and is shown on the  $T - \rho$  phase diagram for reference.



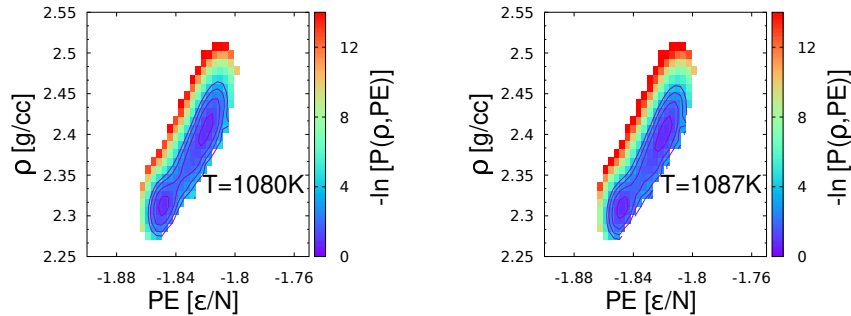


Figure 5.29:  $-\ln[P(\rho, PE)]$  at  $P = -0.3776 \text{ GPa}$  and  $P = -0.51 \text{ GPa}$  obtained by reweighting free energy data from  $P = 0 \text{ GPa}$  which is obtained with NPT USMC simulations of  $N = 512$  particles. The coexistence temperature shown here is identified at each pressure by scanning across temperatures. The LDL and the HDL basins are identified from the respective panels and compiled along with data at  $P = 0 \text{ GPa}$ ,  $0.75 \text{ GPa}$  and  $1.5 \text{ GPa}$  to produce the coexistence curve in the  $T - \rho$  plane.

## 5.3 Discussion

We perform umbrella sampling simulations simultaneously constraining the density and the cluster size for Stillinger-Weber silicon at deeply supercooled conditions. We find that the phase behaviour can be analysed revealing two well-defined metastable liquid states corresponding to two minima in the contracted free energy surface. Co-existence conditions are identified in the sub-critical part of the phase diagram that are in agreement with estimates reported previously from equation of state studies. At each of the state points considered, a clear and significant free energy barrier to nucleation is observed, ruling out the possibility that the low density liquid is a transient artefact resulting from slow, spontaneous crystallisation. We show that the liquid at the lowest temperature studied along one of the isobars is low density with a large fraction of tetrahedrally coordinated particles and zero crystalline ordering. The free energy barrier between the two liquids is found to scale with the barrier height – an important test of the thermodynamic consistency of the free energy calculations performed. We also find that the same analysis finds no evidence of phase separation when performed along an isobar in the super-critical region of the phase diagram, also consistent with the two-critical point scenario. We note that the density difference between the two liquids is small, and remains small as distance from the critical point increases, in contrast to the case of other similar network-forming liquids such as ST2 water [29, 146] and WAC

silica [166,171]. The two liquid states do not differ in density alone, as shown by a free energy reconstruction along two order parameters, density and potential energy per particle, subject to the constraint of low  $n_{\max}$ . In the family of liquids showing LLPT like behaviour, a spectrum of varying degrees of phase separation have been reported, ranging from nearly ideal mixing as in the case of mW water [55, 206], weak phase separation predicted for TIP4P water [153] and strong, entropy driven phase separation in ST2 water [207]. The degree of phase separation, as well as the appropriate order parameter that distinguishes the two liquids, is connected to the relative entropy and enthalpy differences between the two liquids, in turn connected to the locus of the LLPT and its (possibly varying) slope [206]. Microscopically, this transition is thought to be well-characterised by the timescales over which interconversion between the two possible local structures occurs [16, 194]. These are important directions to investigate further and understand both the nature of the LLPT in SW silicon and also to make connections across the range of systems displaying such behaviour.

## Chapter 6

# Kinetic reconstruction of free energies as a function of multiple order parameters

The aim of the exercise is to reconstruct a two-order parameter free energy surface using the MFPT formalism, used so far to construct free energy barriers along a single order parameter in contexts such as crystal nucleation. The MFPT formalism, used with one order parameter, is advantageous - well-suited to cases where the free energy barrier is small and constrained methods such as umbrella sampling produce artefacts for certain order parameters. The steady state probability distribution of the sampled order parameters ( $P_{st}(x, y), P_{st}(x)$ ) can be used in combination with the one-order parameter barrier ( $\beta\Delta G(x)$ ) to generalise the method to higher dimensions.

Our focus is the reconstruction of the Landau free energy surface for systems with possibly multiple metastable states. For the case of supercooled silicon, a two order parameter reconstruction that simultaneously resolves the metastable liquid state(s) and the globally stable crystalline state is desirable. The kinetic reconstruction from the mean first passage time works by considering unconstrained trajectories initiated in the metastable liquid state that crystallise after crossing the nucleation barrier, with an absorbing boundary placed in the post-critical region of the crystallinity order parameter [42, 43]. This method combines the mean first passage time with the steady state sampling probability to obtain the equilibrium sampling probability, related to the free energy by  $\beta\Delta G = -\ln P_{eq}$  without the need to ensure reversible sampling, or the need to make assumptions about the diffusivity of

the order parameter.

We consider the setup used to perform the kinetic reconstruction, with unconstrained trajectories and an absorbing bound near the deep global minimum creating a situation of constant non-zero flux to the absorbing bound. We develop the tools to extend this formalism to multiple order parameters and derive an alternate, equivalent prescription to relate steady state sampling to equilibrium sampling from first principles.

This prescription is tested on a toy model of random walkers in a potential energy landscape, in imitation of the assumed nature of the trajectories in order parameter space, namely, Brownian motion in the high-friction limit. We find that the method works effectively and efficiently for a number of different kinds of landscapes and we evaluate its efficiency and ways in which accuracy can be improved.

## 6.1 2D kinetic reconstruction method

The aim of the exercise is to attempt to reconstruct a 2D free energy surface using the MFPT formalism, which has been used so far to construct 1D free energy barriers in contexts such as nucleation. The steady state probability distribution of the sampled order parameters can be used in combination with the 1D barrier to generalise the method to higher dimensions. Here, the steps to obtain the two order parameter free energy  $\beta\Delta G(x, y)$  from the single order parameter free energy  $\beta\Delta G(x)$  (obtained using the kinetic reconstruction for example) and  $P(x, y)$  are described. This can be derived in the following way. Let us define,

$$P(x) = \int_{-\infty}^{\infty} P(x, y) dy \quad (6.1)$$

This is true for any probability distribution function  $P(x, y)$ , whether equilibrium or steady state. In equilibrium this probability can be related to free energy differences.

$$P_{eq}(x, y) = Ae^{-\beta\Delta G(x, y)} \quad (6.2)$$

This gives us

$$P_{eq}(x) = \int_{-\infty}^{\infty} P_{eq}(x, y) dy = A \int_{-\infty}^{\infty} e^{-\beta\Delta G(x, y)} dy = Ae^{-\beta\Delta G(x)} \quad (6.3)$$

The free energy along  $x$ ,  $\beta\Delta G(x)$ , can thus be related to the quantity  $P_{eq}(x)$  through the normalisation factor, which we can write as:

$$A = P_{eq}(x)e^{\beta\Delta G(x)} \quad (6.4)$$

giving,

$$P_{eq}(x, y) = P_{eq}(x)e^{\beta\Delta G(x)}e^{-\beta\Delta G(x, y)} \quad (6.5)$$

From this, one can rearrange to get

$$e^{\beta\Delta G(x) - \beta\Delta G(x, y)} = \frac{P_{eq}(x, y)}{P_{eq}(x)} \quad (6.6)$$

or,

$$\begin{aligned} \beta\Delta G(x, y) - \beta\Delta G(x) &= -\ln\left(\frac{P_{eq}(x, y)}{P_{eq}(x)}\right) \\ \beta\Delta G(x, y) &= \beta\Delta G(x) - \ln\left(\frac{P_{eq}(x, y)}{P_{eq}(x)}\right) \end{aligned} \quad (6.7)$$

Eq. 6.7 is a relation between free energy and equilibrium probabilities. Note that if the relative weights of sampling different  $y$  for a given  $x$ ,  $P_{st}(y; x)$ , are in equilibrium, then we can substitute  $P_{eq}(x, y)$  with the measured  $P_{st}(y; x)$  in Eq. 6.7 to obtain  $\beta\Delta G(x, y)$ . We need to define  $P_{st}(x) = \int dy P_{st}(y; x)$  for the denominator in Eq. 6.7 to do so. In this case  $\beta\Delta G(x)$  needs to be obtained independently, from some other method like umbrella sampling along  $x$  or the kinetic reconstruction from the MFPT.

One can compare the measured free energy from (say) the single order parameter reconstruction along  $x$ , Eq. 6.9, with the quantity  $G(x)$  which is given by:

$$e^{-\beta\Delta G(x)} = \int_{-\infty}^{\infty} e^{-\beta\Delta G(x, y)} dy \quad (6.8)$$

$$\begin{aligned} B(x) &= -\frac{1}{P_{st}(x)} \left[ \int_x^b P_{st}(x') dx' - \frac{\tau(b) - \tau(x)}{\tau(b)} \right] \\ \beta\Delta G(x) &= \beta\Delta G(x=1) + \ln\left(\frac{B(x)}{B(1)}\right) - \int_1^x \frac{dx'}{B(x')} \end{aligned} \quad (6.9)$$

One should therefore get  $\Delta G(x) = G_p(x)$ . Eq. 6.7 is the result that allows the extension of single order parameter free energies to multiple order parameters. However,

as we will see, this can be used as-is only when sampling along the other order parameters is Boltzmann. When this is not the case, corrections need to be used to obtain the correct free energy, which are discussed in detail in Sec. 6.3.

## 6.2 Description of test system

In this section we describe the system on which we test this method. Random walks on a potential energy landscape are used to mimic the behaviour of trajectories in order parameter space. The potential energy function is equivalent to the free energy landscape explored by trajectories in order parameter space. First the model potential landscape is described, following which the random walk scheme is described with details of the various boundary conditions

### Model potential landscape

A potential of the form in Eq. 6.10 set up (see Fig 6.1).  $N$  non-interacting particles initialised at  $x = 0$  and different  $y$  sampling the Boltzmann distribution. In each MC sweep,  $N$  walkers are chosen with uniform random probability and displaced by a random amount  $dx, dy \in [-S : +S, -S : +S]$ . Here, the value of  $S = 10^{-3}$  is used.

$$\begin{aligned} V_1(x, y) &= -C_1 \left( e^{\left[ \frac{(x-x_1)^2}{\sigma x_1} + \frac{(y-y_1)^2}{\sigma y_1} \right]} \right); V_2(x, y) &= -C_2 \left( e^{\left[ \frac{(x-x_2)^2}{\sigma x_2} + \frac{(y-y_2)^2}{\sigma y_2} \right]} \right) \\ V_3(x, y) &= -C_3 \left( e^{\left[ \frac{(x-x_3)^2}{\sigma x_3} + \frac{(y-y_3)^2}{\sigma y_3} \right]} \right); V_4(x, y) &= +C_4 \left( e^{\left[ \frac{(x-x_4)^2}{\sigma x_4} + \frac{(y-y_4)^2}{\sigma y_4} \right]} \right) \end{aligned}$$

$$V(x, y) = V_1(x, y) + V_2(x, y) + V_3(x, y) + V_4(x, y) \quad (6.10)$$

We have defined the potential such that the barrier along  $x$  of 0.1 and a barrier along  $y$  of 0.04. This constrains our choice of temperatures to be of the order of  $\sim 0.01$  to get effective barrier heights of the order of  $1 - 10 k_B T$  along the  $x$  direction. This is keeping with our expectation for supercooled silicon at the state points of interest.

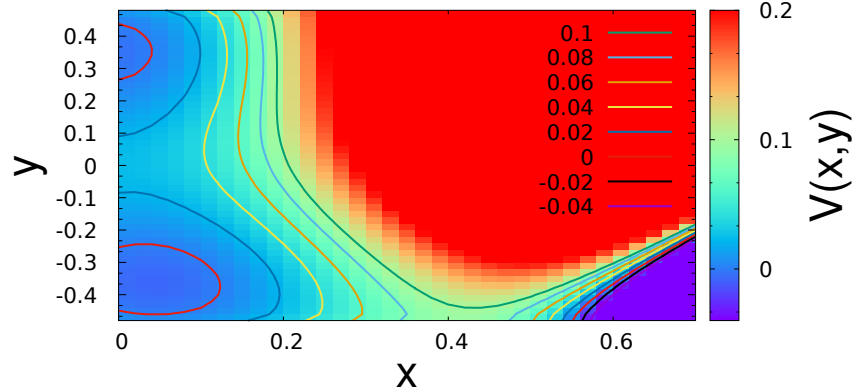


Figure 6.1: The model potential energy landscape for Eq. 6.10.

## Defining Monte Carlo moves

A reflecting boundary condition at  $x = 0$ , absorbing boundary condition at  $x = x_b = 0.75$  for all  $y$ . For the reflecting boundary condition,  $x_{new} = -x_{new}$  if  $x_{new} < 0$ . No boundary conditions are imposed along the  $y$  – axis. Additional harmonic cost potential  $V_c(y) = k_c(|y| - 0.45)^2$  applied to keep random walkers in  $y \in [-0.5, 0.5]$ . Trial particle displacements are accepted or rejected using a Boltzmann weight for the change in energy for every trial move. For this, the “temperature” of the system is varied to compare results. the number of independent trajectories is varied to test effects of more or less sampling.

### 6.2.1 MFPT and steady state probability

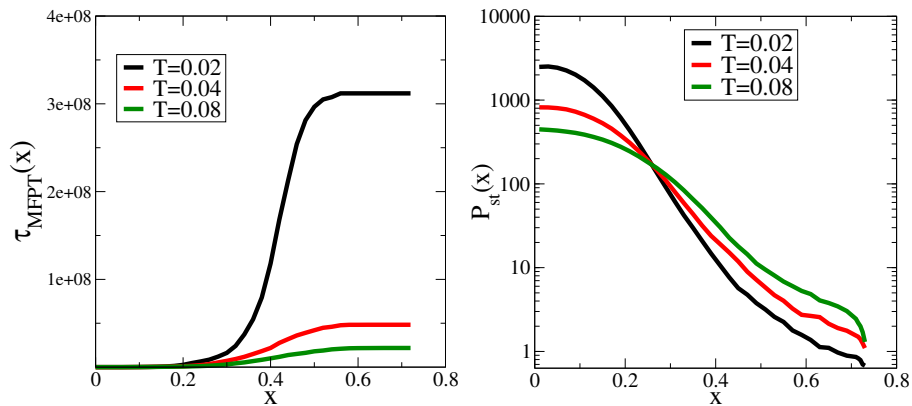


Figure 6.2: Mean first passage time,  $\tau_{MFPT}(x)$  and the steady state probability  $P_{st}(x)$ . Absorbing boundary condition at  $x = 0.75$ , reflecting boundary condition at  $x = 0$ . Number of walkers is  $N = 500$ , giving fairly smooth data.

### 6.2.2 1D free energy barrier

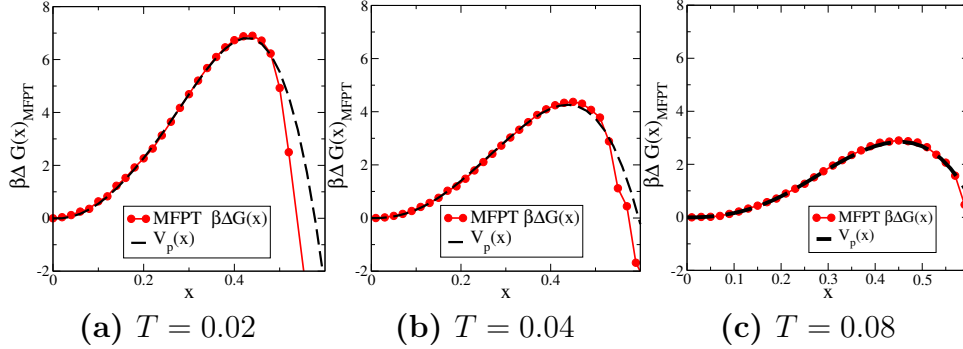


Figure 6.3: The 1D free energy  $\Delta G(x)$  obtained from Eq. 6.9. For reference, the potential dependence is shown by integrating out the  $y$  variation (Eq. 6.8). The number of walkers is  $N = 500$  and the absorbing boundary condition is placed at  $x = 0.75$ . Error is minimised by shifting the curves such that overlap is maximised at the top of the barrier.

### 6.2.3 Sampling along orthogonal order parameters

Here we compare the sampling along the  $y$  direction to the a slice of the potential along  $y$ . We vary different conditions, the temperature, initial distribution of random walkers, number of random walkers and the height of the barrier along  $x$  to understand what affects sampling efficiency along the orthogonal order parameter. Given that the formalism described so far assumes Boltzmann sampling along  $y$ , we test this assumption in this section.

We find that the assumption does not hold, with systematic deviations that depend on the barrier height and the point of initialisation of the trajectories, but not the Monte Carlo step size or the extent of sampling. This is shown in Fig. 6.4.



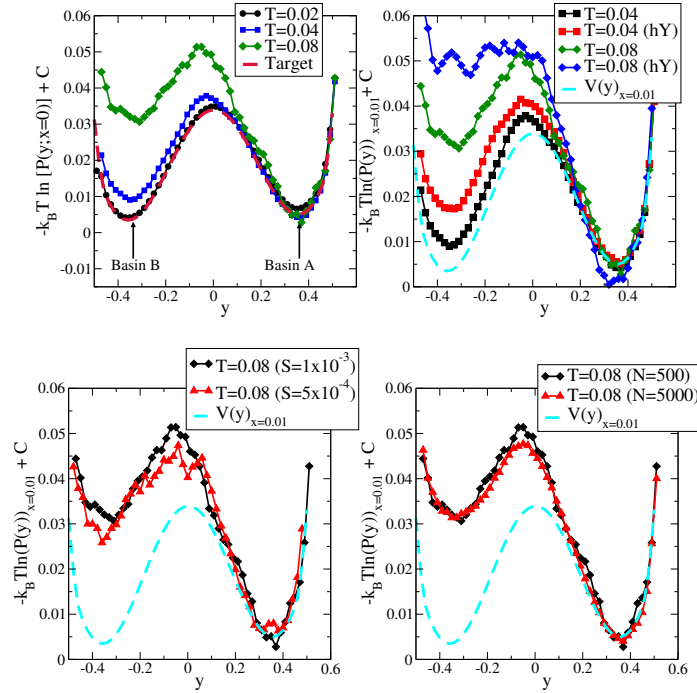


Figure 6.4: Slices at  $x = 0.01$  (i.e.,  $x \in [0.0, 0.02]$ ) are taken along the  $y$  direction.  $-k_B T \log(P(x = 0.01, y))$  is compared with  $V(x = 0.01, y)$ . *Top left:* The temperature is varied - at higher temperatures, the deviation from  $V(y)$  is higher. *Top right:* Results from initialisation at  $x = 0, y \in [-0.5, 0.5]$  with a uniform probability distribution is compared with those from initialisation at  $x = 0, y \in [0.2, 0.4]$  (labelled "hY"). *Bottom left:* The magnitude of largest possible trial displacement is varied. *Bottom right:* The number of independent random walk trajectories is varied.

#### 6.2.4 Summary - Sampling errors for high T/low barrier cases

Errors in the sampling along the orthogonal order parameter,  $y$ , arise from compounding factors:

- When the barrier along  $x$  is low for the temperature applied, the net flux to the absorbing boundary prevents Boltzmann sampling along  $y$  for  $x < x^*$  (where  $x^*$  is the  $x$  corresponding to the barrier).
- When the time taken for a random walker to sample the  $y$  order parameter is comparable to the typical timescale of barrier crossing - this effect is amplified when the initial distribution of random walkers is very different from the Boltzmann distribution along  $y$ .

- We attempt to correct these errors - 3 attempts are described, successively improving our understanding.

## 6.3 Relating steady state sampling to equilibrium sampling

We found in the previous section that sampling in the presence of a low barrier and a constant non-zero flux across it, that the measured sampling along  $y$  deviates from the underlying Boltzmann distribution. In this section we will discuss our approach to correct for this systematic deviation by considering the effect of the flux on sampling. In order to understand this, we begin by considering the rate(s) of traversal across different regions of the order parameter space in the scheme developed in the context of transition state theory [31, 32]. The rate is naturally related to fluxes and to sampling probability, with the relation described in the literature [33, 34]. We go through the necessary steps to arrive at a result that relates equilibrium sampling in the presence of flux balance to steady state sampling in the presence of unequal forward and backward fluxes. This expression is used to then obtain the free energies from steady state sampling achieved in unconstrained simulations.

### 6.3.1 Partition functions over trajectories and defining the rate

Analogous to the sampling probability for points,  $P(x)$ , one can construct the distribution functional for trajectories, which is written for deterministic trajectories as [32]

$$P[\{x_t\}] = P(x_0) \prod_{0 < t' \leq t} \delta(x_{t'} - x_{t'}(x_0)). \quad (6.11)$$

Above,  $P(x_0)$  is the instantaneous sampling probability of an initial condition,  $x_0$ , (generally specifying both positions and momenta),  $x_{t'}(x_0)$  is the point obtained at  $t'$  upon applying the update rule for the initial condition  $x_0$  through a time interval  $t'$ .

Finally, the LHS is the probability of observing a trajectory, i.e., the sequence  $\{x_0, x_1, \dots, x_t\}$ , denoted  $P[\{x_t\}]$ .

For stochastic trajectories, with transition matrix  $\mathbf{T}$  [273]

$$P[\{x_t\}] = P(x_0) \prod_{0 < t' \leq t} \mathbf{T}_{x_{t'-1}x_{t'}} \quad (6.12)$$

For two regions of phase space,  $A$  and  $B$ , the probability of observing a trajectory of length  $t$  connecting them is

$$P_{AB}[\{x_t\}] = h_A(x_0)P[\{x_t\}]h_B(x_t), \quad (6.13)$$

where  $h_A(x) = 1$  if  $x \in x_A$  and 0 otherwise, and  $h_B(x) = 1$  if  $x \in x_B$  and 0 otherwise.  $A$  and  $B$  are treated as absorbing conditions in order to not overcount trajectories or re-crossings [274]. When counting a trajectory that connects  $A$  and  $B$ , we need to only include the segment between last exit from  $A$  and first entry into  $B$ . Likewise, trajectories exiting  $B$  and returning to  $B$  are not counted. Further, trajectories that exit, and return to,  $A$  multiple times before finally visiting  $B$ , cannot be treated as single trajectories counting  $A$  and  $B$ . Summing over all trajectories gives us a partition function

$$Z_{AB}(t) = \sum_{\{x_t\}} h_A(x_0)P[\{x_t\}]h_B(x_t) \quad (6.14)$$

The partition function for trajectories starting  $A$  and ending anywhere is summed over all trajectories to give

$$Z_A = \sum_{\{x_t\}} h_A(x_0)P[\{x_t\}] = \sum_{x_0} h_A(x_0)P(x_0) \quad (6.15)$$

The second equality follows when the distribution  $P(x)$  is an equilibrium distribution, and the probability of each  $x_i$  is drawn from it [32]. The set of all trajectories of length  $t$  will visit each  $x_i$  according to the Boltzmann distribution, and the expressions are equivalent upto normalisation. Note that the trajectory length dependence is dropped from the expression for  $Z_A$  as a result. For deterministic trajectories which are specified entirely by initial positions and momenta, this becomes a weight on initial conditions alone:

$$Z_{AB}(t) = \sum_{x_0} h_A(x_0)P(x_0)h_B(x_t) \quad (6.16)$$

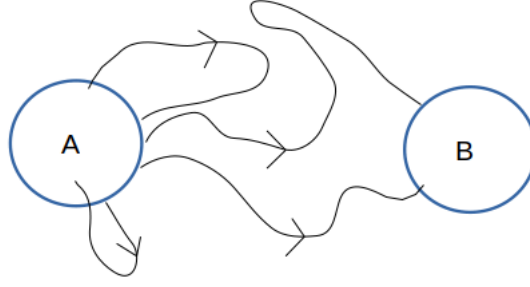


Figure 6.5: Schematic of trajectories going from state  $A$  to state  $B$

The initial conditions here would specify both positions and momenta. For stochastic trajectories, such as those in a Monte Carlo simulation, we need to treat the probability of observing each path explicitly.  $Z_{AB}(t)$  measures the correlation between population at  $A$  at  $t = 0$  and population at  $B$  at time  $t$  [31]. The rate  $k_{AB}$  is related to the ratio of partition functions as:

$$\frac{Z_{AB}(t)}{Z_A} = \frac{\langle h_A(x_0)h_B(x_t) \rangle}{\langle h_A(x_0) \rangle} = k_{AB}t \quad \tau_{mol} \ll t \ll \tau_{reaction} \quad (6.17)$$

for timescales  $t$ , intermediate between that of microscopic/molecular motion and the timescale for the completion of the reaction/depletion from  $A$  [32]. We can see this as follows:

$$C(t) = \frac{Z_{AB}(t)}{Z_A}, \quad (6.18)$$

where  $C(t)$  is the correlator that describes how perturbations to the equilibrium distributions  $\langle h_A(x) \rangle_{eq}$  and  $\langle h_B(x) \rangle_{eq}$  relax. The asymptotic value of  $C(t)$  is  $\langle h_B(x) \rangle_{eq}$ . We assume that there is one characteristic relaxation time for  $C(t)$ , governed by the slowest process, which is assumed to be the transit from  $A$  to  $B$ . Then, we can write:

$$C(t) \approx \langle h_B(x) \rangle_{eq} (1 - e^{-t/\tau_{rxn}}), \quad (6.19)$$

where  $\tau_{rxn}$  is the characteristic relaxation time. For small  $t$ , we can Taylor expand for  $t/\tau_{rxn}$  and get

$$C(t) \approx \langle h_B(x) \rangle_{eq} \frac{t}{\tau_{rxn}} \quad (6.20)$$

In order to find out what  $\tau_{rxn}$  is, we need to make a further assumption as discussed in Ref. [31]. We need to assume that the time evolution of the number of particles in  $A$  or  $B$ , given by

$$N_A(t) = \sum_{i=1}^N h_A(x_i(t)) \quad (6.21)$$

is governed by a linear macroscopic rate law of the form:

$$\frac{d}{dt}N_A(t) = -k_{AB}N_A(t) + k_{BA}N_B(t) \quad (6.22)$$

For the conserved system, and noting that  $\tau_{rxn} = (k_{AB} + k_{BA})^{-1}$  [31], we can write the following equations for  $N_A = \langle h_A(x) \rangle_{eq}$ ,  $N_B$  and  $k_{AB}$

$$N_A + N_B = 1 \quad (6.23)$$

$$N_A = N_B \frac{k_{BA}}{k_{AB}} \quad (6.24)$$

$$k_{AB} = N_B (k_{AB} + k_{BA}) = \langle h_B(x) \rangle_{eq} \tau_{rxn}^{-1} \quad (6.25)$$

Replacing for  $\langle h_B(x) \rangle_{eq} \tau_{rxn}^{-1}$  in Eq. 6.20 gives us our result that  $C(t) = k_{AB}t$  for  $t \ll \tau_{rxn}$ .

Note that we have assumed a purely two state reaction here in which to write the Eq. 6.17. In Sec. 6.3.3, we will discuss whether the same linear approximation holds for a case with more than two states.

One can expand this to weight it over the ensemble of trajectories:

$$k_{AB}t = \frac{Z_{AB}(t)}{Z_A} = \frac{\sum_{\{x_t\}} h_A(x_0) P[\{x_t\}] h_B(x_t)}{\sum_{\{x_t\}} h_A(x_0) P[\{x_t\}]} \quad (6.26)$$

**Justification for a linear dependence of  $Z_{AB}(t)/Z_A$  in Eq. 6.17**

### 6.3.2 Effect of modifying the sampling probability on the rate

The main question we need to address is what type and magnitude of changes to the path ensemble and/or the sampling probability leave  $k_{AB}$  unaltered. Consider the expression for the rate

$$k_{AB}t = \frac{Z_{AB}(t)}{Z_A} = \frac{\sum_{\{x_t\}} h_A(x_0) P[\{x_t\}] h_B(x_t)}{\sum_{\{x_t\}} h_A(x_0) P[\{x_t\}]} \quad (6.27)$$

For stochastic trajectories, we have written the probability of observing a trajectory  $\{x_t\}$  as:

$$P[\{x_t\}] = P(x_0) \prod_{0 < t' \leq t} \mathbf{T}_{x_{t'-1}, x_{t'}} \quad (6.28)$$

If the sampling probability of states is modified under conditions of steady state,  $P(x_0) \rightarrow f(x_0)P(x_0)$ , and the transition probabilities are altered  $\mathbf{T} \rightarrow \mathbf{T}'$  the rate expression is modified to

$$k_{AB}^f t = \frac{\sum_{x_0} h_A(x_0) f(x_0) P(x_0) \prod_{1 < t' \leq t} \mathbf{T}'_{x_{t'-1}, x_{t'}} h_B(x_t)}{\sum_{x_0} h_A(x_0) f(x_0) P(x_0)} \quad (6.29)$$

Clearly in the general case,  $k_{AB} \neq k_{AB}^f$ . In the trivial case of constant modification,  $f(x_0) = f$ , and for the case of deterministic trajectories, where the weight on trajectories can be replaced with the weight on initial conditions,  $k_{AB} = k_{AB}^f$ .

In order to clarify this point, consider if the order parameter separating  $A$  and  $B$  is such that  $x_A < x_B$ , then the functions  $h_A$  and  $h_B$  can be replaced with step functions

$$\begin{aligned} h_A(x) &= \theta(x_A - x) \\ h_B(x) &= \theta(x - x_B) \end{aligned} \quad (6.30)$$

Evaluating the rate expression now gives

$$k_{AB}^f t = \frac{\sum_{x_0} \theta(x_A - x_0) P(x_0) f(x_0) \theta(x_t - x_B)}{\sum_{x_0} \theta(x_A - x_0) P(x_0) f(x_0)} \quad (6.31)$$

The condition for  $k_{AB} = k_{AB}^f$  now reduces to  $f(x_0) = f_A \forall x \in x_A$ .

The modification being relatively constant in the neighbourhood of  $A$  is sufficient for the rates in the two cases to be unchanged. Notably, variations in  $f(x_0)$  outside of  $x_A$  do not alter the rate,  $k_{AB}$ .

We will discuss the scenario for stochastic trajectories for a specific case of interest to us. We start by describing how the addition of an additional absorbing condition,  $C$ , effectively changes the stochastic transition matrix near the absorbing boundary, by a modification of microscopic transition probabilities in the neighbourhood of  $C$ . For this sort of change to  $\mathbf{T}$  and the consequent change to  $P[\{x_t\}]$ , we identify conditions for which  $Z_{AB}(t)/Z_A$  is unaltered.

### 6.3.3 Adding an alternate absorbing condition – steady state flux

We now consider the case of an alternate absorbing condition being introduced. We then have a situation, like in the kinetic reconstruction using the mean first passage time, where the sampling in each  $A$ ,  $B$  is achieved in a condition of steady state flux to the new absorbing condition. We are treating each of  $A$  and  $B$  also as absorbing conditions to define the quantities, but a single long trajectory shuttling between  $A$  and  $B$  can be treated as independent segments (provided exits out of  $A$  and  $B$  are decorrelated [274]) in order to measure  $Z_{AB}(t)$  and  $Z_A$ . The introduction of a new absorbing state to the state space will lead to a modification of the transition matrix  $\mathbf{T} \rightarrow \mathbf{T}'$  in addition to changing the sampling probability of initial states  $P(x_0) \rightarrow f(x_0)P(x_0)$ . Consider Fig. 6.6 for a pictorial description. The first question to

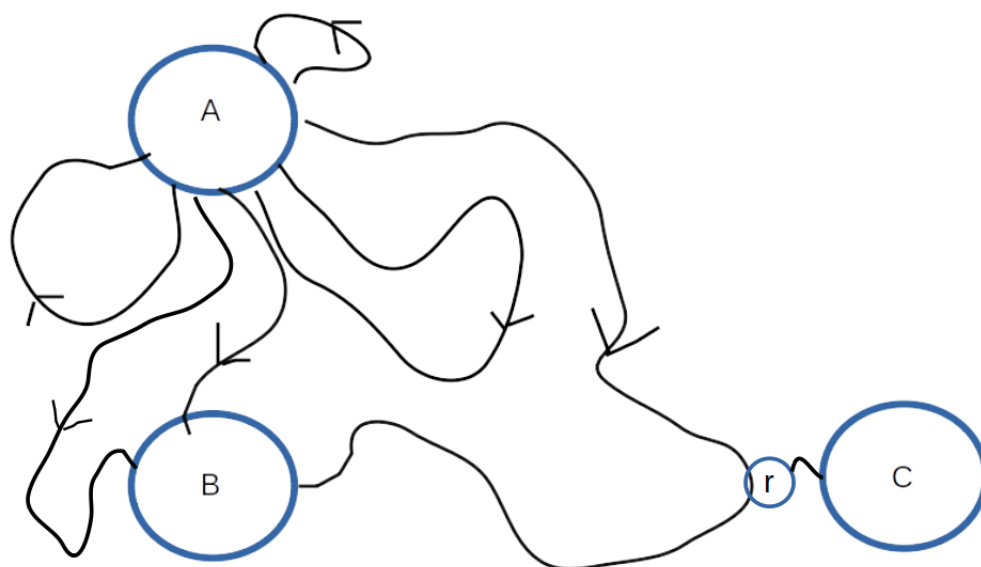


Figure 6.6: Schematic depicting a case with an additional absorbing state introduced at  $C$ . Trajectories exiting  $A$  can now end up in either of the three absorbing states.

address is whether this case also allows a linear form for  $C(t)$ . In order to check this, we need to consider the modified linear rate laws and determine if  $k_{AB}$  can be

similarly related to  $\tau_{rxn}$  as in Eq. 6.25. We consider the following:

$$\frac{d}{dt}N_A(t) = -k_{AB}N_A(t) - k_{AC}N_A(t) + k_{BA}N_B(t) \quad (6.32)$$

$$\frac{d}{dt}N_B(t) = -k_{BA}N_B(t) - k_{BC}N_B(t) + k_{AB}N_A(t) \quad (6.33)$$

$$\frac{d}{dt}N_C(t) = k_{AC}N_A(t) + k_{BC}N_B(t) \quad (6.34)$$

We also have a different conservation rule  $N_A(t) + N_B(t) + N_C(t) = 1$ . Given that this system has a long time accumulation at  $C$ , we need to define the scaled variables  $N_A/(1 - N_C)$  and  $N_B/(1 - N_C)$  to write a conservation rule for  $A$  and  $B$  alone. Using this, and

$$N_B(k_{BA} + k_{BC}) = N_A k_{AB}, \quad (6.35)$$

to replace for  $N_A$  now gives

$$\begin{aligned} k_{AB} &= N_B(k_{BA} + k_{AB} + k_{BC}) \\ k_{AB} &= \langle h_B(x) \rangle_C (k_{BA} + k_{AB} + k_{BC}) \end{aligned} \quad (6.36)$$

giving us a different expression for  $\tau_{rxn} = (k_{BA} + k_{AB} + k_{BC})^{-1}$ . The expression for  $k_{AB}$  in Eq. 6.36 is comparable to the last expression in Eq. 6.25. Note that  $\langle h_B(x) \rangle_{eq}$  in Eq. 6.20 has been replaced here with  $\langle h_B(x) \rangle_C$  indicating that the asymptotic value of  $C(t)$  for this 3 state case is not necessarily the same as for the 2-state case of Eq. 6.25. Replacing the corresponding terms in Eq. 6.20 recovers  $C(t) = k_{AB}t$  for  $t \ll \tau_{rxn}$ .  $\tau_{rxn}$  is the bounding timescale over which  $Z_{AB}(t)/Z_A$  is linear in  $t$  with rate constant  $k_{AB}$ . We stress that this is one case for which the linear approximation is retained. In general, the expression for  $\tau_{rxn}$  is different, but one should recover the linear approximation for the corresponding case.

Now, we can write that outward transition probabilities for a state neighbouring the new absorbing state, labelled  $r$ , are altered by the introduction of the new absorbing state  $C$ . For simplicity, we consider a single such state  $r$ ; this choice should not affect our conclusions. The probability or weight of a path labelled  $\{x_t\}$  becomes:

$$P'[\{x_t\}] = f(x_0)P(x_0) \prod_{1 < t' \leq t} [\mathbf{T}_{x_{t'-1}x_{t'}} + \delta_{r,t'-1}(\mathbf{T}'_{x_{t'-1}x_{t'}} - \mathbf{T}_{x_{t'-1}x_{t'}})] \quad (6.37)$$

Intuitively, the integral over all paths is changed when the fraction of paths between any  $i$  and the state  $j$  of interest, that pass through  $r$  is significant. Otherwise the term in the product remains unchanged. A more exact statement can be made by



considering the shortest time taken by a path from  $A$  to  $B$  that also passes through  $r$ .

### Conditions for invariance of the path probability

Consider the expression for  $Z_{AB}(t)$

$$Z_{AB}(t) = \sum_{\{x_t\}} h_A(x_0) P[\{x_t\}] h_B(x_t) \quad (6.38)$$

For the modified path probability we have

$$\begin{aligned} Z'_{AB}(t) &= \sum_{\{x_t\}} h_A(x_0) P'[\{x_t\}] h_B(x_t) \\ Z'_{AB}(t) &= \sum_{\{x_t\}} h_A(x_0) f(x_0) P(x_0) \prod_{0 < t' \leq t} [\mathbf{T}_{x_{t'-1}x_{t'}} + \delta_{r,t'-1}(\mathbf{T}'_{x_{t'-1}x_{t'}} - \mathbf{T}_{x_{t'-1}x_{t'}})] h_B(x_t) \end{aligned} \quad (6.39)$$

Let us denote the minimum time taken to go from  $A$  to  $r$  and then to  $B$  as  $t_{ArB}^{sp}$ . This is the time taken to go through all three points, taking the shortest possible paths. Clearly we find that if  $t < t_{ArB}^{sp}$ , then  $Z'_{AB}(t) = Z_{AB}(t)$ . The expression is effectively unchanged because none of the paths from  $A$  to  $B$  passed through  $r$ . If the steady state flux from  $A$  to  $B$  is achieved over this shorter timescale, the measured rate will remain the same.

In the framework of transition state theory, the condition for a constant/plateau value for  $k_{AB}$  is that measurements are made over a timescale  $\tau_{mol} \ll t \ll \tau_{reaction}$ .  $\tau_{reaction}$  is the overall relaxation time, given by  $1/(k_{AB} + k_{BA})$  in a two-state reaction [31]. Here, we introduce an alternate upper bound for  $t$ , namely  $t_{ArB}^{sp}$ . For this approximation, subject to a condition that  $C$  be far from typical paths connecting

$A$  and  $B$ , we arrive at the same conclusion as for deterministic trajectories:

$$\begin{aligned}
k_{AB}^f t &= \frac{\sum_{\{x_t\}} \theta(x_A - x_0) P'[\{x_t\}] \theta(x_t - x_B)}{\sum_{\{x_t\}} \theta(x_A - x_0) P'[\{x_t\}]} \\
k_{AB}^f t &= \frac{\sum_{x_0} \sum_{\{x_t\}} \theta(x_A - x_0) P(x_0) f(x_0) \prod_{1 < t' \leq t} \mathbf{T}_{x_{t'-1} x_{t'}} \theta(x_t - x_B)}{\sum_{x_0} \sum_{\{x_t\}} \theta(x_A - x_0) P(x_0) f(x_0) \prod_{1 < t' \leq t} \mathbf{T}_{x_{t'-1} x_{t'}}} \\
k_{AB}^f t &= \frac{f_\lambda}{f_\lambda} k_{AB} t
\end{aligned} \tag{6.40}$$

where, we have again made the demand that  $f(x) = f_\lambda$  for  $x \in A$ , without imposing any restrictions on the form of  $f(x)$  for other values of  $x$ . In writing the second equation above, we have made the assumption that paths between  $A$  and  $B$  do not pass through the neighbourhood of the new absorbing state we have introduced.

We have shown that changes to the steady state/sampling probability and the underlying dynamics do not change the rate  $k_{AB}$ , in the specific case of adding an additional absorbing condition. We have two main approximations that need to be satisfied:

- The steady state sampling be related to the equilibrium sampling by a constant factor  $P_{st}(A) = f_\lambda P_{eq}(A)$  **only** within the region  $A$ .
- The new absorbing boundary,  $C$ , needs to be far enough from the states  $A$  and  $B$  under consideration. If this condition is satisfied, the fraction of paths between  $A$  and  $B$  that pass through the neighbourhood of  $C$  is small enough to be neglected over a reasonable timescale.

However, the total flux from  $A$  to  $B$  does change accompanying the change in sampling probability. We reframe the expression for the rate in terms of the total flux in the coming section. Thereafter, using the result of unaltered rate, we arrive at a relation between steady state sampling in the presence of altered fluxes to the underlying equilibrium sampling, given that  $k_{AB}$  is unaltered. The equations are framed in the context of macroscopic states,  $A$  and  $B$ . However, we shall see in Sec. 6.4 that the results can be used without such coarse-graining as well.

### Relating rate to effective total flux

In this section, we discuss how to evaluate the time derivative of  $C(t)$  to get the rate:

$$k_{AB} = \frac{d}{dt}C(t) = \frac{d}{dt} \left[ \frac{\langle h_A(x_0)h_B(x_t) \rangle}{\langle h_A(x_0) \rangle} \right] \quad \tau_{mol} \ll t \ll \tau_{rxn} \quad (6.41)$$

At steady state, Eq. 6.41 can be written as:

$$k_{AB} = \frac{\langle \Phi_{AB} \rangle_{x_0}}{\langle h_A \rangle_{x_0}} \quad (6.42)$$

In order to understand how one goes from Eq. 6.41 to Eq. 6.42, we follow the arguments described in Refs. [40, 274] to evaluate the expression for the rate. We note that similar arguments are also contained in other works [33, 34, 274]. Recall that trajectories may start anywhere – those that start at  $A$  eventually exit  $A$  with probability 1. Also, since the LHS is a constant,  $k_{AB}$ , the time derivative that we evaluate will not have a time-dependence or a dependence on the initial time. In order to evaluate the ensemble average here, we define the following quantities:

$$t_{\Omega}^b(x_0) = -\max [\{t|x_t \in \Omega \forall t \leq 0\}] \quad (6.43)$$

$$t_{\Omega}^f(x_0) = +\min [\{t|x_t \in \Omega \forall t \geq 0\}] \quad (6.44)$$

These times are the first-entry times of a trajectory from  $x_0$  to  $\Omega$  ( $A$  or  $B$ ) when followed either backward ( $b$ ) or forward ( $f$ ) in time. The minus sign used when defining  $t_{\Omega}^b(x_0)$  ensures both times have positive values. Using these, we define history functions that specify the origin of a trajectory passing through  $x_0$  when integrated backwards or forwards in time. We use this to define the following indicator functions:

$$h_{A,B}^b(x_0) = \begin{cases} 1 & \text{if } t_A^b(x_0) < t_B^b(x_0) \\ 0 & \text{otherwise} \end{cases} \quad (6.45)$$

$$h_{A,B}^f(x_0) = \begin{cases} 1 & \text{if } t_A^f(x_0) < t_B^f(x_0) \\ 0 & \text{otherwise} \end{cases} \quad (6.46)$$

With these indicator functions, we can now consider a case where  $x_0$  is on the boundary of  $B$  and make the following type of replacement

$$h_A(x_{-t}) = h_{A,B}^b(x_0) \quad (6.47)$$

The time derivative of  $h_A(x_0)h_B(x_t) = h_A(x_{-t})h_B(x_0)$  can then be evaluated at  $t = 0$

$$\begin{aligned} \left. \frac{d}{dt} \right|_{t=0} h_A(x_0)h_B(x_t) &= \left. \frac{d}{dt} \right|_{t=0} h_A(x_{-t})h_B(x_0) \\ &= h_{A,B}^b(x_0) \dot{x} \delta(x_0 - x_B), \end{aligned} \quad (6.48)$$

where  $x_B$  is the left boundary of  $B$ . The time derivative operates on  $x$  through the chain rule. The RHS above quantifies the fraction of trajectories about to enter  $B$ , that had their origin in  $A$ . The delta function acts to specify the point at which the time derivative is evaluated. Only those trajectories for which  $\dot{x}$  is positive at the boundary to  $B$  are counted. In order to obtain an expression that can be implemented numerically, this is then re-written as:

$$\left. \frac{d}{dt} \right|_{t=0} h_A(x_0)h_B(x_t) = h_{A,B}^b(x_0) \lim_{\Delta t \rightarrow 0} \left( \frac{1}{\Delta t} \theta(\Delta t - t_B^f(x_0)) \right) = \Phi_{AB}(x_0) \quad (6.49)$$

The step function above indicates trajectories that will reach  $B$  within the next infinitesimal timestep,  $\Delta t$ . The ensemble average over paths connecting  $A$  and  $B$  is now an ensemble average over  $x_0$  for trajectories that will enter  $B$  within an interval  $[0, \Delta t]$ , which have their origin in  $A$  at some unspecified time  $-t$ . Clearly, for some  $x_0$  far from the boundary of  $B$ , there will be no contribution towards this flux.  $\langle \Phi_{AB} \rangle$  is thus the number of trajectories entering  $B$  in the interval  $[0, \Delta t]$ , having been initiated in  $A$  at some point in the past. At steady state this quantity does not depend on the start time for the window, only the duration  $\Delta t$ . The length of the trajectories also do not matter at steady state, but only under the assumption of trajectories being much shorter than  $\tau_{rxn}$ .

The denominator  $\langle h_A(x_0) \rangle$  in Eq. 6.41 is the number of trajectories initiated from  $A$ . We can now write the expression for the rate, relating it to the steady state flux per-unit-time of trajectories from  $A$  to  $B$ , as a fraction of the trajectories initiated in  $A$ .

$$k_{AB} = \frac{\langle \Phi_{AB} \rangle_{x_0}}{\langle h_A \rangle_{x_0}} \quad (6.50)$$

Trajectories entering  $B$  contribute to the flux,  $\Phi_{AB}$ , if and only if its origin is  $A$

rather than  $B$ . The expression for the flux can be split by introducing intermediate states and noting flux through each interface – units are  $t^{-1}$ . This expression will be used in the forthcoming sections, where we will make use of the earlier result showing that the rate  $k_{AB}$  remains unaltered by the addition of a new absorbing state  $C$ , for a time window  $\tau_{mol} \ll t \ll t_{ArB}^{sp}$ . As we have seen, both  $\langle \Phi_{AB} \rangle$  and  $\langle h_A(x_0) \rangle$  are altered by the introduction of  $C$ , but the average velocity of those trajectories which go from  $A$  to  $B$  remains the same (given the two conditions we have imposed).

As mentioned earlier, the steps here follow the discussion in [40, 274]. This expression for the rate is used in a number of path sampling and interface sampling methods such as forward flux sampling [38], transition interface sampling [40] and transition path sampling [32, 274]. In the methods that use interfaces, the flux  $\langle \Phi_{AB} \rangle$  is split into the fluxes through successive interfaces separating  $A$  and  $B$ .

### 6.3.4 Inferring equilibrium sampling to steady state sampling at constant flux

We now discuss how Eq. 6.50 can be used to relate the steady state sampling probability to the equilibrium sampling probability.

In equilibrium,  $\langle \Phi_{AB} \rangle_{eq} = \langle \Phi_{BA} \rangle_{eq}$  (zero current),  $\langle h_A \rangle_{eq} = P_{eq}(A)$ , giving detailed balance condition

$$k_{AB}P_{eq}(A) = \langle \Phi_{AB} \rangle_{eq} = \langle \Phi_{BA} \rangle_{eq} = k_{BA}P_{eq}(B) \quad (6.51)$$

In the presence of an additional absorbing state, we have found that under the specific conditions mentioned while writing Eq. 6.40, one may assume that the rate  $k_{AB}$  is invariant. We discuss how  $\langle \Phi_{BA} \rangle$  and  $\langle h_A(x) \rangle$  change. Assume trajectories cannot be initiated at  $si$  (the new absorbing state). Trajectories exiting  $A$  (or  $B$ ) can now be terminated at  $si$ . ( $si$  is the externally imposed sink absorbing condition) Now, for the same number of trajectory initiations, the absolute number exiting  $A$  and entering  $B$ ,  $\langle \Phi_{AB} \rangle_{st}$ , is less than in scenario without  $si$ . Likewise for  $\langle \Phi_{BA} \rangle_{st}$ . If depletion is avoided, a steady state is achieved – probability a randomly chosen starting point is in  $A$  is now  $\langle h_A \rangle_{st} \equiv P_{st}(A)$ . One has a net current between  $A$  and  $B$  at steady state. The current varies through  $\langle \Phi_{AB} \rangle_{st}$  and  $\langle \Phi_{BA} \rangle_{st}$  and depends on

location of source. In steady state, where  $\langle \Phi_{AB} \rangle_{st} \neq \langle \Phi_{BA} \rangle_{st}$

$$\begin{aligned} \frac{P_{st}(A)}{P_{st}(B)} &= \frac{\langle h_A \rangle_{st}}{\langle h_B \rangle_{st}} \\ &= \frac{\langle \Phi_{AB} \rangle_{st} k_{BA}}{\langle \Phi_{BA} \rangle_{st} k_{AB}} = \frac{\langle \Phi_{AB} \rangle_{st} P_{eq}(A)}{\langle \Phi_{BA} \rangle_{st} P_{eq}(B)} \end{aligned} \quad (6.52)$$

What we want is to infer the equilibrium sampling probability from the measured steady state sampling probability. It is helpful to then re-write the equation above as

$$\frac{P_{eq}(A)}{P_{eq}(B)} = \frac{\langle \Phi_{BA} \rangle_{st} P_{st}(A)}{\langle \Phi_{AB} \rangle_{st} P_{st}(B)} \quad (6.53)$$

### 6.3.5 Using this prescription

We will drop the  $\langle \rangle$  hereafter, when describing  $\langle \Phi_{AB} \rangle$ . We denote our injection point, where trajectories are started, as a source  $so$ . We then calculate the fluxes to and from  $so$  to any other phase point  $(x, y)$ .

- Simulate  $N_{traj}$  trajectories that proceed to the absorbing bound,  $x_b$  through random walk on potential surface  $V(x, y)$ .
- Obtain  $P_{st}(x, y)$  and for a discretised/binning  $(x, y)$  space. Obtain  $\beta\Delta G(x)$  from 1D kinetic reconstruction,  $P_{st}(x) = \sum_y P_{st}(x, y)$ .
- Count number of trajectories that, having visited  $so$  at some time  $t$ , subsequently visit a given  $(x, y)$  bin at some later time  $t' > t$ . Divide this by  $N$  to define  $\Phi_{so \rightarrow xy}$ . Note that this is a per-unit-time quantity but since we calculate the ratio of  $\Phi_{so \rightarrow xy} / \Phi_{xy \rightarrow so}$ , it doesn't reflect in the final expression.
- Obtain  $\Phi_{xy \rightarrow so}$  similarly. Note that  $\Phi_{xy \rightarrow so}$  is sampled poorly beyond the barrier. Far enough beyond the barrier, this quantity goes to 0.
- $so$  specified as point of injection (in basin A). For Boltzmann injection along  $y$ , the same point in basin A is specified as  $so$ .
- The ratio  $\hat{\pi}(x, y) = \frac{\Phi_{so \rightarrow xy}}{\Phi_{xy \rightarrow so}}$  is what we apply as a correction factor in the metastable basin, pre-barrier.

$$\frac{P_{eq}(x, y)}{P_{eq}(so)} = \hat{\pi}(x, y) \frac{P_{st}(x, y)}{P_{st}(so)} \quad (6.54)$$

- Inferring  $P_{eq}(x, y)$  from  $P_{st}(x, y)$  as shown earlier allows us to use Eq. 6.7

$$\begin{aligned}
\beta\Delta G(x, y) &= \beta\Delta G(x) - \ln\left(\frac{P_{eq}(x, y)}{P_{eq}(x)}\right) \\
&= \beta\Delta G(x) - \ln\left(\frac{P_{eq}(x, y)P_{eq}(so)}{P_{eq}(so)P_{eq}(x)}\right) \\
&= \beta\Delta G(x) - \ln\left(\frac{\hat{\pi}(x, y)P_{st}(x, y)P_{eq}(so)}{P_{st}(so)P_{eq}(x)}\right) \\
\beta\Delta G(x, y) &= \beta\Delta G(x) - \ln\left(\frac{\hat{\pi}(x, y)P_{st}(x, y)}{P_{eq}(x)}\right) + const. \tag{6.55}
\end{aligned}$$

- Above we have written terms dependent only on  $so$  as an irrelevant constant.  $P_{eq}(x)$  is defined as

$$\begin{aligned}
P_{eq}(x) &= \int_{-\infty}^{\infty} P_{eq}(x, y) dy \\
&= \frac{P_{eq}(so)}{P_{st}(so)} \int_{-\infty}^{\infty} \hat{\pi}(x, y) P_{st}(x, y) dy, \tag{6.56}
\end{aligned}$$

using Eq. 6.54.  $P_{eq}(x)$  is thus obtained upto a multiplicative constant integrating out the  $y$ -dependence of  $\hat{\pi}(x, y)P_{st}(x, y)$ . We obtain  $\beta\Delta G(x)$  independently and identify  $y$ -dependent corrections as above.

Other schemes can be developed to define pairs for which we can apply Eq. 6.55. Results shown in the subsequent sections consider the definition of  $so$  used above, as the point of injection of the trajectories.

### Similar results in the literature

Similar results have been suggested in the literature, although not leveraged to efficiently calculate free energies. An analysis of trajectory segments in partial-path transition interface sampling (PPTIS) has been shown to reduce to the 1D equivalent of the result here [103]. In this method also, backward fluxes beyond the barrier are not easily obtained; that drawback is shared.

Typical interface sampling and methods that enhance fluxes rely on creating a situation of equal forward and backward flux to achieve equilibrium sampling [39, 103]. In this work, we find that one can use a finite, but unequal, backward flux to infer

equilibrium sampling probability from the measured steady state sampling probability. Such a situation arises naturally where simulations proceed to an absorbing boundary.

### Obtaining a general result for unaltered rates

In the general case, it may be possible to derive a stronger result without an absolute bound  $t_{ArB}^{sp}$ , but instead determine the effect on the partition function explicitly. A possibly useful approach is to consider that the path probability is composed of a Boltzmann factor times a path density of states or density of paths

$$P[\{x_t\}] = P(x_0)f(t)e^{-\beta\Delta G_{x_t;x_0}} \quad (6.57)$$

This is meaningful in a conserved system where the transition probabilities have an energy dependence and their products can be combined and cancelled, leaving behind only a term proportional to the probability of observing a trajectory of length  $t$ .  $f(t)$  is the first passage probability from  $x_0$  to  $x_t$ . This distribution is typically a decaying exponential for first passage to an absorbing condition. As a result, at large  $t$ ,  $f(t)$  may be small, and the contribution to  $P[\{x_t\}]$  may thus be neglected. In this limit, the effect of the additional absorbing boundary is negligible over a range of  $t$ . A more thorough analysis of this aspect has not been attempted but exact results will be useful to obtain.

## 6.4 Tests

Writing

$$\frac{P_{eq}(x, y)}{P_{eq}(s_0)} = \frac{\Phi_{s_0 \rightarrow xy} P_{st}(x, y)}{\Phi_{xy \rightarrow s_0} P_{st}(s_0)}, \quad (6.58)$$

one obtains a correction factor that “works” for either a Boltzmann initialisation or a point injection at some  $y_0$ ,  $x = 0$  (shown in Fig. 6.7).



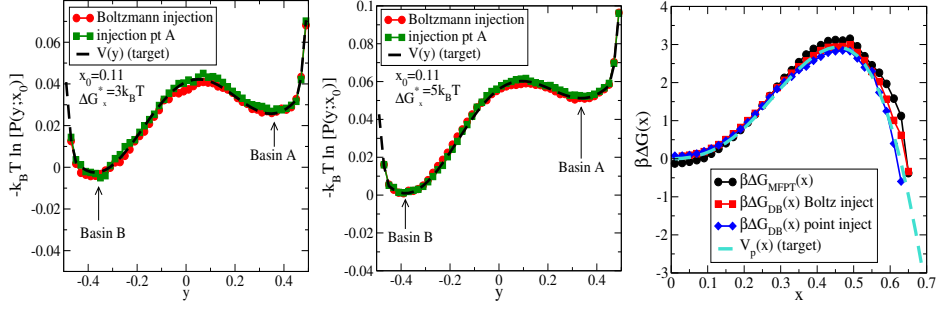


Figure 6.7: Tested here at  $T = 0.08$  for different barrier heights, controlled independently of the diffusivity. A slice is taken along  $x = 0.11$  to compare with the “target” slice  $V(y; x)$ . As expected, this procedure also works for the 1D reconstruction, and is an alternative to the kinetic reconstruction method. The reconstruction along 1D using both the MFPT method and the modified detailed balance (DB) method. Compared against the effective barrier along  $x$ ,  $V_p(x)$  in Eq. 6.8.

### Tests on the two metastable state energy surface

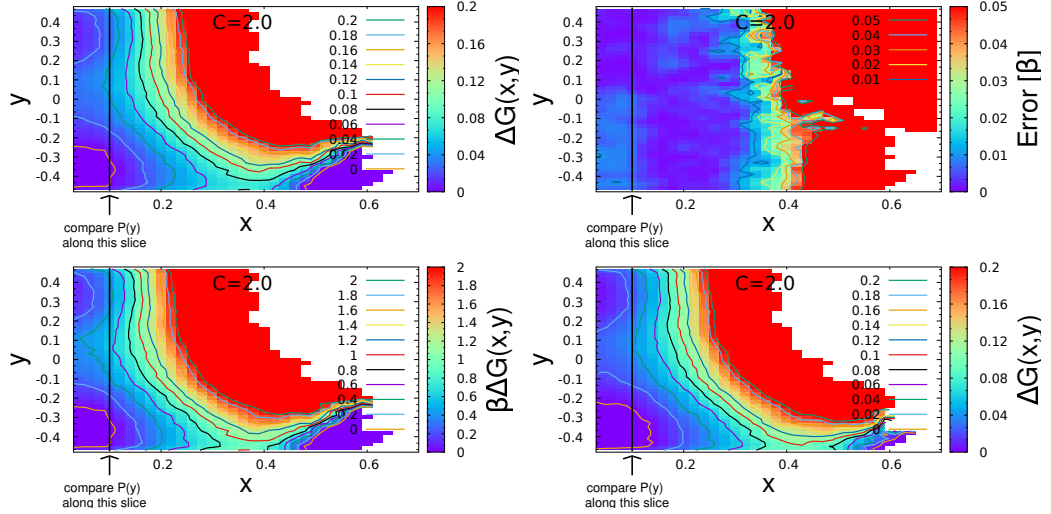


Figure 6.8: *Left Top*: Reconstruction of the 2OP free energy - MFPT + Modified Detailed Balance (MDB). *Left Bottom*: The relative error,  $|\beta\Delta G(x, y) - \beta V(x, y)|$ , units of  $k_B T$ . *Right Top*: 2OP reconstruction in units of  $k_B T$ . *Right Bottom*: 2OP reconstruction using only MDB (no MFPT).

#### 6.4.1 Improving estimates of $\Phi_{so \rightarrow xy}$ and $\Phi_{xy \rightarrow so}$

Given states  $A$  and  $B$  between which we want to measure the flux,  $\langle \Phi_{AB} \rangle$  and  $\langle \Phi_{BA} \rangle$ . If and only if every trajectory from  $A$  to  $B$  and  $B$  to  $A$  passes through an intermediate,  $I$ , (different from the new absorbing condition

*C)* we can write the following

$$\begin{aligned}\Phi_{A \rightarrow B} &= \Phi_{A \rightarrow I} \times \Phi_{I \rightarrow B} \\ \Phi_{B \rightarrow A} &= \Phi_{B \rightarrow I} \times \Phi_{I \rightarrow A}\end{aligned}$$

If this condition is not satisfied, the expression is more complicated, involving segregating trajectories that go from  $A$  to  $B$  (or  $B$  to  $A$ ) without going through  $I$  first. Choosing  $I$  as a hyper-plane separating  $A$  and  $B$  ensures that this condition is met. In the 2D case,  $I$  is a line. In cases of higher dimension, and when the order parameter is not known, defining  $I$  is harder to do. We proceed by testing if estimates can be improved for  $x$  beyond the barrier, from where the flux back to  $so$  may be negligibly small. We place the line at  $x = 0.5$ , beyond the saddle. As a test, we can compare and check if the following equation is true

$$\phi_{so \rightarrow xy} = \phi_{so \rightarrow I} \times \phi_{I \rightarrow xy}, \quad (6.59)$$

for each  $(x, y)$  with  $x > 0.5$ . This is easy to verify because there is a large direct flux from  $so$  to  $(x, y)$  beyond the barrier. We find that it is true through a recalculation of the free energy surface using either  $\phi_{so \rightarrow xy}$  or  $\phi_{so \rightarrow I} \times \phi_{I \rightarrow xy}$  (see Fig. 6.9). We also find that estimates of free energy for  $x > 0.5$  are improved as a result.

It should be noted that for  $xy$  beyond the barrier and close to the absorbing state  $C$ , our assumption that typical paths from  $so$  to  $xy$  and the reverse do not pass through the neighbourhood of  $C$  does not hold. The requirement of a plateau in the time-dependent value of the rate in Eq. 6.17 for  $\tau_{mol} \ll t \ll t_{ArB}^{sp}$  in the presence of  $C$  does not hold.

### Comparison of results with improved estimates

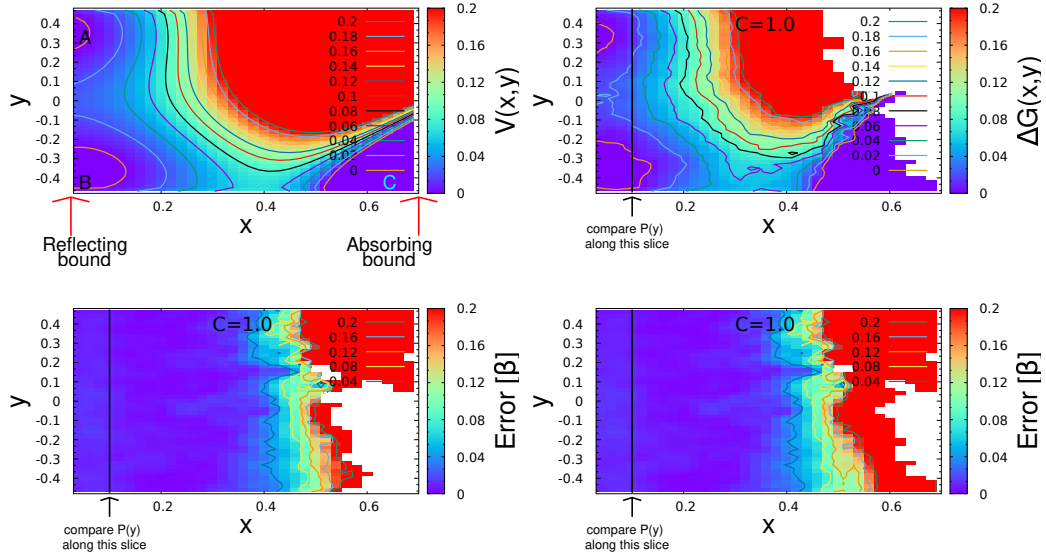


Figure 6.9: *Left Top*: The potential surface. *Right Top*: The two OP reconstruction with the new procedure. *Left Bottom*: Error with old procedure, with no estimates beyond  $x = 0.6$  showing diverging estimates. *Right Bottom*: Error with new procedure.

#### 6.4.2 Introducing a reflecting boundary

An important question here, given the low barriers that we are considering, is how much do we gain by using this prescription with an absorbing boundary, rather than letting natural dynamics take care of achieving equilibrium sampling. In order to test this quantitatively, we perform random walks with a reflecting boundary at large  $x$ , rather than an absorbing boundary. Keeping the same number of random walkers, we look at how the error evolves over MC steps, for a reflecting boundary kept conservatively close to the barrier at  $x = 0.6$ . We find that the depth of the minimum for the globally stable state is what prevents an efficient convergence of the sampling. While in the steady state as well, the backward flux across the barrier along  $x$  is low, our prescription only requires the finite, non-zero backward flux to infer equilibrium sampling from steady state sampling. To achieve equilibrium sampling directly, one needs to either extend trajectories at least an order of magnitude longer, or perform constrained or ratcheted sampling such as in umbrella sampling or Forward Flux sampling to impose the condition of zero flux.

We detail our results from this exercise in Fig. 6.10, Fig. 6.11 and Fig. 6.12. We look at the cases of a low barrier, an intermediate barrier and a high barrier along  $x$ , respectively. In order to compare, we consider the time evolution of the error by looking at well-spaced snapshots and compare it with the mean first passage time along  $x$ ,  $\tau_{MFPT}(x)$ . The  $\tau_{MFPT}(x_b)$ , where  $x_b$  is the location of the absorbing boundary, gives an estimate of how many MC steps are required to obtain converged and accurate estimates of the free energy for the same number of independent random walkers.

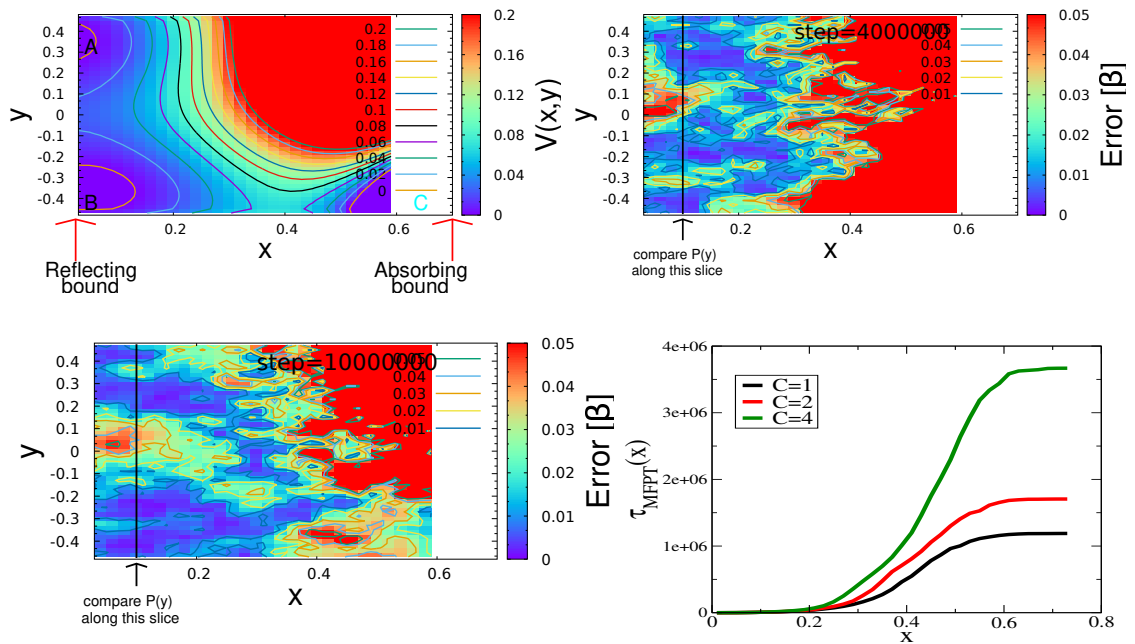


Figure 6.10: We consider the case of imposing a reflecting boundary at  $x = 0.6$  and the time taken for the same number of trajectories,  $N = 600$  to sample the free energy and obtain comparable errors to the case with absorbing boundary at  $x = 0.75$ . We show the potential (*Top left*), the error after  $4 \times 10^6$  MC steps (*top right*) and the error after  $10 \times 10^6$  MC steps (*bottom left*). The MFPT from runs with an **absorbing boundary** are shown in the bottom right.

## Conclusions

More than an order of magnitude greater run length is required to achieve comparable error to the case with absorbing boundary. The MFPT for runs with an absorbing boundary give indication of typical run lengths for each of the 3 cases (low, mid and high barrier). The reflecting boundary is placed at  $x = 0.6$  while absorbing boundary is placed at  $x = 0.75$ .

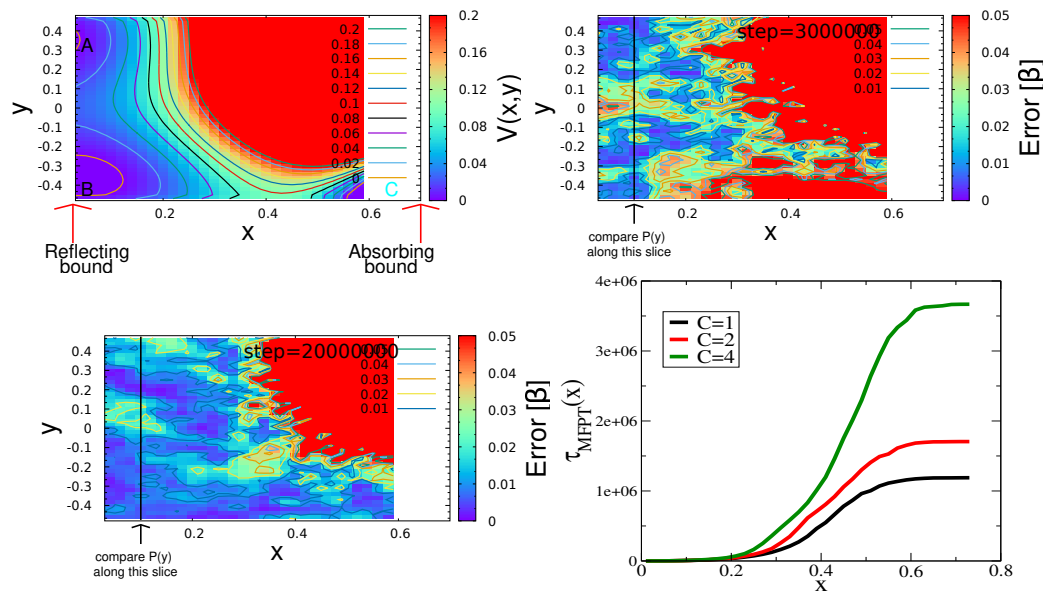


Figure 6.11: We consider the case of imposing a reflecting boundary at  $x = 0.6$  and the time taken for the same number of trajectories,  $N = 600$  to sample the free energy and obtain comparable errors to the case with absorbing boundary at  $x = 0.75$ . We show the potential (*Top left*), the error after  $3 \times 10^6$  MC steps (*top right*) and the error after  $20 \times 10^6$  MC steps (*bottom left*). The MFPT from runs with an **absorbing boundary** are shown in the bottom right.

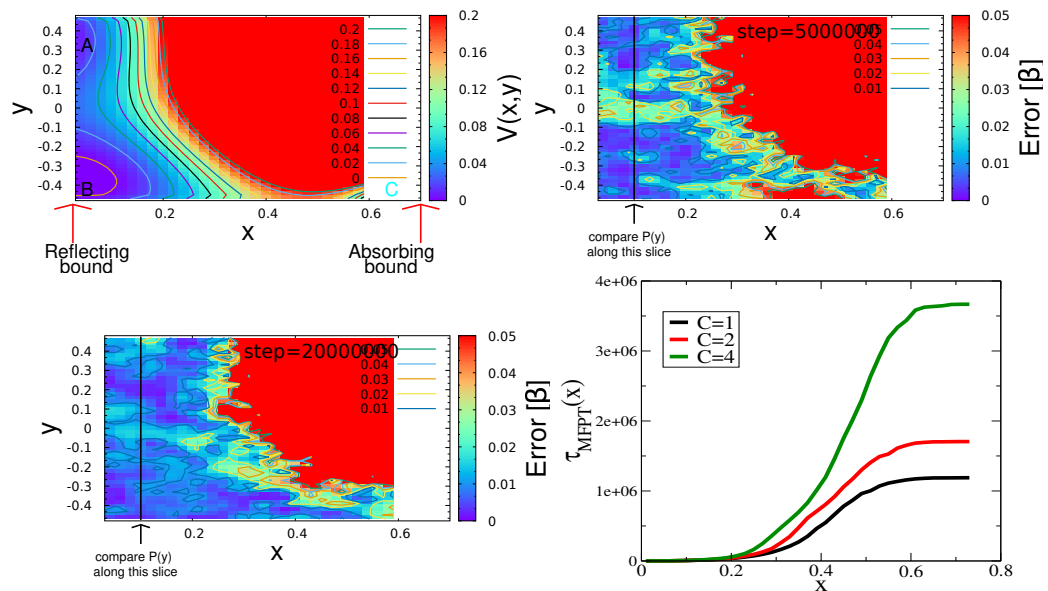
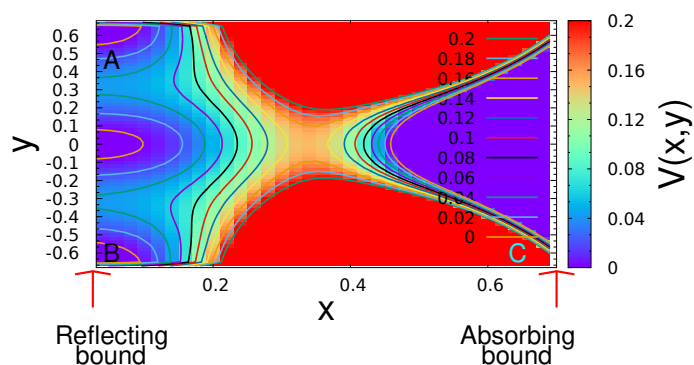


Figure 6.12: We consider the case of imposing a reflecting boundary at  $x = 0.6$  and the time taken for the same number of trajectories,  $N = 600$  to sample the free energy and obtain comparable errors to the case with absorbing boundary at  $x = 0.75$ . We show the potential (*Top left*), the error after  $5 \times 10^6$  MC steps (*top right*) and the error after  $20 \times 10^6$  MC steps (*bottom left*). The MFPT from runs with an **absorbing boundary** are shown in the bottom right.

## 6.4.3 Tests on an alternate potential - 3 metastable basins



A potential with 3 meta-stable basins, an effective barrier height along  $x$  of  $3 k_B T$  and one basin, C, not part of the reaction path (assuming injection at A) to the globally stable D.

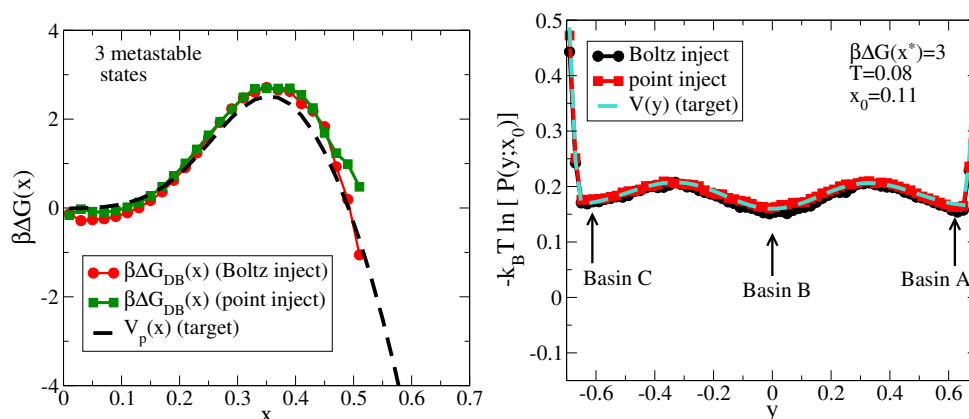


Figure 6.13: Reconstructions of the one order parameter free energy along  $x$  (Left) and for a slice along  $y$  (Right)

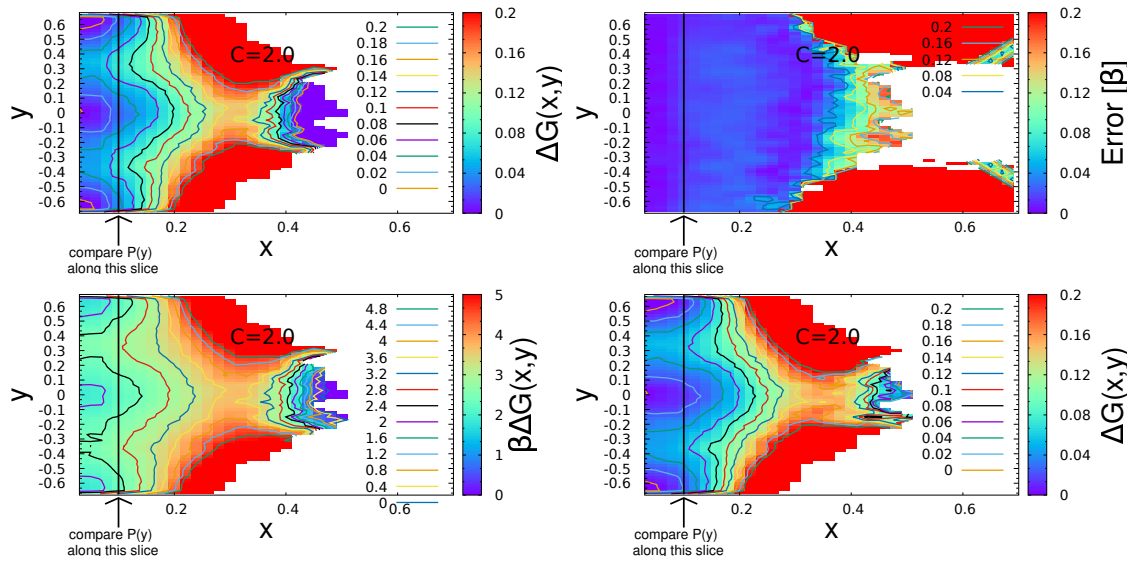


Figure 6.14: *Left Top*: Reconstruction of the 2OP free energy - MFPT + MDB. *Left Bottom*: The relative error,  $|\beta\Delta G(x, y) - \beta V(x, y)|$ , units of  $k_B T$ . *Right Top*: 2OP reconstruction in units of  $k_B T$ . *Right Bottom*: 2OP reconstruction using only MDB (no MFPT).

#### 6.4.4 Tests on an alternate potential - two saddles

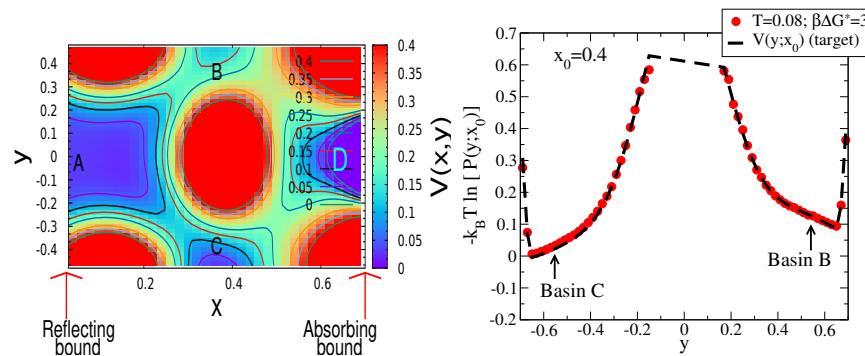


Figure 6.15: A potential with 2 saddles separating metastable states,  $A, B, C$  from global minimum,  $D$ .



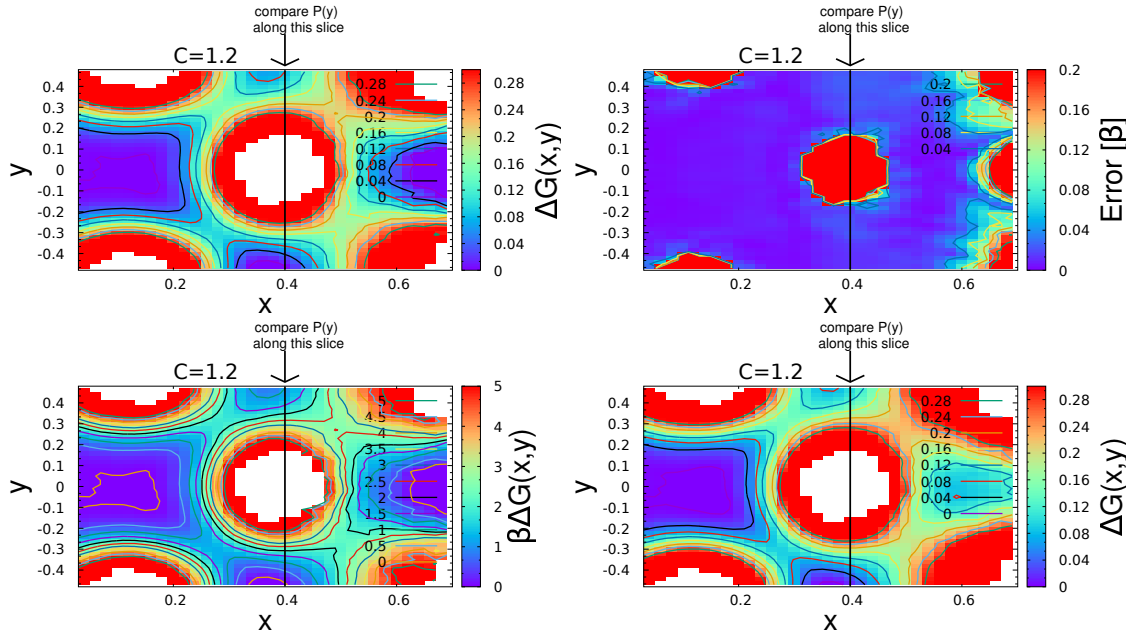


Figure 6.16: *Left Top*: Reconstruction of the 2OP free energy - MFPT + MDB.  
*Left Bottom*: The relative error,  $|\beta\Delta G(x, y) - \beta V(x, y)|$ , units of  $k_B T$ .  
*Right Top*: 2OP reconstruction in units of  $k_B T$ .  
*Right Bottom*: 2OP reconstruction using only MDB (no MFPT).

## 6.5 Discussion

In conclusion, we have described an effective and efficient method to obtain estimates of free energies from unconstrained simulations. This method works by first extending trajectories in order parameter space until some well-chosen absorbing conditions is reached. By treating the trajectories as obeying Brownian motion in the high-friction limit, and assuming a constant diffusivity *of the order parameters* one can obtain the steady state sampling in order parameter space, as well as the various point-to-point fluxes and first passage times in order parameter space. We consider the expression derived for the transition rate, expressed in terms of sampling probability and fluxes, to determine a relation between steady state sampling in the presence of a non-zero constant flux (to an imposed absorbing boundary) to the underlying equilibrium sampling, which can otherwise only be achieved under conditions of zero net flux, which describes detailed balance. This relationship between the steady state sampling and the underlying equilibrium sampling is the key aspect of our method, which allows us to obtain the free energies without the added effort of ensuring the zero flux condition. We show that the method works efficiently for multiple cases by testing it on a toy system of random walkers on a potential

energy landscape. We choose potential energy landscapes that have, in addition to the globally stable state, (i) multiple metastable states, (ii) metastable states that are not on the primary “transition tube” connecting the initial metastable state to the final, globally stable state, and (iii), multiple paths to the globally stable state with multiple saddles of different heights connecting the metastable states to the globally stable state. We find that the method reconstructs the free energy accurately and efficiently in the metastable region provides good estimates of basin depth and barrier height. Issues of poor sampling affect the calculation close to the absorbing boundary and the deep minimum of the globally stable state. We discuss a method based on milestoning to improve these estimates without the need for additional simulation. The application of such an approach to real systems such as liquid silicon or conformational changes in proteins is an important next step. In order to do this, a general prescription needs to be devised to implement this method in different contexts. Key issues include the sampling across the barrier to the globally stable state, the relaxation timescale for transverse degrees of freedom/order parameters (particularly when they are large) and the requirement to have measurable backward fluxes.

# Chapter 7

## Conclusions

This chapter serves to both summarise the main findings from this work, and highlight possible avenues of future work. The core question of this thesis has been, is there a liquid-liquid phase transition for Stillinger-Weber silicon? This question has been investigated in the past. However, investigations by different researchers have yielded different, and contradictory results. Some researchers have found evidence for a first order phase transition exists between two metastable liquid states from equation of state studies. Others have pointed to conceptual problems with drawing conclusions from equation of state studies. The latter researchers have performed free energy calculations and found instead that the liquid is slowly but spontaneously crystallising, with no barrier to crystallisation. The free energy discussed here is the Landau free energy as a function of one or more order parameters.

The goal of this thesis is to determine whether a liquid-liquid transition does actually occur, and if possible, understand the source(s) of discrepancy. Free energy calculations are central to this work, because studies of thermodynamics require that one perform reversible sampling of the state of the substance. Such reversible sampling is only guaranteed with properly performed free energy calculations. Importantly, a key consideration in performing free energy calculations is the choice of order parameter used to distinguish the different states. With the free energy calculations performed in this work, we have sought to answer three questions in the context of silicon:

- Is crystallisation really spontaneous (no free energy barrier) at the considered conditions? Chapter 3 discusses results from free energy calculations that crystallisation is not spontaneous and that a significant barrier to crystallisation exists.

- Why did earlier free energy calculations find no barrier? Chapter 4 has an extensive study of the role of the choice of order parameter. Issues with the choice made in earlier work are identified.
- Is there a liquid-liquid phase transition in silicon? Chapter 5 contains results from a two-order parameter free energy reconstruction. One finds that two metastable liquid phases co-exist at certain conditions and that there is indeed a phase transition.

Finally, Chapter 6 discusses a new method to compute free energies from unconstrained simulations. Applying the method to the case of silicon is the first step ahead beyond this work.

A number of questions remain unanswered at this point. The metastable liquid is sometimes treated as a mixture of particles in two distinct states. However, it has also been argued that there is a continuous spectrum of available states rather than two distinct states [275]. According to the two-state picture, the states differ in energy, geometry of the neighbourhood and in entropy. The extent of non-ideality of the resultant mixture is understood to determine whether the liquid will exhibit a discontinuous phase transition, with or without a critical point, or a continuous change as in the singularity free scenario [3, 194]. Particles switch between the two states on short timescales and the switching rates to and from vary with the conditions, i.e., temperature and pressure. How far is this picture correct for a liquid such as silicon? Can two states be defined that interconvert? Can we write meaningful expressions for the non-ideality of mixing and for the free energies of the two states,  $G_A$  and  $G_{BA}$  in Eq. 1.51 to test such a phenomenological description? Is it possible to predict macroscopic phase behaviour from these microscopic interconversion timescales? How does the crystalline state affect such a description?

Another key issue revolves around the role of the low density liquid in crystallisation. The low density liquid has been found to have a high degree of tetrahedral ordering, sharing the same local density and coordination number as the crystalline state. We found in Chapter 3 that the change in the microscopic structure of the liquid has a profound effect on trends in the free energy barriers to crystallisation. The question here is: Does the increased concentration of particles with local crystalline ordering induce the formation of a bulk tetrahedral liquid phase? Or does the increased tetrahedral ordering in the liquid reduce the free energy cost to crystallisation? What is the role of surface tension here? Most importantly, how does one measure it? Existing results point to the possibility of a two-step nucleation

scenario [15], where the low density liquid acts as an intermediate state to crystallisation, perhaps even facilitating it. While it is clear that the presence of the low density liquid affects how crystallisation occurs, a quantitative statement with clear predictions is important to formulate in this context. It is unclear whether the low density liquid is an intermediate state, as opposed to simply an alternate metastable state with no direct role in crystallisation. A rigorous investigation of this question is interesting to pursue.

The method described in Chapter 6 is promising because it provides a general relation, with caveats, between measured steady state sampling and the underlying equilibrium sampling from which free energies are calculated. We note that the key relation between rates and fluxes in Eq. 6.50 is used in a number of simulation methods that employ interfaces to enhance the sampling of the rate  $k_{AB}$  [33, 103, 274]. The relation between steady state sampling and equilibrium sampling may be applicable to such methods where equilibrium sampling is otherwise ensured with extra backward simulations from  $B$  to  $A$  [39] or simulations with non-linear interfaces across which the backward direction is harder to define [104]. Such extensions may be interesting to explore.

The method described in Chapter 6 has some key drawbacks. The first is the requirement of measurable and proper estimates both forwards and backwards. In particular, being able to measure backward rates is not guaranteed. A prescription to completely address this is needed. Secondly, what happens in situations where the diffusivity of the order parameter, or the rate at which it changes, itself has a dependence on the value of the order parameter at that instant? The formalism described in Chapter 6 does not take such variations into account explicitly. Understanding the implications will improve the utility of the method.

Applying the method to a system such as supercooled silicon would be interesting. However, the method in principle is of broader utility.

The work in this thesis has focussed on providing an answer to the question of whether a first order phase transition occurs between two liquids. With extensive and careful simulations, we have obtained an answer in the affirmative. In the broader community, a lot of thought has gone into formulating models that describe the phenomenology of the LLPT. However, the scope of free energy calculations such as those performed here has been limited, barring exceptions [29], to confirming the existence of two well-defined metastable liquid states. Certain questions remain relatively inaccessible because of the scale of simulations involved. For example,

---

what is the locus of the co-existence line? How can we use this to define an “ordering field” and a “thermal field” as discussed in Sec. 1.5.4? Can we characterise the critical point? Such questions have been studied with equation of state models, but for situations such as silicon, where rapid crystallisation poses challenges, there may be scope to revisit these questions with data from free energy calculations such as those performed here.

# Appendix A

## Appendix

### A.1 Thermodynamics of the liquid state

In this section, we will begin with this *Equation of State* (EOS) description, and use it to understand what state is favoured by a substance under a given set of conditions, with a focus on the liquid state which is of most interest to us. We then describe how this formulation can be used to describe boundaries between these phases and phase transitions. We devote some of the discussion to a particular case that is of core interest to the studies in this thesis – metastability. Briefly, consider if one were to prepare a substance under conditions such that it is most stable as a liquid. Thereafter, if we cool it to temperatures lower than, but close to the freezing temperature, it will remain in the liquid state for a finite amount of time. The expected time that will be taken for the liquid to turn into crystal is understood to be governed by the time taken to overcome a barrier and the liquid is said to be *metastable* with respect to the crystalline state under these conditions. In addition to discussing this aspect in detail, and answering the obvious question of what barrier needs to be overcome, we will also discuss theoretical models that have been developed to describe this process. We focus on one theoretical treatment in particular, first proposed by Kramers [36], which represents the transformation of the liquid to the crystal as a random walk in “state space” where fluctuations enable the system to cross a barrier separating liquid from crystal in this state space. As one can imagine, this representation borrows heavily from the theoretical treatment of Brownian motion, notably the Langevin equation that describes the motion of a Brownian particle. We will discuss how this connection is made.

### A.1.1 The thermodynamic state of a substance

Let us consider the internal energy of a homogeneous system of identical particles:

$$U(S, V, N) = TS - PV + \mu N \quad (\text{A.1})$$

The internal energy is a function of six variables. Importantly, however, 3 of these are control variables whose values specify the state. The internal energy is therefore an explicit function of these 3. For a system to be stable,

$$\delta U|_{S,V,N} = 0, \quad (\text{A.2})$$

and,

$$\delta^2 U|_{S,V,N} > 0. \quad (\text{A.3})$$

Consider  $dU$  written in the following way,

$$dU = \sum_{j=1}^{n+2} \xi_j dX_j, \quad (\text{A.4})$$

where the  $\xi_j$  are the partial derivatives of  $U$  with respect to the independent variables  $X_j$  (entropy, volume, number of particles) and  $n$  is the number of components in the case of a mixture.

One arrives at the following condition for stable or metastable equilibrium,

$$\left( \frac{\partial \xi_{n+1}}{\partial X_{n+1}} \right)_{\xi_1, \xi_2, \dots, \xi_n, X_{n+2}} > 0. \quad (\text{A.5})$$

If we replace the relevant  $N, \mu, S, T, V, P$  in Eq. A.5 above, we get a number of thermodynamic conditions for a system through a set of equivalent stability coefficients (the partial derivatives). In particular,

$$\left( \frac{\partial T}{\partial s} \right)_P = \frac{T}{c_p} > 0, \quad (\text{A.6})$$

and,

$$- \left( \frac{\partial P}{\partial v} \right)_T = \frac{1}{v\kappa_T} > 0. \quad (\text{A.7})$$

In the pair of equations Eq. A.6 and Eq. A.7,  $c_p$  is the specific heat capacity,  $\kappa_T$  is the isothermal compressibility and  $s, v$  are respectively the entropy and volume per molecule. We can multiply each by  $N$  to get the corresponding total volume,



entropy and heat capacity.

These results can be interpreted as, heat added to a stable or metastable system increases its temperature and an isothermally compressed substance has an increased pressure. These are respectively understood as thermodynamic and mechanical conditions for stability.

## Free energies

One can apply Legendre transforms to  $U(S, V, N)$  to get a different set of potentials, known as free energies. The internal energy is defined in terms of 3 extensive properties, the volume ( $V$ ), entropy ( $S$ ) and number of particles ( $N$ ) and the corresponding intensive conjugate fields, pressure ( $P$ ), temperature ( $T$ ) and chemical potential ( $\mu$ ). Similarly, each of the free energies are functions of different triples of thermodynamic coordinates. The commonly used free energies are the Helmholtz free energy,  $A(N, V, T)$  and the Gibbs free energy,  $G(N, P, T)$ . As one might expect, the intensive conjugate field corresponding to any thermodynamic coordinate or variable can be expressed as the partial derivative of a free energy with respect to a given explicit coordinate. For example, the pressure is obtained from the Helmholtz free energy of a system for which  $N$ ,  $V$  and  $T$  are controlled:

$$P = - \left( \frac{\partial A}{\partial V} \right)_{T, N} \quad (\text{A.8})$$

Likewise, the volume of a system where the pressure is controlled is obtained by taking a partial derivative of the Gibbs free energy

$$V = \left( \frac{\partial G}{\partial P} \right)_{T, N} \quad (\text{A.9})$$

The thermodynamic state of a system is defined when the 3 independent or explicit coordinates of a thermodynamic potential are specified. The relationship between the explicit coordinates and any of unspecified coordinates (conjugate to one or the other specified coordinate) is known as an equation of state (EOS). Multiple equations of state correspond to a given thermodynamic potential. For  $A(N, V, T)$  one has  $P(N, V, T)$ ,  $S(N, V, T)$  and  $\mu(N, V, T)$ .

## Limits of stability

The conditions for stable and unstable equilibrium allow us to define the limits within which a substance is stable in a given state. We use the Helmholtz free energy to illustrate this point. Our condition for stability is that the Helmholtz free energy should be a minimum to be stable with respect to fluctuations of a coordinate other than the 3 independent coordinates,  $N, V, T$ . Let us consider the volume  $V$ . We can then write:

$$\begin{aligned} \left(\frac{\partial A}{\partial V}\right)_{T,N} &= -P = 0 \\ \left(\frac{\partial^2 A}{\partial V^2}\right)_{T,N} &= -\left(\frac{\partial P}{\partial V}\right)_{T,N} > 0 \end{aligned} \quad (\text{A.10})$$

Whereas, for unstable equilibrium we have

$$\begin{aligned} \left(\frac{\partial A}{\partial V}\right)_{T,N} &= -P = 0 \\ \left(\frac{\partial^2 A}{\partial V^2}\right)_{T,N} &= -\left(\frac{\partial P}{\partial V}\right)_{T,N} < 0 \end{aligned} \quad (\text{A.11})$$

The locus of the limit of stability is then the set of points that satisfy

$$\left(\frac{\partial P}{\partial V}\right)_{T,N} = 0 \quad (\text{A.12})$$

The definition of the isothermal compressibility  $\kappa_T$  then requires us that  $\kappa_T \rightarrow \infty$  as the stability limit is approached. This locus is known as the spinodal (see Fig. A.1).

## The Spinodal Envelope

If we consider the PT projection of a spinodal curve, all isochores when extrapolated to the limits of stability are tangent to the spinodal. The spinodal is thus an envelope of isochores [13, 227]. To understand this, first we write,

$$dP = \left(\frac{\partial P}{\partial T}\right)_{\xi} dT + \left(\frac{\partial P}{\partial \xi}\right)_T d\xi, \quad (\text{A.13})$$

where  $\xi$  is an intensive property. Along the spinodal,

$$\left(\frac{dP}{dT}\right)_{sp} = \left(\frac{\partial P}{\partial T}\right)_{\xi} + \left(\frac{\partial P}{\partial v}\right)_T \left(\frac{\partial v}{\partial \xi}\right)_T \left(\frac{\partial \xi}{\partial T}\right)_{sp}. \quad (\text{A.14})$$

The spinodal is an envelope of constant- $\xi$  lines, where  $\xi$  is an intensive property. The volume of the system in equilibrium is expected to fluctuate around the equilibrium value determined by the stability condition, with values beyond the stability limit being “forbidden”. At this point two questions arise that we will seek to address. Firstly, what happens to the system when it is kept under conditions where it is not stable? Secondly, it is conceivable (and often the case) that the free energy describing the system has more than one minimum under certain conditions.

### Phase transitions from the metastable to the stable state

In regions of the the  $T - P$  phase diagram where one state, say the vapour, is metastable with respect to the liquid, i.e., the sub-critical region, a first order phase transition occurs from the metastable state to the stable state. At high  $T - P$ , in the *supercritical* region, where the Gibbs free energy has only one minimum, the two states are indistinguishable. There exists a set of  $T - P$  where the depth of the minima is equal – where the two states are said to be in *co-existence*. At this point, the chemical potentials of the two phases are equal. At state points,  $T - P$ , where one basin is deeper than the other, a first order phase transition takes the system from the shallow metastable basin to the deeper, globally stable basin.

The rate at which a phase transition is expected to occur is determined by the frequency with which fluctuations of the volume around the metastable basin take it beyond the barrier separating the two states.

From the van der Waals equation we can write the Gibbs free energy and determine the points of stable and unstable thermodynamic equilibrium. We consider isotherms of the EOS and of the Gibbs free energy. At high temperatures, the EOS obeys  $PV = \text{const}$  and there is only one stable fluid state. As temperature is decreased to a critical temperature, an inflection appears at a “critical point” with the corresponding pressure being the critical pressure. As temperature is decreased further, we see two branches of the isotherm that satisfy  $\partial P/\partial V < 0$  and are therefore stable, and correspondingly two minima in the equation of G and a barrier separating them. The low volume branch with a steep pressure dependence is the liquid branch while the high volume branch is the vapour.

Connecting the  $P, V$  values which satisfy  $\partial P/\partial V = 0$  for each isotherm, one can

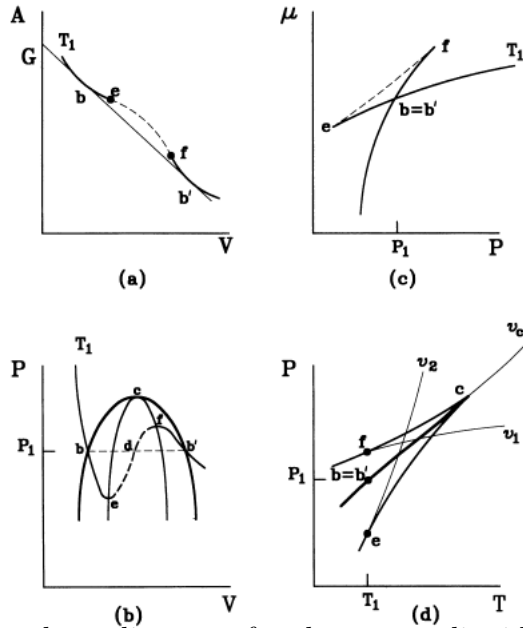


Figure A.1: Schematic phase diagrams for the vapour-liquid transition. (a) Firstly, we assume that the function for the free energy  $A$  is continuous at  $T_1$ . The free energy for a mixture of vapour and liquid will be a linear combination of the free energies for the individual components, and can be represented by cuts across the solid curves. At  $b$  and  $b'$ , the free energy of the mixture is same as that of the components, i.e., they are in equilibrium. The temperature and pressure is also the same, as shown in (b). In panel (b) we consider isotherms in the  $PV$  plane. High  $T$  isotherms follow a curve of the form  $PV = const.$  and pass above  $c$ . For some lower temperature,  $T_c$ , the isotherm passes through  $c$  with a slope  $\partial P/\partial V = 0$  implying diverging compressibility and instability. This is the critical point. Below the critical temperature,  $T_c$ , e.g.,  $T_1$  in panel (b), the curve continues till  $e$  where it flattens out, indicating instability, and an end to the liquid branch. The curve resumes at large  $V$  from  $f$ , which is the vapour branch. The points  $b$  and  $b'$  which have the same pressure for the two branches are the co-existence points. For different  $T$ , the set of points  $b$  and  $b'$  can be traced to  $c$  and constitute the co-existence curve. Likewise, the set of  $f$  and  $e$  also continue to  $c$ . In the region  $be$ , the liquid is superheated and metastable with respect to the vapour. Similarly, the  $b'f$  branch is the supercooled vapour branch. For finite  $N$ , the metastable states persist for finite periods of time. At  $N \rightarrow \infty$ , the system “chooses” and the isotherm exhibits a jump across to the other branch. The curve  $edf$  is a region where the substance would expand under pressure – clearly unphysical and indicative of an unstable region. Panel (c) shows the chemical potential as a function of pressure. The co-existence condition is one for which the liquid and vapour curves for  $\mu(P)$  cross. The lower  $\mu$  state is the stable state. The difference in  $\mu$  between the metastable state (higher curve) and the stable state (lower curve) is the degree of *supersaturation*. Stability condition is given by  $\partial^2 \mu / \partial P^2 = -v\kappa_T$ . In panel (d), the points  $bb'$  collapse to a single point since  $P$  and  $T$  are both the same. The co-existence curve ends at the critical point  $c$ . If the vapour is compressed to higher pressures (at constant  $T$ ) then  $b(b')$ , then the vapour is metastable until  $f$ . If the pressure of the liquid is similarly decreased below  $b(b')$ , then the liquid is metastable until  $e$ . [From *Metastable Liquids* by Pablo G. Debenedetti [227] with permission.]

define the spinodal for the system. The Maxwell equal-area construction defines two additional points for each isotherm, the loci of which are called the binodal. Each stable branch extends beyond the binodal upto the spinodal. The liquid to lower pressures than the binodal pressure and the vapour to higher pressures. These extensions are the regions in which the liquid is metastable to the vapour or *superheated* or the vapour is metastable to the liquid *supercooled*.

### The Landau free energy

At this point, it is helpful to connect the discussion above to the Landau theory of phase transitions. At a given state point, one can write the free energy as a function of the full coordinates of the system  $\{\mathbf{q}_i, \mathbf{p}_i\}$  that describe the phase space. This is often done by encoding the generalised coordinates into a lower dimensional “collective variable”, say  $\phi \equiv \phi(\{\mathbf{q}_i, \mathbf{p}_i\})$ , in terms of which the Landau free energy is written. The volume (or density), discussed above, is a good example of a collective variable that describes the vapour-liquid transition. Purely phenomenologically, the Landau free energy can be written as a Taylor expansion around the stable value of the collective variable to illustrate either first order or continuous phase transitions. In the general case, one does not take recourse to this, considering instead the fact that the Landau free energy can be related to the probability of sampling a specific value of the collective variable, much like the free energy can be written in terms of the partition function.

$$P(\phi) = \frac{\int d\mathbf{r} e^{-\beta H'(\phi(\mathbf{r}))} \delta(\phi(\mathbf{r}) - \phi)}{\int d\mathbf{r} e^{-\beta H'(\phi(\mathbf{r}))}} \quad (\text{A.15})$$

The Landau free energy then can be related to the sampling probability  $P(\phi)$  in the following way:

$$F(\phi) = -k_B T \ln[P(\phi)] + \text{const.} \quad (\text{A.16})$$

One can write the probability of sampling a region of phase space in terms of a Boltzmann factor of the free energy

$$P(\phi) = C e^{-\beta \Delta F(\phi; \phi_{min})} \quad (\text{A.17})$$

Here,  $\beta = 1/k_B T$ ,  $\Delta F(\phi; \phi_{min})$  is the Landau free energy difference,  $F(\phi) - F(\phi_{min})$ , where  $\phi_{min}$  is the value of  $\phi$  for the stable state.  $C$  is a normalisation constant.

One can then write the free energy barrier height as  $\Delta F(\phi^*; \phi_{min})$  where  $\phi^*$  is the

value of  $\phi$  at the top of the barrier. The rate of barrier crossing can then be written as

$$k_{cross} = 0.5Ae^{-\beta\Delta F(\phi^*; \phi_{min})} \quad (\text{A.18})$$

The factor  $A$  is a kinetic pre-factor which accounts for the dynamics of the system and the 0.5 arises because at the top of the barrier there is a probability of half of falling to one side or the other. This factor of 0.5 is a simplistic guess, and considerable work has been done to obtain the true kinetic pre-factor. A more detailed discussion of this calculation of the transition rate is covered Section 1.2.

## A.2 Phase transformations as diffusive barrier crossing

This section describes the details of comparing phase transformations to the diffusive crossing of a free energy barrier by an overdamped Brownian. We first write the Smoluchowski equation that describes the time evolution of a distribution of such particles. Next, the mean first passage time is derived which is related to the crossing rate in the Kramers formulation.

### A.2.1 The Smoluchowski equation

The Smoluchowski equation in Eq. 1.14 is a special case of the Fokker-Planck equation, written in the limit where the friction/collision term dominates over the inertial or mass term in the underlying equations of motion of the Brownian particle. For completeness, we derive the Fokker-Planck equation that governs the distribution of Brownian particles, starting from the demand that the distribution be conserved. We start with the vector form of the Langevin equation:

$$\frac{d\mathbf{x}}{dt} = \mathbf{v}(\mathbf{x}) + \mathbf{F}(t) \quad (\text{A.19})$$

where  $\mathbf{v}$  is some unspecified set of functions. We assume the noise to be Gaussian and delta correlated as before:

$$\langle \mathbf{F}(t)\mathbf{F}(t') \rangle = 2\mathbf{B}\delta(t - t'). \quad (\text{A.20})$$

If we consider the distribution function  $P$ , which is conserved, we can write the following continuity equation:

$$\frac{\partial P}{\partial t} + \nabla_x \left( \frac{d\mathbf{x}}{dt} P \right) = 0. \quad (\text{A.21})$$

Here, the gradient  $\nabla_x$  represents the partial derivative over the vector  $\mathbf{x}$ ,  $\frac{\partial}{\partial \mathbf{x}}$ . Substituting for  $d\mathbf{x}/dt$ , we have

$$\frac{\partial P}{\partial t} = -\nabla_x \left( \mathbf{v}(\mathbf{x})P + \mathbf{F}(t)P \right). \quad (\text{A.22})$$

We define a Liouville-like operator and integrate the resulting solution, with an average over the noise to get,

$$\frac{\partial \langle P(\mathbf{x}, t) \rangle}{\partial t} = -\nabla_x \left( \mathbf{v}(\mathbf{x}) \langle P(\mathbf{x}, t) \rangle \right) + \nabla_x \mathbf{B} \cdot \nabla_x \langle P(\mathbf{x}, t) \rangle. \quad (\text{A.23})$$

This is the Fokker-Planck equation. Note that the average is over the noise at all times leading up to time  $t$  and that the equation solves for the expectation value of the fraction of particles at  $\mathbf{x}$  at time  $t$ . In the following discussion, we will drop the  $\langle \rangle$  in the Fokker-Planck equation for simplicity. Let us now consider the Brownian motion of a particle inside a potential  $U(x)$ . The Langevin equations for this system are:

$$\begin{aligned} \frac{dx}{dt} &= \frac{p}{m} \\ \frac{dp}{dt} &= -U'(x) - \zeta \frac{p}{m} + \delta F_p(t). \end{aligned} \quad (\text{A.24})$$

And we have

$$\langle F_p(t) F_p(t') \rangle = 2\zeta k_B T \delta(t - t'). \quad (\text{A.25})$$

$$\mathbf{B} = \begin{pmatrix} 0 & 0 \\ 0 & \zeta k_B T \end{pmatrix}$$

If we consider the Langevin equation for a Brownian particle in a potential when the time constant defined by  $m/\zeta$  is large (the high friction limit), this equation

reduces to

$$\frac{dx}{dt} = -\frac{1}{\zeta}U'(x) + \frac{1}{\zeta}F(t). \quad (\text{A.26})$$

We can write, with the notation  $D = \frac{k_B T}{\zeta}$ , as

$$\frac{dP}{dt} = D \frac{\partial}{\partial x} \exp(-U(x)/k_B T) \frac{\partial}{\partial x} [\exp(U(x)/k_B T) P]. \quad (\text{A.27})$$

This is called the *Smoluchowski equation*, which describes diffusion in an external potential. Note that  $D$  is the diffusion coefficient as given by the Einstein formula, and when the external potential is turned off, we get the diffusion equation.

The Smoluchowski equation can be written in the form of a continuity equation, by introducing a current density  $j$ , as

$$\frac{dP}{dt} + \frac{\partial j}{\partial x} = 0. \quad (\text{A.28})$$

The current density is defined by

$$j(x, t) = -\frac{1}{\zeta}(U'(x)P) - \frac{k_B T}{\zeta} \frac{\partial P}{\partial x}. \quad (\text{A.29})$$

The condition for equilibrium can be stated by saying that the current density has to be a constant,  $j(x, t) = j^{st}$ .

### A.2.2 The mean first passage time

We derive the mean first passage time in Eq. 1.18 by considering the evolution of the distribution of positions of a set of Brownian particles starting at some initial set of points  $\mathbf{x}_0$ . We are interested specifically in the set of particles that remain in a sub-volume  $V$  within some time  $t$ . If we now specify that the Smoluchowski equation governs the time evolution of the distribution, we get:

$$\begin{aligned} \frac{\partial P}{\partial t} &= -\frac{1}{\zeta} \frac{\partial}{\partial x} (U' P) + D \frac{\partial^2 P}{\partial x^2} = \mathcal{D}P \\ P(x, 0) &= \delta(x - x_0), \quad P(x, t) = 0 \text{ on } \partial V \end{aligned} \quad (\text{A.30})$$



Here,  $\partial V$  denotes the surface on sub-volume  $V$ . We represent a Fokker-Planck operator  $\mathcal{D}$  which also accounts for the boundary conditions applied. We can rewrite the time evolution as

$$P(x, t) = e^{t\mathcal{D}}\delta(x - x_0) \quad (\text{A.31})$$

Here, we should note that as  $t \rightarrow \infty$ ,  $P(x, t) \rightarrow 0 \forall x$  since eventually all Brownian particles leave the sub-volume  $V$ . The number of points remaining in the sub-volume  $V$  at a given time  $t$ , called the *Survival probability*, can be obtained by integrating the distribution over the sub-volume. In general it will depend on the initial distribution.

$$S(t, x_0) = \int_V dx P(x, t) = \int_V dx e^{t\mathcal{D}}\delta(x - x_0) \quad (\text{A.32})$$

We shift our focus to the number of Brownian particles that leave in an interval  $[t, t + dt]$ .

$$S(t, x_0) - S(t + dt, x_0) = \mu(t, x_0)dt \quad (\text{A.33})$$

Here,  $\mu(t, x_0)$  is the distribution of first passage times of particles starting at  $x_0$  and reaching the boundary at time  $t$ . It can be related to the survival probability as

$$\mu(t, x_0) = -\frac{dS(t, x_0)}{dt} \quad (\text{A.34})$$

The mean first passage time is the first moment of the first passage time distribution. A series of steps gives us

$$\begin{aligned} \tau(x_0) &= \int_0^t dt' t' \mu(t', x_0) \\ \tau(x_0) &= -\int_0^t dt' t' \frac{dS(t', x_0)}{dt'} \\ \tau(x_0) &= t' S(t', x_0)|_0^t - \int_0^t S(t', x_0) dt' \\ \tau(x_0) &= \int_0^\infty dt S(t, x_0) \\ \tau(x_0) &= \int_0^\infty dt \int_V dx e^{t\mathcal{D}}\delta(x - x_0) \end{aligned} \quad (\text{A.35})$$

We have used integration by parts and taken the  $t \rightarrow \infty$  limit above (using the fact that  $S(t) \rightarrow 0$  in this limit). We consider that the integrand on the RHS is the inner product of a unit vector with  $e^{t\mathcal{D}}\delta(x - x_0)$  and invoke the adjoint of the

operator,  $\mathcal{D}$ , denoted as  $\mathcal{D}^*$ . We use the definition of adjoints:

$$\langle Tu, v \rangle = (Tu)^* \cdot v = \langle u, T^*v \rangle \quad (\text{A.36})$$

and re-write the mean first passage time in the following way

$$\tau(x_0) = \int_0^\infty dt \int_V dx \delta(x - x_0) (e^{t\mathcal{D}^*} 1) \quad (\text{A.37})$$

where we have taken advantage of the fact that the order in the inner product is interchangeable since all our quantities are real-valued. We thus get, by applying the Delta function and operating on  $\tau$  with the adjoint operator and do a time integral to get

$$\begin{aligned} \tau(a_0) &= \int_0^\infty dt e^{t\mathcal{D}^*} 1 \\ \mathcal{D}^* \tau(x_0) &= \int_0^\infty dt \mathcal{D}^* e^{t\mathcal{D}^*} 1 \\ \mathcal{D}^* \tau(x_0) &= \int_0^\infty dt \frac{d}{dt} e^{t\mathcal{D}^*} 1 = -1 \end{aligned} \quad (\text{A.38})$$

The operator,  $D$  is the Smoluchowski operator, giving us,

$$\begin{aligned} \mathcal{D} &= \frac{\partial}{\partial x} D(x) e^{-\beta U(x)} \frac{\partial}{\partial x} e^{\beta U(x)} \\ \mathcal{D}^* &= e^{\beta U(x)} \frac{\partial}{\partial x} D(x) e^{-\beta U(x)} \frac{\partial}{\partial x} \end{aligned} \quad (\text{A.39})$$

The second equation follows from considering the adjoint of the differential operator and noting that the operator  $\mathcal{D}$  is of the Sturm-Liouville type, which is self-adjoint. Thus, the mean first passage time is the solution of

$$\begin{aligned} e^{\beta U(x)} \frac{\partial}{\partial x} D(x) e^{-\beta U(x)} \frac{\partial}{\partial x} \tau(x) &= -1 \\ \tau(x) &= \int_x^b dy \frac{1}{D(y)} e^{\beta U(y)} \int_a^y e^{-\beta U(z)} dz \end{aligned} \quad (\text{A.40})$$

We note here that the solution for the mean first passage time in more than one dimension is significantly more complicated, and has not been worked out in this thesis. The mean first passage time is easily calculable from simulations and can be related to the potential in which Brownian motion is taking place as seen here. In later sections we will describe how it has been used in the literature to reconstruct the free energy (or potential energy) from the measured mean first passage time.

## A.3 Crystallisation

The sections below describe the details of how free energies and rates are defined in the context of crystallisation.

### A.3.1 The driving force for crystallisation

This section discusses how Eq. 1.22 is used as a starting point to determine what drives the transition to the new phase. The free energy per particle,  $G/N$ , is the chemical potential and the change is the *supersaturation*

$$\Delta\mu = (G_{old} - G_{new})/N \quad (\text{A.41})$$

At co-existence, the  $G_{old} = G_{new}$  and the parent phase is said to be *saturated*.  $\Delta\mu$  is a difficult quantity to calculate. In a specific case such as the liquid-gas transition, or crystallisation in a solution,  $\Delta\mu$  can be related to the change in pressure or the change in concentration/activity respectively. Our interest is in the case of crystallisation from the melt. For this case, we can write:

$$\mu(T) = \mu_e + \int_T^{T_e} s(T')dT' \quad (\text{A.42})$$

This equation is obtained in the isobaric condition from considering that  $(\partial G/\partial T)_P = S$ . We integrate over the per-particle entropy,  $s = S/N$  to get  $\mu$ . This equation can be written for both the old and the new phases to get the difference between the two

$$\mu_{old}(T) - \mu_{new}(T) = \Delta\mu(T) = \int_T^{T_e} \Delta s(T')dT' \quad (\text{A.43})$$

To a first approximation, and without any a-priori knowledge of the functional dependence of  $\mu(T)$  on  $s(T)$ , we Taylor expand around  $T_e$  to get

$$\Delta\mu(T) = -\Delta s_e(T - T_e) - \frac{1}{2} \left( \frac{d\Delta s}{dT} \right)_e (T - T_e)^2 + \dots \quad (\text{A.44})$$

We recall at this point that  $S(T)$  can be related to the isobaric heat capacity as

$$\begin{aligned} S(T) &= \int_0^T \frac{C_P(T')}{T'} dT' \\ \frac{d\Delta S}{dT} &= \frac{\Delta C_P(T)}{T} \\ \frac{d^2\Delta S}{dT^2} &= \frac{\Delta C'_P(T)}{T} - \frac{\Delta C_P(T)}{T^2} \end{aligned} \quad (\text{A.45})$$

$\Delta C_P(T) = C_{P,old}(T) - C_{P,new}(T)$  and  $C'_P(T) = (d\Delta C_P(T)/dT)_{T_e}$ . We can replace appropriately to get

$$\Delta\mu(T) = \Delta s_e \Delta T - \frac{\Delta C_{P,e}}{2T_e} \Delta T^2 + \dots \quad (\text{A.46})$$

Using the latent heat of transformation from the metastable to the stable phase,  $\lambda$ , one gets

$$\Delta s_e = \lambda/T_e \quad (\text{A.47})$$

With this, we are able to quantify the driving force for the phase transition. We note that since  $\mu$  is difficult to obtain, it is often related to other, more accessible quantities, such as the heat capacity to determine the degree of *supercooling* that the metastable parent phase has undergone.

We next determine the work required for the phase transition to occur, noting that a finite free energy barrier exists between the metastable parent phase and the stable new phase.

### A.3.2 Classical nucleation theory

This section describes the details of writing the work to cluster formation in Eq. 1.23. Consider two possible states of the system. State 1 is where the substance is entirely in the metastable parent phase.

$$G_1 = N\mu_{old} \quad (\text{A.48})$$

State 2 is the state where a nucleus of size  $n$  is present

$$G_2(n) = (N - n)\mu_{old} + G(n) \quad (\text{A.49})$$

Here,  $G(n)$  is the free energy cost for a cluster of size  $n$  to exist. In general, we can write the free energy of a cluster of size  $n$  as

$$G(n) = n\mu_{new} + G_{ex}(n) \quad (\text{A.50})$$

The first term in the RHS is simply the free energy of  $n$  particles of the new phase. The second term is an unspecified term that accounts for the excess free energy due to the interaction of the cluster of size  $n$  with the surrounding metastable parent phase (see Fig. 1.3). We can write the work of cluster formation as

$$W(n) = G_2(n) - G_1 \quad (\text{A.51})$$

This gives us

$$W(n) = -n\Delta\mu + G_{ex}(n) \quad (\text{A.52})$$

Here we stress that  $n = 1$  refers to a monomer of the new phase and is distinct from monomers of the parent phase.  $W(1) \neq 0$ .

We now assume that all clusters of size  $n$  take the same shape, which is the most probable shape that minimizes the energy of the system so that  $G_{ex}(n)$  only has a size dependence and not a shape dependence. Of course, the shape of the  $n + 1$  cluster need not be the same as that of the size  $n$  cluster.

### A.3.3 Excess free energy and surface term

The central problem of nucleation theories is to determine the excess free energy  $G_{ex}(n)$ . In order to determine  $G_{ex}(n)$ , let us revisit the free energy of the state 2 with a nucleus of size  $n$ .

$$G_2(n) = F_2(n) + pV \quad (\text{A.53})$$

$$F_2(n) = (N - n)\mu_{old} - pV_{N-n} + n\mu_{new,n} - p_n V_n + \phi(V_n) \quad (\text{A.54})$$

Here, we have specified a dividing surface between the old and new phases such that the total number of particles is conserved and each particle belongs to either one of the two phases. We can write that the total volume is conserved, so  $V = V_N + V_{N-n}$ . We assume that the pressure within the nucleus,  $p_n$ , is different from that of the bulk metastable phase,  $p$ .  $\phi(V_n)$  is the interface energy for a volume  $V_n$ .  $\mu_{new,n}$  is the chemical potential for particles belonging to the new phase in a cluster of size  $n$ , which is in general different from  $\mu_{new}$ , the chemical potential in the bulk. We can

now write

$$G_2(n) = (N - n)\mu_{old} + n\mu_{new,n} - (p_n - p)V_n + \phi(V_n) \quad (\text{A.55})$$

The work done then is

$$W(n) = G_2(n) - G_1 = -(p_n - p)V_n + (\mu_{new,n} - \mu_{old})n + \phi(V_n) \quad (\text{A.56})$$

Thus, we get

$$G_{ex}(n) = \phi(V_n) - (p_n - p)V_n + (\mu_{new,n} - \mu_{new})n \quad (\text{A.57})$$

Here, we need to stress that  $n$  has to be large enough so that  $p_n$ ,  $V_n$  can be well-defined. In mechanical equilibrium, we have  $\partial G/\partial V_n = 0$ . We can also write

$$p_n = p + \frac{d\phi}{dV_n} \quad (\text{A.58})$$

which tells us that the pressure inside the nucleus is the outside pressure plus the rate of change of the surface energy with size.

We can now write

$$\mu_{new,n}(p_n) - \mu_{new}(p) = \frac{1}{n} \int_p^{p_n} V_n(p') dp' \quad (\text{A.59})$$

This equation tells us that in isothermal conditions, the change in chemical potential between particles in the new phase in the cluster and particles in the new phase in the bulk is obtained by integrating the volume between the two pressures, obtained from writing  $(\partial G/\partial P)_T = V$ .

We can then write the excess free energy as

$$G_{ex}(n) = \phi(V_n) - (p_n - p)V_n + \int_p^{p_n} V_n(p') dp' \quad (\text{A.60})$$

At this point, we make an important assumption for condensed phases, namely that the volume per particle of particles in the new phase is constant with pressure.

$$V_n(p_n) = nv_0 \quad (\text{A.61})$$

The second term on the RHS and the integral then cancel out, giving us

$$G_{ex}(n) = \phi(V_n) \tag{A.62}$$

This assumption is perhaps questionable for crystallisation since the volume of crystals decreases linearly with applied pressure. If the pressure dependence of the volume follows an ideal gas equation then the expression for  $G_{ex}(n)$  will change accordingly.

### A.3.4 The surface term

At this point, we have determined that the work required to form a cluster of size  $n$  decreases with  $n$ , proportional to the supersaturation,  $\Delta\mu$  and increases with the surface free energy term,  $\phi(V_n)$ . How then do we calculate the  $\phi$  mentioned in Eq. 1.24?

If we assume the shape of the nucleus to be regular (polyhedral or spherical) and resolve the surface energy into a product of the surface area and a proportionality constant,  $\sigma_n$ , which depends on the size, but is the average over different orientations of interaction between the cluster and the parent phase, we can write the surface term as:

$$\phi(V_n) = c_n \sigma_n V_n^{2/3} \tag{A.63}$$

We use a shape factor,  $c_n$ , whose variation accounts for the different surface areas of different shapes. If we then further assume that  $\sigma$  is size-independent, we can then write an even simpler dependence.

$$\phi(V_n) = a\sigma V_n^{2/3} = a\sigma n^{2/3} \tag{A.64}$$

The second equality follows for condensed phases when  $V_n = nv_0$ . The two assumptions regarding  $\sigma$ , (orientational averaging and size independence) heavily rely on  $n$  being large and are together called the *capillarity approximation*. For small  $n$ , one can consider the change in energy when a particle switches from bulk metastable to the new phase and arrive at a similar expression for  $G_{ex}(n)$ , suggesting that equating  $G_{ex}(n)$  with  $\phi(V_n)$  is true regardless of cluster size [48]. However, how  $\phi$  is calculated matters.

### A.3.5 Equilibrium cluster distribution

This section contains details on how Eq. 1.27 is derived. If the metastable fluid is treated as a multi-component mixture of clusters of different sizes (including 0 size representing the parent state) where we can neglect the interaction between clusters, we write the chemical potential of a cluster of size  $n$  as:

$$\mu_n = G(n) + k_B T \ln [N(n)/N(0)] \quad (\text{A.65})$$

where  $N(n)$  is the concentration (or number) of clusters of size  $n$ . The second term in the RHS is the contribution to the chemical potential from the relative concentration of different species in a mixture.  $G(n)$  is the free energy of one cluster of size  $n$  in a phase of purely  $n$ -sized clusters. We already know therefore that

$$G(n) = n\mu_{new} + G_{ex}(n) \quad (\text{A.66})$$

Further, when  $n$ -sized clusters are in equilibrium with other cluster sizes, such as 1-sized clusters, we have the condition

$$n\mu_1 = n\mu_{old} = \mu_n \quad (\text{A.67})$$

Thus, the work done to form clusters of size  $n$  is given by revisiting Eq. 1.23.

$$W(n) = -n(\mu_{new} - \mu_{old}) + G_{ex}(n) \quad (\text{A.68})$$

Relating the work done to the concentration gives us

$$\begin{aligned} n\mu_{old} &= \mu_n = G(n) + k_B T \ln [N(n)/N(0)] \\ n\mu_{old} &= n\mu_{new} + G_{ex}(n) + k_B T \ln [N(n)/N(0)] \\ n(\mu_{old} - \mu_{new}) - G_{ex}(n) &= k_B T \ln [N(n)/N(0)] \\ -W(n) &= k_B T \ln [N(n)/N(0)] \\ N(n) &= N(0) \exp(-\beta W(n)) \end{aligned} \quad (\text{A.69})$$

### A.3.6 General derivation of the rate expression

This section gives details on how we can go from the master equation in Eq. 1.28. We make some key assumptions which are repeated here for convenience:



- Assume that the clusters are localised and clusters of all sizes are possible.
- Finite non-zero rates with which clusters of size  $n$  become clusters of size  $m$ . This can in general be time-dependent,  $f_{nm}(t)$ .
- All clusters of size  $n$  are equivalent, at least on average, allowing us to simplify our treatment and not worry about shape dependent interconversion rates,  $f_{nm}(t)$ .
- The clusters are otherwise non-interacting.
- The concentration of clusters of size  $n$  at time  $t$ ,  $N(n, t)$ , is assumed to be spatially uniform and homogeneous in the volume.

In general, the rates  $f_{nm}(t)$  need to be known to use this approach to calculate the full rate with this microscopic description. Moreover, the dependence of these rates on conditions  $(T, P, \Delta\mu)$  also need to be known.

The master equation can be written as

$$\frac{d}{dt}N(n, t) = \sum_{m=1}^{M(t)} [f_{mn}(t)N(m, t) - f_{nm}(t)N(n, t)] + K(n, t) - L(n, t) \quad (\text{A.70})$$

$M(t)$  is the total number of available molecules at  $t$ , or the largest possible cluster size.  $K(n, t)$  and  $L(n, t)$  are respectively the probabilities of a cluster of size  $n$  appearing out of thin air at time  $t$  and disappearing into thin air at time  $t$ . In principle, the inclusion of such terms is contingent on a physical basis for them, even if the terms in the sum are insufficient to describe changes in cluster size; they are neglected in the subsequent discussion for simplicity.

For a constant  $M$ , i.e., a closed system,  $K(n, t)$  and  $L(n, t)$  are typically treated equal to 0. We can write a conservation condition

$$\sum_{n=1}^M nN(n, t) = M/V = \text{constant} \quad (\text{A.71})$$

We next consider the number of clusters appearing per unit volume at time  $t$ .

$$j_n(t) = \sum_{m=m'+1}^M \sum_{m=m'}^n [f_{m'm}(t)N(n, t) - f_{mm'}(t)N(m, t)] \quad (\text{A.72})$$

The summand is the flux through  $n$  of all clusters size  $m' \leq n$  growing to size  $m > n$ . Evaluating the expressions for  $j_n(t)$  and  $j_{n-1}(t)$  gives us

$$j_n(t) - j_{n-1}(t) = \sum_{m=1}^M [f_{mn}(t)N(m, t) - f_{nm}(t)N(n, t)] = \frac{d}{dt}N(n, t) \quad (\text{A.73})$$

The rates  $f_{nm}(t)$  are physically understood by considering the processes of monomer and multimer attachment/detachment. A full transition matrix of the different rates can be used to describe this as a Markov process. At this point, if we further assume that the  $f_{mn}$  are time-independent, we can write the condition for a stationary cluster size distribution as  $j_n(t) = 0$ . This is the case of equilibrium. If instead,  $j_n(t) = J_s$  then we have a case where as well  $dN(n, t)/dt = 0$  but this is a steady state with a constant flux. We have an alternate case for the rate of formation of post-critical clusters  $j_{n^*}(t)$  when the size of the critical cluster  $n^*(t)$  is itself time-dependent. In this case, the rate of formation of post-critical clusters is time-varying and we have a case of non-stationary nucleation. This, however, usually requires that the chemical potential difference,  $\Delta\mu$ , or other relevant conditions, themselves change with time.

For the case of stationary nucleation, we will derive an expression for the rate based on the work of formation of clusters of size  $n$ .

### Stationary nucleation rate

Here we describe how to arrive at Eq. 1.30. First we consider the concentration of clusters of size  $n$ ,  $f(n)$ , rather than the total number  $N(n)$  discussed earlier. Doing this removes trivial system size dependences. A standard way to make the connection is to write  $f(n) = N(n)/N(0)$  ( $N(0)$  is the number of monomers). We write the rate of formation of clusters of size  $n$  as [227]:

$$J(n) = f(n-1)A(n-1)\beta(n-1) - f(n)A(n)\alpha(n) \quad (\text{A.74})$$

In Eq. A.74,  $f(n)$  is the concentration of clusters of size  $n$ ,  $A(n)$  is the surface area of a cluster of size  $n$ .  $\beta(n)$  is the flux per unit time of single particles onto the surface of the cluster of size  $n$  and  $\alpha(n)$  is the flux of particles leaving the cluster of size  $n$ .

For an equilibrium distribution of clusters, the rate  $J(n) = 0 \forall n$ . Using this, we

write,

$$p_{eq}(n-1)A(n-1)\beta = p_{eq}(n)A(n)\alpha \quad (\text{A.75})$$

Here, we have made an important assumption that the flux per unit area is independent of the size of the cluster, effectively decoupling the total flux into the product of the flux per unit area and the surface area itself. This assumption is made for both the fluxes, onto and out of the clusters.  $p_{eq}(n)$  is the equilibrium concentration of clusters of size  $n$ , which is in general different from the instantaneous concentration  $f(n)$ .

We substitute the value of  $\alpha$  in Eq. A.75 in Eq. A.74 and obtain the following:

$$J(n) = \beta A(n-1)p_{eq}(n-1) \left[ \frac{f(n-1)}{p_{eq}(n-1)} - \frac{f(n)}{p_{eq}(n)} \right] \quad (\text{A.76})$$

If we consider the case where the instantaneous concentrations of clusters of size  $n-1$  and  $n$  are equal to their equilibrium concentrations, we get a rate of 0. Further, if in Eq. A.74, we calculate the quantity  $J(n) - J(n+1)$ , we recover Eq. 1.29.

$$\frac{\partial f(n,t)}{\partial t} = J(n) - J(n+1) \quad (\text{A.77})$$

This tells us that a time-invariant concentration of droplets is obtained when the rate of growth of droplets is independent of  $n$ . Appropriately modifying the rate equation gives us

$$\frac{J}{\beta A(n-1)p_{eq}(n-1)} = \frac{f(n-1)}{p_{eq}(n-1)} - \frac{f(n)}{p_{eq}(n)} \quad (\text{A.78})$$

We sum both sides from  $n = 2$  to  $n = \Lambda$ , some large cluster size, giving us

$$J \sum_{n=1}^{n=\Lambda} \frac{1}{\beta A(n)p_{eq}(n)} = \frac{f(1)}{p_{eq}(1)} - \frac{f(\Lambda)}{p_{eq}(\Lambda)} \quad (\text{A.79})$$

If we make the assumption here that  $f(1) \approx p_{eq}(1)$  and  $f(\Lambda) \approx 0$ , which is to say that the concentration of the monomers is close to the equilibrium value and that the number of large clusters is vanishingly small, we get the following expression for the rate

$$J = \frac{1}{\sum_{n=1}^{n=\Lambda} \frac{1}{\beta A(n)p_{eq}(n)}} \quad (\text{A.80})$$

Based on this expression, knowing the equilibrium cluster distribution tells us the rate. This equilibrium distribution can be calculated by considering the minimum

work required to form a cluster of size  $n$  as derived in Eq. A.68.

## A.4 Deriving the WHAM equations

In this section, we derive Eq. 2.63. Consider a set of distributions  $f_0, f_1, \dots, f_n$  such that adjacent distributions are overlapping. We can write the free energy differences in terms of the random variable of the distribution as.

$$F_n - F_0 = \Delta F_{0,n} = \Delta F_{0,1} + \Delta F_{1,2} + \dots + \Delta F_{n-1,n} \quad (\text{A.81})$$

Statistical errors in the estimated free energy difference compound and add up quadratically. Reducing this total error is the focus of this section. Specifically, we use the self-consistent weighted histogram method here [234, 235].

Let us begin by considering a system with an energy function  $U_0$ , hereafter, the original system. We can consider modifications of this system that involve the addition of another term in the energy to give us

$$U_i = U_0 + W_i \quad (\text{A.82})$$

Here, we consider the case of each additional energy term,  $W_i$ , the bias potential, as a function of some order parameter  $Q(r^N)$ . We can determine the histogram of  $Q$  values,

$$p_i(Q) = \frac{\int dr^N \exp[-\beta(U_0 + W_i)] \delta(Q - Q(r^N))}{\int dr^N \exp[-\beta(U_0 + W_i)]} \quad (\text{A.83})$$

The actual distribution can be written in terms of the original energy function as

$$p_0(Q) = \frac{\int dr^N \exp[-\beta U_0] \delta(Q - Q(r^N))}{\int dr^N \exp[-\beta U_0]} \quad (\text{A.84})$$

The Landau free energy difference can be written in terms of the distribution of the order parameter as

$$F(Q) = -k_B T \ln(p_0(Q)) \quad (\text{A.85})$$

We now describe the self-consistent method of arriving at  $p_0(Q)$  given a set of  $p_i(Q)$  from sampling distributions in the biased/modified ensemble.

We begin by considering the histogram of sampling events in the interval  $[Q, Q +$

$\Delta Q]$ ,  $H_i(Q)$ , with the total number of points given by  $M_i$ .

$$p(Q)\Delta Q = \langle H_i(Q) \rangle / M_i \quad (\text{A.86})$$

If the number of times  $Q$  is visited in bin  $i$  is considered to be Poisson distributed, then we can write the variance in the estimate  $p_i^{est}(Q)$  as

$$\langle p_i^{est}(Q)^2 \rangle - \langle p_i^{est}(Q) \rangle^2 = \frac{\langle H_i(Q)^2 \rangle - \langle H_i(Q) \rangle^2}{M_i^2} = \frac{H_i(Q)}{M_i^2} \quad (\text{A.87})$$

where we have used the fact that the mean and the variance of a Poisson distribution are equal. We can further substitute above to get

$$\langle p_i^{est}(Q)^2 \rangle - \langle p_i^{est}(Q) \rangle^2 = \frac{p_i(Q)\Delta Q}{M_i} \quad (\text{A.88})$$

For convenience we set  $\Delta Q = 1$  hereafter. Given that we have an expression for the variance in each of the estimated distributions, we now try to determine the original distribution,  $p_0(Q)$ , given the  $p_i(Q)$ . The simplest way to obtain the original distribution from any of the others, assuming that each  $p_i(Q)$  samples the full range of  $Q$  well enough to expect convergence in  $H_i(Q)$  is to use the following:

$$p_0(Q) = \exp(\beta W_i) \frac{z_i}{z_0} p_i(Q) \quad (\text{A.89})$$

Of course, it is often the case that each of the distributions  $p_i(Q)$  only sample some subset of the full  $Q$  range with some overlap between nearby windows. In such a case, the correct way to determine the original distribution would be

$$p_0^{est}(Q) = \sum_{i=1}^N \omega_i(Q) \exp(\beta W_i) \frac{z_i}{z_0} p_i^{est}(Q) \quad (\text{A.90})$$

with the added constraint that the so far undetermined weight functions satisfy

$$\sum_{i=1}^N \omega_i(Q) = 1 \quad (\text{A.91})$$

Given that  $z_i$  and  $z_0$  are also unknown, we need to choose  $\omega_i(Q)$  such that the variance in  $p_i^{est}(Q)$  is minimised.

Here we use two common results for the variance of random variables

- If two random variables are related as  $Y = mX$ , then the variance is related

as

$$Var(Y) = m^2 Var(X) \quad (\text{A.92})$$

- If  $Y = \sum X$  then

$$Var(Y) = \sum Var(X) + 2 \sum_{i < j} Cov(X_i, X_j) \quad (\text{A.93})$$

This then gives us

$$Var(p_0^{est}(Q)) = \sum_{i=1}^N \omega_i^2(Q) \exp(2\beta W_i) \left( \frac{z_i}{z_0} \right)^2 Var(p_i^{est}(Q)) \quad (\text{A.94})$$

substituting for the variance in the distributions  $p_i^{est}(Q)$  from Eq. A.88 gives us

$$Var(p_0^{est}(Q)) = \sum_{i=1}^N \omega_i^2(Q) \exp(2\beta W_i) \left( \frac{z_i}{z_0} \right)^2 \frac{p_i(Q)}{M_i} \quad (\text{A.95})$$

Substituting further from Eq. A.89 then gives

$$Var(p_0^{est}(Q)) = p_0(Q) \sum_{i=1}^N \omega_i^2(Q) \exp(\beta W_i) \frac{z_i}{z_0 M_i} \quad (\text{A.96})$$

We wish to find the set of  $\omega_i$  that minimises the LHS so we differentiate it, applying also the constraint in Eq. A.91. This gives us

$$\frac{\partial Var(p_0^{est}(Q))}{\partial \omega_i(Q)} = 2 \sum_{i=1}^N \omega_i(Q) \exp(\beta W_i) \frac{z_i}{z_0 M_i} = 0 \quad (\text{A.97})$$

We consider a form with an unknown parameter  $\alpha$

$$\omega_i(Q) = \alpha \exp(-\beta W_i) \frac{z_0 M_i}{z_i} \quad (\text{A.98})$$

Writing the constraint then gives

$$\sum_{i=1}^N \alpha \exp(-\beta W_i) \frac{z_0 M_i}{z_i} = 1$$

$$\alpha = \frac{1}{\sum_{i=1}^N \exp(-\beta W_i) \frac{z_0 M_i}{z_i}} \quad (\text{A.99})$$

We replace this expression in Eq. A.90 to get

$$\begin{aligned}
p_0^{est}(Q) &= \sum_{i=1}^N \omega_i(Q) \exp(\beta W_i) \frac{z_i}{z_0} p_i^{est}(Q) \\
p_0^{est}(Q) &= \frac{\sum_{i=1}^N \exp(-\beta W_i) \frac{z_i}{z_0 M_i} \exp(\beta W_i) \frac{z_0 M_i \langle H_i(Q) \rangle}{z_i}}{\sum_{i=1}^N \exp(-\beta W_i) \frac{z_i}{z_0 M_i}} \\
p_0^{est}(Q) &= \frac{\sum_{i=1}^N \langle H_i(Q) \rangle}{\sum_{i=1}^N \exp(-\beta W_i) \frac{z_0 M_i}{z_i}} \tag{A.100}
\end{aligned}$$

We can write the free energy difference  $\Delta F_i$

$$\Delta F_i = -k_B T \ln(z_i/z_0) \tag{A.101}$$

We then get

$$p_0^{est}(Q) = \frac{\sum_{i=1}^N \langle H_i(Q) \rangle}{\sum_{i=1}^N \exp(-\beta(W_i - \Delta F_i)) M_i} \tag{A.102}$$

To find the  $z_i$  and consequently, the  $\Delta F_i$ , we re-write the partition function in terms of the order parameter  $Q$

$$\begin{aligned}
z_i &= \int dr^N \exp[-\beta(U_0 + W_i)] \\
z_i &= \int dQ z_0 p_0(Q) \exp(-\beta W_i) \\
z_i &= \int dQ \exp(-\beta W_i) \frac{\sum_{j=1}^N \langle H_j(Q) \rangle}{\sum_{k=1}^N \exp(-\beta W_k) \frac{M_k}{z_k}} \tag{A.103}
\end{aligned}$$

This now allows us to write

$$\begin{aligned}
\Delta F_i = -k_B T \ln \left( \frac{z_i}{z_0} \right) &= \int dQ \exp(-\beta W_i) \frac{\sum_{j=1}^N \langle H_j(Q) \rangle}{\sum_{k=1}^N \exp(-\beta W_k) \frac{z_0 M_k}{z_k}} \\
\Delta F_i &= -k_B T \ln \left[ \int dQ \exp(-\beta W_i) p_0^{est}(Q) \right] \tag{A.104}
\end{aligned}$$

# List of publications

1. Goswami, Y., Vasisht, V. V., Frenkel, D., Debenedetti, P. G. and Sastry, S. “Thermodynamics and kinetics of crystallization in deeply supercooled stillinger–weber silicon”. *The Journal of Chemical Physics* 155 (19), 194502 (2021).
2. Goswami, Y., Sastry, S., “Metastable liquid-liquid transition in liquid silicon”, *manuscript under preparation*
3. Goswami, Y., Sastry, S., “Kinetic reconstruction of the free energy as a function of multiple order parameters”, *manuscript under preparation*



# Bibliography

- [1] S. Sastry and C. A. Angell, “Liquid–liquid phase transition in supercooled silicon,” *Nature materials*, vol. 2, no. 11, p. 739, 2003.
- [2] V. V. Vasisht, S. Saw, and S. Sastry, “Liquid–liquid critical point in supercooled silicon,” *Nature Physics*, vol. 7, no. 7, p. 549, 2011.
- [3] S. Sastry, P. G. Debenedetti, F. Sciortino, and H. E. Stanley, “Singularity-free interpretation of the thermodynamics of supercooled water,” *Physical Review E*, vol. 53, no. 6, p. 6144, 1996.
- [4] V. V. Vasisht and S. Sastry, “Liquid–liquid phase transition in supercooled silicon,” *Liquid Polymorphism*, vol. 152, pp. 463–517, 2013. arXiv:2108.13713.
- [5] S. Sastry, “Illuminating liquid polymorphism in silicon,” *Proceedings of the National Academy of Sciences*, vol. 107, no. 40, pp. 17063–17064, 2010.
- [6] F. Spaepen and D. Turnbull, “Kinetics of motion of crystal–melt interfaces,” in *American Institute of Physics Conference Series*, vol. 50 of *American Institute of Physics Conference Series*, pp. 73–83, Apr. 1979.
- [7] B. G. Bagley and H. S. Chen, “A calculation of the thermodynamic first order amorphous semiconductor to metallic liquid transition temperature,” in *American Institute of Physics Conference Series*, vol. 50 of *American Institute of Physics Conference Series*, pp. 97–101, Apr. 1979.
- [8] L. Aptekar, “Phase transitions in noncrystalline germanium and silicon,” in *Soviet Physics Doklady*, vol. 24, p. 993, 1979.
- [9] W. Zulehner, “The growth of highly pure silicon crystals,” *Metrologia*, vol. 31, no. 3, p. 255, 1994.
- [10] W. Zulehner, “Historical overview of silicon crystal pulling development,” *Materials Science and Engineering: B*, vol. 73, no. 1-3, pp. 7–15, 2000.

- [11] P. E. Tomaszewski, “Jan czochralski—father of the czochralski method,” *Journal of crystal growth*, vol. 236, no. 1-3, pp. 1–4, 2002.
- [12] G. Dhanaraj, K. Byrappa, V. Prasad, and M. Dudley, *Springer handbook of crystal growth*. Springer Science & Business Media, 2010.
- [13] R. J. Speedy, “Stability-limit conjecture. an interpretation of the properties of water,” *The Journal of Physical Chemistry*, vol. 86, no. 6, pp. 982–991, 1982.
- [14] P. H. Poole, F. Sciortino, U. Essmann, and H. E. Stanley, “Phase behaviour of metastable water,” *Nature*, vol. 360, no. 6402, pp. 324–328, 1992.
- [15] V. V. Vasisht, *Phase behaviour of supercooled liquid silicon*. PhD thesis, Jawaharlal Nehru Centre for Advanced Scientific Research, Bengaluru, 2013.
- [16] H. Tanaka, “Liquid–liquid transition and polyamorphism,” *The Journal of Chemical Physics*, vol. 153, no. 13, p. 130901, 2020.
- [17] O. Mishima and H. E. Stanley, “The relationship between liquid, supercooled and glassy water,” *Nature*, vol. 396, no. 6709, pp. 329–335, 1998.
- [18] D. T. Limmer and D. Chandler, “The putative liquid-liquid transition is a liquid-solid transition in atomistic models of water. ii,” *The Journal of chemical physics*, vol. 138, no. 21, p. 214504, 2013.
- [19] T. Kim, G. Lee, B. Sieve, A. Gangopadhyay, R. Hyers, T. Rathz, J. Rogers, D. Robinson, K. Kelton, and A. Goldman, “In situ high-energy x-ray diffraction study of the local structure of supercooled liquid si,” *Physical review letters*, vol. 95, no. 8, p. 085501, 2005.
- [20] M. Beye, F. Sorgenfrei, W. F. Schlotter, W. Wurth, and A. Föhlisch, “The liquid-liquid phase transition in silicon revealed by snapshots of valence electrons,” *Proceedings of the National Academy of Sciences*, vol. 107, no. 39, pp. 16772–16776, 2010.
- [21] S. Ashwin, U. Waghmare, and S. Sastry, “Metal-to-semimetal transition in supercooled liquid silicon,” *Physical review letters*, vol. 92, no. 17, p. 175701, 2004.

- [22] N. Jakse and A. Pasturel, “Liquid-liquid phase transformation in silicon: evidence from first-principles molecular dynamics simulations,” *Physical review letters*, vol. 99, no. 20, p. 205702, 2007.
- [23] P. Ganesh and M. Widom, “Liquid-liquid transition in supercooled silicon determined by first-principles simulation,” *Physical review letters*, vol. 102, no. 7, p. 075701, 2009.
- [24] M. Dharma-Wardana, D. D. Klug, and R. C. Remsing, “Liquid-liquid phase transitions in silicon,” *Physical review letters*, vol. 125, no. 7, p. 075702, 2020.
- [25] F. H. Stillinger and T. A. Weber, “Computer simulation of local order in condensed phases of silicon,” *Physical review B*, vol. 31, no. 8, p. 5262, 1985.
- [26] L. P. N. Rebelo, P. G. Debenedetti, and S. Sastry, “Singularity-free interpretation of the thermodynamics of supercooled water. ii. thermal and volumetric behavior,” *The Journal of chemical physics*, vol. 109, no. 2, pp. 626–633, 1998.
- [27] C. A. Angell, “Insights into phases of liquid water from study of its unusual glass-forming properties,” *Science*, vol. 319, no. 5863, pp. 582–587, 2008.
- [28] D. T. Limmer and D. Chandler, “The putative liquid-liquid transition is a liquid-solid transition in atomistic models of water,” *The Journal of chemical physics*, vol. 135, no. 13, p. 134503, 2011.
- [29] J. C. Palmer, F. Martelli, Y. Liu, R. Car, A. Z. Panagiotopoulos, and P. G. Debenedetti, “Metastable liquid–liquid transition in a molecular model of water,” *Nature*, vol. 510, no. 7505, p. 385, 2014.
- [30] F. Ricci, J. C. Palmer, Y. Goswami, S. Sastry, C. A. Angell, and P. G. Debenedetti, “A computational investigation of the thermodynamics of the stillinger-weber family of models at supercooled conditions,” *Molecular Physics*, pp. 1–15, 2019.
- [31] D. Chandler, “Statistical mechanics of isomerization dynamics in liquids and the transition state approximation,” *The Journal of Chemical Physics*, vol. 68, no. 6, pp. 2959–2970, 1978.
- [32] P. G. Bolhuis, D. Chandler, C. Dellago, and P. L. Geissler, “Transition path sampling: Throwing ropes over rough mountain passes, in the dark,” *Annual review of physical chemistry*, vol. 53, no. 1, pp. 291–318, 2002.

- [33] R. J. Allen, C. Valeriani, and P. R. Ten Wolde, "Forward flux sampling for rare event simulations," *Journal of physics: Condensed matter*, vol. 21, no. 46, p. 463102, 2009.
- [34] E. Vanden-Eijnden *et al.*, "Transition-path theory and path-finding algorithms for the study of rare events.," *Annual review of physical chemistry*, vol. 61, pp. 391–420, 2010.
- [35] J. B. Anderson, "Predicting rare events in molecular dynamics," *Advances in Chemical Physics*, vol. 91, pp. 381–432, 1995.
- [36] H. A. Kramers, "Brownian motion in a field of force and the diffusion model of chemical reactions," *Physica*, vol. 7, no. 4, pp. 284–304, 1940.
- [37] G. M. Torrie and J. P. Valleau, "Nonphysical sampling distributions in monte carlo free-energy estimation: Umbrella sampling," *Journal of Computational Physics*, vol. 23, no. 2, pp. 187–199, 1977.
- [38] R. J. Allen, D. Frenkel, and P. R. ten Wolde, "Simulating rare events in equilibrium or nonequilibrium stochastic systems," *The Journal of chemical physics*, vol. 124, no. 2, p. 024102, 2006.
- [39] C. Valeriani, R. J. Allen, M. J. Morelli, D. Frenkel, and P. Rein ten Wolde, "Computing stationary distributions in equilibrium and nonequilibrium systems with forward flux sampling," *The Journal of chemical physics*, vol. 127, no. 11, p. 114109, 2007.
- [40] T. S. Van Erp, D. Moroni, and P. G. Bolhuis, "A novel path sampling method for the calculation of rate constants," *The Journal of chemical physics*, vol. 118, no. 17, pp. 7762–7774, 2003.
- [41] A. Laio and M. Parrinello, "Escaping free-energy minima," *Proceedings of the National Academy of Sciences*, vol. 99, no. 20, pp. 12562–12566, 2002.
- [42] J. Wedekind, R. Strey, and D. Reguera, "New method to analyze simulations of activated processes," *The Journal of chemical physics*, vol. 126, no. 13, p. 134103, 2007.
- [43] J. Wedekind and D. Reguera, "Kinetic reconstruction of the free-energy landscape," *The Journal of Physical Chemistry B*, vol. 112, no. 35, pp. 11060–11063, 2008.

- [44] J. Wedekind, G. Chkonia, J. Wölk, R. Strey, and D. Reguera, “Crossover from nucleation to spinodal decomposition in a condensing vapor,” *The Journal of chemical physics*, vol. 131, no. 11, p. 114506, 2009.
- [45] P. G. Debenedetti, F. Sciortino, and G. H. Zerze, “Second critical point in two realistic models of water,” *Science*, vol. 369, no. 6501, pp. 289–292, 2020.
- [46] P.-R. t. Wolde *et al.*, “Simulation of homogeneous crystal nucleation close to coexistence,” *Faraday discussions*, vol. 104, pp. 93–110, 1996.
- [47] A. Reinhardt, J. P. Doye, E. G. Noya, and C. Vega, “Local order parameters for use in driving homogeneous ice nucleation with all-atom models of water,” *The Journal of chemical physics*, vol. 137, no. 19, p. 194504, 2012.
- [48] D. Kashchiev, *Nucleation*. Elsevier, 2000.
- [49] R. Becker and W. Doring, “Kinetic treatment of the nucleation in supersaturated vapors,” 1954.
- [50] M. C. Weinberg, W. H. Poisl, and L. Granasy, “Crystal growth and classical nucleation theory,” *Comptes Rendus Chimie*, vol. 5, no. 11, pp. 765–771, 2002.
- [51] R. Kurita and H. Tanaka, “Drastic enhancement of crystal nucleation in a molecular liquid by its liquid–liquid transition,” *Proceedings of the National Academy of Sciences*, vol. 116, no. 50, pp. 24949–24955, 2019.
- [52] J. W. Cahn and J. E. Hilliard, “Free energy of a nonuniform system. i. interfacial free energy,” *The Journal of chemical physics*, vol. 28, no. 2, pp. 258–267, 1958.
- [53] J. W. Cahn, “Free energy of a nonuniform system. ii. thermodynamic basis,” *The Journal of chemical physics*, vol. 30, no. 5, pp. 1121–1124, 1959.
- [54] E. Mendez-Villuendas, I. Saika-Voivod, and R. K. Bowles, “A limit of stability in supercooled liquid clusters,” *The Journal of chemical physics*, vol. 127, no. 15, p. 154703, 2007.
- [55] V. Holten, D. T. Limmer, V. Molinero, and M. A. Anisimov, “Nature of the anomalies in the supercooled liquid state of the mw model of water,” *The Journal of chemical physics*, vol. 138, no. 17, p. 174501, 2013.
- [56] T. Ramakrishnan and M. Yussouff, “First-principles order-parameter theory of freezing,” *Physical Review B*, vol. 19, no. 5, p. 2775, 1979.

- [57] D. W. Oxtoby, “New perspectives on freezing and melting,” *Nature*, vol. 347, no. 6295, pp. 725–730, 1990.
- [58] R. S. Singh and B. Bagchi, “Correlation between thermodynamic anomalies and pathways of ice nucleation in supercooled water,” *The Journal of chemical physics*, vol. 140, no. 16, p. 164503, 2014.
- [59] A. S. Bharadwaj and Y. Singh, “Density-functional theory for fluid-solid and solid-solid phase transitions,” *Physical Review E*, vol. 95, no. 3, p. 032120, 2017.
- [60] Y. Rosenfeld and P. Tarazona, “Density functional theory and the asymptotic high density expansion of the free energy of classical solids and fluids,” *Molecular Physics*, vol. 95.
- [61] D. Reguera and H. Reiss, “Extended modified liquid drop- dynamical nucleation theory (emld- dnt) approach to nucleation: A new theory,” *The Journal of Physical Chemistry B*, vol. 108, no. 51, pp. 19831–19842, 2004.
- [62] C. R. Buhariwalla, R. K. Bowles, I. Saika-Voivod, F. Sciortino, and P. H. Poole, “Free energy of formation of small ice nuclei near the widom line in simulations of supercooled water,” *The European Physical Journal E*, vol. 38, no. 5, pp. 1–11, 2015.
- [63] P. R. Ten Wolde, M. J. Ruiz-Montero, and D. Frenkel, “Numerical evidence for bcc ordering at the surface of a critical fcc nucleus,” *Physical review letters*, vol. 75, no. 14, p. 2714, 1995.
- [64] P. R. ten Wolde and D. Frenkel, “Enhancement of protein crystal nucleation by critical density fluctuations,” *Science*, vol. 277, no. 5334, pp. 1975–1978, 1997.
- [65] V. Talanquer and D. W. Oxtoby, “Crystal nucleation in the presence of a metastable critical point,” *The Journal of chemical physics*, vol. 109, no. 1, pp. 223–227, 1998.
- [66] D. Gebauer and H. Cölfen, “Prenucleation clusters and non-classical nucleation,” *Nano Today*, vol. 6, no. 6, pp. 564–584, 2011.
- [67] W. Lechner, C. Dellago, and P. G. Bolhuis, “Role of the prestructured surface cloud in crystal nucleation,” *Physical review letters*, vol. 106, no. 8, p. 085701, 2011.

- [68] E. B. Moore and V. Molinero, “Structural transformation in supercooled water controls the crystallization rate of ice,” *Nature*, vol. 479, no. 7374, p. 506, 2011.
- [69] M. Santra, R. S. Singh, and B. Bagchi, “Nucleation of a stable solid from melt in the presence of multiple metastable intermediate phases: wetting, ostwald’s step rule, and vanishing polymorphs,” *The Journal of Physical Chemistry B*, vol. 117, no. 42, pp. 13154–13163, 2013.
- [70] M. Santra, R. S. Singh, and B. Bagchi, “Polymorph selection during crystallization of a model colloidal fluid with a free energy landscape containing a metastable solid,” *Physical Review E*, vol. 98, no. 3, p. 032606, 2018.
- [71] P. Banerjee and B. Bagchi, “Effects of metastable phases on surface tension, nucleation, and the disappearance of polymorphs,” *The Journal of chemical physics*, vol. 149, no. 21, p. 214704, 2018.
- [72] P. Banerjee and B. Bagchi, “Facilitation of nucleation of polymorphic solids due to the presence of multiple metastable phases: Effects of nonclassical surface tension,” *The Journal of Physical Chemistry C*, vol. 123, no. 34, pp. 21207–21212, 2019.
- [73] J. Russo and H. Tanaka, “The microscopic pathway to crystallization in supercooled liquids,” *Scientific reports*, vol. 2, no. 1, pp. 1–8, 2012.
- [74] M. Iwamatsu, “Free-energy landscape of nucleation with an intermediate metastable phase studied using capillarity approximation,” *The Journal of chemical physics*, vol. 134, no. 16, p. 164508, 2011.
- [75] D. James, S. Beairsto, C. Hartt, O. Zavalov, I. Saika-Voivod, R. K. Bowles, and P. H. Poole, “Phase transitions in fluctuations and their role in two-step nucleation,” *The Journal of chemical physics*, vol. 150, no. 7, p. 074501, 2019.
- [76] D. Eaton, I. Saika-Voivod, R. K. Bowles, and P. H. Poole, “Free energy surface of two-step nucleation,” *The Journal of Chemical Physics*, vol. 154, no. 23, p. 234507, 2021.
- [77] B. J. Alder and T. E. Wainwright, “Phase transition for a hard sphere system,” *The Journal of chemical physics*, vol. 27, no. 5, pp. 1208–1209, 1957.
- [78] W. W. Wood and J. Jacobson, “Preliminary results from a recalculation of the monte carlo equation of state of hard spheres,” *The Journal of Chemical Physics*, vol. 27, no. 5, pp. 1207–1208, 1957.

- [79] M. Mandell, J. McTague, and A. Rahman, "Crystal nucleation in a three-dimensional lennard-jones system: A molecular dynamics study," *The journal of chemical physics*, vol. 64, no. 9, pp. 3699–3702, 1976.
- [80] S. Auer and D. Frenkel, "Suppression of crystal nucleation in polydisperse colloids due to increase of the surface free energy," *Nature*, vol. 413, no. 6857, p. 711, 2001.
- [81] S. Auer and D. Frenkel, "Numerical prediction of absolute crystallization rates in hard-sphere colloids," *The Journal of chemical physics*, vol. 120, no. 6, pp. 3015–3029, 2004.
- [82] J. Van Duijneveldt and D. Frenkel, "Computer simulation study of free energy barriers in crystal nucleation," *The Journal of chemical physics*, vol. 96, no. 6, pp. 4655–4668, 1992.
- [83] W. G. Hoover and F. H. Ree, "Use of computer experiments to locate the melting transition and calculate the entropy in the solid phase," *The Journal of Chemical Physics*, vol. 47, no. 12, pp. 4873–4878, 1967.
- [84] W. C. Swope and H. C. Andersen, "10 6-particle molecular-dynamics study of homogeneous nucleation of crystals in a supercooled atomic liquid," *Physical Review B*, vol. 41, no. 10, p. 7042, 1990.
- [85] W. Ostwald, "Studies on the formation and change of solid matter," *Z. Phys. Chem.*, vol. 22, pp. 289–302, 1897.
- [86] J. W. Gibbs, *The Scientific Papers of J. Willard Gibbs: Dynamics*. Dover Publ., 1961.
- [87] S. Alexander and J. McTague, "Should all crystals be bcc? landau theory of solidification and crystal nucleation," *Physical Review Letters*, vol. 41, no. 10, p. 702, 1978.
- [88] D. Frenkel and J. McTague, "Computer simulations of freezing and supercooled liquids," *Annual review of physical chemistry*, vol. 31, no. 1, pp. 491–521, 1980.
- [89] P. R. ten Wolde and D. Frenkel, "Homogeneous nucleation and the ostwald step rule," *Physical Chemistry Chemical Physics*, vol. 1, no. 9, pp. 2191–2196, 1999.



- 
- [90] J. Russo and H. Tanaka, “Crystal nucleation as the ordering of multiple order parameters,” *The Journal of chemical physics*, vol. 145, no. 21, p. 211801, 2016.
- [91] P. Bhimalapuram, S. Chakrabarty, and B. Bagchi, “Elucidating the mechanism of nucleation near the gas-liquid spinodal,” *Physical review letters*, vol. 98, no. 20, p. 206104, 2007.
- [92] D. Moroni, P. R. Ten Wolde, and P. G. Bolhuis, “Interplay between structure and size in a critical crystal nucleus,” *Physical review letters*, vol. 94, no. 23, p. 235703, 2005.
- [93] L. M. Ghiringhelli, C. Valeriani, E. Meijer, and D. Frenkel, “Local structure of liquid carbon controls diamond nucleation,” *Physical review letters*, vol. 99, no. 5, p. 055702, 2007.
- [94] J. Wedekind, L. Xu, S. V. Buldyrev, H. E. Stanley, D. Reguera, and G. Franzese, “Optimization of crystal nucleation close to a metastable fluid-fluid phase transition,” *Scientific reports*, vol. 5, p. 11260, 2015.
- [95] P. Beaucage and N. Mousseau, “Nucleation and crystallization process of silicon using the stillinger-weber potential,” *Physical Review B*, vol. 71, no. 9, p. 094102, 2005.
- [96] F. Romano, E. Sanz, and F. Sciortino, “Crystallization of tetrahedral patchy particles in silico,” *The Journal of chemical physics*, vol. 134, no. 17, p. 174502, 2011.
- [97] F. Romano, J. Russo, and H. Tanaka, “Novel stable crystalline phase for the stillinger-weber potential,” *Physical Review B*, vol. 90, no. 1, p. 014204, 2014.
- [98] J. Russo, F. Romano, and H. Tanaka, “New metastable form of ice and its role in the homogeneous crystallization of water,” *Nature materials*, vol. 13, no. 7, pp. 733–739, 2014.
- [99] B. Sadigh, L. Zepeda-Ruiz, and J. L. Belof, “Metastable–solid phase diagrams derived from polymorphic solidification kinetics,” *Proceedings of the National Academy of Sciences*, vol. 118, no. 9, 2021.
- [100] L. Lupi, A. Hudait, B. Peters, M. Grünwald, R. G. Mullen, A. H. Nguyen, and V. Molinero, “Role of stacking disorder in ice nucleation,” *Nature*, vol. 551, no. 7679, pp. 218–222, 2017.

- 
- [101] M. Fitzner, G. C. Sosso, S. J. Cox, and A. Michaelides, “Ice is born in low-mobility regions of supercooled liquid water,” *Proceedings of the National Academy of Sciences*, vol. 116, no. 6, pp. 2009–2014, 2019.
- [102] V. Thapar and F. A. Escobedo, “Simultaneous estimation of free energies and rates using forward flux sampling and mean first passage times,” *The Journal of chemical physics*, vol. 143, no. 24, p. 244113, 2015.
- [103] L. Qin, C. Dellago, and E. Kozeschnik, “An efficient method to reconstruct free energy profiles for diffusive processes in transition interface sampling and forward flux sampling simulations,” *The Journal of chemical physics*, vol. 150, no. 9, p. 094114, 2019.
- [104] R. S. DeFever and S. Sarupria, “Contour forward flux sampling: Sampling rare events along multiple collective variables,” *The Journal of chemical physics*, vol. 150, no. 2, p. 024103, 2019.
- [105] A. Haji-Akbari, “Forward-flux sampling with jumpy order parameters,” *The Journal of chemical physics*, vol. 149, no. 7, p. 072303, 2018.
- [106] L. Filion, M. Hermes, R. Ni, and M. Dijkstra, “Crystal nucleation of hard spheres using molecular dynamics, umbrella sampling, and forward flux sampling: A comparison of simulation techniques,” *The Journal of chemical physics*, vol. 133, no. 24, p. 244115, 2010.
- [107] J. R. Espinosa, C. Vega, C. Valeriani, and E. Sanz, “Seeding approach to crystal nucleation,” *The Journal of chemical physics*, vol. 144, no. 3, p. 034501, 2016.
- [108] J. Espinosa, C. Navarro, E. Sanz, C. Valeriani, and C. Vega, “On the time required to freeze water,” *The Journal of chemical physics*, vol. 145, no. 21, p. 211922, 2016.
- [109] O. Valsson, P. Tiwary, and M. Parrinello, “Enhancing important fluctuations: Rare events and metadynamics from a conceptual viewpoint,” *Annual review of physical chemistry*, vol. 67, pp. 159–184, 2016.
- [110] D. Quigley and P. Rodger, “A metadynamics-based approach to sampling crystallisation events,” *Molecular Simulation*, vol. 35, no. 7, pp. 613–623, 2009.

- [111] J. C. Palmer, R. Car, and P. G. Debenedetti, “The liquid–liquid transition in supercooled st<sub>2</sub> water: a comparison between umbrella sampling and well-tempered metadynamics,” *Faraday discussions*, vol. 167, pp. 77–94, 2013.
- [112] E. Donovan, F. Spaepen, D. Turnbull, J. Poate, and D. Jacobson, “Heat of crystallization and melting point of amorphous silicon,” *Applied Physics Letters*, vol. 42, no. 8, pp. 698–700, 1983.
- [113] E. Donovan, F. Spaepen, J. Poate, and D. Jacobson, “Homogeneous and interfacial heat releases in amorphous silicon,” *Applied physics letters*, vol. 55, no. 15, pp. 1516–1518, 1989.
- [114] J. T. Okada, P. H.-L. Sit, R. Ishikawa, T. Ishikawa, J. Chen, K. S. Nakayama, K. Maeda, Y. Yokoyama, Y. Watanabe, P.-F. Paradis, *et al.*, “Phase relation between supercooled liquid and amorphous silicon,” *Applied Physics Letters*, vol. 116, no. 9, p. 093705, 2020.
- [115] J. Okada, P.-L. Sit, Y. Watanabe, Y. Wang, B. Barbiellini, T. Ishikawa, M. Itou, Y. Sakurai, A. Bansil, R. Ishikawa, *et al.*, “Persistence of covalent bonding in liquid silicon probed by inelastic x-ray scattering,” *Physical review letters*, vol. 108, no. 6, p. 067402, 2012.
- [116] Y. Shao, F. Spaepen, and D. Turnbull, “An analysis of the formation of bulk amorphous silicon from the melt,” *Metallurgical and Materials Transactions A*, vol. 29, no. 7, pp. 1825–1828, 1998.
- [117] A. Hedler, S. L. Klaumünzer, and W. Wesch, “Amorphous silicon exhibits a glass transition,” *Nature Materials*, vol. 3, no. 11, p. 804, 2004.
- [118] T. Kim, A. Goldman, and K. Kelton, “Structural study of supercooled liquid silicon,” *Philosophical Magazine*, vol. 88, no. 2, pp. 171–179, 2008.
- [119] M. Watanabe, M. Adachi, T. Morishita, K. Higuchi, H. Kobatake, and H. Fukuyama, “Does supercooled liquid si have a density maximum?,” *Faraday discussions*, vol. 136, pp. 279–286, 2007.
- [120] T. Morishita, “How does tetrahedral structure grow in liquid silicon upon supercooling?,” *Physical review letters*, vol. 97, no. 16, p. 165502, 2006.
- [121] N. Jakse and A. Pasturel, “Dynamic aspects of the liquid-liquid phase transformation in silicon,” *The Journal of chemical physics*, vol. 129, no. 10, p. 104503, 2008.

- [122] P. Ganesh and M. Widom, “First-principles coexistence simulations of supercooled liquid silicon,” *Journal of Non-Crystalline Solids*, vol. 357, no. 2, pp. 442–445, 2011.
- [123] G. Zhao, Y. Yu, and X. Tan, “Nature of the first-order liquid-liquid phase transition in supercooled silicon,” *The Journal of chemical physics*, vol. 143, no. 5, p. 054508, 2015.
- [124] G. Zhao, Y. Yu, J. Yan, M. Ding, X. Zhao, and H. Wang, “Phase behavior of metastable liquid silicon at negative pressure: Ab initio molecular dynamics,” *Physical Review B*, vol. 93, no. 14, p. 140203, 2016.
- [125] R. C. Remsing, M. L. Klein, and J. Sun, “Refined description of liquid and supercooled silicon from ab initio simulations,” *Physical Review B*, vol. 97, no. 14, p. 140103, 2018.
- [126] V. L. Deringer, N. Bernstein, G. Csányi, C. B. Mahmoud, M. Ceriotti, M. Wilson, D. A. Drabold, and S. R. Elliott, “Origins of structural and electronic transitions in disordered silicon,” *Nature*, vol. 589, no. 7840, pp. 59–64, 2021.
- [127] C. Angell, S. Borick, and M. Grabow, “Glass transitions and first order liquid-metal-to-semiconductor transitions in 4-5-6 covalent systems,” *Journal of non-crystalline solids*, vol. 205, pp. 463–471, 1996.
- [128] D. Makhov and L. J. Lewis, “Isotherms for the liquid-gas phase transition in silicon from npt monte carlo simulations,” *Physical Review B*, vol. 67, no. 15, p. 153202, 2003.
- [129] J. Broughton and X. Li, “Phase diagram of silicon by molecular dynamics,” *Physical Review B*, vol. 35, no. 17, p. 9120, 1987.
- [130] D. Frenkel and A. J. Ladd, “New monte carlo method to compute the free energy of arbitrary solids. application to the fcc and hcp phases of hard spheres,” *The Journal of chemical physics*, vol. 81, no. 7, pp. 3188–3193, 1984.
- [131] V. V. Vasisht, J. Mathew, S. Sengupta, and S. Sastry, “Nesting of thermodynamic, structural, and dynamic anomalies in liquid silicon,” *The Journal of chemical physics*, vol. 141, no. 12, p. 124501, 2014.
- [132] S. Sengupta, V. V. Vasisht, and S. Sastry, “Diffusivity anomaly in modified stillinger-weber liquids,” *The Journal of chemical physics*, vol. 140, no. 4, p. 044503, 2014.

- [133] C. A. Angell and V. Kapko, “Potential tuning in the s–w system.(i) bringing t c, 2 to ambient pressure, and (ii) colliding t c, 2 with the liquid–vapor spinodal,” *Journal of Statistical Mechanics: Theory and Experiment*, vol. 2016, no. 9, p. 094004, 2016.
- [134] C. Desgranges and J. Delhommelle, “Role of liquid polymorphism during the crystallization of silicon,” *Journal of the American Chemical Society*, vol. 133, no. 9, pp. 2872–2874, 2011.
- [135] P. A. Apte, N. Pingua, A. K. Gautam, U. Kumar, S. Y. Willow, X. C. Zeng, and B. Kulkarni, “The freezing tendency towards 4-coordinated amorphous networks causes an increase in the heat capacity of supercooled stillinger–weber silicon,” *RSC Advances*, vol. 5, no. 55, pp. 44679–44686, 2015.
- [136] X. Mei and J. Eapen, “Dynamic transitions in molecular dynamics simulations of supercooled silicon,” *Physical Review B*, vol. 87, no. 13, p. 134206, 2013.
- [137] B. Shen, Z. Wang, F. Dong, Y. Guo, R. Zhang, Y. Zheng, S. Wang, C. Wang, K. Ho, and L. Chen, “Dynamics and diffusion mechanism of low-density liquid silicon,” *The Journal of Physical Chemistry B*, vol. 119, no. 47, pp. 14945–14951, 2015.
- [138] K. Zhang, H. Li, and Y. Jiang, “Liquid–liquid phase transition in quasi-two-dimensional supercooled silicon,” *Physical Chemistry Chemical Physics*, vol. 16, no. 33, pp. 18023–18028, 2014.
- [139] Y. He, X. Li, H. Li, Y. Jiang, and X. Bian, “Layering transition in confined silicon,” *Nanoscale*, vol. 6, no. 8, pp. 4217–4224, 2014.
- [140] Y. Lü, X. Zhang, M. Chen, and J.-Z. Jiang, “Exploring the nature of the liquid–liquid transition in silicon: a non-activated transformation,” *Physical Chemistry Chemical Physics*, vol. 17, no. 40, pp. 27167–27175, 2015.
- [141] C. Desgranges and J. Delhommelle, “Unraveling liquid polymorphism in silicon driven out-of-equilibrium,” *The Journal of Chemical Physics*, vol. 153, no. 5, p. 054502, 2020.
- [142] D. Dhabal, A. H. Nguyen, M. Singh, P. Khatua, V. Molinero, S. Bandyopadhyay, and C. Chakravarty, “Excess entropy and crystallization in stillinger–weber and lennard-jones fluids,” *The Journal of chemical physics*, vol. 143, no. 16, p. 164512, 2015.

- [143] Y. Liu, A. Z. Panagiotopoulos, and P. G. Debenedetti, “Low-temperature fluid-phase behavior of st2 water,” *The Journal of Chemical Physics*, vol. 131, no. 10, p. 104508, 2009.
- [144] Y. Liu, J. C. Palmer, A. Z. Panagiotopoulos, and P. G. Debenedetti, “Liquid-liquid transition in st2 water,” *The Journal of chemical physics*, vol. 137, no. 21, p. 214505, 2012.
- [145] F. Sciortino, I. Saika-Voivod, and P. H. Poole, “Study of the st2 model of water close to the liquid–liquid critical point,” *Physical Chemistry Chemical Physics*, vol. 13, no. 44, pp. 19759–19764, 2011.
- [146] P. H. Poole, R. K. Bowles, I. Saika-Voivod, and F. Sciortino, “Free energy surface of st2 water near the liquid-liquid phase transition,” *The Journal of chemical physics*, vol. 138, no. 3, p. 034505, 2013.
- [147] J. C. Palmer, P. H. Poole, F. Sciortino, and P. G. Debenedetti, “Advances in computational studies of the liquid–liquid transition in water and water-like models,” *Chemical reviews*, vol. 118, no. 18, pp. 9129–9151, 2018.
- [148] E. Jagla, “Liquid-liquid equilibrium for monodisperse spherical particles,” *Physical Review E*, vol. 63, no. 6, p. 061501, 2001.
- [149] L. Xu, P. Kumar, S. V. Buldyrev, S.-H. Chen, P. H. Poole, F. Sciortino, and H. E. Stanley, “Relation between the widom line and the dynamic crossover in systems with a liquid–liquid phase transition,” *Proceedings of the National Academy of Sciences*, vol. 102, no. 46, pp. 16558–16562, 2005.
- [150] F. Ricci and P. G. Debenedetti, “A free energy study of the liquid-liquid phase transition of the jagla two-scale potential,” *Journal of Chemical Sciences*, vol. 129, no. 7, pp. 801–823, 2017.
- [151] E. B. Moore and V. Molinero, “Ice crystallization in water’s “no-man’s land”,,” *The Journal of chemical physics*, vol. 132, no. 24, p. 244504, 2010.
- [152] E. B. Moore and V. Molinero, “Is it cubic? ice crystallization from deeply supercooled water,” *Physical Chemistry Chemical Physics*, vol. 13, no. 44, pp. 20008–20016, 2011.
- [153] R. S. Singh, J. W. Biddle, P. G. Debenedetti, and M. A. Anisimov, “Two-state thermodynamics and the possibility of a liquid-liquid phase transition

- in supercooled tip4p/2005 water,” *The Journal of chemical physics*, vol. 144, no. 14, p. 144504, 2016.
- [154] J. L. Abascal and C. Vega, “Widom line and the liquid–liquid critical point for the tip4p/2005 water model,” *The Journal of Chemical Physics*, vol. 133, no. 23, p. 234502, 2010.
- [155] Y. Li, J. Li, and F. Wang, “Liquid–liquid transition in supercooled water suggested by microsecond simulations,” *Proceedings of the National Academy of Sciences*, vol. 110, no. 30, pp. 12209–12212, 2013.
- [156] S. Cervený, F. Mallamace, J. Swenson, M. Vogel, and L. Xu, “Confined water as model of supercooled water,” *Chemical reviews*, vol. 116, no. 13, pp. 7608–7625, 2016.
- [157] R. Mancinelli, “The effect of confinement on water structure,” *Journal of Physics: Condensed Matter*, vol. 22, no. 40, p. 404213, 2010.
- [158] A. K. Soper, “Radical re-appraisal of water structure in hydrophilic confinement,” *Chemical physics letters*, vol. 590, pp. 1–15, 2013.
- [159] K. H. Kim, A. Späh, H. Pathak, F. Perakis, D. Mariedahl, K. Amann-Winkel, J. A. Sellberg, J. H. Lee, S. Kim, J. Park, *et al.*, “Maxima in the thermodynamic response and correlation functions of deeply supercooled water,” *Science*, vol. 358, no. 6370, pp. 1589–1593, 2017.
- [160] J. A. Sellberg, C. Huang, T. A. McQueen, N. Loh, H. Laksmono, D. Schlesinger, R. Sierra, D. Nordlund, C. Hampton, D. Starodub, *et al.*, “Ultrafast x-ray probing of water structure below the homogeneous ice nucleation temperature,” *Nature*, vol. 510, no. 7505, pp. 381–384, 2014.
- [161] L. Kringle, W. A. Thornley, B. D. Kay, and G. A. Kimmel, “Reversible structural transformations in supercooled liquid water from 135 to 245 k,” *Science*, vol. 369, no. 6510, pp. 1490–1492, 2020.
- [162] K. H. Kim, K. Amann-Winkel, N. Giovambattista, A. Späh, F. Perakis, H. Pathak, M. L. Parada, C. Yang, D. Mariedahl, T. Eklund, *et al.*, “Experimental observation of the liquid-liquid transition in bulk supercooled water under pressure,” *Science*, vol. 370, no. 6519, pp. 978–982, 2020.

- 
- [163] M. S. Shell, P. G. Debenedetti, and A. Z. Panagiotopoulos, “Molecular structural order and anomalies in liquid silica,” *Physical Review E*, vol. 66, no. 1, p. 011202, 2002.
- [164] J. R. Errington and P. G. Debenedetti, “Relationship between structural order and the anomalies of liquid water,” *Nature*, vol. 409, no. 6818, pp. 318–321, 2001.
- [165] P. H. Poole, M. Hemmati, and C. A. Angell, “Comparison of thermodynamic properties of simulated liquid silica and water,” *Physical review letters*, vol. 79, no. 12, p. 2281, 1997.
- [166] R. Chen, E. Lascaris, and J. C. Palmer, “Liquid–liquid phase transition in an ionic model of silica,” *The Journal of chemical physics*, vol. 146, no. 23, p. 234503, 2017.
- [167] I. Saika-Voivod, F. Sciortino, and P. H. Poole, “Computer simulations of liquid silica: Equation of state and liquid–liquid phase transition,” *Physical Review E*, vol. 63, no. 1, p. 011202, 2000.
- [168] E. Lascaris, M. Hemmati, S. V. Buldyrev, H. E. Stanley, and C. A. Angell, “Search for a liquid-liquid critical point in models of silica,” *The Journal of chemical physics*, vol. 140, no. 22, p. 224502, 2014.
- [169] I. Saika-Voivod, P. H. Poole, and R. K. Bowles, “Test of classical nucleation theory on deeply supercooled high-pressure simulated silica,” *The Journal of chemical physics*, vol. 124, no. 22, p. 224709, 2006.
- [170] I. Saika-Voivod, R. K. Bowles, and P. H. Poole, “Crystal nucleation in a supercooled liquid with glassy dynamics,” *Physical review letters*, vol. 103, no. 22, p. 225701, 2009.
- [171] J. Guo and J. C. Palmer, “Fluctuations near the liquid–liquid transition in a model of silica,” *Physical Chemistry Chemical Physics*, vol. 20, no. 39, pp. 25195–25202, 2018.
- [172] Y. Katayama, Y. Inamura, T. Mizutani, M. Yamakata, W. Utsumi, and O. Shimomura, “Macroscopic separation of dense fluid phase and liquid phase of phosphorus,” *Science*, vol. 306, no. 5697, pp. 848–851, 2004.



- [173] G. Monaco, S. Falconi, W. Crichton, and M. Mezouar, “Nature of the first-order phase transition in fluid phosphorus at high temperature and pressure,” *Physical review letters*, vol. 90, no. 25, p. 255701, 2003.
- [174] Y. Senda, F. Shimojo, and K. Hoshino, “The metal-nonmetal transition of liquid phosphorus by ab initio molecular-dynamics simulations,” *Journal of Physics: Condensed Matter*, vol. 14, no. 14, p. 3715, 2002.
- [175] M. Togaya, “Pressure dependences of the melting temperature of graphite and the electrical resistivity of liquid carbon,” *Physical review letters*, vol. 79, no. 13, p. 2474, 1997.
- [176] G. Galli, R. M. Martin, R. Car, and M. Parrinello, “Melting of diamond at high pressure,” *Science*, vol. 250, no. 4987, pp. 1547–1549, 1990.
- [177] X. Wang, S. Scandolo, and R. Car, “Carbon phase diagram from ab initio molecular dynamics,” *Physical review letters*, vol. 95, no. 18, p. 185701, 2005.
- [178] C. J. Wu, J. N. Glosli, G. Galli, and F. H. Ree, “Liquid-liquid phase transition in elemental carbon: A first-principles investigation,” *Physical review letters*, vol. 89, no. 13, p. 135701, 2002.
- [179] Y. He, H. Li, Y. Jiang, X. Li, and X. Bian, “Liquid-liquid phase transition and structure inheritance in carbon films,” *Scientific reports*, vol. 4, no. 1, pp. 1–6, 2014.
- [180] L. Henry, M. Mezouar, G. Garbarino, D. Sifré, G. Weck, and F. Datchi, “Liquid–liquid transition and critical point in sulfur,” *Nature*, vol. 584, no. 7821, pp. 382–386, 2020.
- [181] H. Tanaka, R. Kurita, and H. Mataka, “Liquid-liquid transition in the molecular liquid triphenyl phosphite,” *Physical review letters*, vol. 92, no. 2, p. 025701, 2004.
- [182] K.-i. Murata and H. Tanaka, “Liquid–liquid transition without macroscopic phase separation in a water–glycerol mixture,” *Nature materials*, vol. 11, no. 5, pp. 436–443, 2012.
- [183] M. Kobayashi and H. Tanaka, “The reversibility and first-order nature of liquid–liquid transition in a molecular liquid,” *Nature communications*, vol. 7, no. 1, pp. 1–8, 2016.

- [184] C. Angell and E. Sare, "Liquid-liquid immiscibility in common aqueous salt solutions at low temperatures," *The Journal of Chemical Physics*, vol. 49, no. 10, pp. 4713-4714, 1968.
- [185] H. Kanno and C. Angell, "Homogeneous nucleation and glass formation in aqueous alkali halide solutions at high pressures," *The Journal of Physical Chemistry*, vol. 81, no. 26, pp. 2639-2643, 1977.
- [186] K.-i. Murata and H. Tanaka, "General nature of liquid-liquid transition in aqueous organic solutions," *Nature communications*, vol. 4, no. 1, pp. 1-8, 2013.
- [187] M. Meyer and H. E. Stanley, "Liquid-liquid phase transition in confined water: A monte carlo study," *The Journal of Physical Chemistry B*, vol. 103, no. 44, pp. 9728-9730, 1999.
- [188] F. Mallamace, M. Broccio, C. Corsaro, A. Faraone, D. Majolino, V. Venuti, L. Liu, C.-Y. Mou, and S.-H. Chen, "Evidence of the existence of the low-density liquid phase in supercooled, confined water," *Proceedings of the national academy of sciences*, vol. 104, no. 2, pp. 424-428, 2007.
- [189] P. Kumar, Z. Yan, L. Xu, M. G. Mazza, S. Buldyrev, S.-H. Chen, S. Sastry, and H. Stanley, "Glass transition in biomolecules and the liquid-liquid critical point of water," *Physical review letters*, vol. 97, no. 17, p. 177802, 2006.
- [190] H. Stanley, S. Buldyrev, P. Kumar, F. Mallamace, M. G. Mazza, K. Stokely, L. Xu, and G. Franzese, "Water in nanoconfined and biological environments:(plenary talk, ngai-ruocco 2009 idmrcs conf.)," *Journal of Non-Crystalline Solids*, vol. 357, no. 2, pp. 629-640, 2011.
- [191] F. Mallamace, C. Corsaro, P. Baglioni, E. Fratini, and S.-H. Chen, "The dynamical crossover phenomenon in bulk water, confined water and protein hydration water," *Journal of Physics: Condensed Matter*, vol. 24, no. 6, p. 064103, 2012.
- [192] G. Schirò, M. Fomina, and A. Cupane, "Communication: Protein dynamical transition vs. liquid-liquid phase transition in protein hydration water," *The Journal of chemical physics*, vol. 139, no. 12, p. 121102, 2013.
- [193] C. Roberts, A. Panagiotopoulos, and P. G. Debenedetti, "Liquid-liquid immiscibility in pure fluids: polyamorphism in simulations of a network-forming fluid," *Physical review letters*, vol. 77, no. 21, p. 4386, 1996.

- 
- [194] M. A. Anisimov, M. Duška, F. Caupin, L. E. Amrhein, A. Rosenbaum, and R. J. Sadus, “Thermodynamics of fluid polyamorphism,” *Physical Review X*, vol. 8, no. 1, p. 011004, 2018.
- [195] M. Silbert and W. Young, “Liquid metals with structure factor shoulders,” *Physics Letters A*, vol. 58, no. 7, pp. 469–470, 1976.
- [196] K. Mon, N. Ashcroft, and G. Chester, “Core polarization and the structure of simple metals,” *Physical Review B*, vol. 19, no. 10, p. 5103, 1979.
- [197] R. Kurita and H. Tanaka, “Critical-like phenomena associated with liquid-liquid transition in a molecular liquid,” *Science*, vol. 306, no. 5697, pp. 845–848, 2004.
- [198] E. Rapoport, “Model for melting-curve maxima at high pressure,” *The Journal of Chemical Physics*, vol. 46, no. 8, pp. 2891–2895, 1967.
- [199] E. Ponyatovsky and O. Barkalov, “Pressure—induced amorphous phases,” *Materials science reports*, vol. 8, no. 4, pp. 147–191, 1992.
- [200] E. Ponyatovsky, “A thermodynamic approach to  $t$ - $p$  phase diagrams of substances in liquid and amorphous states,” *Journal of Physics: Condensed Matter*, vol. 15, no. 36, p. 6123, 2003.
- [201] G. Franzese, G. Malescio, A. Skibinsky, S. V. Buldyrev, and H. E. Stanley, “Generic mechanism for generating a liquid–liquid phase transition,” *Nature*, vol. 409, no. 6821, pp. 692–695, 2001.
- [202] S. Buldyrev, G. Franzese, N. Giovambattista, G. Malescio, M. Sadr-Lahijany, A. Scala, A. Skibinsky, and H. Stanley, “Models for a liquid–liquid phase transition,” *Physica A: Statistical Mechanics and its Applications*, vol. 304, no. 1-2, pp. 23–42, 2002.
- [203] F. Smallenburg, L. Filion, and F. Sciortino, “Erasing no-man’s land by thermodynamically stabilizing the liquid–liquid transition in tetrahedral particles,” *Nature physics*, vol. 10, no. 9, pp. 653–657, 2014.
- [204] F. Smallenburg, L. Filion, and F. Sciortino, “Liquid–liquid phase transitions in tetrahedrally coordinated fluids via wertheim theory,” *The Journal of Physical Chemistry B*, vol. 119, no. 29, pp. 9076–9083, 2015.

- [205] J. Russo, K. Akahane, and H. Tanaka, “Water-like anomalies as a function of tetrahedrality,” *Proceedings of the National Academy of Sciences*, vol. 115, no. 15, pp. E3333–E3341, 2018.
- [206] V. Holten and M. Anisimov, “Entropy-driven liquid–liquid separation in supercooled water,” *Scientific reports*, vol. 2, no. 1, pp. 1–7, 2012.
- [207] V. Holten, J. C. Palmer, P. H. Poole, P. G. Debenedetti, and M. A. Anisimov, “Two-state thermodynamics of the st2 model for supercooled water,” *The Journal of chemical physics*, vol. 140, no. 10, p. 104502, 2014.
- [208] S. Sastry, F. Sciortino, and H. E. Stanley, “Limits of stability of the liquid phase in a lattice model with water-like properties,” *The Journal of chemical physics*, vol. 98, no. 12, pp. 9863–9872, 1993.
- [209] P. H. Poole, F. Sciortino, T. Grande, H. E. Stanley, and C. A. Angell, “Effect of hydrogen bonds on the thermodynamic behavior of liquid water,” *Physical review letters*, vol. 73, no. 12, p. 1632, 1994.
- [210] K. Stokely, M. G. Mazza, H. E. Stanley, and G. Franzese, “Effect of hydrogen bond cooperativity on the behavior of water,” *Proceedings of the National Academy of Sciences*, vol. 107, no. 4, pp. 1301–1306, 2010.
- [211] C. A. Cerdeiriña, J. Troncoso, D. González-Salgado, P. G. Debenedetti, and H. E. Stanley, “Water’s two-critical-point scenario in the ising paradigm,” *The Journal of chemical physics*, vol. 150, no. 24, p. 244509, 2019.
- [212] P. Chitnelawong, F. Sciortino, and P. H. Poole, “The stability-limit conjecture revisited,” *The Journal of chemical physics*, vol. 150, no. 23, p. 234502, 2019.
- [213] E. La Nave, S. Sastry, F. Sciortino, and P. Tartaglia, “Solution of lattice gas models in the generalized ensemble on the bethe lattice,” *Physical Review E*, vol. 59, no. 6, p. 6348, 1999.
- [214] P. Gallo and F. Sciortino, “Ising universality class for the liquid-liquid critical point of a one component fluid: A finite-size scaling test,” *Physical review letters*, vol. 109, no. 17, p. 177801, 2012.
- [215] J. Luo, L. Xu, E. Lascaris, H. E. Stanley, and S. V. Buldyrev, “Behavior of the widom line in critical phenomena,” *Physical review letters*, vol. 112, no. 13, p. 135701, 2014.

- [216] B. Widom, “Equation of state in the neighborhood of the critical point,” *The Journal of Chemical Physics*, vol. 43, no. 11, pp. 3898–3905, 1965.
- [217] J. Wang, C. A. Cerdeiriña, M. A. Anisimov, and J. V. Sengers, “Principle of isomorphism and complete scaling for binary-fluid criticality,” *Physical Review E*, vol. 77, no. 3, p. 031127, 2008.
- [218] D. Fuentesvilla and M. Anisimov, “Scaled equation of state for supercooled water near the liquid-liquid critical point,” *Physical review letters*, vol. 97, no. 19, p. 195702, 2006.
- [219] C. Bertrand and M. Anisimov, “Peculiar thermodynamics of the second critical point in supercooled water,” *The Journal of Physical Chemistry B*, vol. 115, no. 48, pp. 14099–14111, 2011.
- [220] M. E. Fisher and B. Widom, “Decay of correlations in linear systems,” *The Journal of Chemical Physics*, vol. 50, no. 9, pp. 3756–3772, 1969.
- [221] N. Wilding and A. Bruce, “Density fluctuations and field mixing in the critical fluid,” *Journal of Physics: Condensed Matter*, vol. 4, no. 12, p. 3087, 1992.
- [222] S. Saw, N. L. Ellegaard, W. Kob, and S. Sastry, “Structural relaxation of a gel modeled by three body interactions,” *Physical review letters*, vol. 103, no. 24, p. 248305, 2009.
- [223] S. Plimpton, “Fast parallel algorithms for short-range molecular dynamics,” *Journal of computational physics*, vol. 117, no. 1, pp. 1–19, 1995.
- [224] G. J. Martyna, D. J. Tobias, and M. L. Klein, “Constant pressure molecular dynamics algorithms,” *The Journal of chemical physics*, vol. 101, no. 5, pp. 4177–4189, 1994.
- [225] W. Shinoda, M. Shiga, and M. Mikami, “Rapid estimation of elastic constants by molecular dynamics simulation under constant stress,” *Physical Review B*, vol. 69, no. 13, p. 134103, 2004.
- [226] M. E. Tuckerman, J. Alejandre, R. López-Rendón, A. L. Jochim, and G. J. Martyna, “A liouville-operator derived measure-preserving integrator for molecular dynamics simulations in the isothermal–isobaric ensemble,” *Journal of Physics A: Mathematical and General*, vol. 39, no. 19, p. 5629, 2006.

- [227] P. G. Debenedetti, *Metastable liquids: concepts and principles*. Princeton University Press, 1996.
- [228] P. J. Steinhardt, D. R. Nelson, and M. Ronchetti, “Bond-orientational order in liquids and glasses,” *Physical Review B*, vol. 28, no. 2, p. 784, 1983.
- [229] T. A. Kesselring, E. Lascaris, G. Franzese, S. V. Buldyrev, H. J. Herrmann, and H. E. Stanley, “Finite-size scaling investigation of the liquid-liquid critical point in st2 water and its stability with respect to crystallization,” *The Journal of Chemical Physics*, vol. 138, no. 24, p. 244506, 2013.
- [230] R. Zwanzig, *Nonequilibrium statistical mechanics*. Oxford University Press, 2001.
- [231] S. E. Lundrigan and I. Saika-Voivod, “Test of classical nucleation theory and mean first-passage time formalism on crystallization in the lennard-jones liquid,” *The Journal of Chemical Physics*, vol. 131, no. 10, p. 104503, 2009.
- [232] A. Pérez and A. Rubio, “A molecular dynamics study of water nucleation using the tip4p/2005 model,” *The Journal of chemical physics*, vol. 135, no. 24, p. 244505, 2011.
- [233] D. Frenkel and B. Smit, *Understanding molecular simulation: from algorithms to applications*, vol. 1. Elsevier, 2001.
- [234] A. M. Ferrenberg and R. H. Swendsen, “Optimized monte carlo data analysis,” *Computers in Physics*, vol. 3, no. 5, pp. 101–104, 1989.
- [235] S. Kumar, J. M. Rosenberg, D. Bouzida, R. H. Swendsen, and P. A. Kollman, “The weighted histogram analysis method for free-energy calculations on biomolecules. i. the method,” *Journal of computational chemistry*, vol. 13, no. 8, pp. 1011–1021, 1992.
- [236] J. D. Chodera, W. C. Swope, J. W. Pitner, C. Seok, and K. A. Dill, “Use of the weighted histogram analysis method for the analysis of simulated and parallel tempering simulations,” *Journal of Chemical Theory and Computation*, vol. 3, no. 1, pp. 26–41, 2007.
- [237] S. Zhang, L.-M. Wang, X. Zhang, L. Qi, S. Zhang, M. Ma, and R. Liu, “Polymorphism in glassy silicon: Inherited from liquid-liquid phase transition in supercooled liquid,” *Scientific reports*, vol. 5, no. 1, pp. 1–5, 2015.

- [238] L. Maibaum, “Comment on “elucidating the mechanism of nucleation near the gas-liquid spinodal”,” *Physical review letters*, vol. 101, no. 1, p. 019601, 2008.
- [239] S. Chakrabarty, M. Santra, and B. Bagchi, “Chakrabarty, santra, and bagchi reply,” *Physical Review Letters*, vol. 101, no. 1, p. 019602, 2008.
- [240] H. Reiss and R. K. Bowles, “Some fundamental statistical mechanical relations concerning physical clusters of interest to nucleation theory,” *The Journal of chemical physics*, vol. 111, no. 16, pp. 7501–7504, 1999.
- [241] P. Kumar, S. V. Buldyrev, F. Sciortino, E. Zaccarelli, and H. E. Stanley, “Static and dynamic anomalies in a repulsive spherical ramp liquid: Theory and simulation,” *Physical Review E*, vol. 72, no. 2, p. 021501, 2005.
- [242] E. Lascaris, T. A. Kesselring, G. Franzese, S. V. Buldyrev, H. J. Herrmann, and H. E. Stanley, “Response functions near the liquid-liquid critical point of st2 water,” in *AIP Conference Proceedings*, vol. 1518, pp. 520–526, American Institute of Physics, 2013.
- [243] J. B. Kuipers, *Quaternions and rotation sequences: a primer with applications to orbits, aerospace, and virtual reality*. Princeton university press, 1999.
- [244] B. Peters, P. G. Bolhuis, R. G. Mullen, and J.-E. Shea, “Reaction coordinates, one-dimensional smoluchowski equations, and a test for dynamical self-consistency,” *The Journal of chemical physics*, vol. 138, no. 5, p. 054106, 2013.
- [245] S. R. Elliott, “Medium-range structural order in covalent amorphous solids,” *Nature*, vol. 354, no. 6353, pp. 445–452, 1991.
- [246] M. F. Thorpe, “Continuous deformations in random networks,” *Journal of Non-Crystalline Solids*, vol. 57, no. 3, pp. 355–370, 1983.
- [247] A. C. Belch and S. A. Rice, “The distribution of rings of hydrogen-bonded molecules in a model of liquid water,” *The Journal of chemical physics*, vol. 86, no. 10, pp. 5676–5682, 1987.
- [248] U. Gasser, F. Ziese, and G. Maret, “Characterization of local structures with bond-order parameters and graphs of the nearest neighbors, a comparison,” *The European Physical Journal Special Topics*, vol. 223, no. 3, pp. 455–467, 2014.

- [249] D. Franzblau, “Computation of ring statistics for network models of solids,” *Physical Review B*, vol. 44, no. 10, p. 4925, 1991.
- [250] A. K. Soper and M. A. Ricci, “Structures of high-density and low-density water,” *Physical review letters*, vol. 84, no. 13, p. 2881, 2000.
- [251] Z. Yan, S. V. Buldyrev, P. Kumar, N. Giovambattista, P. G. Debenedetti, and H. E. Stanley, “Structure of the first-and second-neighbor shells of simulated water: Quantitative relation to translational and orientational order,” *Physical Review E*, vol. 76, no. 5, p. 051201, 2007.
- [252] A. Malins, S. R. Williams, J. Eggers, and C. P. Royall, “Identification of structure in condensed matter with the topological cluster classification,” *The Journal of chemical physics*, vol. 139, no. 23, p. 234506, 2013.
- [253] J. D. Honeycutt and H. C. Andersen, “Molecular dynamics study of melting and freezing of small lennard-jones clusters,” *Journal of Physical Chemistry*, vol. 91, no. 19, pp. 4950–4963, 1987.
- [254] C. L. Kelchner, S. Plimpton, and J. Hamilton, “Dislocation nucleation and defect structure during surface indentation,” *Physical review B*, vol. 58, no. 17, p. 11085, 1998.
- [255] A. Stukowski, “Structure identification methods for atomistic simulations of crystalline materials,” *Modelling and Simulation in Materials Science and Engineering*, vol. 20, no. 4, p. 045021, 2012.
- [256] E. A. Lazar, J. Han, and D. J. Srolovitz, “Topological framework for local structure analysis in condensed matter,” *Proceedings of the National Academy of Sciences*, vol. 112, no. 43, pp. E5769–E5776, 2015.
- [257] P. M. Larsen, S. Schmidt, and J. Schiøtz, “Robust structural identification via polyhedral template matching,” *Modelling and Simulation in Materials Science and Engineering*, vol. 24, no. 5, p. 055007, 2016.
- [258] A. Goswami and J. K. Singh, “A hybrid topological and shape-matching approach for structure analysis,” *The Journal of Chemical Physics*, vol. 154, no. 15, p. 154502, 2021.
- [259] E. Duboué-Dijon and D. Laage, “Characterization of the local structure in liquid water by various order parameters,” *The Journal of Physical Chemistry B*, vol. 119, no. 26, pp. 8406–8418, 2015.



- [260] W. F. Reinhart and A. Z. Panagiotopoulos, “Automated crystal characterization with a fast neighborhood graph analysis method,” *Soft matter*, vol. 14, no. 29, pp. 6083–6089, 2018.
- [261] T. Zhou, E. Martinez-Baez, G. Schenter, and A. E. Clark, “Pagerank as a collective variable to study complex chemical transformations and their energy landscapes,” *The Journal of chemical physics*, vol. 150, no. 13, p. 134102, 2019.
- [262] P. M. Piaggi and M. Parrinello, “Entropy based fingerprint for local crystalline order,” *The Journal of chemical physics*, vol. 147, no. 11, p. 114112, 2017.
- [263] P. M. Piaggi, O. Valsson, and M. Parrinello, “Enhancing entropy and enthalpy fluctuations to drive crystallization in atomistic simulations,” *Physical review letters*, vol. 119, no. 1, p. 015701, 2017.
- [264] P. M. Piaggi and M. Parrinello, “Predicting polymorphism in molecular crystals using orientational entropy,” *Proceedings of the National Academy of Sciences*, vol. 115, no. 41, pp. 10251–10256, 2018.
- [265] P. Tiwary and B. Berne, “Spectral gap optimization of order parameters for sampling complex molecular systems,” *Proceedings of the National Academy of Sciences*, vol. 113, no. 11, pp. 2839–2844, 2016.
- [266] Z. Smith, D. Pramanik, S.-T. Tsai, and P. Tiwary, “Multi-dimensional spectral gap optimization of order parameters (sgoop) through conditional probability factorization,” *The Journal of chemical physics*, vol. 149, no. 23, p. 234105, 2018.
- [267] S.-T. Tsai, Z. Smith, and P. Tiwary, “Sgoop-d: Estimating kinetic distances and reaction coordinate dimensionality for rare event systems from biased/unbiased simulations,” *Journal of Chemical Theory and Computation*, vol. 17, no. 11, pp. 6757–6765, 2021.
- [268] D. Mendels, G. Piccini, and M. Parrinello, “Collective variables from local fluctuations,” *The journal of physical chemistry letters*, vol. 9, no. 11, pp. 2776–2781, 2018.
- [269] Q. Li, B. Lin, and W. Ren, “Computing committor functions for the study of rare events using deep learning,” *The Journal of Chemical Physics*, vol. 151, no. 5, p. 054112, 2019.

- 
- [270] L. Bonati, G. Piccini, and M. Parrinello, “Deep learning the slow modes for rare events sampling,” *Proceedings of the National Academy of Sciences*, vol. 118, no. 44, 2021.
- [271] L. Woodcock, C. Angell, and P. Cheeseman, “Molecular dynamics studies of the vitreous state: Simple ionic systems and silica,” *The Journal of chemical physics*, vol. 65, no. 4, pp. 1565–1577, 1976.
- [272] N. B. Wilding, “Simulation studies of fluid critical behaviour,” *Journal of Physics: Condensed Matter*, vol. 9, no. 3, p. 585, 1997.
- [273] C. Dellago, P. G. Bolhuis, F. S. Csajka, and D. Chandler, “Transition path sampling and the calculation of rate constants,” *The Journal of chemical physics*, vol. 108, no. 5, pp. 1964–1977, 1998.
- [274] T. S. Van Erp and P. G. Bolhuis, “Elaborating transition interface sampling methods,” *Journal of computational Physics*, vol. 205, no. 1, pp. 157–181, 2005.
- [275] “General discussion,” *Faraday Discuss.*, vol. 167, pp. 109–143, 2013.